The New Idria Serpentinite

A thesis presented

by

Marcus Robinson Van Baalen, II

to

The Department of Earth and Planetary Sciences

in partial fulfillment of the requirements
for the degree of
Doctor of Philospohy
in the subject of
Geology
Harvard University
Cambridge, Massachusetts

May, 1995

HARVARD UNIVERSITY

THE GRADUATE SCHOOL OF ARTS AND SCIENCES

THESIS ACCEPTANCE CERTIFICATE

The undersigned, appointed by the

Division

Department Earth and Planetary Sciences

Committee

have examined a thesis entitled

"The New Idria Serpentinite"

presented by Marcus van Baalen

candidate for the degree of Doctor of Philosophy and hereby certify that it is worthy of acceptance.

Signature Heinrich D Holland

Typed name Prof. Heinrich D. Holland

Signature Charles W. Burnham

Typed name Prof. Charles W. Burnham

Signature James B. Thompson

Typed name Prof. James B. Thompson

Roberta L. Rudnick

Asst. Prof. Roberta L. Rudnick

Date May 3rd 1995

Date

Abstract

This thesis describes the mineralogy and petrology of the serpentinite massif at New Idria, California, USA. This serpentinite is an oval, 23 x 8 km body, interpreted as a part of the Mesozoic Coast Range Ophiolite. Diapiric emplacement within the Coast Ranges has resulted in a piercement structure or tectonic window, lying just east of the San Andreas fault system northeast of Parkfield. The mineralogy of the serpentinite is dominated by chrysotile; New Idria is one of the largest deposits of chrysotile asbestos in the world. A model for the generation of short fiber chrysotile asbestos is proposed. Locally within the serpentinite, tectonic blocks or "knockers" of several distinct rock types are preserved. Some blocks contain exotic Ti-rich minerals that previously were regarded as metasomatic; these are reinterpreted as the products of essentially isochemical metamorphism. Blocks of all types have experienced M1 and M2 metamorphism, of blueschist/greenschist and sub-greenschist facies respectively. It is proposed that M2 metamorphism is related to passage of the Mendocino Triple Junction in the Miocene. Blocks consisting of chlorite + diopside + Ti-garnet are interpreted as metapyroxenites. Blocks containing the rare Ti-minerals benitoite and neptunite are interpreted as re-metamorphosed Franciscan mafic schists and greenstones. Massive antigorite blocks have a thermal history separate in part from the rest of the serpentinite. Approximately 300 chemical analyses of Ti-andradite and Ti-grossular garnets and their coexisting minerals are presented.

Public policy issues, related to the largely unfounded concerns about health hazards of chrysotile asbestos, have brought recent attention to New Idria. Fluvial transport of chrysotile asbestos from New Idria eastward into the San Joaquin Valley has been taking place for as much as 12 million years. Since the completion of the California Aqueduct, some of the chrysotile asbestos has gone into the canal, mainly under flood conditions. Therefore the downstream users of this water have found chrysotile asbestos fibers in the water. Concern about the possible health hazards of this condition has been greatly overstated; the hazard is negligible. It will be a matter for science and public policy together to find a safe and economical solution to these issues.

Principal Advisor: Prof. Heinrich D. Holland

Table of Contents

Chapter 1 - Introduction and Regional Geology

Chapter 2 - History of Scientific Investigations of the New Idria District

Chapter 3 - Mineralogy & Petrology of the New Idria Serpentinite

Chapter 4 - Mineralogy and Petrology of the Tectonic Inclusions

Chapter 5 - Compositions and Mineral Associations of Garnets from the New Idria Serpentinite

Chapter 6 - Titanium Mobility in Metamorphic Systems

Chapter 7 - Discussion and Conclusions

List of Plates

List of Figures

List of Tables

To Louisa and Emily

Acknowledgements

The successful completion of this thesis is due in large part to the good advice and counsel that I received from a large number of people. In this section I will try to acknowledge these contributions as best I can, but inevitably some people will be left off the list. To these unnamed people, thank you nonetheless.

First I want to thank Prof. Heinrich D. Holland, my principal advisor, for his unflagging support and assistance, and for the battles on the back of envelopes, as described in song by Tony Lasaga. I was very fortunate to be able to show Dick something of New Idria, albeit under ferocious weather conditions, during a post-GSA field trip in 1991.

Next, I am indebted to Prof. James B. Thompson, Jr., who provided early encouragement and wisdom in the thesis project, as well as theoretical and field-oriented guidance during the course of the investigations. When I began this study, Jim was my principal advisor; at the time of his retirement and change to emeritus status, he was succeeded in this role by Dick Holland. This change was a bonanza to me as a graduate student, because thenceforth I enjoyed, in practice, the benefits of *two* principal advisors. Their encouragement, seemingly limitless patience, and keen insights from complementary points of view, were critical success factors in the study.

Next, I wish to acknowledge the long-time friendship and support of Prof. Charles W. Burnham. As of this writing I have known Charlie for 29 years; it was he who first encouraged me to take up the study of geology in a rigorous fashion. During these years he has been a mentor and unfailing friend. During the thesis project he was a continual source of mineralogical wisdom, and of reality checks on some of my more outlandish hypotheses.

This thesis would never have been written without the impetus provided by Elizabeth A. Zbinden, of Stanford University. Elizabeth introduced me to the New Idria District, and equally importantly, to many fine colleagues at Stanford. She served as my field assistant during the 1989 field season, and as a good friend during some of the discouraging times that seem to be an inescapable part of graduate study.

Dr. David S. O'Hanley of the University of Saskatchewan played a key role in this study. Dave introduced me to the complexities of serpentine textures and phase relations. I was pleased to visit New Idria on two occasions with him.

At one time or another I consulted about my project with nearly every faculty member in the Dept. of Earth and Planetary Sciences at Harvard; in particular I want to thank Visiting Prof. Theresa S. Bowers and Profs. Göran Ekstrom, the late John Haller, Stein B. Jacobsen, Ulrich Petersen, Roberta Rudnick, Jane Selverstone, Raymond Siever, and Joann Stock.

Many members of the professional staff of the EPS Dept at Harvard. also contributed to my project. These include Dr. Antje Danielson, Joan Donahue, Dr. Carl Francis, Dr. Joan Fryxell, Dave Lange, Bill Metropolis, Dr. Ron Pflaum, Debbie Rich, Dr. Ed Roedder, Pauline Solomon, Harold Thompson and Connie Wick. Special thanks go to Larry Pitman and the corps of volunteers at the Harvard Mineralogical Museum. Additional thanks go to Pete Dawson of U. Mass. Amherst.

Much of the field work for this study was supported by grants from the Reginald Daly Fund at Harvard, as well as the Graduate Student Council. I am indebted to the Geology Dept. at Stanford for providing an intellectual "base camp" and the use of their field vehicles for my investigations at New Idria, which is about a four hour drive from the Stanford campus. I particularly want to thank Profs. Gordon E. Brown, Jr., Robert G. Coleman, George A. Parks, and Jonathan F. Stebbins for their encouragement and advice. I also want to thank Dr. Barbara M. Bekken and Prof. Michael F. Hochella for intellectual and logistical support.

Many faculty members at other universities and government institutions also helped significantly. In particular I wish to acknowledge John Ayers (Vanderbilt), Rob Berman (GSC), Wally Bothner (UNH), Bob Christiansen (USGS), Barb Dutrow (LSU), Marta Flohr (USGS), Reto Gieré (ETH), Tim Grove (MIT), Chuck Guidotti (Maine), George Guthrie (Los Alamos), Bob Jachens (USGS), Jo Laird (UNH), Marvin Lanphere (USGS), Mac Ross (USGS), George Rossman (Cal Tech), Cathy Skinner (Yale), Joe Smyth (Colorado), and Walt Trzcienski (Montreal).

Many ranchers, miners, and government officials in the New Idria area also helped my cause. Some of these include Buzz Gray (Gem Mine), Dave and Sharon Teague (Los

Gatos Creek Ranch), Roger Hopper and John Myers (KCAC), Dan Meer and Dick Procunier (EPA, San Francisco), and Tim Moore and Ron Smith (BLM, Hollister).

No graduate student can really survive without the friendship and support of fellow-traveler students. I particularly wish to acknowledge the friendship and useful scientific conversations with John Arnason (Stanford), Gary Axen, Ximena Barrientos, Bill Carey, Lou Derry, Chip Green, Harry Hummel, Raymond Jannas, Carlos Jove (Stanford), Ro Kinzler (MIT), Claudia Lewis, Mark Linker, Suzanne MacEnroe (U. Mass.), Andy MacFarlane, Othmar Müntener (ETH), English Pearcy, Kirsten Peters, Rob Rye, Giovanni Ruggieri (Firenze), Zeke Snow, Naylor Stone and Marc Willis (Washington).

My field work at New Idria was made more pleasant and productive through the assistance of Mr. Stephen L. Hansen and his wife Deborah, and their three daughters Anna, Sarah, and Naomi. The Hansens provided food and lodging at their remote cabin, and tireless field assistance throughout the area.

I wish also to acknowledge the support and encouragement of present and former members of the Harvard administration in this project, particularly Dale P. Flecker, Robert H. Scott, Stephen C. Hall, Howard L. Resnikoff and Ronald Orcutt.

In the end of course it was the patience and understanding of my family that made the entire effort both possible and enjoyable. My wife Louisa, my daughter Emily, my father Joseph and my sister Frieda were a limitless source of inspiration and unstinting love to me; without their help, all my efforts would have been for nought.

Cambridge, Massachusetts
May, 1995

Frontispiece - Infrared LANDSAT photograph of the central California coast from Monterey to the San Joaquin Valley, September 6, 1992. The San Andreas Fault traverses the image from lower right to upper left. The oval New Idria Serpentinite and the surrounding anticlinal structures protrude, thumb-like, eastward from the Diablo Range in the right central portion of the image. Photograph courtesy of EROS Data Center, Sioux Falls, S.D.

Chapter 1 - Introduction and Regional Geology

Chapter 1

Introduction and Regional Geology

Chapter 1 - Introduction and Regional Geology

I. Outline and Statement of Purpose

The major purpose of this thesis is to describe the mineralogy and petrology of the serpentinite massif at New Idria, California. Of particular interest is the evolution of exotic mineral suites contained in tectonic blocks or "knockers" within the serpentinite body. These blocks contain minerals enriched in titanium, an element with extremely low abundance (< 1 ppm) in the bulk serpentinite outside the blocks. Some tectonic blocks are characterized by the assemblage chlorite + diopside + Ti-garnet; these blocks are interpreted as metapyroxenites. Other blocks contain the rare minerals benitoite and neptunite; these blocks are interpreted as altered mafic schists and greenstones; still others contain near end-member jadeite; following Coleman (1961) jadeite-bearing blocks are also interpreted as altered mafic schists.

Chapter 1 introduces the New Idria District and describes the methods of study employed. Field and laboratory study of rocks in the southern portion of the serpentinite, along with reconnaissance study of rocks in the northern portion, were undertaken in the years 1988-1993.

Chapter 2 describes in the history of scientific work at New Idria; the District has been the focus of investigations with a variety of purposes for nearly 150 years. These include mining studies (including oil exploration), mineralogical studies of rare minerals, geophysical studies (especially since the destructive Coalinga earthquake of 1983), and most recently asbestos-related studies by the Environmental Protection Agency.

Chapter 3 discusses the mineralogy and petrology of the serpentinite as a whole, exclusive of the tectonic blocks. The protolith of the serpentinite is seen to be dunite with lesser amounts of harzburgite and other ultramafic rock types. The entire massif is interpreted as an ophiolitic flake of oceanic crust or underlying mantle, of Jurassic to Cretaceous age.

Chapter 4 describes the mineralogy and petrology of the tectonic inclusions in the serpentinite. These inclusions are subdivided into three groups: metapyroxenites, metamorphosed Franciscan mafic schists and greenstones, and antigorite knockers. A model is proposed for the formation of exotic minerals in the blocks as products of essentially isochemical metamorphism.

Chapter 5 discusses the most prominent of the titaniferous minerals of the District, garnet. Approximately 300 chemical analyses of garnets and coexisting minerals are presented, along with a discussion of chemical variation using exchange vectors and crystal chemical constraints.

Chapter 6 discusses the possibilities for mobility of titanium in aqueous fluids as a factor in the paragenesis of titaniferous minerals. Ti mobility on a length scale of only about one meter can be shown at New Idria. Comparative studies of Ti mobility are also discussed.

Chapter 7 offers a regional interpretation for the evolution of the New Idria Serpentinite. The chapter also summarizes the conclusions of the thesis and lays out a framework for further investigations.

Each of these chapters contains a chapter table of contents and a brief summary of the regional geology, so that it is possible to read the chapters in any order.

II. The New Idria District of California

A. Location

The New Idria District includes portions of San Benito and Fresno Counties; it is roughly bounded on the north and south by the towns of Panoche and Coalinga respectively (**Figure 1.1**). The District lies between the western margin of the San Joaquin Valley and the San Benito River in the southern portion of the Diablo Range, a constituent member of the Coast Ranges Province of California. (Page, 1966). The Diablo Range, as defined by Anderson & Pack (1915), forms the eastern margin of the Coast Ranges between Carquinez Straits at San Francisco Bay and Polonio Pass in San Luis Obispo County, a distance of some 300 km. The highest summits of this range lie within the District: wooded San Benito Mt. (1579 m.) and barren Santa Rita Peak, (1574 m.). The eastern side of the Diablo Range forms a precipitous escarpment; the relief from the summit of Santa Rita Peak to the junction of Cantua Creek and Arroyo Leona, 7 km to the east, is over 1000 m. The total relief from the crest of the range to the San Joaquin Valley 25 km. east is 1500 m. The New Idria District is sparsely inhabited, mainly by isolated ranchers living in the valleys. Only one settlement lies fully within the District: New Idria, also known as Idria, now nearly a ghost town, at the site of the abandoned New Idria mercury mines.

Drainage of the region is to the west, via the San Benito River, and to the east, via Cantua Creek and a network of intermittent streams descending to the San Joaquin Valley and the California Aqueduct. To the southeast, drainage is also into the San Joaquin Valley, via the perennial Los Gatos Creek and the Arroyo Pasajero.

Figure 1.1 - Map of Central California, showing the region from Monterey Bay to the San Joaquin Valley. This map covers approximately the same area as the satellite photo in the frontispiece. The New Idria District lies to the east of the San Andreas Fault.

Figure 1.1 - Map of Central California

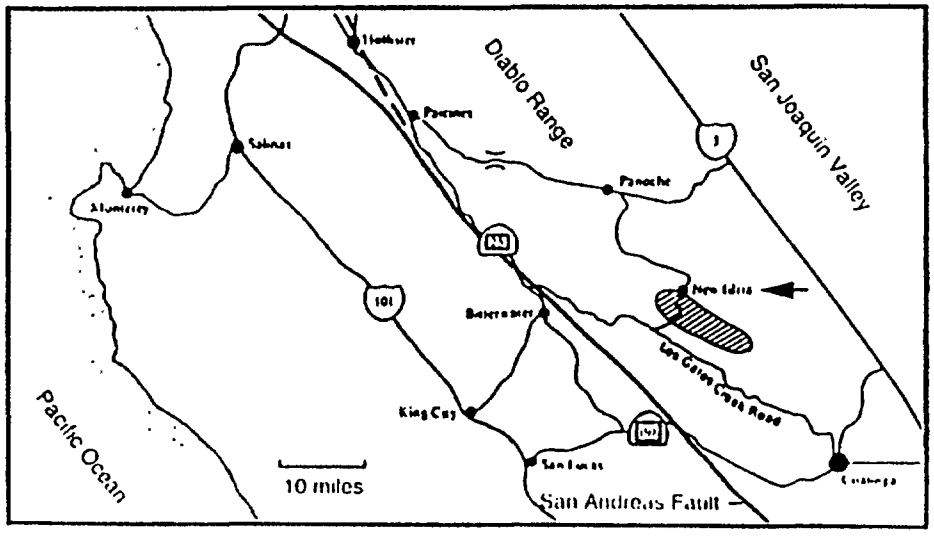

redrawn after Coleman, 1986

Physical access to the edge of the District is via paved road, about a four hour drive from San Francisco. The Coalinga-Bitterwater Road, diverging from SR 25 at Bitterwater, and following the San Benito River and Los Gatos Creek valleys, provides access from the west and south. County Road J1, that runs from Paicines south of Hollister through the Panoche Valley to Idria, provides access from the north. Within the District a bewildering maze of unpaved and generally unmaintained roads makes a four wheel drive vehicle essential in moving about. The Bureau of Land Management (BLM) office in Hollister has current information about access to the District. As of 1993, BLM has proposed to limit vehicular access to what is termed the Hazardous Asbestos Area, that generally coincides with the zone of serpentinite rock.

The frontispiece of this study shows a satellite photograph of the central Coast Ranges using infrared film, at a scale of approximately 1:1,000,000. The oval outline of the anticlinal structure containing the New Idria Serpentinite can be seen to the east of the San Andreas Fault.

B. Description

The term *New Idria District*, referred to in this study simply as *the District*, was first used by Becker to describe the general region encompassing the historic mercury mines at New Idria, California (Becker, 1888). The most remarkable feature of the District is an oval, 23 by 8 km, fault bounded, serpentinite massif flanked by steeply dipping, locally overturned, sedimentary and metamorphic rocks of the Jurassic-Cretaceous Franciscan and the Cretaceous to Pliocene Great Valley Sequence of California (**Figure 1.2**). The serpentinite is older than the sandstones and shales of the Great Valley Sequence. The outcrop area of serpentinite rock exceeds 150 km^2. The New Idria Serpentinite is a

serpentinite diapir (Coleman, 1957), a part of the Coast Range Ophiolite in California. The age of the ophiolite is 153 to 165 Ma. (Hopson et al., 1981); its emplacement within the Franciscan Formation is related to subduction of the Farallon plate in the Jurassic. The tectonic setting of the ophiolite was a forearc basin lying between the Sierra Nevada volcanic arc to the east and a trench-subduction complex to the west, represented by the Franciscan Formation (Bartow, 1990). A piece of oceanic crust or underlying mantle was obducted onto the North American continent, later to rise through the Franciscan Formation as a serpentinite diapir. The structural trend of the serpentinite body and related folds and faults is 300°, and so is inclined 20° degrees to the San Andreas fault system, that trends 320° in this part of California.

Emplacement of the New Idria Serpentinite as a diapir within the Franciscan has resulted in a piercement structure or tectonic window, lying just east of the San Andreas fault system northeast of Parkfield. The serpentinite body was shown by Coleman (1957) to be fault bounded on all sides (**Plate 1.2**), with the sense of shear where it could be determined showing upward movement of the serpentinite against the country rock. No evidence of contact metamorphism was found. The diapir breached the surface in the Miocene, as recorded by the sudden appearance of serpentine boulder conglomerates in the Big Blue member of the Tremblor Formation.

The New Idria Serpentinite lies in the core of one of a series of anticlines that characterize the Coast Ranges in this part of California (Arnold & Anderson, 1908; Taliaferro, 1943; Eckel & Myers, 1946; Zigler et al., 1986). Numerous other partially to completely serpentinized peridotites lie in a similar structural position along the east side of the San Andreas fault in central and northern California. During the Miocene, the New Idria Serpentinite experienced an interval of rapid uplift, sub-greenschist facies metamorphism, and intrusion of small syenite stocks.

Figure 1.2 - Simplified geologic map of the New Idria District. See the Santa Cruz 1:250,000 geologic map, (Jennings & Strand, 1958) for more detail.

Figure 1.2 - Simplified Geologic Map of the New Idria District

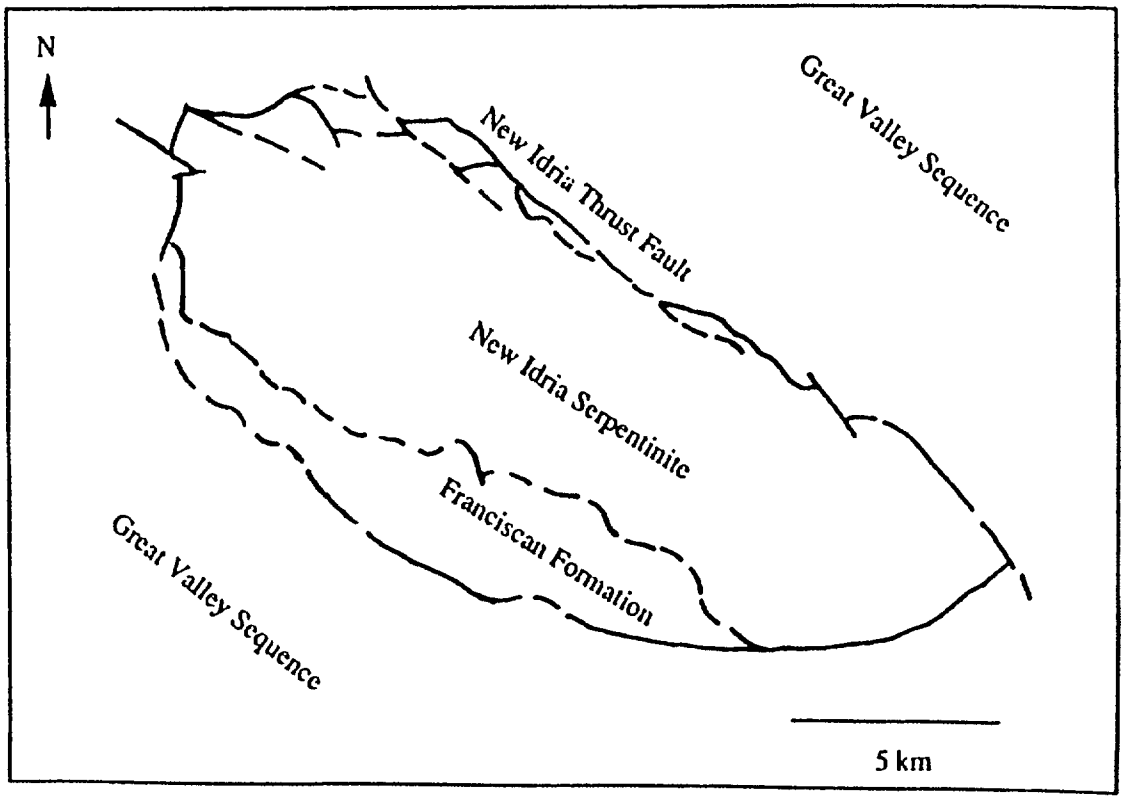

Plate 1.2 - Photograph of the fault contact between the New Idria Serpentinite and the Cretaceous Great Valley Sequence, at the Corbett-Byles Mine.

The mineralogy of the serpentinite is dominated by chrysotile. Brucite, accessory magnetite, and minor lizardite and antigorite are also present. The protolith for the serpentinite was a depleted peridotite consisting of dunite with minor harzburgite. Locally within the serpentinite, tectonic blocks of metapyroxenite, greenstone, mafic schist, and massive antigorite are preserved. These blocks are of limited extent, with sheared contacts against the surrounding serpentinite. They are recognizable in the field by distinct soil color and erosion properties, contrasting vegetation above, and anomalous mineral assemblages within. The bulk composition of the blocks is significantly different from that of the bulk serpentinite.

New Idria is one of the largest known deposits of chrysotile asbestos in the world. Indeed, Klein (1993) has proposed that eolian erosion from New Idria is the main contributor to background levels of airborne chrysotile asbestos in the northern hemisphere. At this time, the Environmental Protection Agency (EPA) has designated two sites in the District as Superfund sites under the Comprehensive Environmental Response Compensation and Liability Act of 1980 (CERCLA). At the same time, the only remaining asbestos mine (KCAC) in the United States continues in operation in the District.

The District is rich in mineral resources, including mercury, magnesite, chromite, petroleum, asbestos, and gemstone minerals. The District has a rich human history, chiefly on account of these mineral deposits. The most valuable economic commodities have been mercury and petroleum, that occur at the margin or entirely outside the serpentinite body. In California the occurrences of mercury and petroleum are generally linked spatially, and perhaps genetically (Peabody, 1989; Peabody & Einaudi, 1992).

The New Idria District is renowned as a mineral collecting area, with over 100 mineral species reported to date. The District lies partly in San Benito County and partly in Fresno County, so that New Idria minerals are also known by these geographic names, e.g. San Benito garnets. The minerals for which the District is known are, for the most part, associated with the boundary faults of the serpentinite or with tectonic blocks of various rock types included in the serpentinite.

C. Index Maps

1. Geographical Maps

The USGS Santa Cruz 1:250,000 map, the Coalinga 1:100,000 metric topographic map, the 15 minute New Idria quadrangle, as well as the 7.5 minute Santa Rita Peak, San Benito Mt., Idria and Hernandez Reservoir quadrangles, cover the area described in this study.

2. Geological Maps

There is a dearth of published geologic maps at suitable scales for work in the New Idria District. A State geologic map or especially the 1:750,000 Isostatic Residual Gravity Map (Roberts et al., 1990) are needed to place the New Idria District in its regional context. The 1:250,000 Geologic Map of California, Santa Cruz sheet (Jennings & Strand, 1958) provides further details of the southern Diablo Range. The general map of the New Idria Serpentinite produced by Eckel & Myers (1946) is thus far the only complete geologic map of the serpentinite, and as such has been used as a base map for other geologic compilations for the past 50 years. Unpublished maps by T.W. Dibblee (Dibblee, 1971, 1979) are useful in the study of the rocks immediately adjacent to the serpentinite.

Several of the engineering and soil maps prepared for the EPA by Levine-Fricke Consultants (Levine-Fricke, 1989) are also useful.

This study presents a geologic map of the Santa Rita Peak quadrangle, at a scale of 1:24,000 (**Plate 1.1**, in pocket). This map is compiled from field work during this study as well as from the above sources.

3. A Note on Place Names

Description of a remote area is made more difficult by the lack of commonly accepted place names. The geological and geophysical literature may use different names for the same features, confounding the reader. For example, in the asbestos industry the New Idria District is more generally known as the *Coalinga asbestos deposit.* Some of the EPA studies have used the name *New Idria Formation* in reference to the New Idria Serpentinite exclusive of the Franciscan rocks. This term is inappropriate, and its use is discouraged. In this study, official names are used where available, but informal names are used as well. A glossary of place names is included as an appendix to this chapter.

D. Flora

Approaching New Idria from a distance, one is struck by the overall white color of the ridges and open slopes of the *serpentine barren*, in contrast with the red-brown color of the vegetation and soil of surrounding areas that have different bedrock types. Likewise, there is a strong contrast in the vegetation that grows on the serpentine soil: a unique serpentine chapparal replaces open oak woodland (Kruckeberg, 1982). Brewer (1861) commented on the desolate nature of the region but did not connect the vegetation with the unusual soil type. At the present time, the vegetative cover varies considerably within the region, perhaps due to the pattern of recent forest fires.

To the non-specialist, the most prominent plants of the arid serpentine barren are the scrubby chaparrals that grow on the mountain slopes and frequently make access to outcrops a difficult struggle. Characteristic plants are the orange-barked manzanita with red berries, *Arctstaphylos franciscana;* the scrubby oak *Quercus durata*; and the spiny buckthorn *Ceanothus jepsonii.* Where trees are found on wooded slopes, they are a mixture of pines bearing pineapple-sized cones, mainly the digger *Pinus sabiniana*, but locally are the jeffrey *P. jeffreyi*, the coulter *P. coulteri*, and hybrids of these two (Dann, 1988). Occasionally cypresses are found; *Cupressus sargentii* is the characteristic species. A variety of small bushes and grasses cling to life on otherwise barren slopes. The small Parishes buckwheat *Erigonum parishii* has hardly any foliage, while the aromatic rabbit bush *Chrysothamnus graveoleus* is able to colonize the wastelands of abandoned mines, e.g. at the J.M. Christie mine. This characteristic should be noted by those attempting reclamation of mining land.

Recently the San Benito evening primrose *Camissonia benitensis* has been designated a threatened species under the Endangered Species Act, which means that special management concerns exist for its habitat, which is concentrated in the Clear Creek watershed at the northern end of the serpentinite.

Some of the larger tectonic inclusions within the serpentinite support a "normal" vegetation for California, e.g. the live oak *Quercus agrifolia.*. The occurrence of these prominent trees allows the geologist to locate soil, and hence bedrock, of a contrasting type within the serpentinite. From any of the higher summits, the margin of the serpentinite can be easily recognized once this vegetation contrast is understood.

Soils developed on serpentine are shallow and stony, typically enriched strongly in Mg and the heavy metals Cr and Ni, but seriously depleted in Ca, K, N and P, making normal plant growth difficult. The soil pH at New Idria is ca. 7.2 (Kruckeberg, 1982). Locally, however, acid mine drainage from the mercury mines at Idria produces a stream pH as low as 1.7.

E. Fauna

Little work has been done on the endemic fauna of serpentinites, but the visitor immediately notices the general absence of mammals, particularly small rodents. During four field seasons the author never had any food snitched by furry creatures at a campsite. The lack of an important food source for snakes contributes to their low population in the serpentinite. While rattlesnakes are abundant in the surrounding hills, they are generally absent within the serpentinite, and where found tend to be living on one of the tectonic blocks, e.g. at the Gem Mine. An exception is the two-striped garter snake, that has a small habitat around Spanish Lake. Small lizards are ubiquitous. During the hot season (June - October) flies are occasionally annoying.

The characteristic birds of the District are the frequently heard but seldom seen wrentit, along with the scrub jay, plain titmouse, townsend's warbler, olive-sided flycatcher, red-tailed hawk, and turkey vulture. In the surrounding valleys one also sees the yellow-billed magpie, california quail, mourning dove, roadrunner, rough winged swallow, red-shafted flicker, and western bluebird.

III. Parts of the Serpentinite

In this study the New Idria Serpentinite is subdivided into its constituent parts for convenience.

A. The Serpentinite Massif

The mineralogy and petrology of the serpentinite and its ultramafic protolith are discussed in Chapter 3.

B. The Tectonic Blocks

The mineralogy and petrology of the tectonic blocks entrained by the serpentinite are the subject of Chapter 4.

C. The Mercury Mines

As described in Chapter 2, it was the 1852 discovery of the cinnabar deposits at New Idria that brought this region to the attention of the outside world. The mines became in time the largest operating mercury mines in the United States, prior to closing for environmental reasons in 1972.

The mercury mineralization is chiefly cinnabar with minor metacinnabar, and is fault controlled. The deposits are hydrothermal in nature. Peabody (1989) and Peabody & Einaudi (1992) proposed that the mercury has been remobilized from sedimentary rocks of the Great Valley Sequence. The geology of the mercury mineralization at the New Idria Mines has been described by Henderson (1965). The technology of mercury mining

is the subject of numerous reports in the Bulletin of the California Bureau of Mines and some of the older references that are given in Chapter 2.

This study does not deal *per se* with the mercury mines, but it is important to note their physical placement around the margins of the serpentinite, astride the boundary faults. A few mines are located within the serpentinite body. These may be related to throughgoing faults that are parallel or subparallel to the eastern boundary fault. This fault is generally known as the New Idria Thrust Fault (**Plate 1.1**). Further indication of the existence of throughgoing faults is suggested by the 2 km.-long row of silicified serpentine outcrops near Spanish Lake, also shown in **Plate 1.1.** In these outcrops, chalcedony or locally quartz has apparently precipitated from fault-related fluids.

D. The New Idria Syenite

The New Idria Serpentinite is intruded by small syenite stocks of Miocene age, here collectively named the New Idria Syenite. Stream boulders of this syenite were noted by Anderson & Pack (1915), and their source was traced to the headwaters of White Creek. The original description of the syenite was of this stock in the White Creek valley, hence the body was named the White Creek Stock (Robertson, 1940). Since there are additional outcrops not in the White Creek drainage, it is here proposed that that name be abandoned in favor of the name New Idria Syenite. Significantly, these stocks form a linear array on the map (**Plate 1.1**); their emplacement may be partially fault controlled. It is significant that the White Creek Stock intrudes the boundary between the serpentinite and the adjacent Panoche Shale. Coleman (1957) also described the New Idria Syenite.

The New Idria Syenite is a soda syenite, composed almost entirely of sodic feldspar and kaersutite (formerly barkevikite) amphibole. The rock is very coarse grained in places,

with amphibole crystals up to 30 cm. long. Elsewhere the rock is fine-grained with only millimeter-sized amphibole crystals. Enclaves of coarse grained rock are found in fine grained rock, and vice-versa. In places, olivine and pyroxene are found; Coleman (1957) described that facies as camptonite. Accessory minerals include biotite, apatite, titanite (sphene), magnetite, ilmenite, pyralspite garnet and zircon. Deuteric and later alteration products include zoisite, prehnite, zeolites, white mica, chlorite and calcite.

Table 1.1 presents some whole-rock analyses of the syenite. A CIPW norm calculation shows that in all cases the rock is nepheline normative. Table 1.2 presents some kaersutite amphibole analyses.

The abundance of tectonic blocks of several types in the New Idria Serpentinite raises the question of whether the syenite outcrops are intrusive or not. At a large syenite outcrop named The Nose, located to the west of Perovskite Knob, the serpentinite surrounding the syenite has been contact metamorphosed: both antigorite and prograde olivine are present. The aureole grades outward to the "normal" serpentinite rock consisting of chrysotile and lizardite. This observation shows that the contact is indeed intrusive; the margins of other tectonic blocks do not have contact aureoles.

The age of the New Idria Syenite has been determined by Marvin Lanphere of the U.S. Geological Survey using the $^{40}Ar/^{39}Ar$ total fusion technique on an amphibole mineral separate. This unpublished age is 12.4 ± 0.8 Ma (M. Lanphere, written communication, 1993). Such an age is consistent with the intrusive nature of the contact, assuming that the serpentinite as a whole has a late Jurassic age.

The occurrence of the prehnite-zoisite pair in deuterically altered syenite provides a pressure estimate at the time of alteration. The stability fields of prehnite and zoisite

overlap only between 1 and 3 kb (Frey et al., 1991). Therefore the outcrop presently at the surface lay at a depth of 3.5 to 10 km. at the time of alteration, assuming an average density of 2.8 g/cm^3 for the rock formerly overlying the outcrop (the average density of several syenite samples was determined to be 2.8 g/cm^3 using a Jolly balance; the density of serpentinite was found to be 2.4 to 2.8 g/cm^3). This is the only quantitative pressure estimate obtained during the course of this study, although mineral parageneses described in Chapters 3 and 4 provide general estimates.

If the 12.4 Ma age of the syenite measured by Lanphere is close to the time of deuteric alteration, which is reasonable for a small intrusion, then the unroofing rate since the late Miocene may be calculated. The average unroofing rate is calculated to be 0.3 to 0.8 mm/year for the past 12 million years. This calculation agrees well with the estimated rate of 1 mm/year for the Coast Ranges, obtained using other data (Ring & Brandon 1994).

IV. Laboratory Analytical and Computational Techniques

Field and laboratory study of rocks in the southern portion of the serpentinite, along with reconnaissance study of rocks in the northern portion, were undertaken in the years 1988-1993. Sample locations are shown in **Figure 1.3.**

In this study several analytical techniques have been used, which are described below.

A. Petrography

Approximately 100 thin sections were studied using an Olympus BH2 polarizing microscope. With few exceptions the thin sections were prepared by Mr. Harold Thompson of Harvard University.

B. Mineral Analyses

Harvard's Cameca MBX electron microprobe with three crystal spectrometers and Tracor automation and Bence-Albee matrix correction was used extensively. The microprobe laboratory runs under the direction of Mr. David Lange. Normal operating conditions for anhydrous minerals were 15 kV accelerating voltage, 15 nA absorbed current, and a point beam. Hydrous minerals were analyzed using a 2K raster beam, with 800X and special calibration used for some serpentine samples. WDS standards used were the natural or synthetic silicate standards at Harvard. REE standards were specially obtained for this project from the Smithsonian Institution (Jarosewich & Boatner, 1991). EDS spectrometry was used frequently for phase identification and qualitative analyses. All specimens were examined using BSE prior to chemical analysis.

In an effort to understand the uncertainty of element concentrations measured in this study, a project working standard was chosen early in the study. This standard was a point in a relatively homogeneous portion of a Ti-rich garnet; the point was repeatedly analyzed for during the course of the study to determine precision and accuracy.

Error analysis shows that nearly all of the variability in analyses of the working standard can be explained by the counting statistics in the detectors on the crystal spectrometers. The compositions reported in this study are considered to be accurate to approximately 1-2% of the amount reported. Chapter 5 discusses compositional errors further.

Figure 1.3 - Sample locations in the Santa Rita Peak 7.5 minute quadrangle. A: 34-50 locality; B: Perovskite Knob; C: Melanite Mine; D: The Nose; E: Gem Mine; F: 990-1 locality; G: The Teeth; H: KCAC Mine; I: Atlas Mine site.

Figure 1.3 - Sample Locations in the Santa Rita Peak Quadrangle

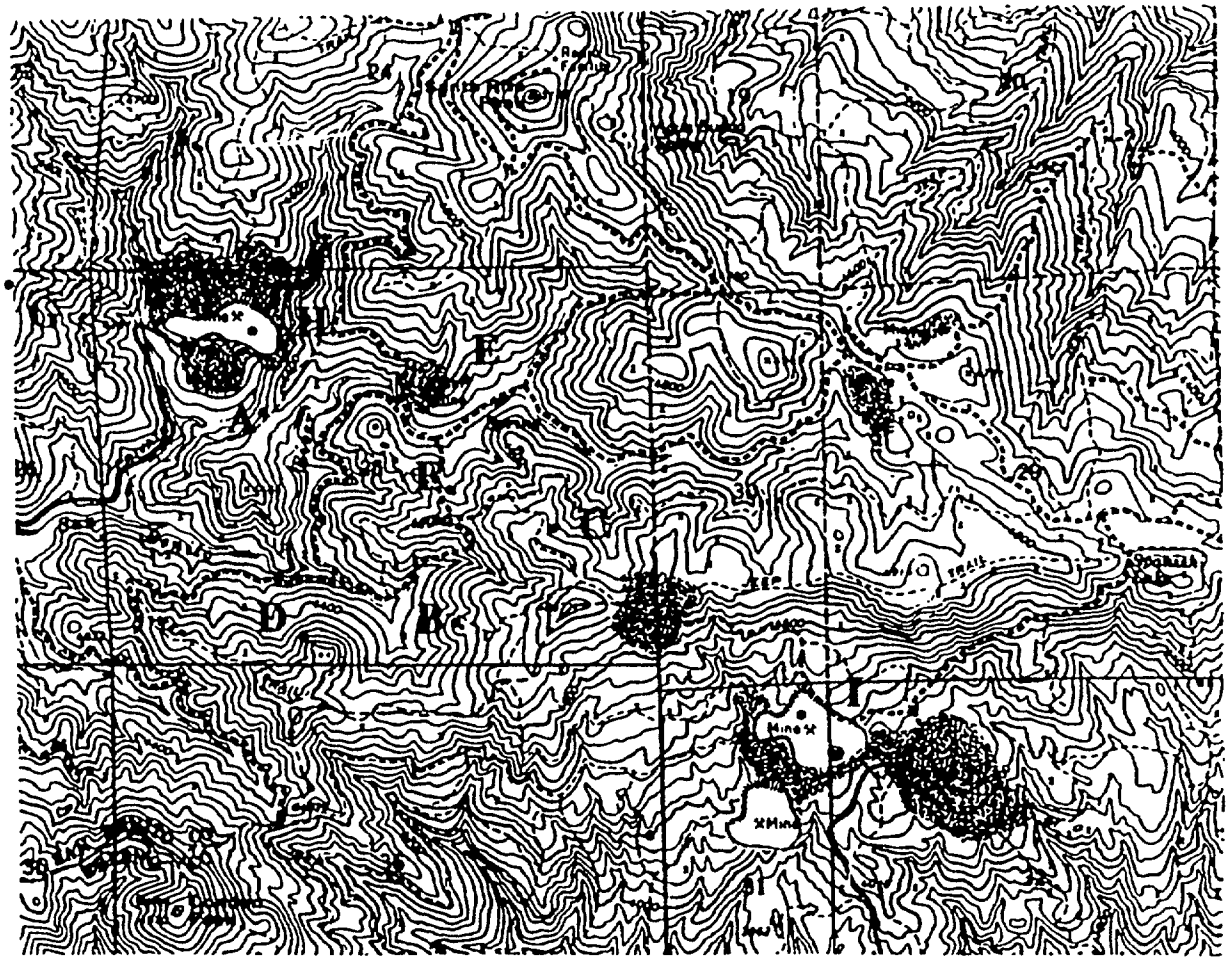

1 km

C. Whole Rock Analyses

The Siemens MRS 400MP and Siemens SRS gold tube XRF spectrometers at the University of Massachusetts, Amherst, were used for whole rock analyses, major and trace respectively. This laboratory runs under the direction of Dr. Michael Rhodes and Mr. Peter Dawson. Sample preparation procedures were according to University of Massachusetts standards, following the techniques of Gardner (1990). Duplicate analyses using dual standards were performed.

D. X-ray Diffraction

The Scintag XDS 2000 diffractometer at Harvard was used in this study for large samples. Cu- Kα radiation was used; operating conditions were 45 KV, 35 Ma, 1° per minute scan rate for most continuous scans. This laboratory operates under the direction of Prof. Charles W. Burnham. Small crystals were studied with a Gandolfi camera mounted on a Philips X-ray generator, also using Cu-Kα radiation at 45 KV. Mr. Lawrence C. Pitman performed Gandolfi X-ray experiments for the author.

E. Fluid Inclusion Microthermometry

Fluid inclusion measurements were done using the Fluid, Inc. modified USGS heating/freezing stage at Harvard. Calibration using synthetic fluid inclusions was completed prior to the measurements reported in this study. The precision and accuracy of measurements are considered to be 0.1°C and 1.0°C respectively.

F. Thermodynamic Modeling

Some modeling of mineral equilibria was done using the SUPCRT (Helgeson et al., 1978) and SUPCRT 92 (Johnson et al., 1991) computer codes, running on a Sun 386i workstation or a Macintosh computer respectively. Thermochemical data for a few phases were added to the SUPCRT database from various external sources including Robie et.al., (1978) and Berman (1990). The TWQ2S (Berman, 1991) computer code, also known as GE0CALC, was used for calculations of mineral equilibria in Chapters 3 and 4. This code was run on a Sun 386i workstation.

G. Norm Calculations

CIPW norm calculations were performed using an Excel spreadsheet on a Macintosh computer, and using the program NORMCALC obtained from the Geology Dept. at Stanford University. NORMCALC ran on a VAX computer at the Harvard Psychology Dept. The CIPW norm calculation (Cross et al., 1902) was originally designed for feldspar-bearing rocks that crystallized at low pressures, and is not appropriate for high pressure rocks that crystallized above the stability field of anorthite. A modified Excel calculation procedure was developed for these rocks by the author, in which low pressure phases were replaced by their high pressure equivalents. Albite was replaced by jadeite, anorthite by spinel + clinopyroxene. A few extremely calcic rocks also required a fictive wollastonite component to accommodate Ca; in actuality such rocks would accommodate excess Ca in garnet. A computer code widely used in Switzerland (MANNOR, written by P. Ulmer) has adopted a similar strategy.

H. Bond Distance Calculations

The BDTEA computer code of L.W. Finger was used for bond distance calculations in Chapter 3.

I. Mineral Abbreviations

In this study the abbreviations for minerals recommended by Kretz (1983) have been used. Note that abbreviations for mineral names are capitalized but abbreviations for chemical components are not capitalized, to distinguish them from mineral names. The following table lists the principal abbreviations employed:

Name	Abbreviation
andradite	Adr
anorthite	An
antigorite	Atg
brucite	Brc
chlorite	Chl
chromite	Chr
chrysotile	Ctl
diopside	Di
enstatite	En
forsterite	Fo
hedenbergite	Hd
garnet	Grt
grossular	Grs
magnesite	Mgs
magnetite	Mag
olivine	Ol
spinel	Spl
talc	Tlc
tremolite	Tr

V. Conclusions

The main points of this chapter that will be used in other chapters are:

1. The New Idria Serpentinite is a serpentinite diapir, a part of the Coast Range Ophiolite in California. The age of the ophiolite is 153 to 165 Ma. (Hopson et al., 1981); its emplacement within the Franciscan Formation is related to subduction of the Farallon plate in the Jurassic. The serpentinite is a tectonic window in the Coast Ranges.

2. The mineralogy of the serpentinite is dominated by chrysotile; New Idria is one of the largest deposits of chrysotile asbestos in the world and the site of the only operating asbestos mine in the United States at the present time.

3. The New Idria Serpentinite contains small syenite stocks of Miocene age, here collectively named the New Idria Syenite. The syenite is shown to have an intrusive relationship with the surrounding serpentinite. In the contact aureole around the intrusive syenite, prograde olivine replaces antigorite. The aureole grades outwards to a mixture of chrysotile and lizardite.

4. The age of the New Idria Syenite has been determined by Marvin Lanphere to be 12.4 ± 0.8 Ma, using the $^{40}Ar/^{39}Ar$ total fusion technique on an amphibole mineral separate from the syenite.

5. Coexisting prehnite and zoisite in deuterically altered syenite provide a pressure estimate at the time of alteration. The stability fields of prehnite and zoisite overlap only between 1 and 3 kb (Frey et al., 1991). Therefore the outcrop presently at the surface lay

at a depth of 3.5 to 10 km. at the time of alteration, assuming an average density of 2.8 g/cm^3 for the rock formerly overlying the outcrop.

6. If the 12.4 Ma age of the syenite measured by Lanphere is close to the time of deuteric alteration, which is reasonable for a small intrusion, then the unroofing rate since the late Miocene may be calculated. The average unroofing rate is calculated to be 0.3 to 0.8 mm/year for the past 12 million years. This calculation agrees well with the estimated rate of 1 mm/year for the Coast Ranges, obtained using other data (Ring & Brandon 1994).

Appendix A - Glossary of Place Names

All localities, unless otherwise noted, lie in the USGS Santa Rita Peak 7.5 minute quadrangle map.

Atlas Mine: The large open pit mine and abandoned mill of the Atlas Asbestos Co. cover several acres on the south-facing escarpment of the serpentinite in the White Creek drainage. A gated road from Spanish Lake that descends to the White Creek valley transects the mine site. The mine and mill are now an EPA Superfund site.

Butler Estate Pit: This moderately large, north-facing, U-shaped excavation was formerly a chromite mine. The mine, also known as the Mistake Mine, lies in the extreme southeast corner of the serpentinite in the Pine Creek drainage. The New Idria thrust fault crops out on the headwall of the pit.

J.M. Christie Pit: This large open pit asbestos mine, formerly operated by Johns Manville, lies high on the western slope of Wright Mt. in the drainage of the Arroyo Leona.

Corbett-Byles Pit: This moderately large open pit was formerly a chromite mine. The mine lies in the southeast corner of the serpentinite in the White Creek drainage. The New Idria thrust fault crops out on the headwall of the pit. The Archer Mine, a mercury mine, lies in the fault zone directly underneath the Corbett-Byles pit.

Gem Mine: This small open pit benitoite mine lies at the toe of a ridge extending southwest from the summit of Santa Rita Peak, in the valley of the San Benito River. The mine is a patented claim and is marked by a sign warning of private property.

KCAC Mine: This large open pit asbestos mine is operated by the KCAC Co. of King City, California. The mine was formerly operated by the Union Carbide Co. The mine lies on the western slope of Santa Rita Peak and can be reached via a gated, private paved road from the Coalinga-Bitterwater Rd. The private road is known as the KCAC Road.

Hill 4857: This prominent unnamed hill is marked on the USGS Santa Rita Peak 7.5 minute quadrangle map with its elevation. The hill is south of Santa Rita Peak, east of Condon Peak, and west of the Atlas Mine site. Perovskite Knob lies on the western slope of Hill 4857, the Melanite Mine on the north.

Melanite Mine: This small excavation on the north slope of hill 4857 lies in a gully above the south branch of the Santa Benito River, which splits into a north and a south branch just upstream of the Gem Mine.

New Idria Thrust Fault: This high angle thrust or reverse fault forms the northeastern boundary of the New Idria Serpentinite. The fault represents a breached anticline. The continuation of the anticlinal axis to the southeast is known as the Coalinga Anticline, and still further to the south the Kettleman Hills Anticline.

Nose: This name is given to the prominent syenite dike that crops out on the north side of Snakebite Hill directly uphill from a 90 degree bend in the San Benito

River where its course alters from south to west. Large syenite boulders are found at the stream bend. This is the dike that was mapped by Coleman (1957).

Perovskite Knob: This prominent, 15 m. high knob lies on the western slope of Hill 4857 and looks westward to Snakebite Hill. The Santa Rita Peak, Condon Peak, the Nose and the Teeth are visible from Perovskite Knob.

Snakebite Hill: This name is given to a low, twin-summited hill that lies between Hill 4857 and Condon Peak. The name comes from the map pattern on the quadrangle map, on which the contour lines about the twin summits resemble a snake bite. The hill may be reached via a very rough 4WD road from the west.

Teeth: This name is given to a pair of 3 m. high resistant serpentine knobs that lie on a ridge that lies to the west of and above the KCAC Mine, facing southwards towards the San Benito River valley. The Teeth can be reached by a rough 4WD road leading directly uphill to the west from the KCAC Mine road at the point where it enters the mine pit. About 100 m. to the north of the Teeth lies the syenite/camptonite outcrop mentioned by Coleman (1957). As of this writing the syenite outcrop has completely disintegrated and the only sample fragments for this study were obtained by uprooting a bush and digging a small pit.

Victor Claim: This small staked claim consists of set of outcrops lies on the north slope of San Benito Mt., in a side valley off the Clear Creek Valley, approximately one km. from the Clear Creek Road and 0.5 km upstream from a small mercury mine. The Victor Claim is marked by a monument post. about 10 m. above the bed of a small stream. The locality is found on the USGS San Benito Mt. 7.5 minute quadrangle map.

The 34-50 locality: This set of four rocky knobs, 2-3 m. tall, lies at an elevation of about 1300 m. on a southward projecting ridge above the bed of the San Benito River just to the south of the KCAC Mine and just to the west of the Gem Mine. The locality is reached via a short spur road. The name is the one given by R.G. Coleman in 1950.

Table 1.1 - Whole-rock analyses of the New Idria Syenite					
	1	2	3	4	5
Sample ->	989-8	989-39	A&A, 1910	Coleman	Coleman
location ->	White Crk.	The Nose	White Crk.	White Crk.	White Crk.
SiO2	51.46	47.85	60.00	48.96	51.42
TiO2	1.53	2.44	0.42	2.01	2.20
Al2O3	18.56	15.38	16.88	15.72	16.58
Fe2O3	8.42	10.61	1.83	0.36	1.48
FeO	n.d.	n.d.	3.02	9.65	7.62
MnO	0.14	0.16	0.12	0.17	0.23
MgO	2.92	9.45	1.40	6.52	3.68
CaO	6.11	9.03	3.16	7.76	6.77
Na2O	9.89	3.27	9.31	5.22	6.04
K2O	0.42	1.47	0.94	0.75	1.06
P2O5	0.50	0.14	0.14	n.d.	0.49
H2O+	n.d.	n.d.	1.53	2.29	1.41
H2O-	n.d.	n.d.	0.43	0.42	0.34
Total wt. %	99.94	99.79	99.18	99.83	99.32
Trace (ppm)					
Nb	39.87	25.30	n.d.	n.d.	n.d.
Zr	260.83	123.50	300	n.d.	trace
Sr	836.15	410.35	200	n.d.	800
Zn	90.41	88.53	n.d.	n.d.	n.d.
Ni	9.28	24.03	n.d.	n.d.	n.d.
Cr	0.00	0.60	0	n.d.	n.d.
V	64.68	314.23	n.d.	n.d.	n.d.
Ce	58.98	30.08	n.d.	n.d.	n.d.
Ba	562.37	441.39	600	500	trace
La	23.00	11.61	n.d.	n.d.	n.d.
Analyses 1&2 anhydrous; all Fe expressed as Fe2O3					
In analysis 3, CO2=0.59 wt. %					
In analysis 5, CO2=0.45 wt. %					
Analyses 1 & 2 (this study)					
Analysis 3 from Arnold & Anderson (1910)					
Analyses 4&5 from Coleman (1957)					

Table 1.1

Table 1.2 - Amphibole in the New Idria Syenite		
Sample ->	990-39.3	990-39.4
SiO2	39.81	40.65
TiO2	3.25	3.31
Al2O3	13.40	13.65
Cr2O3	0.00	0.00
Fe2O3	n.d.	n.d.
FeO*	9.67	9.99
MnO	0.10	0.10
MgO	14.45	14.60
CaO	11.20	11.16
ZnO	0.02	0.00
BaO	0.02	0.01
Na2O	2.66	2.62
K2O	0.85	0.86
F	0.01	0.01
Cl	0.02	0.02
H2O (diff)	4.54	3.02
Totals	100.00	100.00
note: all Fe as FeO		

Table 1.2

Chapter 2

History of Scientific Investigations of the New Idria District

Chapter 2 - History of Scientific Investigations of the New Idria District

Chapter 2 - History of Scientific Investigations of the New Idria District

Prologue:

Two sixteenth century events separated by only four years set the backdrop for studies of the New Idria District. In 1542, Juan Cabrillo became the first European to sight California (Morison, 1974). He sailed as far north as Bodega Bay, and anchored in the shadow of the serpentine-rich Franciscan hills. In 1546, the first modern text on mineralogy, *De Fossilium Naturum*, was published in Basel by Georg Bauer, writing under the pseudonym of Georgius Agricola. In this book, Agricola first used the term *serpentenaria* to refer to serpentine rock. The histories of California and *serpentenaria* have been intertwined ever since. One of the mysteries of the early exploration of California is that the Golden Gate remained undiscovered by coastal sailors, including the redoubtable Sir Francis Drake, for over two hundred years: this narrow pass through the Franciscan Formation of the Coast Ranges, and the bay of San Francisco behind it, were discovered from land by the Portola expedition in 1769. The Fages expedition of 1772 was the first group to traverse the lands to the south and east of San Francisco Bay, and so discovered the San Benito River. This river was forded and named by Fray Juan Crespi, a member of the Fages expedition (Bolton, 1927). The New Idria District lies at the headwaters of the San Benito River, and benitoite from the District has become the California state gemstone.

I. Geological studies prior to 1950

Almost eighty years later in 1851, a silver prospector named Jesse Smith made the inadvertent discovery of cinnabar in the New Idria District, which opened the rich mining history of this region (Gilbert, 1984). Smith established the Aurora Silver Mine, which

promptly went under, owing to the absence of silver. Further exploration in 1854, however, led to the opening of the New Idria Quicksilver Mine in 1855. Intrigue and bloodshed accompanying these events are described in a Bret Harte novel, *The Story of a Mine* (1877). This mine became one of the largest producers of mercury in the U.S., and together with the nearby San Carlos mine produced nearly 500,000 76 lb. flasks of mercury prior to closing in 1972 for environmental reasons. Gilbert (1984), has written a history of the legal disputes (which were litigated before the U.S. Supreme Court) and mining operations at the New Idria mines.

The New Idria District and the mines were visited in 1861 by a party from the Geological Survey of California under J.D. Whitney[1] (Whitney, 1865). The region was described and metamorphic rocks including serpentine were mentioned, but the 1873 map produced by the Whitney Survey appears to have been lost to history. W.H. Brewer, a member of the 1861 party, described a forbidding scene in in his journal (Brewer, 1861, 1966):

> "... chain after chain of mountains, most barren and desolate. No words can describe one chain, at the foot of which we had passed on our way - gray and dry rocks or soil, furrowed by ancient streams into innumerable canyons, now perfectly dry, without a tree, scarcely a shrub or other vegetation - *none*, absolutely, could be seen. It was a scene of unmixed desolation, more terrible for a stranger to be lost in than even the snows and glaciers of the Alps.... How still it was! - no sound of a bird in the evening twilight, no chirrup of insect, but silence, deathly stillness reigned."

---

1 J.D. Whitney later joined the faculty at Harvard, where he served as Sturgis Hooper Professor of Geology from 1875 until his death in 1896.

Plate 2.1, a modern view to the northeast from the summit of San Benito Mt., includes a part of the barren vista described by Brewer. Assuming that the serpentine vegetation in 1861 was roughly comparable to that of the present day, Brewer's description may apply to the arid region that lies to the northeast in the wind shadow of the New Idria massif.

New Idria appeared on the first state geologic map of California, (Plate 2.2, Guillemin-Tarayre, 1867), but the accompanying text is incomplete, and the extant portion does not mention the mining operations at New Idria. Perhaps in the future both the missing Whitney maps and the Guillemin-Tarayre text will emerge from some forgotten archive.

Early references which deal with New Idria concentrated on mining methods and production statistics for the mercury mines, (e.g. Becker, 1888; Forstner, 1903; Bradley, 1918). Other references described efforts to produce magnesite, chromite, and gem-quality benitoite (e.g. Gale, 1912; Louderback, 1907, 1909). Becker (1888) described the geology of the New Idria district, but the accompanying map included only the immediate vicinity of the mercury mines at New Idria. Arnold and Anderson (1910) were the first to describe the huge extent of the serpentinite, which extends far beyond the limits of their map. Significantly, their report also mentioned the occurrence of asbestos, and the intimate relations between asbestos-bearing rocks and the Franciscan formation. They also mentioned the White Creek syenite, which crops out on the southern margin of the serpentinite. The first published map showing the New Idria district as an extensive serpentinite mass was that of Anderson & Pack (1915), who were mainly interested in the oil potential of the area. Later, R.C. Mielenz described the stratigraphy and structure of part of the district in an unpublished doctoral thesis (Mielenz, 1939). The White Creek syenite at the southern end of the New Idria district was the subject of an unpublished M.A. thesis by M.S. Robertson (Robertson, 1940). Taliaferro (1943), in describing the structure of the Diablo Range, concluded that the steeply dipping New Idria Thrust Fault

Plate 2.1 - View of the New Idria Serpentinite and adjacent regions from the summit of San Benito Mt., looking northeast. Prominent peaks, from L-R, are Samson Peak, Idria Peak, and San Carlos Peak. Boundary of serpentinite can be distinguished as a change in vegetation and soil color on open slopes: serpentinite soil is greenish grey, sandstone is light brown.

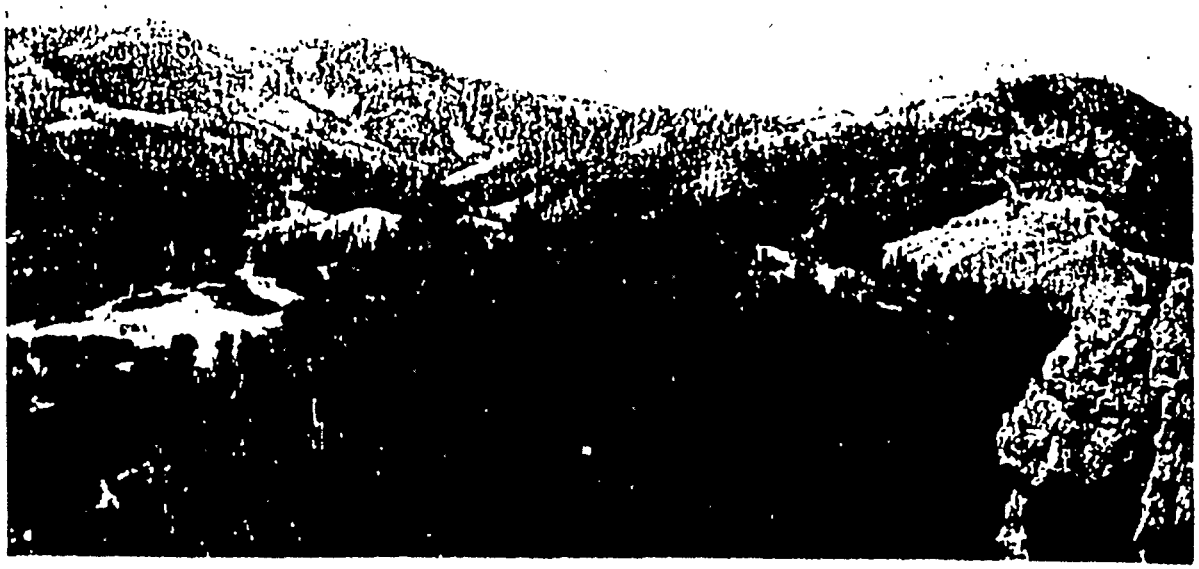

Plate 2.2 - The first geologic map of California and adjoining regions, prepared by Edmond Guillemin-Tarayre in 1867. New Idria is shown on the eastern side of the Coast Range near latitude 37°.

GÉOLOGIQUE
CALIFORNIE
NEVADA

was responsible for an appreciable part of the uplift of the Diablo Range in this section. He also showed how serpentine formed the cores of anticlines within the Franciscan formation, and suggested a subsurface connection between the New Idria serpentinite and the Laguna Mountain body to the west.

To the extent that early studies mentioned the origin of the serpentinite body, they generally attributed it to an igneous intrusion of an ultrabasic magma (e.g. Taliaferro, 1943). In 1922, Laizure noted the establishment of a small asbestos mining operation on Clear Creek, but used the adjective "desultory" to describe the asbestos industry at that time. The study by Eckel & Myers (1946) focussed mainly on the quicksilver mines at New Idria, but brief mention of the serpentinite was made, and a geologic sketch map of the serpentinite was included. This map, modified and enhanced by others, has been the "base map" for the majority of recent studies of the District.

II. Studies of Coleman and others, 1950 onward

Starting in 1950, R.G. Coleman of Stanford University began a study of the serpentinite and its remarkable suite of associated minerals (Coleman, 1957). He was assisted by a well-timed forest fire which burned over a portion of the District and facilitated access to remote outcrops. His study was the first to attempt to explain the New Idria District in an overall petrologic and structural context. He showed that the serpentinite body was fault bounded on all sides, with the sense of shear where it could be determined showing upward movement of the serpentinite against the country rock. Coleman showed that the intrusion of the serpentinite took place at low temperatures, given the lack of contact metamorphism of the country rock, and suggested that the entire massif was a diapir, that rose because of the density contrast between the serpentinite and the surrounding country rocks, aided by tectonic overpressure related to development of the fold systems.

Coleman concluded that some of the exotic mineral suites were associated with tectonic blocks entrained by the serpentinite, while others were due to metasomatic alteration of the serpentinite, probably due to the intrusion of small igneous bodies. Subsequent generations of students have visited the District, frequently for topical studies, but no general re-evaluation of the rocks studied by Coleman has been undertaken. Several field trip guides have been prepared in recent years, and these serve as useful introductions to the District (e.g. Brown et al., 1985; Coleman, 1986).

The guidebook prepared by E.J. Fowkes (1982) of West Hills College in Coalinga is an excellent sourcebook for the stratigraphy, structure, and paleontology of the region. The guidebook has many useful photographs and local maps.

III. Mineralogical studies

The unique suite of minerals found at the Gem Mine, particularly benitoite, neptunite, and joaquinite, have received much attention (e.g. Louderback, 1907, 1909; Bradley, 1909; Laird & Albee, 1972; Wise & Gill, 1977). Millage (1981) completed a mineralogical study of the Victor Claim, another benitoite and neptunite locality in the District. Other mineralogical studies have included specimens from the District, e.g. that of Lager et.al. (1989) on Ti-bearing garnets, and that of Murdock & Ingram (1966) on REE-enriched vesuvianites. These mineralogical studies have generally investigated isolated mineral specimens and have not delved into the petrology and geochemistry of the District.

IV. More Mining Studies

The mercury mines of the New Idria District are fault controlled. Henderson (1965) studied the cinnabar deposits at the New Idria Mines and proposed a low temperature hydrothermal model for their origin.

Beginning in 1960, the New Idria District became widely known for the industrial properties of the short fiber chrysotile asbestos that occurs here in abundance, and an "asbestos rush" occurred with several companies establishing large open pit mines. Some of the literature for this time is proprietary and unpublished, with only brief mention in trade journals of the period. The modern asbestos mining history is summarized by Levine-Fricke (1989). As of 1995, only one mine, the KCAC mine, remains in operation; indeed KCAC is now the only operating asbestos mine in the United States. Mumpton and Thompson (1975) described the mineralogy of the serpentinite and suggested that the short fiber chrysotile resulted from milling, or repeated recrystallization under shearing stress.

V. Geophysical Studies, 1943 onward

There is a large literature on the structure and tectonics of the California Coast Ranges; it is beyond the scope of this paper to review that literature A useful starting point however is the monograph *Geotectonic Development of California* (Ernst, 1981). There has been renewed interest in geophysical studies of the region in the wake of the destructive May 2, 1983 Coalinga earthquake. The Coast Ranges, including the Diablo Range, have been the subject of regional studies by a variety of geophysical methods, including gravity and aeromagnetic measurements, as well as seismographic techniques. Starting in the 1920s, refraction and reflection seismology were used mainly in support of oil company

exploration efforts, but helped to unravel the deep structure underlying the Coast Ranges and San Joaquin Valley (Vaughan, 1943). Byerly (1954) studied the regional gravity profile of the Coast Ranges in Central California. He reported that a 60 mgal negative anomaly underlies the New Idria Serpentinite, with the minimum value reached at the southern end. Byerly concluded that the serpentinite body is thickest at the southern end, and that no large body of unserpentinized peridotite underlies the serpentinite at the surface (or alternatively, if such a body exists it must be deeply buried). Later studies by Jachens (1991), with a higher station density, supported this conclusion. Aeromagnetic measurements in this region have generally been inconclusive, or have merely served to reinforce conclusions obtained by other methods (Vaughan, 1943; Coleman 1986).

The region around and immediately to the south of the New Idria District is seismically active today, as shown in **Figure 2.1.** There are swarms of magnitude 1-3 earthquakes and an occasional larger event (e.g. the 1926 Idria, M_W = 5.5, 1982 M_W=5.4 New Idria, 1983 M_W=6.5 Coalinga, and 1985 M_W=6.1 Kettleman Hills events, ref. Stein & Ekström, (1992)). The 1983 earthquake of magnitude 6.5 effectively levelled the town of Coalinga, but stimulated research interest in this part of California (e.g. Rymer & Ellsworth, 1990). The 1983 event occurred near the crest of the Coalinga Anticline, a southerly continuation of the New Idria Thrust Fault. The predominant mode of recent seismicity has been reverse or thrust faulting, due to crustal shortening from compressional stress normal to the strike of the San Andreas fault, (e.g. Montgomery, 1993; Bartow, 1990; Wentworth & Zoback, 1989). Another part of the seismic activity may be due to continued diapiric rise of the serpentinite massif, expressed as small movements on the boundary faults.

Figure 2.1 - Recent Seismicity in Northern California

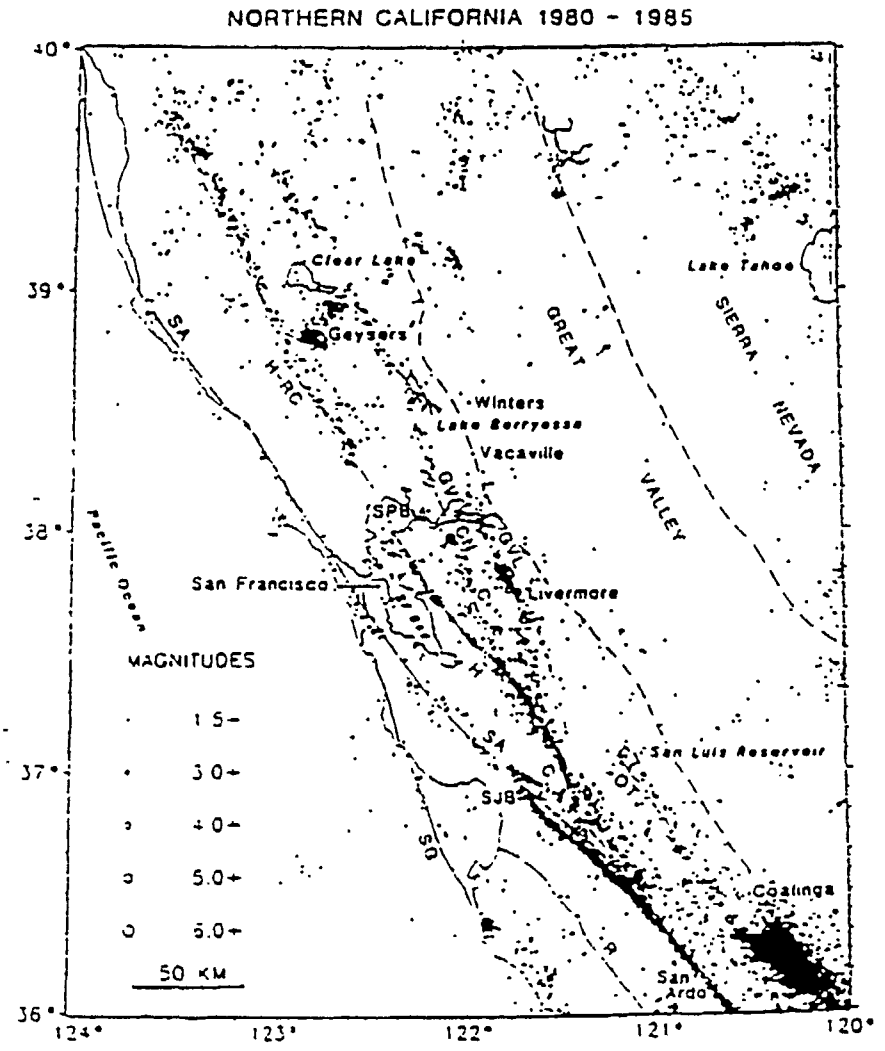

Figure 2.1 data from Hill et al. (1991). New Idria lies just to the north of the town of Coalinga. Recent seismicity has been concentrated in the region immediately to the south and east of New Idria.

VI. Studies by the EPA, 1982 onward

The California Aqueduct, completed in 1967, transports municipal and agricultural water from northern California to southern California. The aqueduct forms a barrier to stream drainage eastward from the New Idria District, especially at the Arroyo Pasajero east of Coalinga. Starting in 1982, public concern was expressed about the amount of chrysotile asbestos in the drinking water of the communities served by the California Aqueduct, chiefly Los Angeles. This concern resulted in a series of studies by the Environmental Protection Agency (EPA) to locate the source of this asbestos and to evaluate the perceived public health hazard. (e.g. Levine-Fricke, 1989; Woodward-Clyde, 1990). Stream runoff from the New Idria District was shown to be the major chrysotile asbestos source, particularly drainage through Los Gatos Creek and the Arroyo Pasajero. Notwithstanding the lack of evidence for any health hazard associated with ingestion of chrysotile asbestos in drinking water, the EPA moved to establish two Superfund sites in the District, one at the abandoned Atlas Mine, the other at the abandoned Coalinga Asbestos Mill site in Pine Canyon. Both of these locations are listed by EPA as uncontrolled hazardous waste sites under the provisions of the Comprehensive Environmental Response, Compensation, and Liability Act, or CERCLA (Superfund). Continued public pressure has resulted in a number of planned remedial actions, the estimated cost of which is now approaching $1 billion. The Bureau of Land Management has implemented a series of access control procedures, in order to reduce the disturbance of unstable hillsides by trail bikes and off-road vehicles in the Clear Creek Management Area. The Levine-Fricke (1989) study, done under contract to the EPA, includes a good summary of the geomorphology and stratigraphy of the District.

As noted above, the EPA was also concerned about the environmental impact of mercury mining at the New Idria Mines, which led to the closing of these mines in 1972. Acid

mine drainage from the sulfide-rich mine dumps results today in a pH as low as 1.7 in the stream that drains the area. The stream drains into a sparsely inhabited region, and no active remediation is taking place at the present time. The remote town of Idria is presently occupied by a drug rehabilitation program operated by the Futures Foundation of San Jose, California.

Most recently, concern has been expressed about the habitat of the San Benito evening primrose, which has been designated a threatened species under the Endangered Species Act. Botanical studies supervised by the Bureau of Land Management in Hollister provide an additional source of information on the District.

Epilogue:

Both the historical and scientific literature of the New Idria District are extremely scattered, making research time-consuming. This chapter is offered in the hope of saving a great deal of time for future investigators.

The greatest body of scientific literature concerning the New Idria District in the next few years is likely to be related to geophysical and tectonic studies of the Coast Ranges, and to environmental and engineering studies of the asbestos deposits.

Chapter 3

Mineralogy and Petrology of the New Idria Serpentinite

Chapter 3 - Mineralogy & Petrology of the New Idria Serpentinite

Chapter 3 - Mineralogy & Petrology of the New Idria Serpentinite

I. Introduction

This chapter describes the mineralogy and petrology of the New Idria Serpentinite and its accessory minerals exclusive of the tectonic blocks and igneous intrusives, which are described in Chapter 4 and Chapter 1 respectively. After a brief description of the geological setting of the New Idria District, a brief summary of serpentine mineralogy as it applies to the rocks of the District is offered. The process of progressive alteration of ultramafic rocks is shown to be responsible for the present mineralogy and rock textures observed at New Idria. The likely protolith for the serpentinite is discussed. Finally, accessory minerals of the serpentinite are described.

II. Geological Setting of the New Idria District

The term *New Idria District*, referred to in this study simply as *the District*, was first used by Becker to describe the general region encompassing the historic mercury mines at New Idria, California (Becker, 1888). The most remarkable feature of the District is an oval, 23 by 8 km, fault bounded, serpentinite massif flanked by steeply dipping, locally overturned, sedimentary and metamorphic rocks of the Jurassic-Cretaceous Franciscan and the Cretaceous to Pliocene Great Valley Sequence of California.

The New Idria Serpentinite is a part of the Coast Range Ophiolite in California (Hopson et al., 1981). Its emplacement within the Franciscan Formation is related to subduction of the Farallon plate in the Jurassic. The tectonic setting of the ophiolite was a forearc basin

lying between the Sierra Nevada volcanic arc to the east and a trench-subduction complex to the west, represented by the Franciscan Formation (Bartow, 1990). A piece of oceanic crust or underlying mantle was obducted onto the North American continent, later to rise through the Franciscan Formation as a serpentinite diapir. Emplacement of the New Idria Serpentinite as a diapir within the Franciscan has resulted in a piercement structure or tectonic window, lying just east of the San Andreas fault system northeast of Parkfield. Further details about the geological environment of the District can be found in Chapter 1.

III. Serpentine and Serpentinites

Serpentine is the name of a *mineral* family; serpentinite is a *rock type* consisting of one or more of the serpentine minerals, along with accessory phases, typically brucite, magnetite and chromite. The mineralogy and petrology of the New Idria Serpentinite have received much less attention than those of the related mineral deposits within and along its margins. Bradley (1918) noted that "The most striking feature of the geology of this district is the large area of serpentine...", but limited his description of this serpentine to a single paragraph in a lengthy report. His accompanying map simply showed undifferentiated serpentine. The 1946 Eckel & Myers map, which has been used as a base map for most geologic work for the past 50 years, showed some of the heterogeneity within the serpentinite. While Coleman (957) studied the physical emplacement of the serpentinite, he discussed the serpentine minerals themselves only briefly; he suggested that the dominant mineral was antigorite. Coleman also noted the local occurrence of tabular bastite-rich rock, resulting from serpentinization of harzburgite. (Bastite is the term used to describe serpentine that has formed after a chain silicate mineral, commonly orthopyroxene.) More recently, it has become apparent that the serpentinite is chrysotile-dominated (e.g. Mumpton & Thompson, 1975; Coleman, 1980; this study). Mumpton &

Plate 3.1 - General view of the New Idria serpentinite looking northeast from Condon Peak. Rolling hills are partially covered with scrubby vegetation on nearly white soil. Numerous rough roads, abandoned mines and exploration pits dot the landscape. The rocky knob to the left is Santa Rita Peak (1574 m), an antigorite knob. Beyond the peak is a steep escarpment which descends to the San Joaquin Valley. Summits of the Sierra Nevada are visible in the distance.

among these three minerals. The reader is referred to Wicks & O'Hanley (1988) for a discussion of serpentine polymorphism and polytypism.

The serpentine minerals have many structural features in common. Divalent cations, chiefly Mg, in six coordination with oxygen and hydroxyl groups, form an octahedral sheet with a b dimension of 9.4Å. Tetravalent cations, chiefly Si, form a tetrahedral sheet with a b dimension of 9.1Å, i.e. slightly smaller than the octahedral sheet. It is this misfit that is presumed to lead to the observed structural variations in the serpentine minerals. The apices of the tetrahedra are bonded to one side of the octahedral sheet. Hydroxyl groups lie at the center of the six-coordinated rings of the tetrahedral sheet, and at the same level as apical oxygens. Hydroxyl groups also lie in the basal plane of the octahedral sheet on the side opposite the tetrahedral sheet. Weak bonds involving hydrogen connect the layers of the serpentine structure; geometric variations in the positioning of adjacent layers allow for extensive polytypism. **Figure 3.1a** shows the ideal serpentine structure in perspective view, seen perpendicular to c*. The unit cell dimension along c is approximately 7Å.

Fe and Al are the principal compositional variants in serpentine. Compositional variation occurs along the three exchange vectors $Al_2Mg_{-1}Si_{-1}$ (Tk); $FeMg_{-1}$ (Fm); and $Fe^{3+}Al_{-1}$ (Fa). The dioctahedral vacancy substitution $[]Al_2Mg_{-3}$ is not known to occur in serpentine. Trace amounts of Ca, Na, and K reported in serpentine analyses may represent mixtures of other silicates with serpentine in the analyzed samples.

Serpentine group minerals most often form by hydration of minerals in ultramafic rocks, chiefly olivine and pyroxene. Other parageneses of serpentine are rare but do occur: at Globe, Arizona, at Newbury, Massachusetts, and at Bolton, Massachusetts, chrysotile

has formed as an alteration product after tremolite or forsterite, which have in turn formed by contact metamorphism of siliceous dolomite.

If the hydration of peridotite occurs at temperatures above the stability field of serpentine minerals, then other phases may form instead of serpentine minerals: e.g. anthophyllite, talc, and members of the humite group, especially if the activity of water (a_{H_2O}) in the fluid is low. At New Idria no evidence for the formation of these minerals has been found, and it is shown below that serpentinization at relatively low temperatures took place. For this reason the complex phase relations of these minerals are omitted from the following discussions.

A. Lizardite

The planar structure of lizardite is conceptually the simplest of the serpentine minerals, and approaches the ideal structure shown in **Figure 3.1a.** Lizardite accommodates the misfit between the octahedral and tetrahedral sheets by two mechanisms: cation substitution, and minor geometric adjustments that include tetrahedral rotation and changes in thickness of the sheets. Substitution of Fe^{2+}, Fe^{3+} and Al for Mg^{2+} occur in the octahedral sites, and Fe^{3+} and Al for Si^{4+} in the tetrahedral sites. Introduction of Fe^{3+} and Al in the octahedral sheet reduces the dimensions of this sheet, and therefore improves the fit with a pure Si tetrahedral sheet. Fe^{3+} and Al in the tetrahedral sheet increase the dimensions of this sheet, also improving the fit. Fe^{2+} in the octahedral sheet, on the other hand, worsens the fit. O'Hanley & Dyar (1993) suggest that Al and Fe^{2+} are favored in the octahedral sites; Fe^{3+} appears to be favored in the tetrahedral sites.

Tetrahedral rotation, on the other hand, has the effect of reducing the size of the tetrahedral sheet, which would appear to worsen the fit in near-end-member

Figure 3.1a - The lizardite 1T structure viewed normal to c*

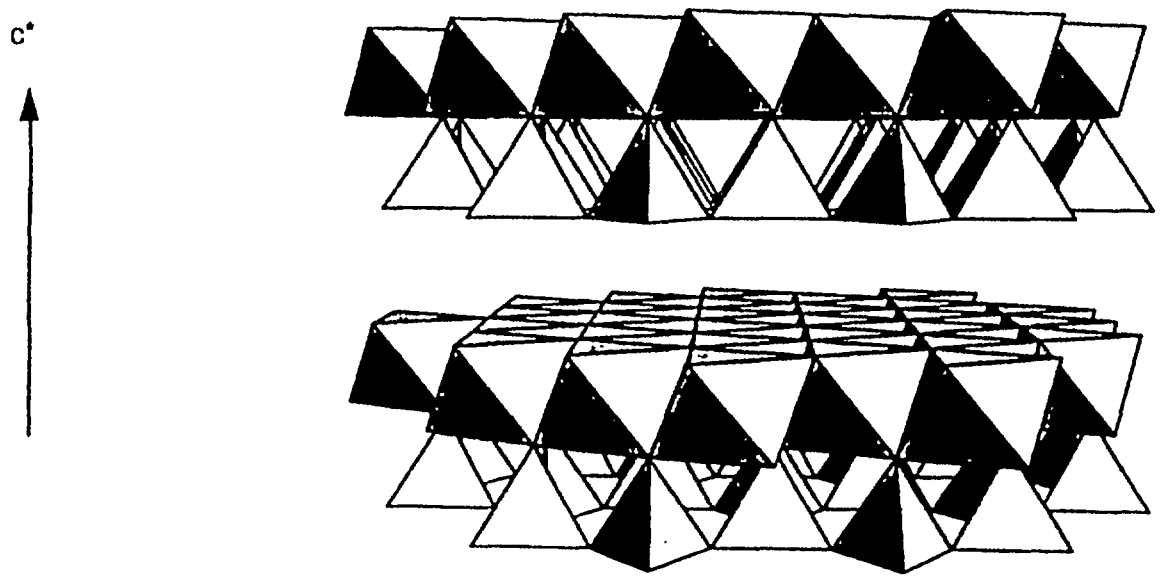

$Mg_3Si_2O_5(OH)_4$

compositions. The ionic substitutions could in principle increase the dimensions of the tetrahedral sheet so that it becomes larger than the octahedral sheet, as in micas. In these cases, tetrahedral rotation could reduce the size of the tetrahedral sheet to achieve proper fit. However, Mellini & Zanazzi (1987) found small tetrahedral rotations with $|\alpha| < 6°$ in near-end-member compositions. In their study the magnitude and sign of the rotation varied according to the lizardite polytype.

The tetrahedral rotation observed in lizardite is not what one would expect from observation of the structures of similar minerals. New calculations using the BDTEA computer code of L.W. Finger and the data of Mellini & Zanazzi (1987), Perdikatsis & Burzlaff (1981), Zigan & Rothbauer (1967) and Hazen (1976) show that the unshared edges of the octahedral sheet in lizardite are 3.07Å compared with 3.22Å in brucite, and 2.97Å in talc. The octahedral edge dimension in a slab from the periclase structure is 2.98Å. In lizardite and talc the unshared edge dimensions must be the same as the apical oxygen distances in the tetrahedral sheet. The lateral dimensions of the octahedral sheet in lizardite are less than in brucite but greater than in periclase; this must be due to the presence of the single tetrahedral sheet in the 1:1 lizardite structure. In talc, a mineral with many structural similarities to lizardite (except that two tetrahedral sheets are attached in the 2:1 structure), tetrahedral rotation in the end member composition is extremely small ($\alpha = 3.6°$, Evans & Guggenheim, 1988). The unshared edge length in talc is smaller than in lizardite: I would therefore expect that tetrahedral rotation in talc would be greater, not less, than in lizardite. The opposite appears to be true. The unshared edges in lizardite might be expected to be shorter on the tetrahedral side than on the non-tetrahedral side, but the difference is less than 0.001Å. The shared octahedral edges in lizardite are 2.78Å compared with 2.79Å in brucite, 2.98Å in periclase and 2.50Å in talc. As is common in sheet silicates, the octahedral sheet in lizardite is compressed along the c axis compared with the dimensions of a sheet of regular MgO_6 or $Mg(OH)_6$ octahedra. This slight

compression also reduces the lateral dimensions of the octahedral sheet by a small amount, improving the fit.

The formation of lizardite is promoted by the availability of Al (Caruso & Chernosky, 1979), Fe (Wicks & Plant, 1979), and relatively high oxygen fugacity (O'Hanley & Dyar, 1993). Lizardite formation is favored over chrysotile by a relatively low activity of water (O'Hanley et al., 1989, and references therein). The lizardite 1T polytype is the most common product of the retrograde alteration of olivine (Wicks & Whittaker, 1977) and is the most abundant of the serpentine minerals (Wicks & O'Hanley, 1988). In parageneses involving both lizardite and chrysotile, the presence of unserpentinized olivine in the rock tends to depress a_{H_2O}, resulting in early lizardite. Once olivine has been consumed and the activity of water has risen, late chrysotile tends to form (Prichard, 1979). Prichard suggested that the composition of serpentinizing fluids may change once olivine has been consumed, and that this is the explanation for the late stage appearance of chrysotile. Another possibility is that the water content of lizardite is lower than that of chrysotile, as discussed in the section on chrysotile. Alternatively, it is possible that kinetic factors control which "polymorph" appears in the formation of serpentine after olivine.

At New Idria, lizardite is much less abundant than chrysotile, possibly due to the recrystallization of earlier lizardite under shearing stress (Mumpton & Thompson, 1975). An alternative explanation for the abundance of chrysotile is the extensive growth of cataclastic fabric due to the predominance of dunite in the protolith (D. O'Hanley, personal communication, 1993). This idea is also discussed below in the section on progressive serpentinization, and in Chapter 7.

B. Antigorite

The next most abundant serpentine mineral is antigorite, which employs a different strategy for resolving misfit in the structure. Antigorite has a modulated structure, in which the misfit between the tetrahedral and octahedral sheets is accommodated by corrugations in the two sheets (Kunze, 1956). The continuous, undulatory octahedral sheet is always concave towards the tetrahedral sheet. The tetrahedral sheet is also continuous, but inverts at the corrugation boundaries or points of inflection, so that the tetrahedral apices point alternately towards +c and -c. This modulated structure causes octahedral sites to be "lost" at the corrugation boundaries or points of inflection, with the result that antigorite is Mg and (OH) - deficient, or Si-enriched, compared to the ideal serpentine formula. The proper end member formula for antigorite is necessarily arbitrary since it depends on the supercell periodicity: Thermochemical data for the following approximation to the antigorite formula are given by Berman (1988) and Helgeson et al. (1978):

$$Mg_{48}Si_{34}O_{85}(OH)_{62}$$

Figure 3.1b shows in schematic form the antigorite structure with the corrugations flattened out in order to see the bonding between layers. It is apparent that the Si-O-Si bonds at the points where the tetrahedral sheets invert are responsible for the tough, resistant nature of antigorite compared with lizardite or chrysotile, in which the adjacent layers are held together by weak bonds involving hydrogen. This toughness is well displayed in the resistant antigorite knobs at New Idria. Consideration of the antigorite chemistry and structure also suggest that antigorite should be a member of a polysomatic series between lizardite and talc (e.g. Otten, 1993; Sanford, 1978). The above antigorite formula is equivalent to 15 Liz + 1 Tlc. If the wavelength of the modulation were to

Figure 3.1b - Simplified Antigorite Structure Projected onto [010]

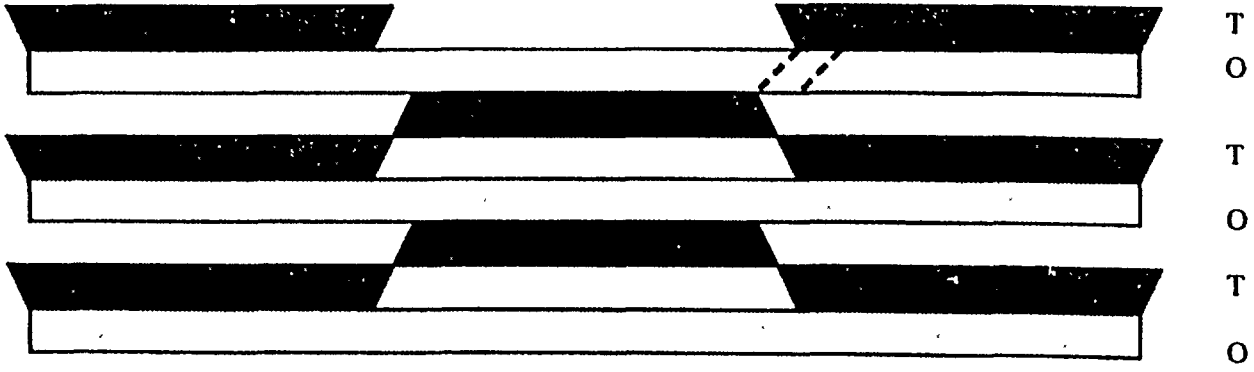

decrease the structure would become increasingly talc-like, while if the wavelength were to increase the structure would become increasingly lizardite-like. In the 1:1 lizardite structure, each octahedron is bonded to two apical oxygens and four hydroxyl groups; the apical oxygens lie on the same side of the octahedral sheet. In the 2:1 talc structure each octahedron is bonded to four apical oxygens and two hydroxyl groups; the apical oxygens lie on both sides of the octahedral sheet. In the antigorite structure, at the point in each layer where the tetrahedral sheet inverts, there is a distinct type of octahedron bonded to four apical oxygens and two hydroxyls; the apical oxygens lie on both sides of the octahedral sheet. The position of one of these special talc-like octahedra is shown by the heavy black lines in **Figure 3.1b**. Sanford (1978) considered polysomatic models of the antigorite structure. Polysomatic models for the antigorite structure based on HRTEM studies were also proposed by Spinnler (1985) and Otten (1993), who considered more complex structural building blocks than talc and lizardite.

The stability field of antigorite extends to higher temperatures than that of the other serpentine minerals - in this sense it is the high T "polymorph". Antigorite does not often form as a retrograde alteration product of olivine; it generally forms as a prograde metamorphic product, together with brucite, after pre-existing lizardite and chrysotile, according to the endothermic reaction:

$$17Mg_3Si_2O_5(OH)_4 \rightarrow Mg_{48}Si_{34}O_{85}(OH)_{62} + 3Mg(OH)_2 \qquad (1)$$

chrysotile antigorite brucite

Using the data of Berman (1988), I find this reaction consumes 2 kJ/mol chrysotile at 1 bar and 25°C. At New Idria, antigorite is found principally in tough, resistant knobs which are interpreted as tectonic inclusions or knockers in the chrysotile-dominated serpentinite (**Plate 3.1**). Antigorite knockers are discussed further in Chapter 4.

One of the unexpected phenomena associated with serpentinites is that during hydration of peridotite at low temperatures, antigorite rarely forms; instead one sees lizardite or chrysotile. On the other hand, dehydration of a serpentinite by progressive metamorphism produces antigorite, which eventually dehydrates with rising temperature to form olivine. Why does hydration of olivine not produce antigorite? One possible explanation has to do with the relationship between P_{H_2O} and P_{total}. Sanford (1981) proposed that the lower limit of the antigorite stability field may be bypassed during serpentinization when $P_{H_2O} < P_{total}$, typical of infiltration of water along cracks at shallow depths, while antigorite is stabilized during prograde metamorphism of serpentinites when $P_{H_2O} = P_{total}$. Sanford's model did not, however, consider the formation of lizardite versus chrysotile.

C. Chrysotile

Another structural variant in the serpentine family is chrysotile. Although the least abundant of the serpentine minerals, chrysotile dominates at New Idria. The structure of chrysotile accommodates the misfit between the octahedral and tetrahedral sheets by rolling up the sheets into cylinders; the tetrahedral sheet faces the concave side of the octahedral sheet. The result is that crystallites of chrysotile are actually hollow tubules with diameters of up to several microns, easily visible with a scanning electron microscope (Yada, 1967). The tubules may aggregate into fibers which form chrysotile asbestos, although massive chrysotile also occurs at New Idria. Chrysotile asbestos, representing 95% of commercial production, is the subject of much current medical research because of concerns about its pathogenicity in lung tissue (e.g. Guthrie & Mossman, 1993).

Chrysotile 2M is the most abundant chrysotile polytype; it commonly forms at low temperatures as a late stage alteration product of olivine. As noted in the discussion of lizardite stability, low temperature progressive serpentinization of olivine usually produces lizardite until olivine has been consumed, followed by late stage formation of chrysotile. At the time olivine is completely consumed, a_{H_2O} rises and the composition of the serpentinizing fluids may possibly change (Prichard, 1979). If a_{H_2O} by itself affects the formation of lizardite versus chrysotile, then the assumption that the water content of lizardite and chrysotile is equal must be challenged.

The dioctahedral analogue of lizardite is kaolinite ($Al_2Si_2O_5(OH)_4$). A related hydrated form of kaolinite known as halloysite ($Al_2Si_2O_5(OH)_4 \cdot 2H_2O$) has interlayer molecular water; its structure tends to roll up into tubules, somewhat like tubules of chrysotile (except that in halloysite the octahedral layer is convex towards the tetrahedral layer, not concave as in chrysotile). The molecular water in the halloysite structure could possibly correspond to (thus far undetected) water in the chrysotile structure. This would lead to a hypothetical chrysotile formula of $Mg_3Si_2O_5(OH)_4 \cdot nH_2O$. If this could be established by experiment, the interaction between a_{H_2O} and the chrysotile might be explained by the reaction pair:

$$\text{olivine} + \text{water} = \text{lizardite} + \text{brucite}$$

$$\text{lizardite} + n \cdot \text{water} = \text{chrysotile}$$

The equilibrium constant for both of these reactions obviously depends on a_{H_2O}. For the second reaction, that produces chrysotile, we have the relation $K = 1/[a_{H_2O}]^n$. The value of n is uncertain, but is probably small, perhaps less than 1. It is noteworthy that Faust & Fahey (1962) found that some, but not all, chrysotile dehydration curves using the DTA

technique had a double peak while antigorite always had a single peak. They believed that excess water in chrysotile was a surface absorbtion phenomenon.

V. Phase Relations among the Serpentine Minerals

The phase relations among the serpentine minerals are difficult to show schematically, and are not completely understood. In general, lizardite and chrysotile are the low temperature serpentine minerals; antigorite is the high temperature phase. The stability field of lizardite probably extends to higher temperature than that of chrysotile, due to the effect of ionic substitutions of Al and Fe (O'Hanley et al., 1989). The presence of lizardite and antigorite in blueschist facies serpentinites suggests these two phases are the stable high pressure phases. Reversed experiments showing the above relationships remain to be done; no reliable thermochemical data for lizardite have been published. Attempts to synthesize lizardite in the laboratory have almost invariably produced chrysotile, making reversal experiments difficult (but see Chernosky, 1975). Substitution of Fe and Al probably expands the thermal stability of lizardite relative to the other serpentine minerals. Antigorite is the stable serpentine mineral at high temperature conditions; the reaction boundaries separating antigorite from lizardite and chrysotile are not simple polymorphic transitions, but probably correspond to reaction (1) above. **Figure 3.2** shows the calculated univariant curve for reaction (1) using the TWQ2S program of Berman (1991-1994) and thermodynamic data of Berman (1988). The upper stability limit of chrysotile is less than 300°C at 1 bar; the univariant line has a negative slope. This is consistent with the observations of Sanford (1981) and of Evans et al., (1976). All of these observations are summarized in the following schematic diagram:

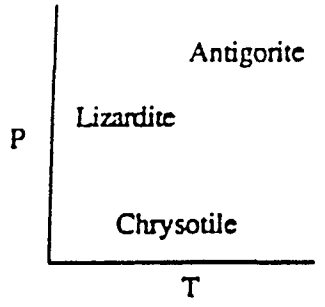

Due to the importance of Fe and Al, discussion of serpentine phase relations in MSH alone is probably unproductive; MASH is the simplest realistic system (O'Hanley, D.S., personal communication 1993). The reader is referred to O'Hanley et al. (1989) for complex phase diagrams in the MgO-SiO_2-H_2O (MSH) and MgO-Al_2O_3-SiO_2-H_2O (MASH) systems, constructed using the method of dual networks (Kujawa, 1965). The MSH system, however, can be used as a first-order approximation for formulating phase relations between serpentine minerals and other minerals found in serpentinites. These relations are explored in the next section.

VI. Phase Relations in Serpentinites

The thermal stabilities of common phase assemblages in serpentinites are limited by the univariant reactions shown in **Figure 3.2.** This figure is calculated using the TWQ2S program for the MSH system and includes only the stable reactions for the portion of MSH in which chrysotile + brucite are the low temperature assemblage. The calculated positions of the univariant equilibria agree well with experimental evidence (Bowen & Tuttle, 1949), and field evidence (Evans et al., 1976).

Figure 3.2 - Univariant reactions in the magnesian portion of the MSH system, for bulk compositions corresponding to mixtures of forsterite and enstatite. Compositions more magnesian than forsterite or more siliceous than enstatite not shown. Calculations using the TWQ2S code (Berman, 1991). Numbered reactions given in text. Abbreviations are Ctl:chrysotile, Brc:brucite, Atg:antigorite, Fo:forsterite, Tlc:talc, En:enstatite, W:water.

Figure 3.2

Univariant Reactions in the Magnesian Portion of the MSH System

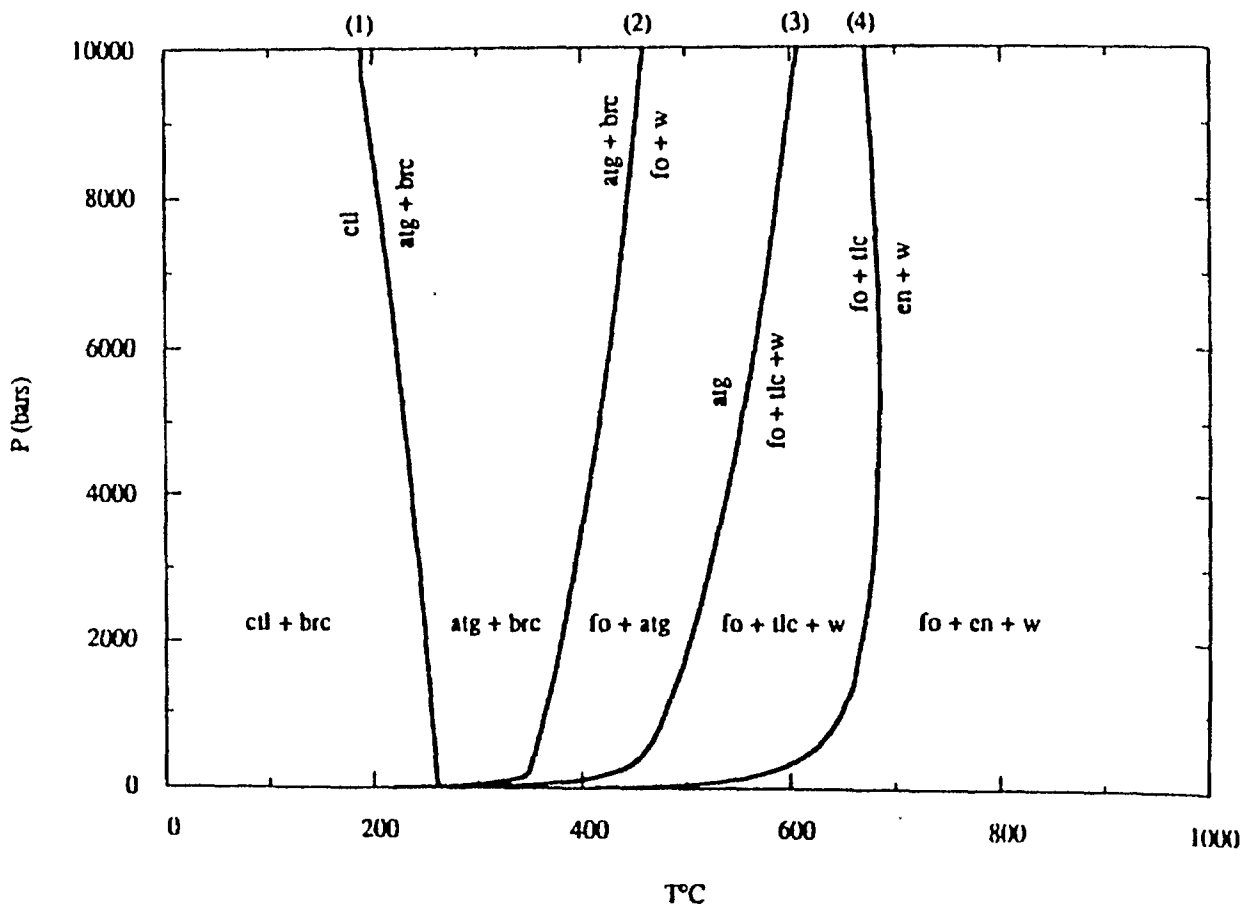

The univariant reactions in MSH with a fluid phase of pure H_2O are, in addition to reaction (1):

$$Mg_{48}Si_{34}O_{85}(OH)_{62} + 20Mg(OH)_2 = 34Mg_2SiO_4 + 51H_2O \quad (2)$$

antigorite brucite forsterite

$$Mg_{48}Si_{34}O_{85}(OH)_{62} = 4Mg_3Si_4O_{10}(OH)_2 + 18Mg_2SiO_4 + 27H_2O \quad (3)$$

antigorite talc forsterite

$$2Mg_2SiO_4 + 2Mg_3Si_4O_{10}(OH)_2 = 10MgSiO_3 + 2H_2O \quad (4)$$

forsterite talc enstatite

The following discussion of progressive metamorphic reactions assumes that the low-temperature serpentine mineral is chrysotile, since there are no thermochemical data available for lizardite. Accessory oxide minerals are also ignored; they do not significantly affect the stabilities of coexisting silicate minerals. At New Idria, the dominant phase assemblage of chrysotile + brucite indicates an Mg/Si ratio lying between forsterite and enstatite, and a low temperature equilibrium (<250°C), in the divariant field below reaction (1). Antigorite knockers described in Chapter 4 have a higher temperature assemblage; they lie in the divariant field between reactions (1) and (2). In the contact aureole around the intrusive New Idria syenite, prograde olivine replacing antigorite shows that reaction boundary (2) was encountered. No evidence was found at New Idria for higher grade metamorphism, i.e. reaction (3) or higher. I therefore conclude that at New Idria, based on evidence from the serpentinite itself, the rocks equilibrated at temperatures at or below that of the greenschist facies. Note that in the bulk compositions modelled here, with fluids consisting of pure H_2O, talc does not appear as a low temperature mineral, but rather as a metamorphic mineral in the amphibolite facies. Bulk compositions more siliceous than enstatite, in which chrysotile + talc are stable at low temperatures, were not found in this study. Bulk compositions more magnesian than

forsterite were also not found in this study; ultramafic rocks with such compositions are extremely rare in nature. If these unusual compositions were explicitly considered, Figure 3.2 would require two more univariant reactions for the dehydration of talc and brucite respectively, at upper amphibolite grade. Likewise, if the aqueous phase were not pure H_2O, the above univariant reactions would become divariant in P-T-a_{H_2O} space, and talc might appear as a low-T phase.

VII. Distinguishing Among the Serpentine Minerals

In many cases it is difficult to distinguish among the serpentine group minerals with a single test, particularly since more than one serpentine mineral may exist in a single sample. X-ray diffraction analysis (XRD) is often ambiguous for two reasons: the peaks which distinguish the serpentine minerals are weak, and their intensities may be affected by preferred orientation of the sample. Large single crystals of serpentine are rare, making single crystal analysis difficult. Observation of optical properties, using the criteria of Wicks & Whittaker (1977), are another useful, but not definitive method. Elevated Al contents in a serpentine chemical analysis suggest the presence of lizardite, as noted above. In this study, determinations of serpentine mineralogy were done by a combination of XRD and chemical analyses, as well as the optical and textural criteria of Wicks & Whittaker (1977), as simplified by Wicks & O'Hanley, (1988). (see Table 3.3). In some cases the specific serpentine minerals present could not be determined unambiguously. These cases are noted in the text.

To illustrate these points, sample 989-45 from New Idria was studied using all of the above techniques. 989-45 is a dark green, sheared rock from Perovskite Knob. Table 3.1 gives a measured XRD pattern for this sample. The indexed pattern suggests that

Plate 3.2 - Photomicrograph of serpentinized harzburgite, sample 989-45. Bastite grain in center shows development of both lizardite and chrysotile. Crossed nicols with gypsum plate. Crossed nicols; field of view 1 mm.

this sample contains a mixture of chrysotile and aluminous lizardite. High Al contents (1.45%) in whole rock analytical data in **Table 3.2** (column 1), electron microprobe analysis of individual grains, and petrographic observations using the Wicks & Whittaker criteria, confirm that the sample contains a mixture of chrysotile and lizardite. **Plate 3.2** shows a portion of this sample in which serpentine of both positive and negative sign of elongation occurs within a single bastite grain, because of the presence of chrysotile and lizardite respectively. The replacement appears to be controlled by exsolution lamellae or cleavage planes in the orthopyroxene. Bastite, the pseudomorphic replacement of chain silicates by serpentine, is widely distributed at New Idria.

VIII. Progressive Alteration of Ultramafic Rocks

It is important to view the formation of serpentinites as a multi-stage process, in which earlier minerals may recrystallize or be replaced more than once along their path from protolith to geologist's sample bag. The term *progressive serpentinization* is used here to describe this multi-stage process. The following discussion assumes a depleted ultramafic protolith of dunite and/or harzburgite, and that the model reactions are in the MSH system (i.e. the fluid phase is pure H_2O). Chapter 4 extends this analysis to the CMASH system.

Olivine and orthopyroxene are not stable at low temperatures in the presence of water, as shown in **Figure 3.2**. If hydration takes place at temperatures below reaction boundary (1), one of the following component reactions may occur:

$$2Mg_2SiO_4 + 3H_2O = Mg_3Si_2O_5(OH)_4 + Mg(OH)_2 \qquad (5)$$

forsterite serpentine brucite

$$Mg_2SiO_4 + MgSiO_3 + 2H_2O = Mg_3Si_2O_5(OH)_4 \quad (6)$$

forsterite enstatite serpentine

$$6MgSiO_3 + 3H_2O = Mg_3Si_4O_{10}(OH)_2 + Mg_3Si_2O_5(OH)_4 \quad (7)$$

enstatite talc serpentine

In reaction (5) pure forsterite reacts with water to produce serpentine, and, since magnesia is in excess, brucite. The resulting serpentine-brucite assemblage may persist, may undergo recrystallization by prograde metamorphism in some later thermal event, or may undergo further replacement reactions, particularly if CO_2-rich meteoric waters are present. Evidence for all three of these processes is abundant at New Idria. When orthopyroxene is present as a reactant, modal brucite is reduced - to zero in the case of reaction (6), from which only serpentine is produced. As the ratio of orthopyroxene to olivine increases beyond 1:1 molar proportions, talc may appear as a product together with serpentine. Reaction (7), with olivine absent, produces the assemblage talc + serpentine in equal proportions. Therefore, at low temperatures in this model system, in which the hydrous phases have essentially fixed compositions, the amount of modal brucite depends on the orthopyroxene/olivine ratio. If iron in solid solution is added as an additional component, reactions (8a), (8b) and (9) described below in Section X may produce magnetite; the coexisting hydrous minerals will be low in Fe (but see Section X concerning the formation of Fe-rich brucite).

The fractionation of oxygen isotopes between serpentine and magnetite has been used to record the temperature of serpentinization (Wenner & Taylor, 1971). Application of this technique to New Idria samples would provide useful information on the evolution of the serpentinite. ∂D-$\partial^{18}O$ studies of the serpentine minerals at New Idria also hold promise for constraining the environment of serpentinization, potentially distinguishing ocean-

floor serpentinization from serpentinization that took place after emplacement of the ophiolite.

In principle, serpentinized ultramafic rocks could contain talc as part of the low temperature assemblage, when the serpentinizing fluid is pure H_2O. In fact, this is rare, because the required silica-rich bulk composition would place the parent rock in the "olivine orthopyroxenite" field of the IUGS classification, which is an extremely rare rock type. Therefore, talc does not normally appear as a low temperature mineral when fluids are pure H_2O, but instead as a prograde metamorphic replacement of antigorite at roughly staurolite grade (Trommsdorff & Evans, 1974). If the serpentinizing fluids are rich in CO_2, however, then magnesite and talc or tremolite may indeed appear as low temperature products. This has not happened at New Idria but has happened in the Appalachian serpentinites of Vermont and Quebec. See Sanford (1978) for a discussion of serpentinization with CO_2-rich fluids.

A. Progressive Serpentinization of Dunite

Serpentinite formed after dunite often has a knobby outcrop texture formed by intersecting serpentine/brucite veins which isolate rounded kernels of unserpentinized dunite. This macroscopic texture is well displayed in resistant boulders at New Idria (Plate 3.3, 3.4). O'Hanley (1992) has shown that this *kernel pattern* results from a volume increase during serpentinization. Development of the intersecting veins is aided by the relatively isotropic nature of dunite - there is no preferred direction for vein development, and strain is not partitioned along well-developed shear planes. At New Idria, the nearly complete pulverization of the original bedrock in the southern half of the District may be explained by positive feedback between progressive serpentinization and decreasing rock competency. This feedback, in an environment of shear stress due to tectonic

overpressure, may lead to the development of additional vein systems and continued serpentinization, which further weaken the rock. At the KCAC Mine, large rounded boulders, which populate the waste pile, are mainly kernels of dunite. Chapter 7 uses these concepts to propose a model for development of short-fiber chrysotile asbestos at New Idria.

Microtextures of serpentine also show the kernel pattern, as illustrated in **Plate 3.5**. In this photomicrograph, the intersecting fractures of the parent rock isolate olivine and pyroxene cores into polygonal kernels. The serpentine minerals here are a mixture of lizardite and chrysotile; the vein filling mineral is mostly chrysotile. This texture is pseudomorphic and is common. Opaque minerals are magnetite and chromite.

B. Progressive Serpentinization of Harzburgite

Serpentinite formed after harzburgite often has a slabby texture, and the serpentinized rock fractures leaving sharp edges, rather than the rounded kernels of serpentinized dunite. Two aspects of the harzburgite protolith are responsible for this difference - mineralogy and layering. Harzburgite differs from dunite in having significant amounts of orthopyroxene, which is frequently found in parallel layers that give the rock a banded appearance. These layers may be a primary igneous feature or may have been produced by deformation of the harzburgite prior to serpentinization. At New Idria harzburgite outcrops are not numerous; the banding is displayed only faintly due to the advanced degree of serpentinization. Fractures along which serpentinizing fluids flow tend to form preferentially parallel to the layers, rather than at random angles as in dunite. The resulting serpentinization tends to produce angular blocks as shown in **Plate 3.6**. The presence of orthopyroxene also inhibits the production of brucite, according to reaction (6) above. Brucite is unstable in the presence of CO_2 - rich meteoric fluids, altering

Plate 3.3 - Serpentinized dunite at Butler Estate Mine showing early development of kernel texture by intersecting veins.

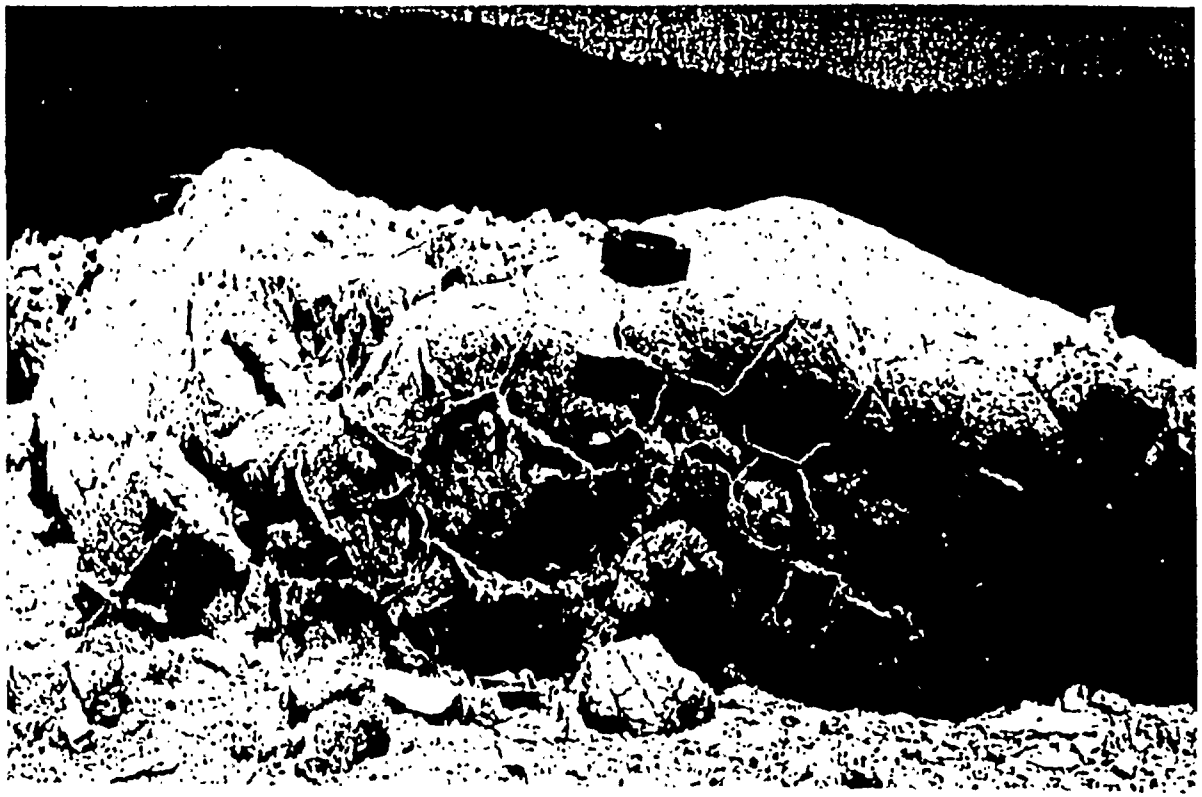

Plate 3.4 - Serpentinized dunite at J.M. Christie Pit showing progressive development of kernel texture as isolated, rounded masses.

Plate 3.5 - Photomicrograph of kernel texture with relict cores of olivine (center) and pyroxene (left). Intersecting veinlets isolate kernels as serpentinization proceeds. Opaques include magnetite and chromite. Crossed nicols; field of view 2 mm.

Plate 3.6 - Photo of hand sample of partially serpentinized harzburgite, showing slabby texture, bastite grains and weathering rind.

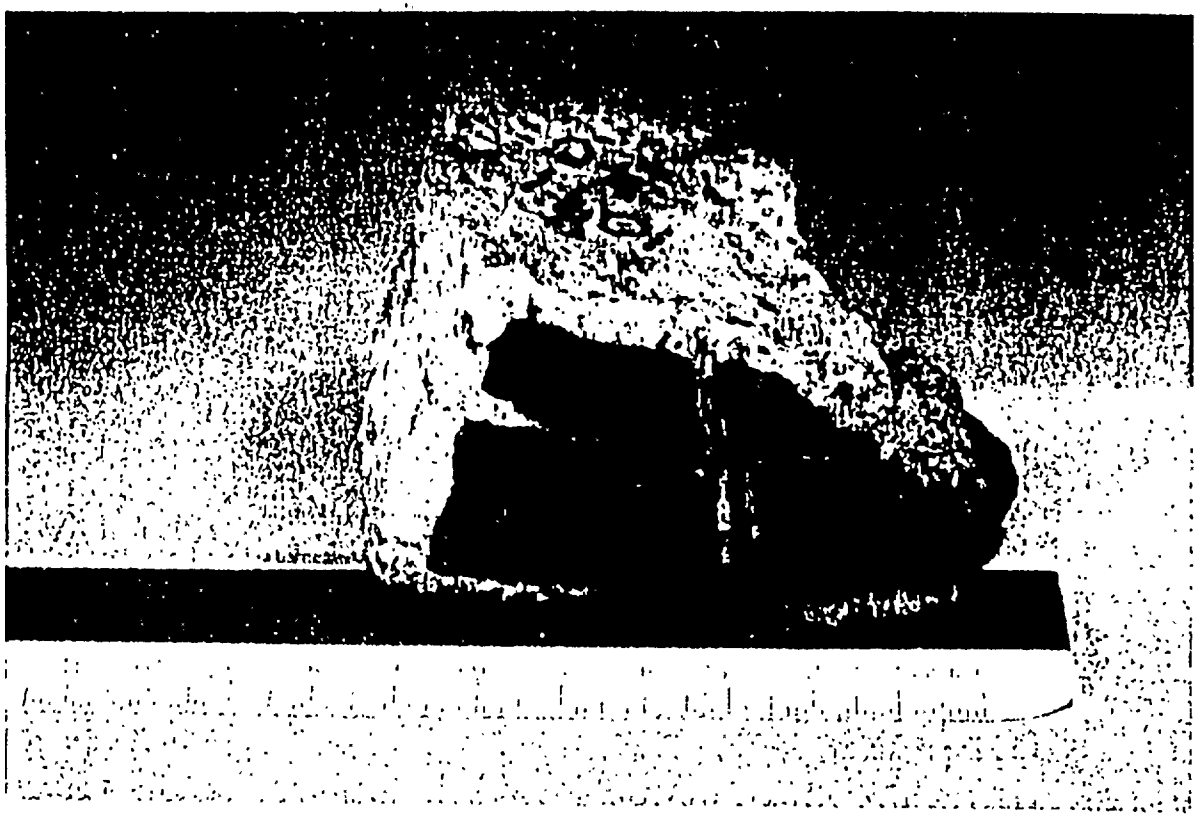

quickly to one of the Mg carbonates. Reactive brucite therefore tends to destabilize the rock mechanically, while in its absence the rock retains much of its original strength until serpentinization is quite advanced (see Chidester et al., 1978).

Serpentine formed after orthopyroxene tends to preserve the original rock texture as bastite pseudomorphs. Bastite is found in samples at New Idria, where orthopyroxene has been more resistant to serpentinization than has olivine. The bastite grains, visible in hand sample as dark spots, also contribute to maintaining the physical integrity of the rock and enhance its resistance to further degradation.

The mineralogy and textures of serpentinites depend on several factors, particularly on the protolith but also on the temperature at which serpentinization occurs. **Table 3.3** summarizes processes and resulting microtextures inferred by Wicks and co-workers. In this study the simplified classification scheme of Wicks and O'Hanley (1988) is used unless otherwise stated. A factor in the production of antigorite, not shown directly in **Table 3.3** is the importance of prograde metamorphism of low-temperature serpentine minerals, following reaction (1) above. Most antigorite forms by this process.

IX. Petrology of the New Idria Serpentinite

A. Compositional Analysis

Serpentine group minerals most often form as alteration products of minerals in ultramafic rock, chiefly olivine and pyroxene. Ultramafic rocks are conveniently studied in the ternary projection forsterite-enstatite-diopside (Ol-Opx-Cpx), projected from a specified aluminous phase, as shown in **Figure 3.3**. Serpentinized ultramafic rocks may also be

studied in this projection, so long as one keeps in mind that mobile components such as Ca may be lost during serpentinization, resulting for example in an underestimate of the modal clinopyroxene of the protolith.

Table 3.2 gives representative whole rock analyses of the New Idria serpentinite from this study and from other sources. Examination of this table shows that Mg, Si, and Fe account for almost all of the cations in the anhydrous analyses. The two drill hole samples (columns 2 and 4) are more similar to each other than either is to the "hard rock" samples. The variations in major element chemistry are quite significant - a large number of whole rock analyses would be required to estimate adequately the mean bulk composition of the serpentinite.

Table 3.4 displays the anhydrous bulk compositions of **Table 3.2** recalculated into the normative Ol-Opx-Cpx-spinel ultramafic system, using a method called "spinel norm". The CIPW norm calculation (Cross et al., 1902), was originally designed for feldspar-bearing rocks which crystallized at low pressures, and is not appropriate for high pressure rocks which crystallized above the stability field of anorthite. Modal mineralogy produced by the CIPW norm does not correspond to that present in high pressure ultramafic rocks. I therefore utilized a modified calculation procedure called "spinel norm" for these rocks, in which low pressure phases are replaced by their high pressure equivalents, and the resulting ternary plots are projected through spinel. I replaced albite by jadeite and anorthite by spinel + clinopyroxene; the Tschermak (Tk) component of the pyroxenes was set to zero for these samples. A few extremely calcic rocks also required a fictive wollastonite component to accommodate Ca: in actuality such rocks would accommodate excess Ca in garnet. A computer code widely used in Switzerland (MANNOR, written by P. Ulmer) has adopted a similar strategy.

Figure 3.3 - IUGS (1973) classification scheme for ultramafic rocks. The units in the ultramafic ternary are modal (volume) percent, very nearly equal to oxygen equivalent percent.

Figure 3.3 - IUGS Classification of Ultramafic Rocks

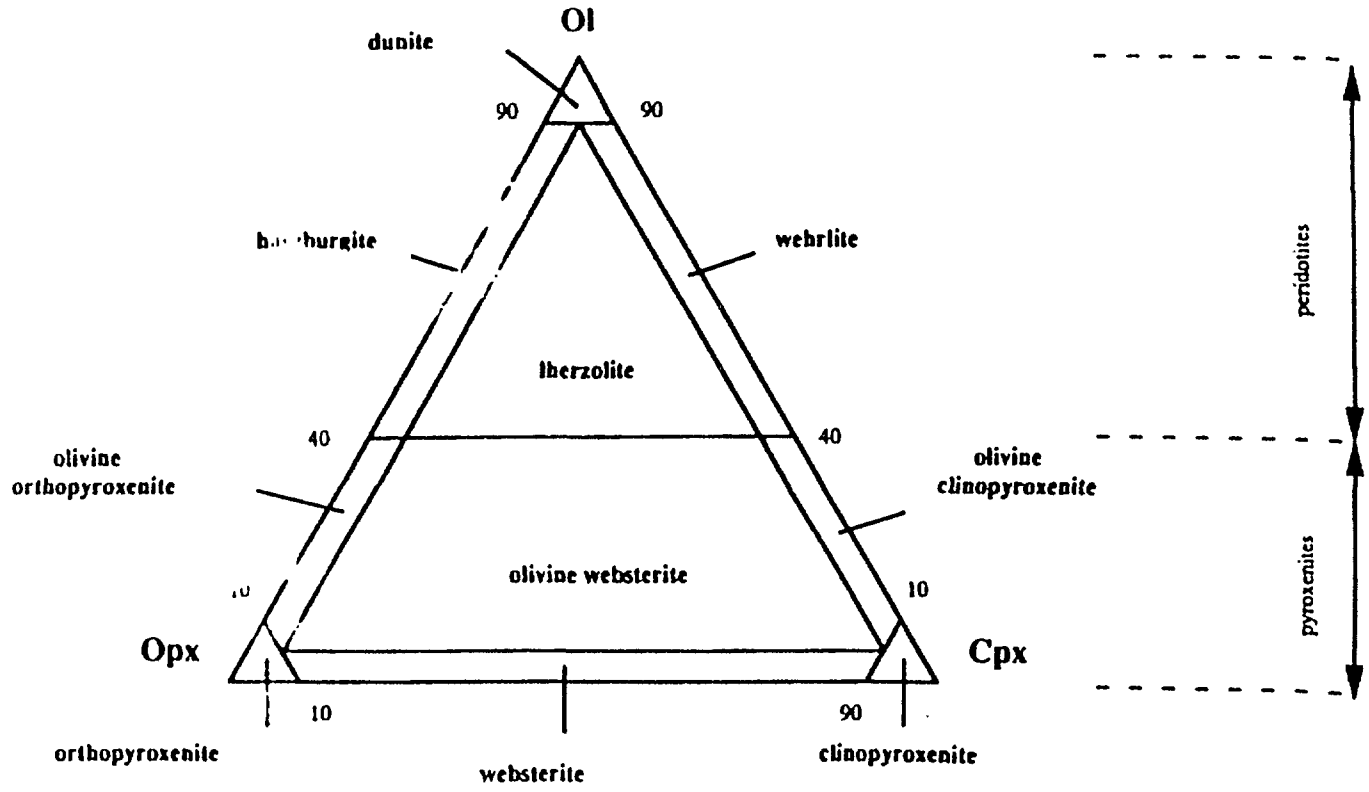

Figure 3.4 - Projection of serpentinite bulk compositions into the ultramafic ternary of Figure 3.3. See Figure 3.3 for field boundaries. Projection through spinel. Note analyses lie in two distinct groups (see text).

Figure 3.4 - Projection of Serpentinite Bulk Compositions

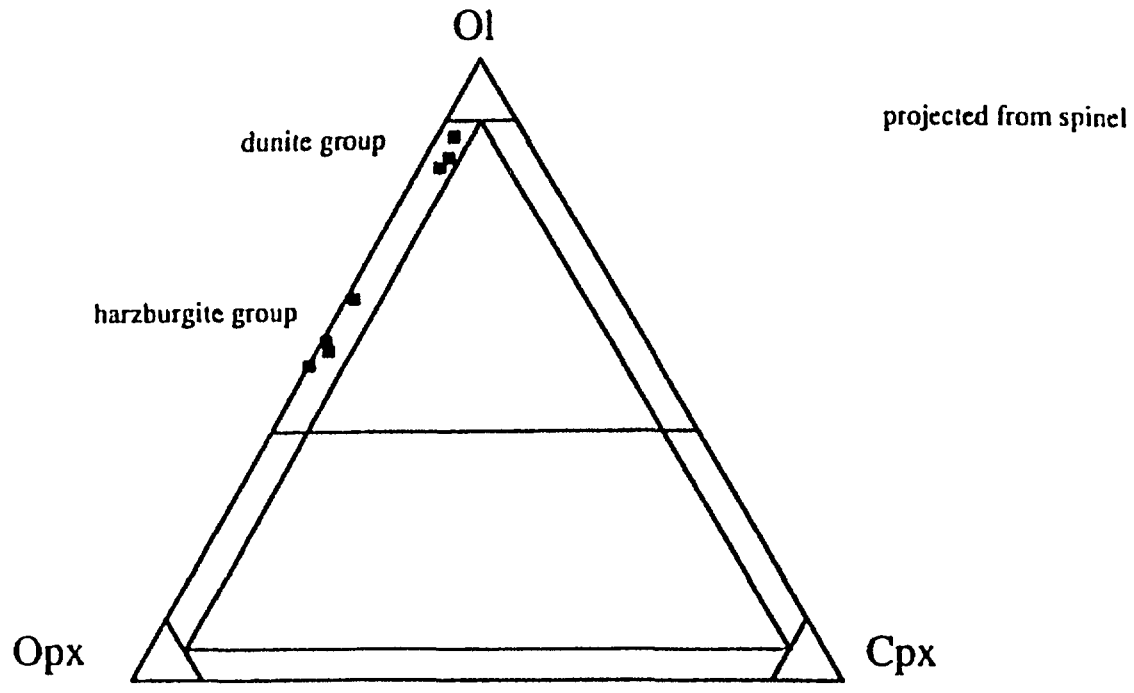

Figure 3.5 - Compositional variation in serpentinites expressed as mixing line between end members of pure serpentine, and a mixture of brucite + magnetite appropriate to the Mg-Fe ratio in host rock.

Figure 3.5 - Compositional Variation in Serpentinites

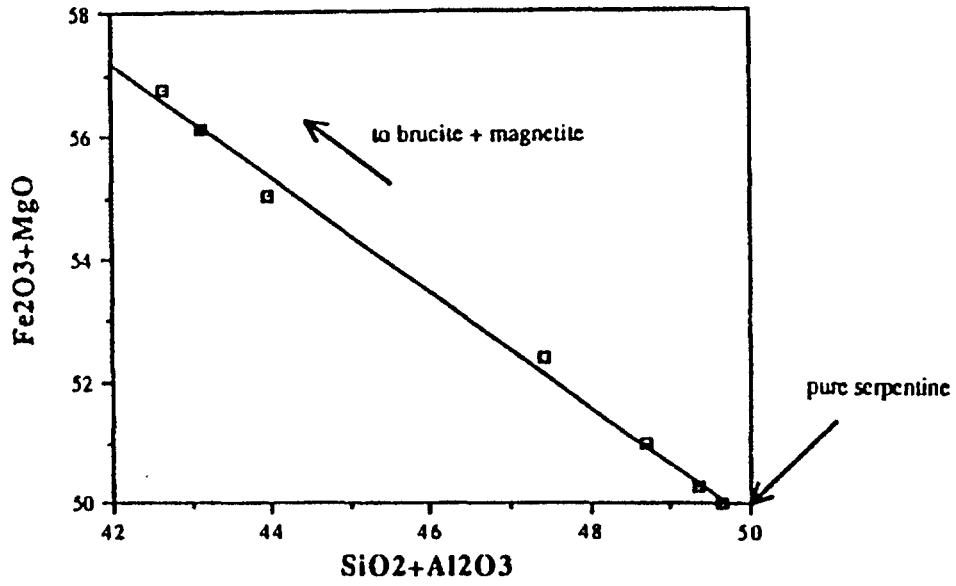

Figure 3.4 projects the calculated compositions of Table 3.3 into the ultramafic ternary system Ol-Opx-Cpx, where they plot along the Ol-Opx join. The analyses fall into two groups, a "dunite group" low in Opx and a "harzburgite group" rich in Opx. Although both groups lie within the harzburgite field according to the IUGS classification scheme, in this study it is convenient to refer to the rocks as dunite and harzburgite. In the field, these two groups are readily distinguishable by their mineralogy and alteration properties.

Figure 3.5 shows the inverse correlation, observed in the whole rock serpentinite analyses, between $SiO_2 + Al_2O_3$ (which are contained in modal serpentine minerals), and "excess" MgO and Fe_2O_3, which are contained in modal brucite and magnetite respectively. The compositional trend is a mixing line between two end members defined in the following way: a pure serpentine composition containing 50 wt. % MgO, and a composition consisting of a mixture of brucite + magnetite, in proportions appropriate to the Mg/Fe ratio of the rock. MgO and Fe_2O_3 were added together and are defined as "excess" when their sum exceeds 50 wt. %. This excess amount then represents variation toward an end member component of brucite + magnetite. Nearly all of the bulk analyses of the serpentinite plot along or close to this mixing line.

The New Idria serpentinite is far from homogeneous, with mineralogical and petrological variations on several scales. The rock consists principally of fractured and sheared serpentine rock of several types, weathered to a depth of several meters in places. This weathered zone is best seen in the southern portion of the District - a powdery matrix of crumbled chips and pulverized sheets consisting principally of chrysotile. The fractured serpentine rock underlies the weathered zone and stands out in positive relief as knobs and towers in a variety of shapes. These knobs and towers are frequently green in color when freshly exposed, weathering to a brick red after a short time. In general at New

Idria, knobs and towers of all rock types weather to about the same brick red color. The abundance of resistant knobs and towers increases north of San Benito Mountain.

Within the serpentinite there are numerous tectonic inclusions of contrasting rock type which may also form resistant knobs: these are discussed in Chapter 4.

Finding representative rock samples in this environment is difficult because of the uncertain mixture of resistant and crumbled rock. This may explain the differences in bulk mineralogy reported by previous workers. In an environment dominated by crumbly rock there is a tendency to oversample the resistant portions. This may be the reason why Coleman (1957) originally suggested that the serpentinite is dominated by antigorite, while later studies (e.g. Mumpton & Thompson, 1975; Coleman, 1980; this study) conclude that chrysotile is the dominant phase, and that antigorite and lizardite are less abundant.

Based on bulk composition and relict textures in the serpentinite, I conclude that the ultramafic protolith was a peridotite consisting of dunite and harzburgite, together with minor lherzolite and pyroxenite. The serpentinization process has not affected these rock types equally.

The ultramafic protolith at New Idria was apparently richer in harzburgite in the northern half of the district; serpentinization and weathering are less complete there. While the first asbestos mine was in the northern end of the District, (Laizure, 1922) all of the large open pit asbestos mines opened since 1960 have been located in the southern half of the district where serpentinization after dunite is more complete. Magnetite and chromite are both found as accessory minerals in serpentinized harzburgite, as in dunite.

B. Geothermometry from Relict Igneous Minerals

As noted earlier, the ultramafic protolith at New Idria was a peridotite consisting mainly of dunite and harzburgite. However, a low outcrop near Perovskite Knob consists of harzburgite crosscut by a late stage lherzolite vein. The vein at this locality is the only sample found in this study containing unserpentinized cores of relict olivine, orthopyroxene, and clinopyroxene in the same rock. If prior to serpentinization this lherzolite was an equilibrium phase assemblage, and if serpentinization has not affected the composition of the relict cores, then it is possible to calculate the crystallization temperature of this lherzolite. If successful, this would be an important clue to the origin of the New Idria District.

Table 3.5 shows representative igneous pyroxene and olivine compositions from New Idria (under the above assumptions) compared with similar pyroxenes in other alpine serpentinites. Coexisting olivine compositions from New Idria are also given. The pyroxene analyses are plotted in the pyroxene quadrilateral, **Figure 3.6**. New Idria pyroxene compositions are very similar to those of the other igneous pyroxenes; they differ from the others in the table mainly by having lower Al contents. The ratio Mg/(Mg+Fe) or X_{Mg} in Cpx is higher than in coexisting Opx for all samples in the sample set, reflecting apparent equilibrium partitioning of Mg and Fe between these phases. X_{Mg} in olivine is essentially equal to that in coexisting Opx, for the magnesian compositions found in this study. Bowen & Schairer (1935), however, showed that for more iron-rich compositions, X_{Mg} in olivine is less than that in coexisting Opx. Combining these facts we have:

$$X_{Mg}^{Cpx} \geq X_{Mg}^{Opx} \geq X_{Mg}^{Ol}$$

It is interesting to speculate on the crystal chemical reasons for unequal Mg-Fe partitioning between Cpx and Opx. Apparently it is energetically less favorable to accommodate Fe in the Cpx structure. The order of preference for the larger M2 site in pyroxene is Ca > Fe > Mg. In Cpx, most of the 8 coordinated M2 site is occupied by Ca, forcing Fe into the smaller M1 site. In Opx, however, where Ca is minor, Fe can more readily occupy the distorted 6-coordinated M2 site. Ohashi & Burnham (1975) discussed the relationship between ionic substitution and structural changes in clinopyroxenes.

We may apply the pyroxene geothermometer of Wells (1977) to the New Idria samples. This solvus model is based on the solubility of Opx in coexisting Cpx, for which the equation of equilibrium is:

$$(Mg_2Si_2O_6)_{opx} = (Mg_2Si_2O_6)_{cpx}$$

An activity model, based on that of Wood & Banno (1973), represents the distribution of cations between the M1 and M2 sites in pyroxene: Ca^{2+}, Na^{+} and Mn^{2+} are assigned uniquely to M2; Al^{3+}, Cr^{3+}, Ti^{4+}, and Fe^{3+} to M1. Mg^{2+} and Fe^{2+} are initially assumed to be randomly distributed between M1 and M2, with a small empirical correction applied later. The parametric equation for the Wells model is as follows:

$$T\,(^{\circ}K) = \frac{7341}{\left[3.355 + 2.44\, X_{Fe}^{opx} - \ln\left(\frac{a_{Mg_2Si_2O_6}^{cpx}}{a_{Mg_2Si_2O_6}^{opx}}\right)\right]}$$

This model yields 877°C for the crystallization temperature, which is almost certainly below the solidus temperature for this bulk composition. Therefore these pyroxenes have probably re-equilibrated in sub-solidus conditions and the 877°C temperature estimate applies to pre-serpentinization but post-igneous crystallization conditions in the mantle.

Figure 3.6 - Igneous pyroxene compositions in the pyroxene quadrilateral. Data from Table 3.5. Units are mole fraction. Note Cpx is more magnesian than coexisting Opx.

Figure 3.6 - Pyroxene Compositions

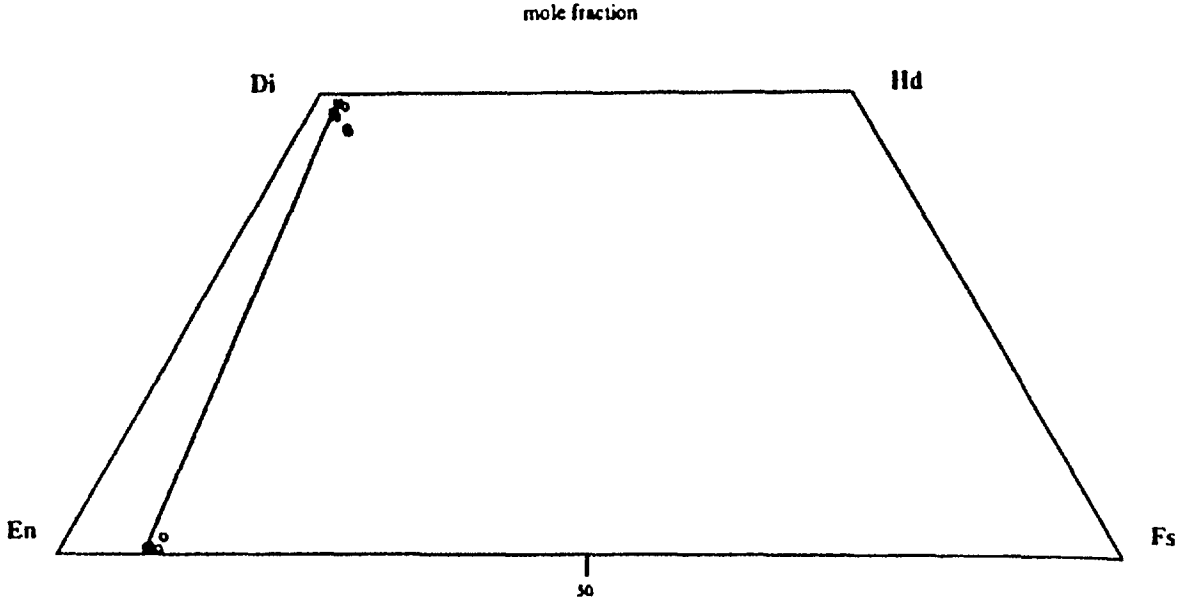

Figure 3.7 - P-T subsolidus phase diagram for lherzolite (CMAS), showing the nature of the aluminous phase as a function of pressure (Hall, 1987).

Figure 3.7 - A Phase Diagram for Lherzolite

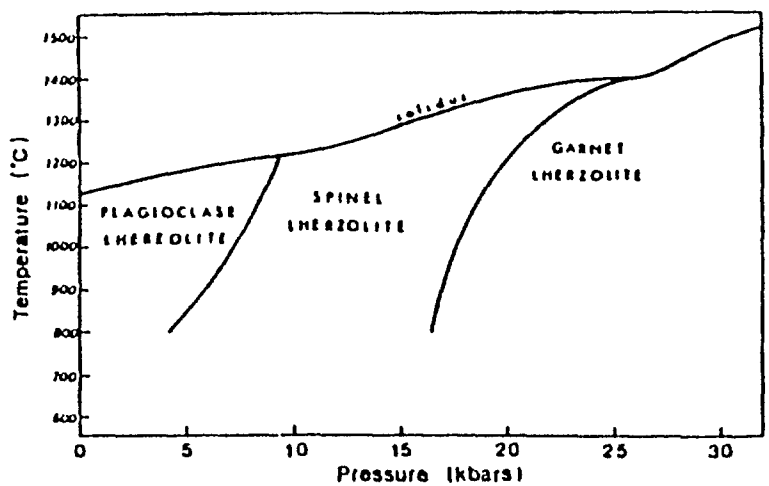

The Boyd (1973) geothermometer is based on Ca partitioning between coexisting orthopyroxene and clinopyroxene. Boyd provided a table with experimentally determined points on the diopside-enstatite solvus; applying his geothermometer is simply a matter of calculating the Ca/(Ca + Mg) ratio (atom fraction) for the Cpx phase, and interpolating temperature in his table. The Boyd model yields a temperature of about 900°C, which is in good agreement with the estimate provided by the Wells model.

How reliable are the temperature estimates? All of these models suffer from the possibility of errors in formulation of the activity - composition relationships, and all require an assumption of phase equilibrium. Neither of these conditions can in general be proved beyond reasonable doubt. Therefore, the temperature estimates should be considered a useful, but not definitive, guide.

None of the existing Al-in-Opx geobarometers can be used in the present case owing to lack of plagioclase or garnet. The Al content of Opx coexisting with either plagioclase or garnet depends strongly on pressure, a circumstance favorable to the development of geobarometers. The corresponding relationship of Al content in Opx in assemblages containing spinel depends only weakly on pressure. This gap in workable geobarometers is a stumbling block for petrologists today. Evans (1977) reviewed potential geothermometers and geobarometers for ultramafic rocks; he presented many more thermometers than barometers. More recently, Carswell & Gibb (1987) reviewed geothermometers and geobarometers for garnet lherzolites.

Another approach to obtaining a rough pressure estimate is the examination of the phases present in the New Idria serpentinite itself. The lherzolite phase diagram (Figure 3.7), shows that if the pressure of equilibration was below 9 kb, I would expect to see relict plagioclase or its alteration products, e.g. amphibole or epidote. If the equilibrium

pressure was between 9 and 20 kb, I would expect to see spinel. If the equilibrium pressure was 30 kb or higher I would expect to see pyrope garnet or its alteration products, e.g. chlorite pseudomorphs, and I would expect to see a significant chrome diopside component in the clinopyroxene. At New Idria, since igneous (pyrope) garnet, plagioclase, and their alteration products are absent from the least altered samples, and the Cr content of primary Cpx is very low (less than 0.50 wt. % Cr_2O_3 in microprobe analyses - see **Table 3.5**), the best estimate of pressure of original equilibration lies within the spinel stability field of 9-20 kb. This corresponds to a depth estimate of 30-60 km.

X. Accessory Minerals of the Serpentinite

As noted earlier, the remarkable minerals for which the District is known are, for the most part, associated with the boundary faults of the serpentinite or with tectonic blocks within the serpentinite. There are also accessory minerals found within the serpentine mass *per se*. In this section I focus on some of these minerals. Some of the occurrences are quite typical of alpine serpentinites, while others are anomalous and merit further study. In this study no attempt was made to survey accessory minerals of the serpentinite; those mentioned here were studied only as encountered.

A. Brucite

Brucite is a common product of the serpentinization of dunite, as in reaction (2). At New Idria, brucite is widely distributed but is inconspicuous and easily overlooked. It was suggested by Mumpton & Thompson (1975) that extreme weathering and alteration of the serpentinite has resulted in a brucite depletion zone in the uppermost 10 m. of the

deposit. X-ray diffraction analysis of samples taken from the surface of the deposit generally show no identifiable brucite peaks, as in **Table 3.1.** However, X-ray analysis of sample 29653 did show the presence of brucite; this sample was retrieved from a drill hole 100 ft. below the surface. As discussed below in the section on carbonates, the near-surface absence of brucite may be due to reactions with CO_2-rich meteoric waters, and the presence of brucite at deeper levels may show that meteoric waters have not yet reacted with brucite there. Many thin sections of massive serpentinite examined in this study contain no observable brucite; in the Mumpton & Thompson (1975) study about half of their massive samples contained brucite. Where observed in thin section, brucite is frequently found in sheared chrysotile/lizardite rock as bundles of slip fibers showing first order interference colors. The fibrous form of brucite is called nemalite (Whittaker & Middleton, 1979). The modal abundance of brucite does not exceed 5% in most samples. Brucite was occasionally found as dispersed grains in antigorite rock, with a mode of < 1%. In this study no brucite compositions were determined; Mumpton & Thompson (1975) however, commented on the anomalously high Fe content of New Idria brucite; they suggested that the elevated Fe content contributed to the rapid brucite breakdown in the surface weathering zone, resulting in the production of the basic carbonates pyroaurite ($Mg_6Fe_2CO_3(OH)_{16}\cdot 4H_2O$) and coalingite ($Mg_{10}Fe_2CO_3(OH)_{24}\cdot 2H_2O$), which give open slopes at New Idria their characteristic light brown color.

Coleman (1977) noted that Fe-Mg partitioning among brucite, olivine and serpentine, follows the relationship:

$$X_{Mg}^{Srp} > X_{Mg}^{Ol} > X_{Mg}^{Brc}$$

B. Magnetite

Magnetite is ubiquitous at New Idria and is the most easily recognized accessory mineral in the serpentinite. In this regard New Idria is typical of alpine serpentinites. At least two generations of magnetite were found in this study. Magnetite occurs as disseminated grains, in foliation-parallel stringers, and as drusy coatings in open fractures. Magnetite was formed from the fayalite component of olivine under relatively reducing conditions during serpentinization, probably by a reaction similar to that proposed by Betechtin (1961):

$$6(Mg_{1.5}Fe_{0.5})SiO_4 + 7H_2O = 3Mg_3Si_2O_5(OH)_4 + Fe_3O_4 + H_2 \qquad (8a)$$

olivine serpentine magnetite

or alternatively, since $2H_2O = 2H_2 + O_2$,

$$6(Mg_{1.5}Fe_{0.5})SiO_4 + 6H_2O + 0.5O_2 = 3Mg_3Si_2O_5(OH)_4 + Fe_3O_4 \qquad (8a)$$

olivine serpentine magnetite

Ramdohr (1967) suggested that serpentinization of olivine under strongly reducing conditions would produce serpentine, magnetite, and native iron or iron alloys. One possible reaction with these products is:

$$8(Mg_{1.5}Fe_{0.5})SiO_4 + 8H_2O = 4Mg_3Si_2O_5(OH)_4 + Fe_3O_4 + Fe^0 \qquad (9)$$

olivine serpentine magnetite

Some alpine serpentinites have preserved such extremely reduced assemblages including native metals and the nickel-iron alloy awaruite, $Ni_{2-3}Fe$ (e.g. Peretti et al., 1992), but only limited evidence for native iron or iron alloys at New Idria has been found so far.

Coleman (1986) included josephinite in his list of New Idria minerals, but did not comment on its occurrence. Josephinite is actually a rock type, consisting of taenite, awaruite, and andradite at its type locality (Botto & Morrison, 1976). However, many workers now consider josephinite to be a synonym of awaruite. On the basis of this limited evidence, I conclude in this study that the environment during serpentinization was relatively reducing.

The occurrence of magnetite at New Idria includes randomly dispersed opaques with varying modal abundance (0-2%) within serpentine rock, but also includes filamentous and undulatory bands parallel to schistosity in schistose serpentine. In massive antigorite serpentinite, magnetite may occur as randomly dispersed, irregular grains up to a few hundred microns across, or may be finely comminuted where the texture is mylonitic. Finely dispersed magnetite in serpentine gives the rock an overall black color. Foliation-parallel magnetite bands in some rocks suggest pressure solution of the surrounding rock; this texture deserves further investigation. Finally, magnetite appears as a second generation vein-filling mineral, or as drusy coatings on walls of veins and vugs. In many of these cases, perfectly formed octahedra of magnetite up to 1 mm in diameter are found coating rock surfaces. Sometimes these black coatings resemble black garnets which also form drusy coatings, as described in Chapter 4. A pocket magnet is an essential field tool for identifying the mineralogy of these fine-grained coatings.

Most New Idria magnetites appear to have compositions near the ideal end member formula. Magnetite compositions were not studied intensively, but using EDS analysis, in which the detection limit for minor elements is about 1%, no discernable ulvospinel or hercynite components were found in the samples examined.

C. Sulfides

Copper sulfides are not abundant but are widely distributed in all types of New Idria rocks. Chalcopyrite is found within serpentinite rock, while djurleite ($Cu_{31}S_6$) is found within altered mafic schists. At the Gem Mine locality, chrysocolla forms alteration haloes around sulfide grains, typically the low temperature phase djurleite. In chlorite-diopside rocks, chalcopyrite is sometimes overgrown by garnet (**Plate 3.7**).

D. Chromite

The peridotite from which the serpentinite formed contained chromite. The occurrence of chromite within the serpentinite is widespread but irregular. There are few concentrations of economic grade. Exceptions are those of the Butler Estate, Corbett-Byles and Big Ridge mines in the southern portion of the District. At these mines boulders are found containing 75% or more chromite with interstitial serpentine minerals. Mining of chromite as a strategic commodity took place until the late 1950s, when cheaper sources became available in politically stable areas. Matthews (1961) discussed the mining operations and historical background of the Butler Estate chromite mine.

Table 3.6 shows representative analyses of New Idria chromites. There are two groups in the table, a primary group and an altered group. The primary group includes chromites with appreciable contents of Cr, Fe, Mg, and Al, but only trace amounts of Ti, Mn, Ni, and Zn. The compositions are typical of chromites from alpine-type ultramafic bodies worldwide, and are properly named *ferroan magnesiochromites*. The key ratios Mg/(Mg+Fe), Cr/(Cr+Al), and Fe/(Fe+Cr+Al), given in **Table 3.6**; all plot within the alpine peridotite field of Irvine (1967). These chromites are interpreted as primary magmatic products. They are unzoned, with no discernable compositional variation

Plate 3.7 - Photomicrograph of chalcopyrite grain overgrown by filigree of Ti-garnet, in a matrix of chlorite. Perimeter of garnet overgrowth is decorated with octahedra of magnetite. Sample 989-46b. Backscatter electron imaging, 400X; field of view 25 μm.

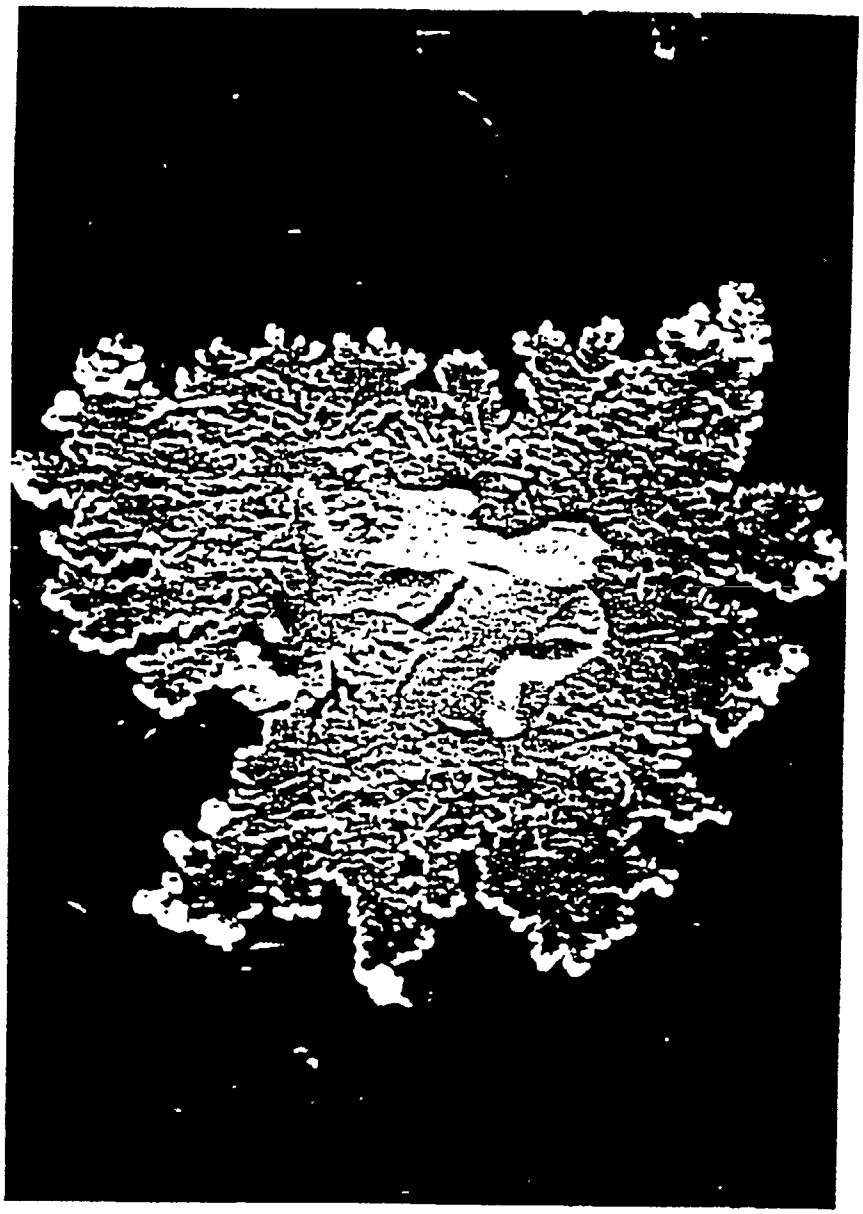

between core and rim. In thin section they range from deep red to opaque. Unaltered chromite grains occur in fully serpentinized ultramafic rock. A few chromites contain ovoid inclusions of serpentine, which may be serpentinized primary olivine inclusions. The compositions of the chromites may be adequately expressed in terms of the quaternary system chromite ($FeCr_2O_4$), magnesiochromite ($MgCr_2O_4$), magnetite ($FeFe_2O_4$), and spinel ($MgAl_2O_4$). Only limited solid solution towards magnetite is observed. Igneous clinopyroxene associated with chromite has a small chrome-diopside component (less than 0.50 wt. % Cr_2O_3 in microprobe analyses - see **Table 3.5**). Ramdohr (1967) noted that chromite is the only opaque mineral commonly found in serpentinites which is likely to have persisted from the ultramafic protolith. At New Idria this interpretation is consistent with field evidence, which shows that chromite alteration haloes overprint the serpentine fabric and therefore postdate serpentinization.

The altered group of chromites shown in **Table 3.6** occurs in rocks which have clearly undergone post-serpentinization metamorphism, tentatively assigned to the M2 event (see Chapter 4). Altered chromites are frequently found rimmed by the chromian chlorite kammererite; this chlorite overprints the surrounding serpentine fabric in these rocks. Chromian garnet is also associated with chromite alteration (see below). These altered chromites are cryptically zoned, with Cr-rich cores and Cr-poor rims, as shown in **Table 3.6**. The rim compositions are slightly chromian magnetites: Mg and Al occur at the trace level, while Ni and sometimes Mn are enriched compared with the primary chromite compositions. This enrichment may be due to Fe, Ni, and Mn all behaving similarly during M2 metamorphism.

Table 3.7 shows representative compositions of kammererite which rims altered chromite. Under the metamorphic conditions in which the chromite and kammererite

formed, Cr, Al and Mg partitioned strongly in to the chlorite phase, while Fe was concentrated in the oxide phase, an impure magnetite.

The question may be raised whether any P-T information can be garnered from the compositions of chromite and coexisting minerals. Sack & Ghiorso (1991) reviewed the role of chromite as a petrogenetic indicator, and in particular discussed the olivine-spinel geothermometer. This avenue is worth pursuing in the future, provided that suitable samples from New Idria can be gathered.

E. Chromian Andradite Garnets

Andradite garnets containing up to 38 mole percent uvarovite component are found in slabby serpentinized harzburgite blocks. These garnets are anhedral, emerald green, and often associated with relict chromite grains. They form irregular masses up to 1 mm. in size. **Table 3.8** gives garnet analyses from several grains in a sample from New Idria, along with comparative analyses from other localities. The principal variation in the New Idria garnet analyses is the ratio of Cr/Fe; Ca is relatively constant, Al, Ti, Mg, and Mn are all minor. All of the analysis totals are under 100%, suggesting that these garnets may be hydrous. **Figure 3.8** shows the positions of these ugrandite garnets in the ugrandite ternary space (uvarovite-grossular-andradite). Additional published garnet analyses from other localities are also plotted. The New Idria specimens are essentially chromian andradites; compositional variation in the ternary system may be almost completely accounted for by the exchange vector $CrFe_{-1}$. **Figure 3.9** shows the near-perfect inverse correlation between Cr and Fe in New Idria uvarovites, consistent with the $CrFe_{-1}$ exchange vector.

Figure 3.8 - Projection of Cr garnet compositions into the Ugrandite garnet ternary space using mole fractions. New Idria garnets are chromian andradites. Symbols as follows: filled squares: New Idria samples (this study); open squares, Val Malenco samples, (Müntener, 1991); filled triangles, Ontario samples (Duke & Bonardi, 1982); open circles, South Africa and Finland samples, undifferentiated: see Table 3.8 for details.

Figure 3.8 - Compositions of Chromian Garnets

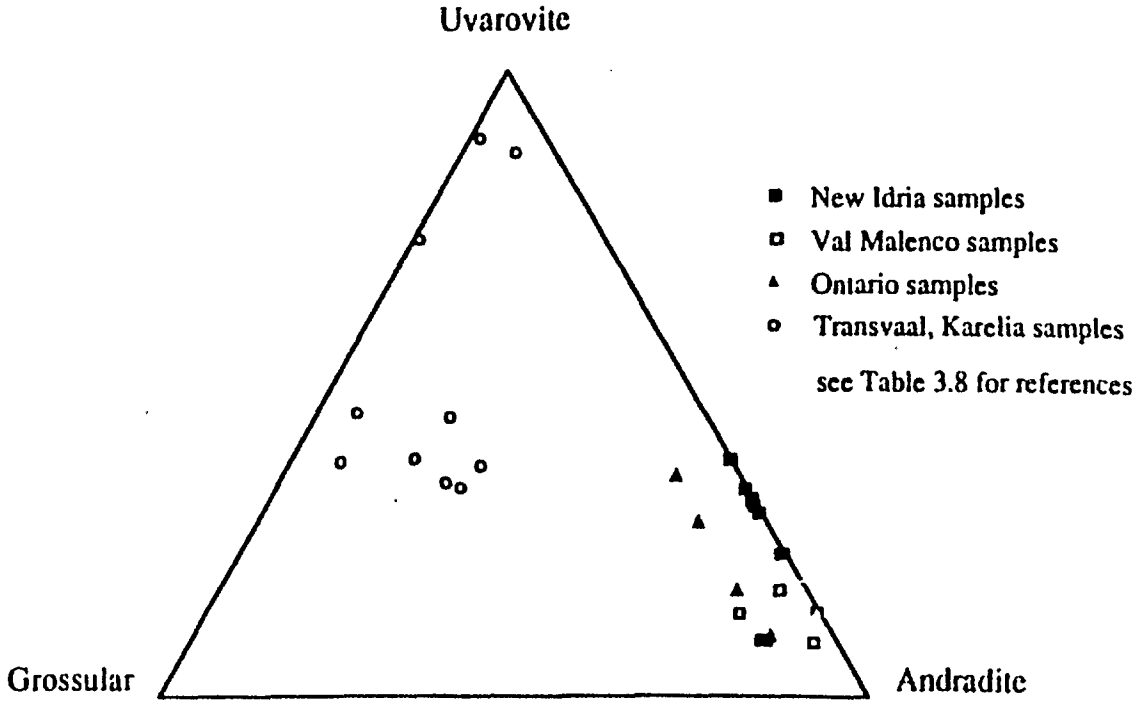

mole proportions, projected through
pyralspite components, Ti, and water.

Figure 3.9 - Octahedral Fe and octahedral Cr in New Idria garnets, showing near-perfect inverse correlation, demonstrating progress along the $CrFe_{-1}$ exchange vector.

Figure 3.9 - Cr-Fe Exchange in New Idria Garnets

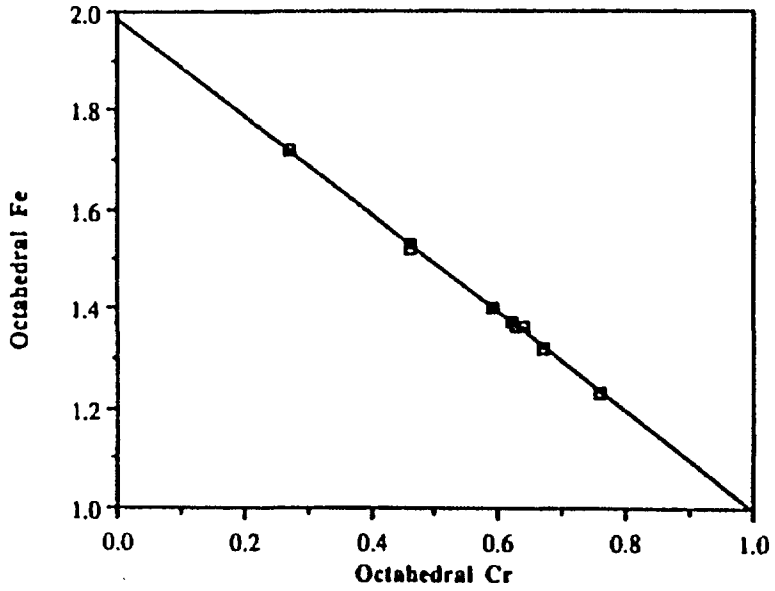

Figure 3.10 - Si variation in chromian andradites, expressed as SiO_2 weight % against (100% - oxide totals). Good correlation is evidence for hydrogarnet H_4Si_{-1} exchange.

Figure 3.10 - Si variation in Chromian Garnets from New Idria

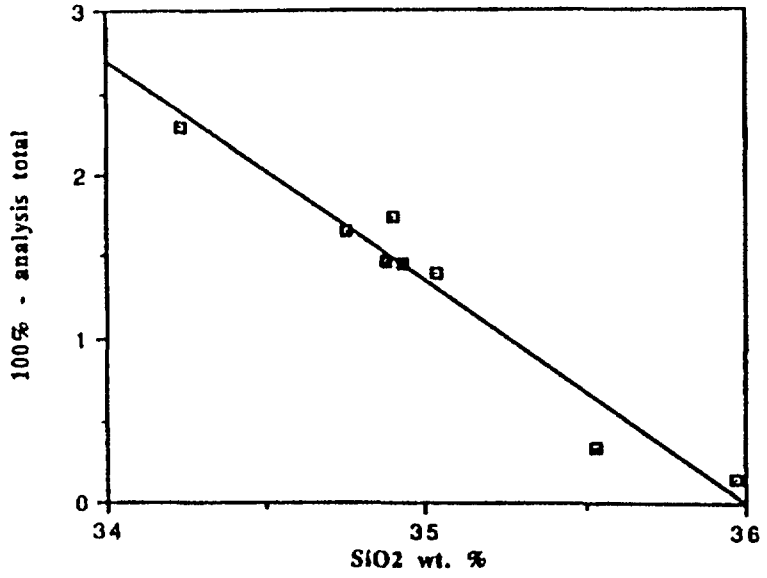

With few exceptions, chromian garnets from other localities are aluminous (Isaacs, 1965; Kalamarides & Berg, 1988); they vary along the join uvarovite-grossular, according to the exchange vector $CrAl_{-1}$. **Figure 3.8** shows that the New Idria samples are the least aluminous of the garnets plotted. The chromian garnets from the Val Malenco serpentinite are most similar to the New Idria garnets, but have less Cr and more Al. The Ontario samples (Duke & Bonardi, 1982) are garnets from a serpentinized wehrlite in Ontario. Two other occurrences are not shown in **Figure 3.8**: Jan et al. (1984) reported chromian andradites from a chromitite layer in Pakistan. Rost et al. (1979) also reported chromian andradite from the Urals, but their paragenesis is unknown. The New Idria specimens are believed to be the first chromian andradites reported from the United States.

Table 3.8 shows also that the New Idria garnets have low totals and may be hydrous, as are many other New Idria garnets. Therefore the relation between Si and the analysis total was studied. **Figure 3.10** shows a good correlation between SiO_2 wt % and the deficiency in the analysis total. This trend is to be expected if the deficiency is due to presence of tetrahedral OH groups substituting for Si. However, the amount of apparent water thus calculated exceeds the amount predicted by simple progress along the hydrogarnet exchange vector H_4Si_{-1}. It is also possible that some other divalent cations have been overlooked. EDS analysis, however, did not show any additional elements other than those presented in **Table 3.8.**

X-ray refinement of the cell edge in one sample (by L.C. Pitman) gives a value of 12.071Å ± 0.017, compared with tabulated values for uvarovite (11.990Å) and andradite (12.059Å), as reported by Meagher (1982). Shoji (1974) reported a steep positive relationship between the cell edge and progress along the hydrogarnet exchange vector in grossular; the same is probably true for andradite, and one would expect the cell edge for a hydrous andradite to exceed 12.059Å. The refined cell edge of 12.071Å therefore

suggests and is consistent with compositional variation along the two exchange vectors $CrFe_{-1}$ and H_4Si_{-1}. Future study, particularly including IR measurements, is required to resolve this question quantitatively.

F. A Blue Amphibole

An unidentified blue sodic-calcic amphibole was found in veins within antigorite serpentinite along the KCAC road near the western margin of the New Idria serpentinite. The locality was brought to the author's attention by D.S. O'Hanley and R.G. Coleman. The amphibole composition lies roughly one third of the way between winchite and eckermannite (**Figure 3.11**); the paragenesis is a new one.

Winchite is an A-site-empty sodic-calcic amphibole with a general formula of:

$$NaCa(Mg,Fe,Mn,Al)_5Si_8O_{22}(OH)_2$$

Winchite is related to tremolite by the two exchange vectors $NaSiCa_{-1}Al_{-1}$ (plag) and $Al_2Mg_{-1}Si_{-1}$ (tk). Winchite is found in mafic schists of the medium pressure series. Winchite has not previously been reported from a serpentinite.

Eckermannite is an A-site-occupied sodic amphibole, with a general formula of:

$$NaNa_2Mg_4Al_5Si_8O_{22}(OH)_2$$

Eckermannite is related to tremolite by the exchange vectors $NaAl[]_{-1}Si_{-1}$ (edenite), $NaSiCa_{-1}Al_{-1}$ (plagioclase), and $Al_2Mg_{-1}Si_{-1}$ (tk). Extensive substitution of both ferrous

Figure 3.11 - Condensed Space for Sodic-Calcic Amphiboles, redrawn after Thompson (1981). Lower left corner of cube is the tremolite composition $Ca_2Mg_5Si_8O_{22}(OH)_2$, other amphibole compositions obtained via the exchange vectors shown. Shaded plane is limit of accessible compositions for clinoamphibole, in which all tetrahedral sites are occupied by Si. Symbols are Tr: tremolite; Et: edenite; Wn: winchite; Rt: richterite; Kt: katophorite; Br: barroisite; Tm: taramite; Gl: glaucophane; Ek: eckermannite, Mi: miyashiroite; At: $Ca_2Mg_4Al_2Si_7O_{22}(OH)_2$; Pg: pargasite; Ap: $NaCa_2Mg_3Al_5Si_5O_{22}(OH)_2$. Black striped ball is the blue amphibole from this study, lying in the shaded plane about 1/3 of the distance from Wn to Ek.

Figure 3.11 - Condensed Space for Sodic-Calcic Amphiboles

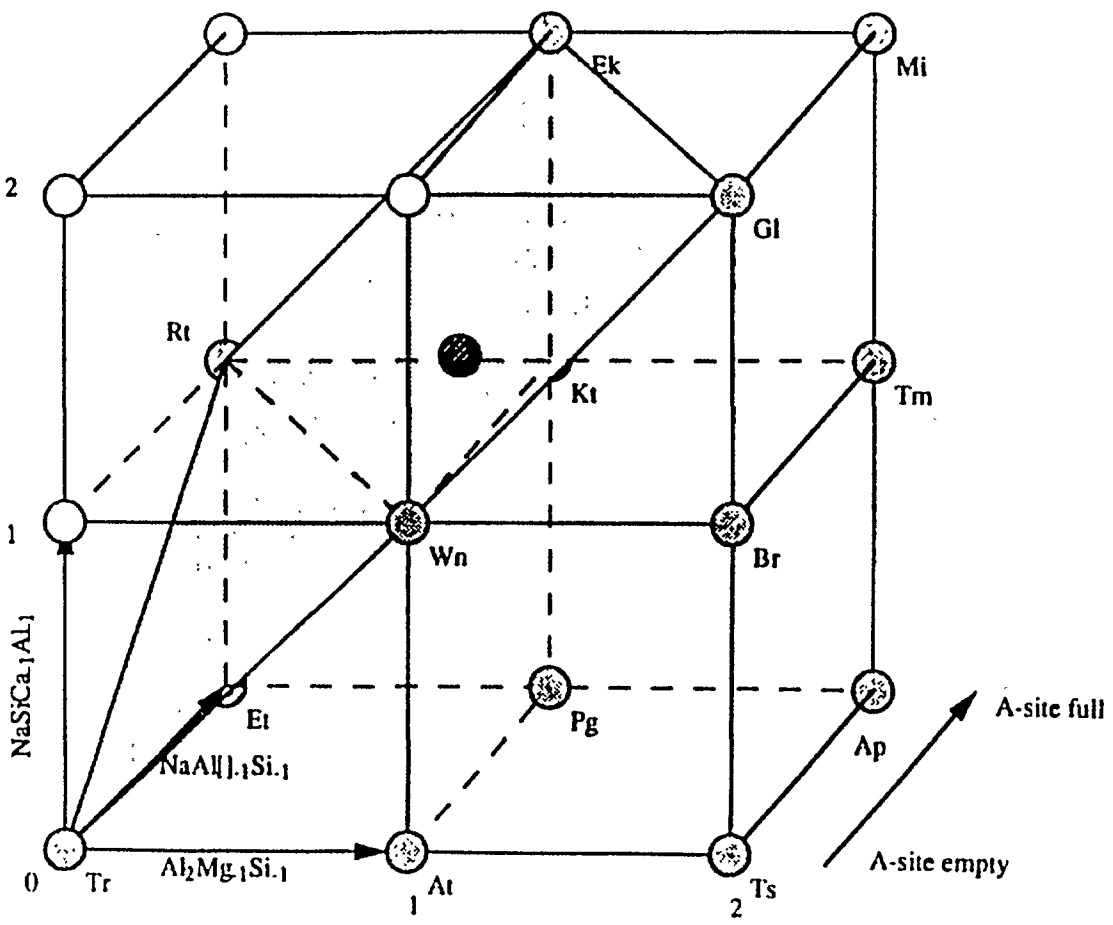

and ferric iron for Mg and Al occurs. The ferroan members of this family are blue. Eckermannite is a rare mineral, normally associated with peralkaline igneous rocks. To the best of the author's knowledge, no occurrence of eckermannite in serpentinites has been reported (but see Matsyuk et al., 1991, for a report of K-richterite in dunite).

The New Idria amphibole specimens were examined petrographically, by EDS analysis, and by X-ray analysis. Petrographic examination showed birefringent fibrous mats with fibers too small to obtain interference figures. Many fibers are curved, especially those near the center of the veins. Associated minerals in the veins are andradite garnet and chromite. Some of the chromite has altered to kammererite. **Table 3.9** gives a representative microprobe analysis and possible structural formula for this amphibole. Measurable F and Cl were present in all analyses. No significant compositional variation was observed between amphibole in the vein center and that along the vein walls.

The M4-site of the structure is inferred by stoichiometry to be shared between Na and Ca with a small amount of Fe^{2+}. K and excess Na must partially fill the A-site; the A site occupancy could be as low as 0.16, depending on the ferrous/ferric ratio chosen. A gravimetric analysis would be needed in order to determine this ratio. In an end-member eckermannite the A-site would be completely filled, and in winchite empty. An approximate formula for this amphibole, under the above assumptions, is:

$$(Na,K)_{0.31}(Na,Ca,Fe^{2+})_2(Mg,Fe^{3+},Fe^{2+},Al,Cr,Mn,Ti)_5Si_{8.00}O_{22}(OH,Cl,F)_2$$

A small fragment was studied by X-ray powder diffraction; **Table 3.10** displays the indexed pattern. The pattern is similar to those of richterite and winchite.

A definite statement about the formation of these amphibole veins in antigorite would be premature, but the physical proximity to the boundary fault, at which the serpentine is faulted against Franciscan greywackes and metavolcanics, suggests that the occurrence may be metasomatic: the required Na may have been advected in aqueous fluids from the Franciscan rocks. The environment is Al deficient, resulting in a strongly peralkaline composition when Na is added. The conditions of metamorphism are unknown, but the appearance of winchite is consistent with the medium to high pressure, low temperature assemblages found in some tectonic blocks at New Idria.

G. Secondary Alteration Minerals

Many episodes of metamorphism and mineralization have occurred during the evolution of the New Idria District. One process, ongoing today, is the formation of a variety of carbonate minerals due to the percolation of meteoric water through the serpentinite. Calcite, the basic Mg carbonates hydromagnesite ($4MgCO_3 \cdot Mg(OH)_2 \cdot 4H_2O$) and artinite ($MgCO_3 \cdot Mg(OH)_2 \cdot 3H_2O$), and complex Fe-Mg carbonates such as coalingite and pyroaurite (see Section A) are products of this process.

Calcite is found frequently as an alteration product of all the rock types in the District; textures indicate that calcite precipitation was mainly along veins and fractures. As noted by Coleman (1977), Ca-rich ground waters are ubiquitous in serpentinites; the original source of Ca at New Idria may have been Cpx in the protolith. The formation of calcite must postdate serpentinization, because serpentine itself is unstable relative to a mixture of talc and magnesite in the presence of CO_2-bearing fluids, (e.g. fluids with $XCO_2 \geq 0.01$ at 350°C, 1000 bars) according to the component reaction:

$$2Mg_3Si_2O_5(OH)_4 + 3CO_2 = Mg_3Si_4O_{10}(OH)_2 + 3MgCO_3 + 3H_2O \quad (10)$$

serpentine talc magnesite

The assemblage talc + magnesite has not been found at New Idria, but is common in metamorphosed ultramafics from Vermont where CO_2-rich fluids infiltrated during Acadian metamorphism (Sanford, 1981; Chidester et al., 1978).

The basic carbonates hydromagnesite, artinite and dypingite ($Mg_5CO_3 \cdot Mg(OH)_2 \cdot 3H_2O$) are common at New Idria, where they have formed through reactions between CO_2-bearing meteoric waters and the minerals of the serpentinite. Brucite, a product of primary serpentinization through reaction (2) or of prograde metamorphism of serpentinite through reaction (1), is nonetheless scarce in outcrop. Brucite is reactive and has largely disappeared from the weathering zone (upper 10 m.) because of component reactions similar to:

$$4Mg(OH)_2 + 3CO_2 = 3MgCO_3 \cdot Mg(OH)_2 \cdot 3H_2O \quad (11)$$

brucite hydromagnesite

Analogous reactions are probably responsible for the appearance of artinite and dypingite. Artinite forms in fractures and cavities where open space allows spheroids of radial artinite fibers to grow to centimeter size. Dypingite forms millimeter-sized non-fibrous pisolites which coat vein walls. However, hydromagnesite also locally has a pisolitic habit, making field identifications somewhat uncertain. Ordinarily, however, hydromagnesite forms in intersecting veins which quickly destroy the integrity of the host rock (**Plate 3.8**).

H. An Unidentified Blue Coating

A bluish grey coating found on fracture walls and slickensided serpentine surfaces was sampled in this study. X-ray analysis by Malcolm and Daphne Ross (personal communication, 1993) showed the material to be at least partially crystalline. The material is apparently a polyphase material, with detectable peaks for montmorillonite, quartz, and feldspar. Chemical tests showed the blue coating to be insoluble in HCl and moderately soluble in concentrated NaOH. This blue coating has been observed in Appalachian serpentinites by the author, but its exact origin is unknown.

Plate 3.8 - Photo of hydromagnesite veins in a serpentinite outcrop on San Carlos Peak. Hydromagnesite forms by reaction between brucite and meteoric waters.

XI. Discussion and Conclusions

The mineralogy and petrology of the New Idria Serpentinite is seen to be complex, yet not without parallels in other alpine serpentinites and ultramafic bodies. The very high degree of alteration and weathering has obscured much of the evidence at New Idria, but there remain telltale signs of the evolution of this body.

The protolith for the New Idria Serpentinite was a depleted dunite with lesser amounts of harzburgite, lherzolite and pyroxenite. The dunites and harzburgites are probably residues of one or more partial melting events. The lherzolites described in this chapter occur in crosscutting veins and have relatively depleted compositions. These ultramafic rocks probably represent pieces of oceanic crust or underlying mantle from the Farallon plate, that were obducted onto the western margin of North America in the late Jurassic. The serpentinized ultramafic rocks rose as a diapir through the overlying Franciscan Formation and Great Valley Sequence.

Many of the mineral associations and compositions at New Idria are similar to those at Burro Mt., California, which lies on the west side of the San Andreas Fault (Loney et al., 1971). Serpentinization at Burro Mt. is much less complete that at New Idria. Loney et al. interpreted Burro Mt. as a dismembered portion of the Coast Range Ophiolite. It is likely that Burro Mt., which was not visited in the present study, contains important clues to the origin of the New Idria Serpentinite.

The main points of this chapter that will be used in other chapters are:

1. The phase relations among the serpentine minerals are difficult to show schematically, and are not completely understood. In general, lizardite and chrysotile are the low temperature serpentine minerals; antigorite is the high temperature phase.

2. Due to the importance of Fe and Al, discussion of serpentine phase relations in MSH alone is probably unproductive; MASH is the simplest realistic system. The MSH system, however, can be used as a first-order approximation for formulating phase relations between serpentine minerals and other minerals found in serpentinites.

3. A necessary condition for the serpentine minerals to be true polymorphs is that they be chemically identical: it is now clear that antigorite, chrysotile and lizardite are not chemically identical. Each occupies a compositional range, and these ranges partially overlap.

4. Compositional variation in serpentine occurs along the three exchange vectors $Al_2Mg_{-1}Si_{-1}$ (Tk); $FeMg_{-1}$ (Fm); and $Fe^{3+}Al_{-1}$ (Fa). The dioctahedral vacancy substitution $[]Al_2Mg_{-3}$ is not known to occur in serpentine. Trace amounts of Ca, Na, and K reported in serpentine analyses may represent mixtures of other silicates with serpentine in the analyzed samples.

5. The unshared edges of the octahedral sheet in lizardite are 3.07Å compared with 3.22Å in brucite, and 2.97Å in talc. The octahedral edge dimension in a slab from the periclase structure is 2.98Å. The unshared edges in lizardite might be expected to be shorter on the tetrahedral side than on the non-tetrahedral side, but the difference is less than 0.001Å.

6. The unshared edge length in talc is smaller than in lizardite: I would therefore expect that tetrahedral rotation in talc would be greater, not less, than in lizardite. The opposite appears to be true.

7. In antigorite, the Si-O-Si bonds at the points where the tetrahedral sheets invert are responsible for the tough, resistant nature of antigorite compared with lizardite or chrysotile, in which the adjacent layers are held together by weak bonds involving hydrogen. Antigorite is a member of a polysomatic series between lizardite and talc (e.g. Otten, 1993; Sanford, 1978; Thompson, 1978). The conventional antigorite formula is equivalent to 15 Liz + 1 Tlc. If the wavelength of the modulation were to decrease the structure would become increasingly talc-like, while if the wavelength were to increase the structure would become increasingly lizardite-like.

8. If a_{H_2O} by itself affects the formation of lizardite versus chrysotile, then the assumption that the water content of lizardite and chrysotile is equal must be challenged. The molecular water in the halloysite structure could possibly correspond to (thus far undetected) water in the chrysotile structure. This would lead to a hypothetical chrysotile formula of $Mg_3Si_2O_5(OH)_4 \cdot nH_2O$. The value of n is unknown but is probably small.

9. At New Idria, the dominant phase assemblage of chrysotile + brucite indicates an Mg/Si ratio lying between forsterite and enstatite, and a low temperature equilibrium (<250°C). Antigorite knockers described in Chapter 4 record a higher temperature.

10. At New Idria, lizardite is much less abundant than chrysotile, possibly due to the recrystallization of earlier lizardite under shearing stress. An alternative explanation for the abundance of chrysotile is the extensive growth of cataclastic fabric due to the predominance of dunite in the protolith.

11. In principle, serpentinized ultramafic rocks could contain talc as part of the low temperature assemblage, when the serpentinizing fluid is pure H_2O. In fact, this is rare, because the required silica-rich bulk composition would place the parent rock in the "olivine orthopyroxenite" field of the IUGS classification, which is an extremely rare rock type. Therefore, talc does not normally appear as a low temperature mineral when fluids are pure H_2O, but instead as a prograde metamorphic replacement of antigorite at roughly staurolite grade (Trommsdorff & Evans, 1974). If the serpentinizing fluids are rich in CO_2, however, then magnesite and talc or tremolite may indeed appear as low temperature products. This has not happened at New Idria but has happened in the Appalachian serpentinites of Vermont and Quebec.

12. Serpentine formed after dunite often has a knobby outcrop texture formed by intersecting serpentine/brucite veins which isolate rounded kernels of unserpentinized dunite.

13. Serpentine formed after harzburgite often has a slabby texture, and the serpentinized rock fractures, leaving sharp edges rather than the rounded kernels of serpentinized dunite.

14. Based on bulk composition and relict textures in the serpentinite, I conclude that the ultramafic protolith was a peridotite consisting of dunite and harzburgite, together with minor lherzolite and pyroxenite. The ultramafic protolith at New Idria was apparently richer in harzburgite in the northern half of the district; serpentinization and weathering are less complete there.

15. Relict olivine, orthopyroxene and clinopyroxene are locally preserved in lherzolite veins. Their compositions are related by the inequality:

$$X_{Mg}^{Cpx} \geq X_{Mg}^{Opx} \geq X_{Mg}^{Ol}$$

reflecting apparent equilibrium partitioning of Mg and Fe among these phases. The Wells (1977) geothermometer based on solubility of Opx-in-Cpx yields a crystallization temperature of 877°C for an Opx-Cpx mineral pair from a lherzolite vein. The Boyd (1973) geothermometer based on Ca-partitioning yields a temperature of 900°C, which is in good agreement. These pyroxenes have probably re-equilibrated in sub-solidus conditions and the 877°-900°C temperature estimate applies to pre-serpentinization but post-igneous crystallization conditions in the mantle. .

16. At New Idria, since igneous (pyrope) garnet, plagioclase, and their alteration products are absent from the least altered samples, and the Cr content of primary Cpx is very low, the best estimate of pressure of original equilibration lies within the spinel stability field of 9-20 kb. This corresponds to a depth estimate of 30-60 km.

17. On the basis of trace occurrences of awaruite (josephinite), I conclude that the environment during serpentinization was relatively reducing.

18. Accessory chromite includes two groups, a primary group and an altered group. The primary group includes chromites with appreciable contents of Cr, Fe, Mg, and Al, but only trace amounts of Ti, Mn, Ni, and Zn. The compositions are typical of chromites from alpine-type ultramafic bodies worldwide, and are properly named *ferroan magnesiochromites* .

19. The altered group of chromites occurs in rocks which have clearly undergone post-serpentinization metamorphism. Altered chromites are frequently found rimmed by the chromian chlorite kammererite; this chlorite overprints the surrounding serpentine fabric in these rocks. These altered chromites are cryptically zoned, with Cr-rich cores and Cr-poor rims.

20. Andradite garnets containing up to 38 mole percent uvarovite component are found in slabby serpentinized harzburgite blocks. These garnets are anhedral, emerald green, and often associated with relict chromite grains. Chromian andradites are very rare: these are believed to be the first chromian andradites reported from the United States.

21. A blue amphibole was found in veins within antigorite serpentinite along the KCAC road near the western margin of the New Idria serpentinite. The amphibole has a partially filled A-site and appears to lie approximately one-third of the distance between a winchite and eckermannite; the paragenesis is a new one. An approximate formula for this amphibole is:

$$(Na,K)_{0.31}(Na,Ca,Fe^{2+})_2(Mg,Fe^{3+},Fe^{2+},Al,Cr,Mn,Ti)_5Si_{8.00}O_{22}(OH,Cl,F)_2$$

Table 3.1 - XRD Data for Serpentine Sample 989-45

2 Theta degrees	intensity I/I°	d-spacing Å	hkl
12.15	100	7.279	002
19.40	10	4.572	020
19.91	4	4.456	
24.45	59	3.638	004
26.00	4	3.424	
26.28	5	3.389	121
35.52	27	2.525	-202 chrysotile
35.72	26	2.512	-202 lizardite
35.90	31	2.499	202
36.38	4	2.468	
36.68	4	2.448	
37.00	4	2.428	
38.58	5	2.332	
41.91	7	2.154	023
42.05	8	2.147	132
46.22	4	1.963	
59.68	4	1.548	
60.02	6	1.540	330
60.27	10	1.534	029

Table 3.2 - Selected Whole Rock Analyses of the New Idria Serpentinite

Analysis ->	1	2	3	4	5	6	7
sample	989-45	29653	MT8	MT2	MT7.3	RGC34-50	MT7.6
SiO2	47.89	43.44	48.40	43.12	45.76	47.16	42.38
TiO2	0.00	0.01	0.00	nd	nd	0.05	nd
Al2O3	1.45	0.51	1.23	nd	1.65	1.54	0.28
Fe2O3*	6.44	9.36	4.72	9.26	9.02	10.02	9.49
MnO	0.16	0.12	nd	nd	nd	0.27	nd
MgO	43.83	45.67	45.28	46.85	43.37	40.97	47.29
CaO	0.06	0.67	0.38	0.77	0.19	0.00	0.56
Na2O	0.16	0.20	nd	nd	nd	0.00	nd
K2O	0.00	0.02	nd	nd	nd	0.00	nd
P2O5	0.00	0.00	nd	nd	nd	0.00	nd
Total wt %	100.00	100.00	100.00	100.00	100.00	100.00	100.00
Mg/Si atomic ratio	1.36	1.57	1.39	1.62	1.41	1.29	1.66

Notes:

Analyses 1-2 XRF (anhydrous), recalculated to 100 %; all Fe expressed as Fe2O3

Analysis 1, this study, specimen 989-45, Perovskite Knob

Analysis 2, this study, drill hole sample, 100 ft. level

Analysis 3, from Mumpton & Thompson, 1975, Table 8, antigorite from Santa Rita Peak

Analysis 4, from Mumpton & Thompson, 1975, Table 2, drill hole sample, 50 ft. level

Analysis 5, from Mumpton & Thompson, 1975, Table 7, serpentine boulder

Analysis 6, from Coleman, 1957, Table 25: FeO 5.57 and Fe2O3 2.62 recalculated to Fe2O3*

Analysis 7, from Mumpton & Thompson, 1975, Table 7, serpentine boulder

Table 3.3 - Petrographic identification of serpentine microtextures

Wicks & Whittaker (1977) criteria:

Type	falling T	rising T	unsheared	sheared	antig	no antig	result
1	x		x		x		rare
2	x			x	x		probably does not occur
3	x		x			x	most common, lizardite ± brucite, pseudomorphic mesh texture
4	x			x		x	very common: slickensided, "fish scale", chrysotile dominated
5		x	x			x	progressive interlocking texture, lizardite + chrysotile dominated
6		x		x		x	"Coalinga" type, sheared, chrysotile dominated; similar to type 4
7		x	x		x		non-pseudomorphic texture, antogorite dominated
8		x		x	x		foliated non-pseudomprphic texture, antogorite dominated

Wicks & O'Hanley (1988) simplified this somewhat:

A	x		-	-	x		very rare, pseudomorphic: combine 1 and 2 above
B	x		-	-		x	common pseudomorphic: combine 3 and 4 above
C		x	-	-		x	transitional: combine 5 and 6 above
D		x	-	-	x		non-pseudomorphic: combine 7 and 8 above

Notes:

Sheared/unsheared factor affects texture but not mineralogy - resulting rock will be massive/foliated respectively

Low activity of water, in primary serpentinization of olivine, favors production of lizardite

In most cases lizardite is length-fast while antigorite and chrysotile are length-slow

Table 3.3

Table 3.4 - Spinel-Norm Calculation of Serpentinite Analyses

Oxide	Weight %	GFW	M-Prop.	Ap	Ilm	Or	Jd	Wo	Spl	Di	En	Ol	Totals	Mg# =	93
sample	989-45														Si balance
SiO2	48.21	60.090	0.802			0.000	0.010	0.000		0.002	0.415	0.375	0.802		0.802
TiO2	0.00	79.700	0.000		0.000								0.000		
Al2O3	1.46	101.940	0.014			0.000	0.003		0.012	0.000			0.014		Si excess
Cr2O3	0.00	152.020	0.000										0.000		0.000
Fe2O3	0.00	159.700	0.000										0.000		
FeO	5.83	71.850	0.084										0.000	7%	Ol mols
MnO	0.16	70.940	(in FeO ^)		0.000				0.012	0.001	0.415	0.750	1.178	1.178	0.375
MgO	44.12	40.320	1.094										0.000	93%	
CaO	0.06	56.080	0.001	0.000				0.000		0.001			0.001		Tk in Cpx
Na2O	0.16	61.980	0.003				0.003						0.003		0.000
K2O	0.00	94.200	0.000			0.000							0.000		
P2O5	0.00	141.850	0.000	0.000									0.000		
H2O	0.00	18.016	0.000										0.000		
Totals	100.00														
Oxy Equivalents				0.000	0.000	0.000	0.031	0.000	0.047	0.006	1.245	1.500	2.829		
Est Mode				0.0	0.0	0.0	1.1	0.0	1.7	0.2	44.0	53.0	100.0		
Ol-Opx-Cpx coordinates										0.2	45.3	54.5	100.0		
Mol proportion										0.001	0.415	1.500	1.916		
Mol Fraction norm to 1.0										0.05	21.66	78.29	100		

Table 3.4 folio 1

Oxide	Weight %	GFW	M·Prop.	Ap	Ilm	Or	Jd	Wo	Spl	Di	En	Ol	Totals	Mg# =	90
sample	29653													Si balance	
SiO2	43.85	60.090	0.730			0.001	0.013	0.000		0.024	0.132	0.559	0.729		0.729
TiO2	0.01	79.700	0.000		0.000								0.000		
Al2O3	0.51	101.940	0.005			0.000	0.003		0.002	0.000			0.005	Si excess	
Cr2O3	0.00	152.020	0.000										0.000		0.000
Fe2O3	0.00	159.700	0.000										0.000		
FeO	8.51	71.850	0.120										0.000	10%	Ol mols
MnO	0.12	70.940	(in FeO ^)		0.000				0.002	0.012	0.132	1.118	1.263	1.263	0.559
MgO	46.10	40.320	1.143										0.000	90%	
CaO	0.68	56.080	0.012	0.000				0.000		0.012			0.012	Tk in Cpx	
Na2O	0.20	61.980	0.003				0.003						0.003		0.000
K2O	0.02	94.200	0.000			0.000							0.000		
P2O5	0.00	141.850	0.000	0.000									0.000		
H2O	0.00	18.016	0.000										0.000		
Totals	100.00														
Oxy Equivalents				0.000	0.000	0.003	0.039	0.000	0.008	0.072	0.396	2.236	2.753		
Est Mode				0.0	0.0	0.1	1.4	0.0	0.2	2.6	14.4	81.2	100.0		
Ol-Opx-Cpx coordinates										2.7	14.6	82.7	100.0		
Mol proportion										0.012	0.132	2.236	2.380		
Mol Fraction norm to 1.0										0.51	5.54	93.95	100		

Table 3.4 folio 2

Oxide	Weight %	GFW	M-Prop.	Ap	Ilm	Or	Jd	Wo	Spl	Di	En	Ol	Totals	Mg# =	95
sample	MT8														Si balance
SiO2	48.63	60.090	0.809			0.000	0.000	0.000		0.014	0.423	0.373	0.809		0.809
TiO2	0.00	79.700	0.000		0.000								0.000		
Al2O3	1.23	101.940	0.012			0.000	0.000		0.012	0.000			0.012		Si excess
Cr2O3	0.00	152.020	0.000										0.000		0.000
Fe2O3	0.00	159.700	0.000										0.000		
FeO	4.26	71.850	0.059										0.000	5%	Ol mols
MnO	0.00	70.940	(in FeO ^)		0.000				0.012	0.007	0.423	0.746	1.188	1.188	0.373
MgO	45.49	40.320	1.128										0.000	95%	
CaO	0.38	56.080	0.007	0.000				0.000		0.007			0.007		Tk in Cpx
Na2O	0.00	61.980	0.000				0.000						0.000		0.000
K2O	0.00	94.200	0.000			0.000							0.000		
P2O5	0.00	141.850	0.000	0.000									0.000		
H2O	0.00	18.016	0.000										0.000		
Totals	100.00														
Oxy Equivalents				0.000	0.000	0.000	0.000	0.000	0.048	0.041	1.268	1.492	2.849		
Est Mode				0.0	0.0	0.0	0.0	0.0	1.7	1.4	44.5	52.4	100.0		
Ol-Opx-Cpx coordinates										1.5	45.3	53.3	100.0		
Mol proportion										0.007	0.423	1.492	1.922		
Mol Fraction norm to 1.0										0.35	22.00	77.64	100		

Table 3.4 folio 3

Oxide	Weight %	GFW	M·Prop.	Ap	Ilm	Or	Jd	Wo	Spl	Di	En	Ol	Totals	Mg# =	91
sample	MT2														Si balance
SiO2	43.52	60.090	0.724			0.000	0.000	0.000		0.028	0.117	0.580	0.724		0.724
TiO2	0.00	79.700	0.000		0.000								0.000		
Al2O3	0.00	101.940	0.000			0.000	0.000		0.000	0.000			0.000		Si excess
Cr2O3	0.00	152.020	0.000										0.000		0.000
Fe2O3	0.00	159.700	0.000										0.000		
FeO	8.41	71.850	0.117										0.000	9%	Ol mols
MnO	0.00	70.940	(in FeO ^)		0.000				0.000	0.014	0.117	1.159	1.290	1.290	0.580
MgO	47.29	40.320	1.173										0.000	91%	
CaO	0.78	56.080	0.014	0.000				0.000		0.014			0.014		Tk in Cpx
Na2O	0.00	61.980	0.000				0.000						0.000		0.000
K2O	0.00	94.200	0.000			0.000							0.000		
P2O5	0.00	141.850	0.000	0.000									0.000		
H2O	0.00	18.016	0.000										0.000		
Totals	100.00														
Oxy Equivalents				0.000	0.000	0.000	0.000	0.000	0.000	0.084	0.351	2.318	2.752		
Est Mode				0.0	0.0	0.0	0.0	0.0	0.0	3.0	12.7	84.2	100.0		
Ol-Opx-Cpx coordinates										3.0	12.7	84.2	100.0		
Mol proportion										0.014	0.117	2.318	2.449		
Mol Fraction norm to 1.0										0.57	4.77	94.66	100		

Table 3.4 folio 4

Oxide	Weight %	GFW	M·Prop.	Ap	Ilm	Or	Jd	Wo	Spl	Di	En	Ol	Totals	Mg# =	90
sample	MT7													Si balance	
SiO2	46.18	60.090	0.768			0.000	0.000	0.000		0.007	0.343	0.419	0.768		0.768
TiO2	0.00	79.700	0.000		0.000								0.000		
Al2O3	1.66	101.940	0.016			0.000	0.000		0.016	0.000			0.016	Si excess	
Cr2O3	0.00	152.020	0.000										0.000		0.000
Fe2O3	0.00	159.700	0.000										0.000		
FeO	8.19	71.850	0.114										0.000	10%	Ol mols
MnO	0.00	70.940	(in FeO ^)		0.000				0.016	0.003	0.343	0.837	1.200	1.200	0.419
MgO	43.77	40.320	1.086										0.000	90%	
CaO	0.19	56.080	0.003	0.000				0.000		0.003			0.003	Tk in Cpx	
Na2O	0.00	61.980	0.000				0.000						0.000		0.000
K2O	0.00	94.200	0.000			0.000							0.000		
P2O5	0.00	141.850	0.000	0.000									0.000		
H2O	0.00	18.016	0.000										0.000		
Totals	100.00														
Oxy Equivalents				0.000	0.000	0.000	0.000	0.000	0.065	0.021	1.028	1.674	2.789		
Est Mode				0.0	0.0	0.0	0.0	0.0	2.3	0.7	36.9	60.0	100.0		
Ol-Opx-Cpx coordinates										0.8	37.8	61.5	100.0		
Mol proportion										0.003	0.343	1.674	2.020		
Mol Fraction norm to 1.0										0.17	16.97	82.86	100		

Table 3.4 folio 5

Oxide	Weight %	GFW	M·Prop.	Ap	Ilm	Or	Jd	Wo	Spl	Di	En	Ol	Totals	Mg# =	89
sample	RGC-34-50													Si balance	
SiO2	47.79	60.090	0.795			0.000	0.000	0.000		0.000	0.450	0.346	0.796		0.796
TiO2	0.00	79.700	0.000		0.000								0.000		
Al2O3	1.56	101.940	0.015			0.000	0.000		0.015	0.000			0.015	Si excess	
Cr2O3	0.00	152.020	0.000										0.000		0.000
Fe2O3	0.00	159.700	0.000										0.000		
FeO	9.14	71.850	0.127										0.000	11%	Ol mols
MnO	0.00	70.940	(in FeO ^)		0.000				0.015	0.000	0.450	0.692	1.157	1.157	0.346
MgO	41.52	40.320	1.030										0.000	89%	
CaO	0.00	56.080	0.000	0.000				0.000		0.000			0.000	Tk in Cpx	
Na2O	0.00	61.980	0.000				0.000						0.000		0.000
K2O	0.00	94.200	0.000			0.000							0.000		
P2O5	0.00	141.850	0.000	0.000									0.000		
H2O	0.00	18.016	0.000										0.000		
Totals	100.00														
Oxy Equivalents				0.000	0.000	0.000	0.000	0.000	0.061	0.000	1.349	1.384	2.794		
Est Mode				0.0	0.0	0.0	0.0	0.0	2.2	0.0	48.3	49.5	100.0		
Ol-Opx-Cpx coordinates										0.0	49.4	50.6	100.0		
Mol proportion										0.000	0.450	1.384	1.834		
Mol Fraction norm to 1.0										0.00	24.52	75.48	100		

Table 3.4 folio 6

Oxide	Weight %	GFW	M-Prop.	Ap	Ilm	Or	Jd	Wo	Spl	Di	En	Ol	Totals	Mg# =	91
sample	MT7													Si	balance
SiO2	42.79	60.090	0.712			0.000	0.000	0.000		0.020	0.093	0.599	0.712		0.712
TiO2	0.00	79.700	0.000		0.000								0.000		
Al2O3	0.28	101.940	0.003			0.000	0.000		0.003	0.000			0.003	Si	excess
Cr2O3	0.00	152.020	0.000										0.000		0.000
Fe2O3	0.00	159.700	0.000										0.000		
FeO	8.62	71.850	0.120										0.000	9%	Ol mols
MnO	0.00	70.940	(in FeO ^)		0.000				0.003	0.010	0.093	1.198	1.304	1.304	0.599
MgO	47.74	40.320	1.184										0.000	91%	
CaO	0.56	56.080	0.010	0.000				0.000		0.010			0.010	Tk	in Cpx
Na2O	0.00	61.980	0.000				0.000						0.000		0.000
K2O	0.00	94.200	0.000			0.000							0.000		
P2O5	0.00	141.850	0.000	0.000									0.000		
H2O	0.00	18.016	0.000										0.000		
Totals	100.00														
Oxy Equivalents				0.000	0.000	0.000	0.000	0.000	0.011	0.060	0.280	2.396	2.747		
Est Mode				0.0	0.0	0.0	0.0	0.0	0.4	2.2	10.2	87.2	100.0		
Ol-Opx-Cpx coordinates										2.2	10.2	87.6	100.0		
Mol proportion										0.010	0.093	2.396	2.499		
Mol Fraction norm to 1.0										0.40	3.73	95.87	100		

Table 3.4 folio 7

Table 3.5 - Representative Pyroxene and Olivine Compositions

Phase ->	Cpx	Cpx	Cpx	Opx	Opx	Opx	Cpx	Opx	Cpx	Opx	Cpx	Opx
Loc. ->	Idria	Idria	Idria	Idria	Idria	Idria	Totalp	Totalp	Albert	Albert	Trinity	Trinity
Sample ->	793-15a	793-15a	793-15a	793-15a	793-15a	793-15a	avg(7)	avg(2)	avg(5)	avg(5)	#9030	#9030
SiO2	54.18	54.79	54.67	56.98	57.14	57.18	52.47	54.25	53.10	55.70	52.08	55.90
TiO2	0.01	0.02	0.01	0.00	0.00	0.00	n.d.	n.d.	0.09	0.02	0.25	0.11
Al2O3	1.02	1.17	0.69	1.40	1.45	1.29	6.83	3.40	3.17	4.18	3.25	2.59
Cr2O3	0.45	0.44	0.29	0.31	0.35	0.25	n.d.	n.d.	0.95	0.82	1.08	0.55
FeO*	1.61	1.35	1.36	5.55	5.51	5.49	2.73	6.20	1.88	6.03	2.67	6.39
MnO	0.08	0.07	0.06	0.10	0.07	0.08	n.d.	n.d.	0.07	0.13	0.09	0.19
MgO	18.11	17.71	18.41	35.34	35.25	35.63	16.03	34.25	17.19	33.40	17.39	33.62
CaO	24.16	24.70	24.64	0.45	0.48	0.42	20.76	1.05	24.09	0.35	22.65	0.79
Na2O	0.03	0.01	0.02	0.00	0.00	0.00	1.66	n.d.	0.22	n.d.	0.23	0.03
Total	99.65	100.26	100.15	100.13	100.25	100.34	100.47	99.15	100.75	100.61	99.69	100.17
Si	1.97	1.98	1.98	1.96	1.96	1.96	1.88	1.89	1.92	1.91	1.90	1.96
Ti	0.00	0.00	0.00	0.00	0.00	0.00	0.00	0.00	0.00	0.00	0.01	0.00
Al	0.04	0.05	0.03	0.06	0.06	0.05	0.29	0.14	0.13	0.17	0.14	0.05
Cr	0.01	0.01	0.01	0.01	0.01	0.01	0.00	0.00	0.03	0.02	0.03	0.01
Fe*	0.05	0.04	0.04	0.16	0.16	0.16	0.08	0.18	0.06	0.17	0.08	0.16
Mn	0.00	0.00	0.00	0.00	0.00	0.00	0.00	0.00	0.00	0.00	0.00	0.00
Mg	0.98	0.95	0.99	1.81	1.80	1.82	0.86	1.78	0.92	1.71	0.95	1.82
Ca	0.94	0.96	0.95	0.02	0.02	0.02	0.80	0.04	0.93	0.01	0.89	0.02
Na	0.00	0.00	0.00	0.00	0.00	0.00	0.12	0.00	0.02	0.00	0.02	0.00
Total	4.00	3.99	4.01	4.01	4.01	4.01	4.03	4.04	4.01	4.00	4.01	4.01
Wo	0.48	0.49	0.48	0.01	0.01	0.01	0.46	0.02	0.49	0.01	0.46	0.01
En	0.50	0.49	0.50	0.91	0.91	0.91	0.49	0.89	0.48	0.90	0.49	0.91
Fs	0.02	0.02	0.02	0.08	0.08	0.08	0.05	0.09	0.03	0.09	0.04	0.08
Xmg	0.95	0.96	0.96	0.92	0.92	0.92	0.91	0.91	0.94	0.91	0.92	0.92

Notes: total Fe expressed as FeO*

Totalp samples from Peters (1968), Albert samples from MacGregor & Basu (1979), Trinity samples from Quick (1981)

Table 3.5 - Representative Olivine Compositions

Phase ->	Ol	Ol	Ol	Ol	Ol	Ol	Ol	Ol	Ol
Location ->	New Idria	New Idria	New Idria	New Idria	New Idria	New Idria	Albert	Albert	Albert
Sample ->	793-15a	793-15a	793-15a	793-15a	1091-75	1091-75	817	826	835
SiO2	40.24	40.22	40.12	40.11	40.54	40.28	38.23	38.38	39.44
TiO2	0.00	0.00	0.00	0.00	0.00	0.01	n.d.	n.d.	n.d.
Al2O3	0.00	0.00	0.00	0.00	0.00	0.00	n.d.	n.d.	n.d.
Cr2O3	0.00	0.02	0.01	0.00	0.06	0.08	n.d.	n.d.	n.d.
FeO*	8.59	8.53	8.71	8.66	8.23	9.30	9.18	8.80	9.70
MnO	0.11	0.12	0.10	0.12	0.27	0.34	0.10	0.09	0.11
MgO	50.03	49.74	49.92	49.91	49.89	49.11	51.66	51.65	50.24
NiO	0.43	0.38	0.39	0.38	0.29	0.16	0.26	0.23	0.29
CaO	0.02	0.02	0.01	0.01	0.03	0.10	n.d.	n.d.	n.d.
Na2O	0.01	0.00	0.00	0.00	0.00	0.00	n.d.	n.d.	n.d.
Total	99.43	99.03	99.26	99.19	99.31	99.38	99.43	99.15	99.78
Si	0.99	0.99	0.99	0.99	1.00	0.99	0.95	0.95	0.97
Ti	0.00	0.00	0.00	0.00	0.00	0.00	n.d.	n.d.	n.d.
Al	0.00	0.00	0.00	0.00	0.00	0.00	n.d.	n.d.	n.d.
Cr	0.00	0.00	0.00	0.00	0.00	0.00	n.d.	n.d.	n.d.
Fe*	0.18	0.18	0.18	0.18	0.17	0.19	0.19	0.18	0.20
Mn	0.00	0.00	0.00	0.00	0.01	0.01	0.00	0.00	0.00
Mg	1.83	1.83	1.83	1.83	1.83	1.81	1.91	1.91	1.85
Ni	0.01	0.01	0.01	0.01	0.01	0.00	0.00	0.00	0.01
Ca	0.00	0.00	0.00	0.00	0.00	0.00	n.d.	n.d.	n.d.
Na	0.00	0.00	0.00	0.00	0.00	0.00	n.d.	n.d.	n.d.
Total	3.01	3.01	3.01	3.01	3.00	3.01	3.05	3.05	3.05
Xmg	0.91	0.91	0.91	0.91	0.92	0.90	0.91	0.91	0.90

Notes: total Fe expressed as FeO*

Totalp samples from Peters (1968), Albert samples from MacGregor & Basu (1979), Trinity samples from Quick (1981)

Table 3.6 - Primary Chromites								
Sample ->	1091-70.1	1091-70.2	1091-70.3	1091-70.4	1091-70.5	1091-70.6	1091-70.7	579
	New Idria	New Idria	New Idria	New Idria	New Idria	New Idria	New Idria	Mont Albert
TiO2	0.10	0.11	0.12	0.11	0.10	0.10	0.12	0.01
Al2O3	9.61	9.62	9.75	9.73	9.90	10.03	9.91	29.22
Cr2O3	59.33	59.84	59.81	60.90	60.20	57.45	58.48	38.13
Fe2O3*	5.36	5.40	5.41	5.22	5.34	4.97	4.99	3.51
FeO*	11.23	11.32	11.35	10.95	11.20	10.43	10.46	16.27
MnO	0.16	0.18	0.21	0.20	0.12	0.15	0.21	0.30
MgO	14.64	14.83	14.80	14.93	14.70	14.55	15.00	13.41
NiO	0.10	0.08	0.07	0.06	0.10	0.12	0.03	0.06
ZnO	0.02	0.02	0.05	0.04	0.03	0.04	0.04	n.d.
Total wt %	100.55	101.40	101.58	102.14	101.69	97.84	99.24	100.91
Ti	0.00	0.00	0.00	0.00	0.00	0.00	0.00	0.00
Al	0.36	0.36	0.36	0.36	0.37	0.39	0.38	1.03
Cr	1.50	1.50	1.50	1.51	1.50	1.49	1.49	0.90
Fe3+	0.13	0.13	0.13	0.12	0.13	0.12	0.12	0.08
Fe2+	0.30	0.30	0.30	0.29	0.30	0.29	0.28	0.41
Mn	0.00	0.00	0.01	0.01	0.00	0.00	0.01	0.01
Mg	0.70	0.70	0.70	0.70	0.69	0.71	0.72	0.60
Ni	0.00	0.00	0.00	0.00	0.00	0.00	0.00	0.00
Zn	0.00	0.00	0.00	0.00	0.00	0.00	0.00	0.00
Total cations	3.00	3.00	3.00	3.00	3.00	3.00	3.00	3.03
Mg/(Mg+Fe2+)	0.70	0.70	0.70	0.71	0.70	0.71	0.72	0.60
Cr/(Al+Cr)	0.81	0.81	0.80	0.81	0.80	0.79	0.80	0.47
Fe3+/(Cr+Al+Fe3+)	0.06	0.06	0.06	0.06	0.06	0.06	0.06	0.04
Fe2+/Fe (total)	0.70	0.70	0.70	0.70	0.70	0.70	0.70	0.84
Notes: Fe analyzed with microprobe as FeO; Fe2O3 calculated from stoichiometry, 3 cations pfu								
Notes: Mont Albert sample from McGregor & Basu, 1979								

Table 3.6 - Altered New Idria Chromites						
Sample ->	KCAC-RD.8	KCAC-RD.1	KCAC-RD.2	KCAC-RD.3	KCAC-RD.4	
	core	intermediate	intermediate	rim	rim	
TiO2	0.16	0.07	0.09	0.05	0.05	
Al2O3	0.09	0.02	0.08	0.01	0.05	
Cr2O3	15.29	6.23	6.75	2.34	1.08	
Fe2O3*	52.79	63.28	62.31	65.60	67.80	
FeO*	29.09	30.63	30.17	30.38	30.02	
MnO	0.75	0.17	0.27	0.06	0.07	
MgO	0.13	0.07	0.09	0.09	0.30	
NiO	0.42	0.64	0.64	0.63	0.57	
ZnO	0.09	0.02	0.02	0.01	0.00	
Total wt %	98.81	101.13	100.41	99.17	99.94	
Ti	0.00	0.00	0.00	0.00	0.00	
Al	0.00	0.00	0.00	0.00	0.00	
Cr	0.47	0.19	0.20	0.07	0.03	
Fe3+	1.53	1.81	1.79	1.92	1.96	
Fe2+	0.94	0.97	0.96	0.99	0.97	
Mn	0.02	0.01	0.01	0.00	0.00	
Mg	0.01	0.00	0.01	0.01	0.02	
Ni	0.01	0.02	0.02	0.02	0.02	
Zn	0.01	0.00	0.00	0.00	0.00	
Total cations	3.00	3.00	3.00	3.00	3.00	
Mg/(Mg+Fe2+)	0.01	0.00	0.01	0.01	0.02	
Cr/(Al+Cr)	0.99	1.00	0.98	0.99	0.94	
Fe3+/(Cr+Al+Fe3+)	0.77	0.91	0.90	0.96	0.98	
Fe2+/Fe (total)	0.38	0.35	0.35	0.34	0.33	
Notes: Fe analyzed with microprobe as FeO; Fe2O3 calculated from stoichiometry, 3 cations pfu						

Table 3.7 - Kammererite (Cr-chlorite) Analyses		
Sample ->	KCAC-RD.5	KCAC-RD.6
SiO2	32.27	32.90
TiO2	0.00	0.00
Al2O3	7.31	7.43
Cr2O3	5.76	5.30
FeO*	19.25	17.14
MnO	0.07	0.05
MgO	22.14	23.97
CaO	0.26	0.27
Na2O	0.02	0.02
H2O	12.92	12.92
Totals	100.00	100.00
Si	3.38	3.40
Ti	0.00	0.00
Al	0.90	0.90
Cr	0.48	0.43
Fe*	1.69	1.48
Mn	0.01	0.00
Mg	3.45	3.69
Ca	0.03	0.03
Na	0.00	0.00
H	9.02	8.90
Totals	18.96	18.83
Mg/Al	3.83	4.08
Cr/(Al+Cr)	0.35	0.32
Cr/Fe (total)	0.28	0.29
Mg(Mg+Fe)	0.67	0.71
Notes: Fe analyzed as FeO; H2O calculated by difference		

Table 3.8 - Chromian Garnet Analyses

location ->	NI	NI	NI	NI	NI	NI	NI	NI	NI	VM	VM	VM
sample ->	688-2.1	688-2.2	688-2.3	688-2.4	688-2.5	688-2.6	688-2.7	688-2.8	688-2.9	2.A.1	4.A.1	4.A.2
SiO2	34.88	34.50	34.75	34.93	34.90	34.23	35.03	35.53	35.97	35.49	35.30	34.90
TiO2	0.09	0.18	0.09	0.07	0.10	0.04	0.07	0.05	0.11	1.30	0.23	1.14
Al2O3	0.11	0.09	0.11	0.08	0.11	0.07	0.08	0.10	0.08	0.64	1.90	0.76
Cr2O3	3.92	8.60	9.57	9.07	6.57	10.73	9.13	6.76	8.63	2.38	2.64	4.82
Fe2O3	26.12	20.08	19.85	20.38	22.62	18.32	20.48	23.41	21.31	26.28	25.14	23.79
MnO	0.07	0.03	0.02	0.03	0.04	0.06	0.04	0.06	0.07	0.04	0.00	0.00
MgO	0.16	0.96	0.11	0.15	0.30	0.61	0.13	0.22	0.12	0.12	0.03	0.10
CaO	33.18	32.56	33.85	33.84	33.62	33.65	33.65	33.53	33.57	33.82	33.89	33.73
Totals	98.53	97.00	98.35	98.55	98.26	97.71	98.61	99.66	99.86	100.07	99.13	99.24
Mole fraction in UGA space:												
UGA mols	0.19	0.18	0.19	0.19	0.19	0.19	0.19	0.19	0.19	0.19	0.19	0.19
Uvarovite	13.54	30.88	33.43	31.73	23.24	37.95	31.76	23.16	29.72	8.39	8.98	16.85
Grossular	0.57	0.48	0.57	0.42	0.58	0.37	0.42	0.51	0.41	3.37	9.64	3.96
Andradite	85.89	68.64	66.00	67.86	76.18	61.68	67.82	76.33	69.87	88.24	81.39	79.18
100-total	1.47	3.00	1.65	1.45	1.74	2.29	1.39	0.34	0.14			
SI	34.88	34.50	34.75	34.93	34.90	34.23	35.03	35.53	35.97			

Notes on Location:

NI analyses from New Idria, this study

VM analyses from Val Malenco, Italy; Müntener, 1991

Notes on analysis totals (weight %):

New Idria garnets (NI) frequently have low totals and are probably hydrous

Table 3.8 - Chromian Garnet Analyses											
location ->	VM	VM	ONT	ONT	ONT	ONT	TR	TR	TR	TR	TR
sample ->	4.A.3	4.A.4	2	3	4	5	4	5	6	7	10
SiO2	33.97	34.25	35.37	34.88	35.51	35.19	33.50	34.64	36.86	33.33	34.52
TiO2	0.43	0.16	0.32	0.33	0.45	0.55	1.97	2.24	0.40	2.50	1.68
Al2O3	2.04	2.22	1.83	2.06	1.89	1.76	9.12	9.44	8.98	7.50	8.05
Cr2O3	2.64	3.91	2.93	5.34	8.47	10.54	11.16	11.49	11.54	11.70	14.83
Fe2O3	24.80	23.51	26.34	23.95	19.66	17.41	9.17	8.21	5.47	9.05	6.61
MnO	0.04	0.00	n.d.	n.d.	n.d.	n.d.	0.03	n.d.	n.d.	0.02	0.03
MgO	0.07	0.03	0.23	0.11	0.47	0.47	1.67	0.78	0.62	1.28	1.86
CaO	34.02	33.71	33.18	33.34	33.46	33.78	33.70	33.26	35.93	35.12	32.81
Totals	98.01	97.79	100.20	100.01	99.91	99.70	100.32	100.06	99.80	100.50	100.39
Mole fraction in UGA space:											
UGA mols	0.19	0.19	0.20	0.21	0.20	0.20	0.22	0.22	0.20	0.21	0.22
Uvarovite	9.01	13.21	9.53	17.11	28.23	35.44	33.33	34.42	38.29	37.14	44.76
Grossular	10.39	11.18	8.88	9.84	9.39	8.83	40.62	42.17	44.44	35.51	36.23
Andradite	80.60	75.61	81.59	73.05	62.38	55.73	26.06	23.42	17.27	27.35	19.00
Notes on Location:											
ONT analyses from Reaume Township, ONtario; Duke & Bonardi, 1982											
TR analyses from Transvaal, South Africa; Frankel, 1959											
KAR analyses from Karelia, Finland; von Knorring, 1954											

Table 3.9 - Chemical Analysis and Site Assignments for a Blue Amphibole						
Sample ->	KCAC-RD.3					
SiO2	56.32					
TiO2	0.06					
Al2O3	0.10					
Cr2O3	0.14					
FeO*	16.86					
MnO	0.09					
MgO	14.53					
CaO	3.62					
ZnO	0.02					
BaO	0.00					
Na2O	5.75					
K2O	0.23					
F	0.07					
Cl	0.02					
H2O	2.22					
Total	100.00					
			site assignments			
atom	pfu	A	M4	M1-M3	T	(OH,F,Cl)
Si	8.00				8.00	
Ti	0.01			0.01		
Al	0.02			0.02		
Cr	0.02			0.02		
Fe3	0.94			0.94		
Fe2	1.06		0.13	0.93		
Mn	0.01			0.01		
Mg	3.08			3.08		
Ca	0.55		0.55			
Zn	0.00			0.00		
Ba	0.00			0.00		
Na	1.58	0.27	1.32			
K	0.04	0.04				
F	0.06					0.06
Cl	0.01					0.01
OH	1.93					1.93
Structural formula:		0.31	2.00	5.00	8.00	2.00
Notes:	'All Fe as FeO* in probe analysis, Fe2/Fe3 by stoichiometry					

Table 3.10 - XRD Data for Blue Amphibole 793-19a

2 Theta degrees	intensity I/I°	d, Å
10.53	45	8.393
16.44	37	5.386
18.21	12	4.868
19.74	24	4.494
26.01	57	3.424
26.27	100	3.390
27.31	16	3.263
28.65	48	3.113
30.23	12	2.954
33.06	55	2.707
33.18	50	2.698
34.61	18	2.590
35.25	24	2.544
35.44	26	2.531
38.80	11	2.319
39.26	13	2.293
40.87	31	2.206
41.68	15	2.165
42.61	17	2.120
60.68	20	1.545

Chapter 4

Tectonic Blocks of the New Idria Serpentinite

Chapter 4 - Mineralogy and Petrology of the Tectonic Inclusions

Chapter 4 - Mineralogy and Petrology of the Tectonic Inclusions

I. Introduction

The New Idria Serpentinite is locally heterogeneous: numerous rock bodies of limited extent and contrasting physical character are included within the mass of the serpentinite. These bodies are isolated from each other, have sheared contacts with the surrounding serpentinite, and show evidence of brittle to ductile deformational processes; they are interpreted as *tectonic blocks* or *knockers*. A consequence of this interpretation is that the tectonic blocks have a history separate in part from the rest of the serpentinite. Coleman (1957) noted the lithologic similarity between many of these blocks and the Franciscan rocks found at the margin of the serpentinite; following a suggestion made by Louderback (1909), he proposed that some tectonic blocks were derived from the Franciscan section during emplacement of the serpentinite. The pre-entrainment history of some of the blocks is fairly clear; for others the evidence is equivocal.

The dimensions of the blocks range from 1-1000 meters; many of the larger blocks are elongate and have a southeast-northwest orientation. Most of the smaller blocks and some of the larger blocks have hidden margins, so that their shape and orientation cannot be determined unambiguously. The blocks can be distinguished in the field by distinct soil color and erosion properties, contrasting vegetation above, and anomalous mineral assemblages within.

These exotic rock bodies have attracted much attention from mineralogists and mineral collectors for the past century: they are the host rocks for museum-quality specimens of titanium-rich, chromium-rich, and rare-earth-rich minerals, including perovskite,

schorlomite garnet (containing up to 16 wt. % TiO_2), chromian garnet, REE-vesuvianite (idocrase), titanite (sphene), zirconolite, benitoite, neptunite, joaquinite, and a numerous other accessory minerals. The renowned San Benito County garnets are hosted in blocks of chlorite-diopside-garnet rock; benitoite, the state gemstone of California, is hosted in blocks of mafic schist. Coleman (1986), Millage (1981) and Wise & Gill (1977) have prepared lists of mineral species from the New Idria District.

Figure 4.1 shows the orientation of some structural features related to tectonic blocks. Examination of Figure 4.1 shows that there are two preferred structural trends - northwest and northeast. Northwest trending features parallel to the regional structure and the New Idria Thrust Fault include the physical orientation of elongate tectonic blocks and foliation in the larger blocks. The northeast-trending features include tension cracks and shear and fracture planes within blocks. Crosscutting relationships show that the northwest trending features generally predate the northeast trending features.

Coleman (1957) recognized and mapped numerous tectonic blocks; he demonstrated that the exposed contacts of the blocks are faulted against the surrounding serpentinite. Evidence of shearing and development of slickensides is common. However, in many cases the actual contacts are not exposed, and the relationship of the blocks to the host serpentinite is obscured. In this study, most of Coleman's larger blocks in the southern portion of the District were re-examined; some of the smaller blocks could not be located in the dense brush and may have disintegrated, or disappeared under landslides. A few new localities not described by Coleman were visited and studied.

Coleman (1957) established five categories of tectonic blocks based upon their mineralogy; one category was reserved for jadeite-bearing rocks. In the present study these five categories have been collapsed into the single category of Mafic Schists and Greenstones.

Some of the rocks regarded by Coleman as metasomatic veins are reinterpreted as tectonic blocks. In the present study only three categories of tectonic blocks are defined, based upon mineralogy, bulk composition, and probable history.

Descriptions of these categories of tectonic blocks follow; while numerous examples of each type of tectonic block exist in the New Idria District, in most cases the exposures are poor and the geologic interpretation ambiguous. Therefore, this study concentrates on a few key outcrops at which contrasting rock types and in some cases geologic contacts are exposed.

Tectonic Block Category, this Study	Coleman Category
A. Chlorite-Diopside-Garnet Rocks	*Metasomatic chlorite-rich rocks*
B. Mafic Schists and Greenstones	*Tectonic blocks I-IV, jadeite-bearing rocks, and metasomatic soda-rich rocks*
C. Antigorite Knockers	*Rock of Santa Rita Peak*

All types of tectonic blocks show evidence of two metamorphic events, here defined as M1 and M2. M1 metamorphism is associated with the development of penetrative foliation in the chlorite-diopside-garnet rocks and the mafic schists, and the interpenetrating fabric of the antigorite blocks. Some of the M1 metamorphism must have been of the high-pressure blueschist type. M1 metamorphism occurred prior to entrainment of the blocks, because

Figure 4.1 - Orientations of structural features at New Idria. Northwest-trending features are sub parallel to regional structure and the New Idria Thrust Fault, oblique to the San Andreas Fault. Northeast-trending features crosscut northwest set.

Figure 4.1 - Orientations of Structural Features

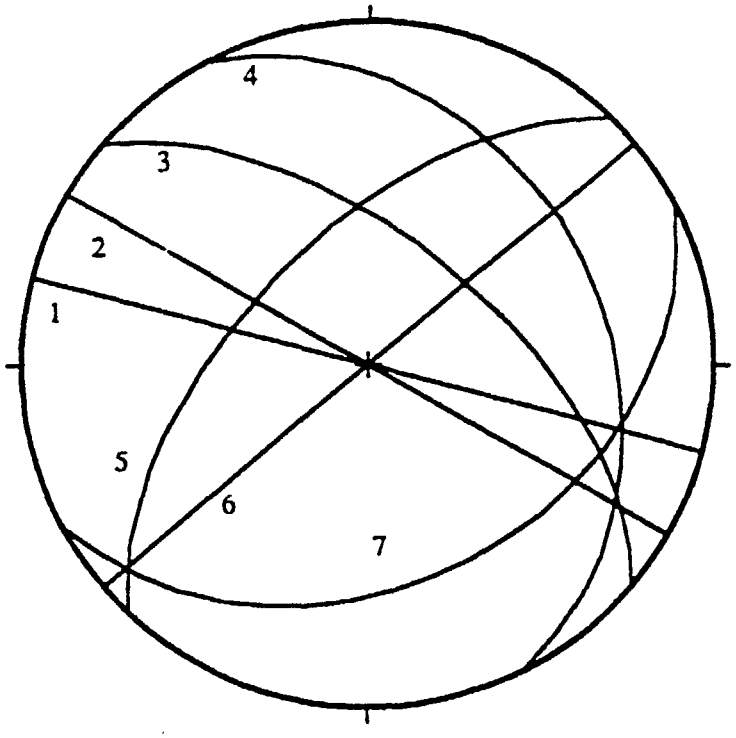

Legend:

1 - Foliation at Gem Mine
2 - Strike of New Idria Thrust Fault
3 - Foliation at Melanite Mine
4 - Foliation at 34-50 locality
5 - Pyroxenite layers near Perovskite Knob
6 - Shear planes at Santa Rita Peak
7 - Fractures at Melanite Mine

the penetrative foliation of the blocks is not matched by development of adjacent schistose serpentine. M1 metamorphism in blocks of different rock types may have occurred at different times prior to entrainment, and for some blocks the M1 event may have been a series of pre-entrainment events. M2 metamorphism is associated with the development of tension cracks and veins that crosscut the M1 foliation in chlorite-diopside-garnet blocks and mafic schists, and with crosscutting garnet veins in the antigorite knockers. M2 metamorphism took place after entrainment, and may have occurred for all blocks at the same time, probably in the Miocene. The only quantitative age controls on the timing of M2 metamorphism are contained in the mafic schists that host benitoite and neptunite at the Gem Mine, described below. M2 metamorphic reactions in most blocks were essentially isochemical, with only water required as an open system component. There may have been Ca metasomatism associated with M2 metamorphism of antigorite knockers. It is proposed here that M2 metamorphism is related to passage of the Mendocino Fracture Zone in the Miocene, with attendant regional uplift, sudden appearance of clastic serpentine in the sediments of the Great Valley Sequence, and development of the northeast-trending structural features described in this chapter.

II. Geological Setting of the New Idria District

The term *New Idria District*, referred to in this study simply as *the District*, was first used by Becker to describe the general region encompassing the historic mercury mines at New Idria, California (Becker, 1888). The most remarkable feature of the District is an oval, 23 by 8 km, fault bounded, serpentinite massif flanked by steeply dipping, locally overturned, sedimentary and metamorphic rocks of the Jurassic-Cretaceous Franciscan and the Cretaceous to Pliocene Great Valley Sequence of California.

The New Idria Serpentinite is a part of the Coast Range Ophiolite in California (Hopson et al., 1981). Its emplacement within the Franciscan Formation is related to subduction of the Farallon plate in the Jurassic. The tectonic setting of the ophiolite was a forearc basin lying between the Sierra Nevada volcanic arc to the east and a trench-subduction complex to the west, represented by the Franciscan Formation (Bartow, 1990). A piece of oceanic crust or underlying mantle was obducted onto the North American continent, later to rise through the Franciscan Formation as a serpentinite diapir. Emplacement of the New Idria Serpentinite as a diapir within the Franciscan has resulted in a piercement structure or tectonic window, lying just east of the San Andreas fault system northeast of Parkfield. Further details about the geological environment of the District can be found in Chapter 1.

III. Chlorite-Diopside-Garnet Rocks

A. General Statement

These green to yellow-weathering, blue-grey to white, foliated rocks consist mainly of chlorite and diopside, with melanite garnet (1-5 wt % TiO_2), schorlomite garnet (> 5 wt % TiO_2), variable amounts of serpentine and magnetite, and several Ti-rich accessory minerals, notably vesuvianite (idocrase), perovskite, and titanite (sphene), along with minor chromite, kammererite, chromian garnet, apatite, zirconolite, pyrolusite and copper sulfides. Other accessory minerals have also been reported (e.g. Coleman, 1986). Carbonate minerals including calcite and hydromagnesite sometimes fill voids in the rock. These surface alteration minerals were probably precipitated from meteoric waters and are not part of the metamorphic phase assemblage. The rocks are poorly exposed in most places; exceptions occur where a slab of more resistant serpentine cap rock overlies the chlorite-diopside-garnet rock. The best exposures of these rocks occur at Coleman locality

34-50, at Perovskite Knob, and at the Melanite Mine, all in the southern portion of the District (Figure 1.3). Chlorite-diopside-garnet rocks have not been reported from the northern half of the District.

B. The 34-50 locality

At this locality a set of four resistant rock towers surrounded by talus sits astride a low north-south ridge at an elevation of 4360 ft. (1329 m.) MSL, above the stream bed of the San Benito River, a short distance downstream from the Gem Mine. The coordinates are 36°20'.07 N, 120°36'.86 W. The KCAC Mine is clearly visible to the north, the Gem Mine to the east, and a syenite dike referred to in this study as *The Nose* on a prominent hill to the south. The locality name of 34-50 as used in this study is carried forward from Coleman (1957). Access to the outcrop is via a short spur from the (usually) graded road leading up from the KCAC mine to Santa Rita Peak.

The four towers are 2-3 m. tall and arranged roughly in a 5 x 10 m. rectangle oriented with its long axis SE-NW (Figure 4.2). The towers and associated talus cover approximately 100 sq. m. and are surrounded by dense brush. Each of the towers is capped by dark green, sheared but relatively resistant serpentine, under which lies a slab of light green to white, chlorite-diopside-garnet rock dipping gently to the east. The four towers are apparently the eroded remnants of a once-continuous slab of chlorite-diopside-garnet rock capped by serpentine. The strike and dip of this slab vary from 25-27°E and 14-32°S respectively, subparallel to the New Idria Thrust Fault. The outer contacts of the slab are not exposed, so its original lateral dimensions are unknown. However, the upper contact of chlorite-diopside-garnet rock against the serpentinite is exposed in each tower, and in the NW tower the upper and lower contacts are both exposed, so that a complete cross section is visible. Plate 4.1 is a photograph of the west face of the NW tower, showing both

contacts. **Figure 4.3** shows the essential features of this outcrop, in schematic form (see also Coleman, 1957).

The chlorite-diopside-garnet rock of the 34-50 locality is divided into a central chlorite-rich zone and two diopside-rich outer zones, an upper and a lower. The central zone includes the prominent horizontal green band in **Plate 4.1**, while the outer zones include the white horizontal bands in that photograph. The mineralogy of the three zones is similar, but the modal proportions of the minerals vary. This locality is remarkable for the absence of magnetite, a nearly ubiquitous accessory mineral at New Idria.

The contacts between the various zones are abrupt to gradational; locally there is considerable interfingering, especially between diopside and serpentine in the outer margin. The rock of the outcrop is strongly sheared. The interfingering has probably resulted from recrystallization of diopside and serpentine under shearing stress, and possibly from local mobility of Ca in metamorphic fluids (e.g. Labotka & Albee, 1979).

1. Central Zone

Chlorite gives a green color and imparts a strong foliation to the chlorite-rich central zone. Petrographic study reveals foliated M1 chlorite in nearly monomineralic bands, fine grained (< 100 μm) M1 diopside in nearly monomineralic bands, and domains containing both foliated chlorite and fine grained diopside (**Plate 4.2**). The width of these bands is quite variable, on a scale of millimeters. At the boundaries between chlorite-rich and diopside-rich domains, the foliation is disrupted and chlorite occurs in a variety of orientations. This may be due to mineral growth under shearing stress at a point of contrast in rock competency. The chlorite in the central zone has normal birefringence and does not display anomalous blue interference colors. This chlorite has an intermediate Fe-Mg ratio as

Figure 4.2 - Geologic sketch map of the 34-50 locality; geology revised from Coleman, 1957. The four towers are the eroded remnants of a once-continuous, easterly dipping slab.

Figure 4.2 - Geologic Sketch Map of 34-50 Locality

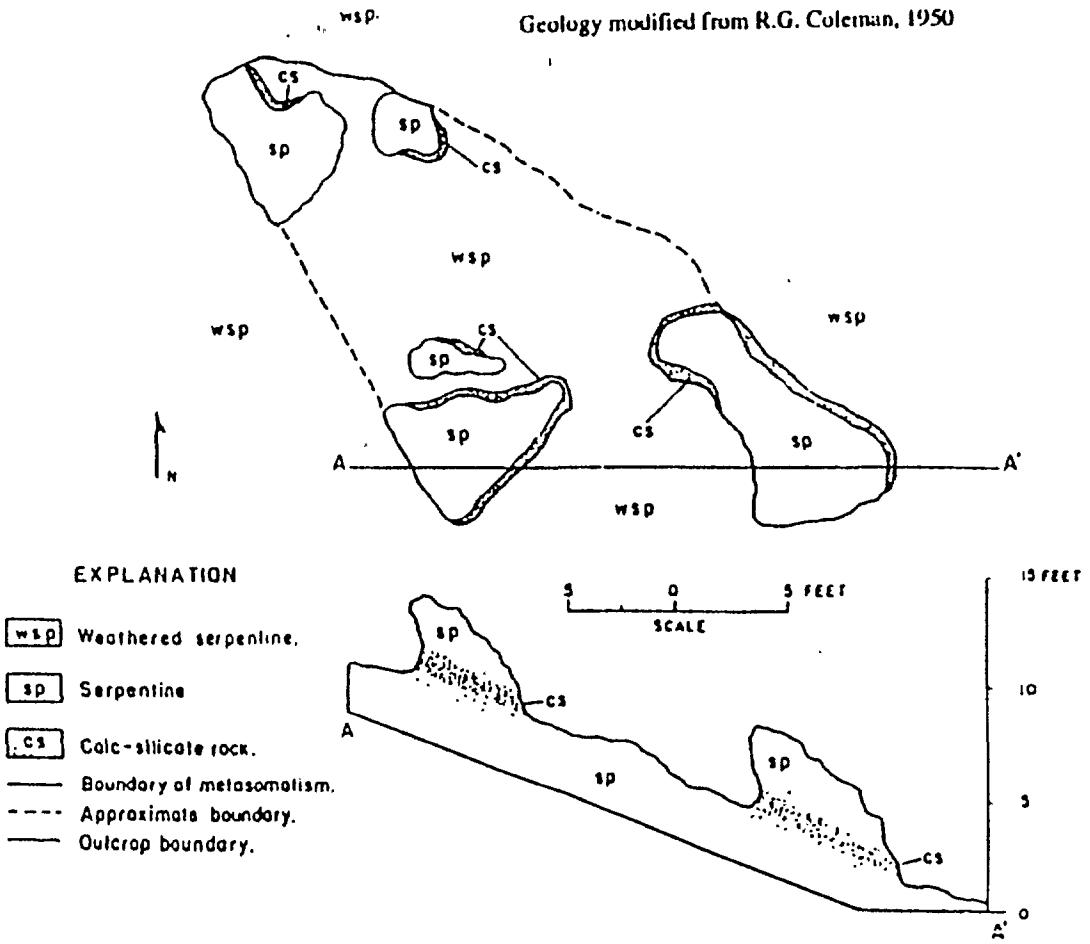

Plate 4.1 - Photo of the NW tower at the 34-50 locality. Serpentinite cap rock protects a 1 m. high slab of chlorite-diopside-garnet rock that dips gently away from the viewer. Green, foliated rock near hammer head is an M1 chlorite-rich domain. White band near hammer handle is an M1 diopside-rich domain. A second white band is visible in the lower portion of the photo, just above the green serpentinite that underlies the slab.

Figure 4.3 - Schematic diagram of northwest tower of 34-50 locality (see Plate 4.1), showing mineralogical variation with mirror symmetry about a horizontal plane.

Figure 4.3 - Schematic of 34-50 Locality

Measured Vertical Section

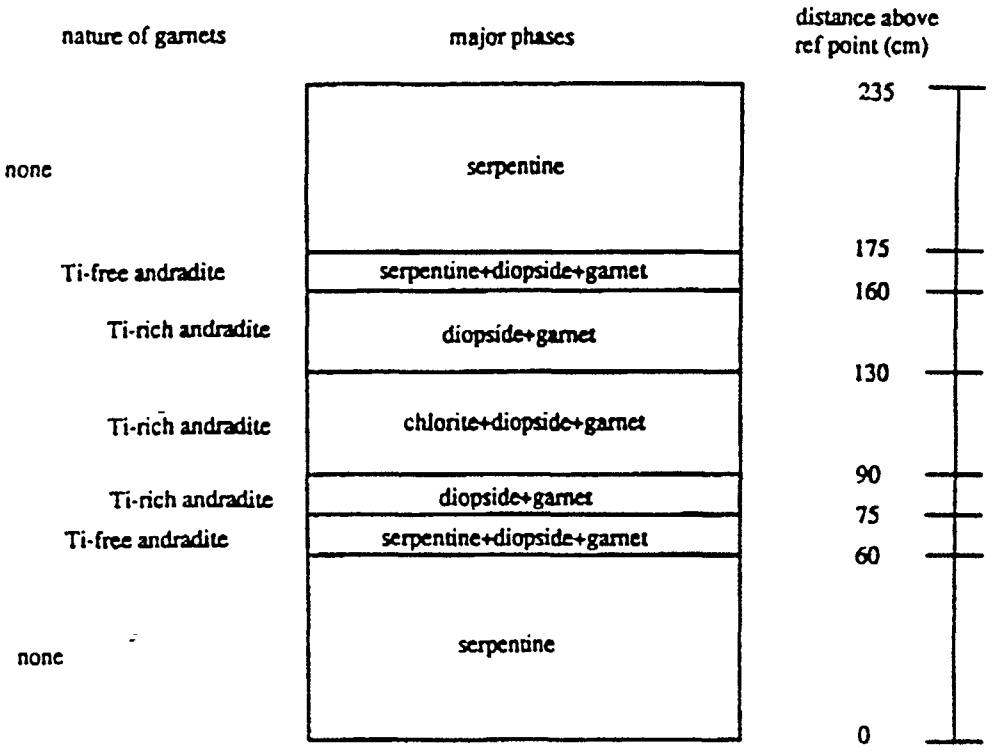

Plate 4.2 - Photomicrograph of sample 990-22 from 34-50 locality, showing foliated M1 chlorite at top and bottom of photo, fine grained M1 diopside lens in center, and stringers of black M1 Ti-garnet. Crossed nicols with gypsum plate. Field of view 4 mm.

Plate 4.3 - Photomicrograph of sample 990-15 from 34-50 locality, in a diopside-rich domain. Stubby crystals of M1 diopside show good cleavage. Isolated M1 garnets visible near left and right of photo, minor M1 chlorite in lower left. Crossed nicols with gypsum plate. Field of view 4 mm.

shown in Table 4.2. Small amounts of a serpentine mineral may also be intergrown with the chlorite; distinguishing these phases optically is difficult. Chromite and its alteration products kammererite and chromian garnet are minor accessories.

Recrystallized metamorphic diopside occurs in at least two generations: (M1) massive, fine to occasionally coarse grained diopside and (M2) bladed diopside associated with vein-filling garnet. No significant compositional differences were found between the first and second generations of diopside. **Table 4.1** and **Table 4.2** show compositions of metamorphic diopside and chlorite respectively from the 34-50 locality. The diopside here and at other localities is more Mg-rich (higher X_{Mg}) than coexisting chlorite. Comparison of diopside compositions with those of the relict igneous clinopyroxenes in **Table 3.5** shows them to be very similar, although the metamorphic pyroxenes are slightly richer in Fe than the igneous (X_{Mg} = 0.92 and X_{Mg} = 0.95 respectively).

Ti-rich andradite garnet is present in all samples examined. Metamorphic Ti-garnets are anhedral to subhedral and occur in two generations. M1 garnets occur as isolated matrix crystals or blebs and stringers parallel to the foliation; M2 vein-filling garnets are associated with bladed M2 diopside in millimeter-wide veins that crosscut the foliation nearly at right angles. The veins appear to radiate outward from the central zone. M1 garnet blebs conform to local crenulations in the foliation and therefore predate the crenulation. At 34-50, most of the Ti-rich garnet of both generations is isotropic to slightly birefringent. Under straight nicols the garnet varies in color from light pink to reddish brown. Occasionally earlier, low Ti, slightly birefringent M1 garnet is overgrown by later, Ti-rich, isotropic M2 garnet in a crosscutting vein. Along the walls of veins, M2 diopside is seen to crystallize as thin whiskers or blades, some of which are in turn overgrown by garnet, occasionally resulting in a "bearded" appearance at the contact between vein filling garnet

and the vein wall. Open spaces in the veins are frequently filled by late stage calcite precipitated from ground waters.

2. Outer Zone

Examination of samples from the diopside-rich outer zone reveals moderately coarse-grained M1 diopside (1 mm) with minor M1 chlorite, and ubiquitous chromite (and chromian alteration minerals). Some coarse diopside grains exhibit an equant texture, with good cleavage (**Plate 4.3**). Others have an elongate bladed shape. Some early diopside crystals are seen to have been fractured and bent. The larger (1 mm) blades are parallel to the foliation while the smaller blades are randomly oriented. The compositions of the two types of M1 diopside are indistinguishable; they average $X_{Mg} = 0.92$, which is the same as diopside from the central zone. At the outermost edge of the diopside-rich zone serpentine interfingers with the diopside. The M1 chlorite is strongly foliated, and frequently shows anomalous blue interference colors, suggesting an Fe-rich composition. However, as shown in **Table 4.2**, the chlorite in the outer zone is generally more magnesian than in the central zone. Unaltered chromite has a deep red color, and is always surrounded by chlorite; chromite was never seen in contact with Cpx. This chromite has the same composition and optical properties as the unaltered chromite discussed in Chapter 3. However, some chromite grains have been partially replaced by a mixture of chlorite and a green Cr-rich garnet that also contains up to 3 wt. % TiO_2. Magnetite is conspicuously absent at 34-50.

The outer zone is also crosscut by tension cracks with vein-filling M2 minerals similar to those in the central zone. No significant compositional or textural differences were observed between M2 assemblages in the central and outer zones.

3. Comparison of Central and Outer Zones

The textures and compositions described above suggest that the chlorite-diopside-garnet slab seen at the 34-50 locality is a strongly sheared and almost completely recrystallized rock embedded within the serpentinite. The foliated rock texture is inconsistent with a simple metasomatic replacement of lizardite and chrysotile; nor do the M1 minerals appear to have precipitated in a hydrothermal vein.

Shearing is manifest in the central zone by strong foliation of the dominant Fe-rich M1 chlorite, and in the outer zone by fracturing and recrystallization of M1 diopside. These observations show that the M1 metamorphism was synkinematic. The anhedral to subhedral Ti-rich garnets of the central zone occur in two generations. The first garnet generation (M1) is associated with the shearing and recrystallization event which produced the M1 chlorite, while the vein-filling M2 garnets which crosscut the foliation formed later. The veins that host the garnet are probably tension cracks; the minerals in the veins have beautifully preserved, delicate textures with no sign of post-mineralization deformation. Therefore the M2 mineralization is postkinematic.

C. Perovskite Knob

This prominent red knob, 25 m. long and 30 m. wide, rises 15 m. above its base elevation of 4520 ft. (1378 m.) MSL on the western slope of Hill 4857 (Plate 4.4 and Figure 4.4). The coordinates are 36° 19'.65 N, 120° 36'.31 W. The knob is best reached by descending a short spur road from a higher gravel road which traverses the western slope of Hill 4857. This gravel road was blocked in 1990 by a steel gate placed by the Bureau of Land Management (BLM) to prevent vehicle access to the EPA Superfund site at the abandoned Atlas Mine that lies on the eastern side of Hill 4857. As of this writing, it is

generally no longer possible to drive to Perovskite Knob without special arrangements with BLM. Another approach from the unnamed stream valley below is possible but involves ascending through dense brush. The origin of the name Perovskite Knob is unknown, but presumably was given by local mineral collectors who found perovskite there.

The rock of the knob consists of three sub-horizontal zones (**Figure 4.4, 4.5**). The topmost zone, consisting mostly of red-weathering, dark green, tough serpentinite, is resistant to erosion and is the main reason for survival of the knob. This cap rock is about 3 meters thick; it is a dense rock consisting mainly of antigorite with a sugary texture; it is similar to the rock at the summit of Santa Rita Peak. The cap rock is underlain by strongly sheared serpentine rock consisting of a mixture of lizardite and massive chrysotile, that forms the middle zone, about 10 m. thick. This rock tends to split along the boundaries of lenticular blocks or *phacoids*. The overall appearance is reptilian and scaly; the field term "dragon skin" is used to describe this rock. The classic reptilian appearance of serpentine gave rise to the Latin term *serpentenaria*, first used by Agricola in 1546 to describe serpentine rock. This rock weathers to an orange-red color, but fresh surfaces show a variety of colors from brown to green to white. Dragon skin rock is slippery and treacherous in wet weather. In both the tough antigorite rock and the sheared serpentine rock, magnetite is abundant, sometimes as macroscopically visible grains but frequently as finely disseminated particles which give the rock a dark color.

The lowermost zone consists of dark, blue-grey massive chlorite-diopside-garnet rock containing a host of accessory minerals. The contact between the chlorite-diopside-garnet rock and the dragon skin rock is sharp in most places (**Plate 4.5**). Mapping of this contact around the base of the knob shows that the contact surface is roughly planar, dipping gently to the south: the dip varies from 10-20°. The contact may be followed along the base of the north side of Perovskite Knob, generally about 1 m above present ground level. It is

Plate 4.4 - Photo of Perovskite Knob from the north. Knob rises 15 m. above its base and is capped with resistant , red-weathering antigorite. Bush in foreground is manzanita; trees are digger pines.

Figure 4.4 - Geological sketch map of Perovskite Knob, showing antigorite cap rock, sheared serpentine "dragon skin" rock, and underlying slab of southerly dipping chlorite-diopside-garnet rock. Compare with Figure 4.2.

Figure 4.4 - Geological Sketch Map of Perovskite Knob

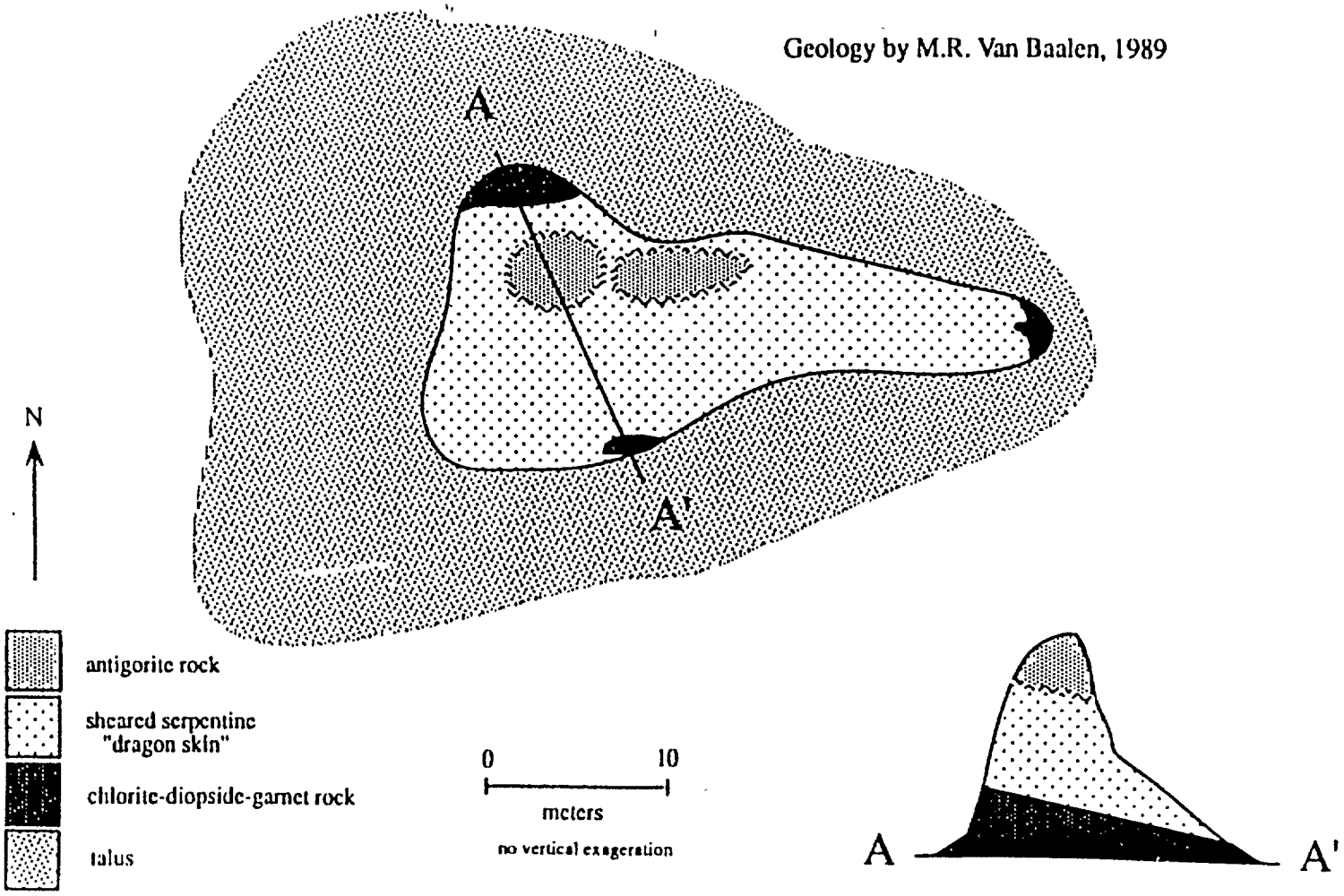

Figure 4.5 - Schematic diagram of Perovskite Knob, showing mineralogical variation. Compare with Figures 4.3, 4.4.

Figure 4.5 - Schematic of Perovskite Knob

Measured Vertical Section

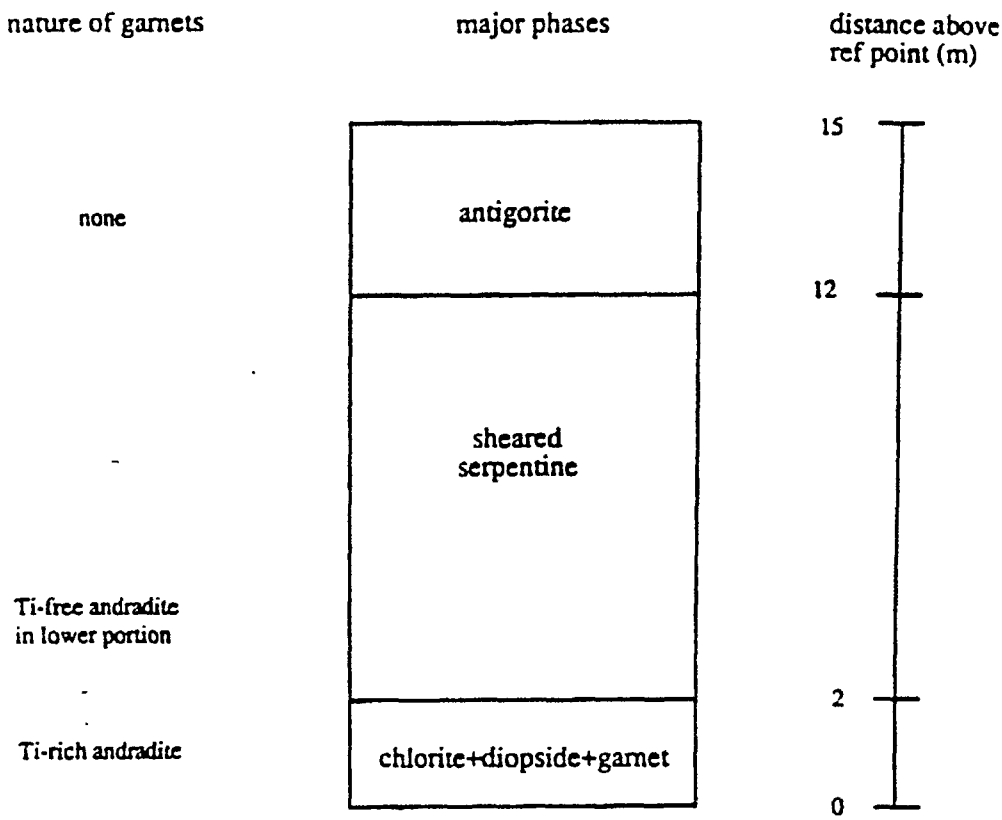

Plate 4.5 - Photo of base of Perovskite Knob on the north side. Hammer sits on subhorizontal fracture surface of yellow-weathering, chlorite-diopside-garnet rock that underlies Perovskite Knob. Contact with overlying sheared, green serpentinite is the prominent fracture, 1 m. above hammer, that dips 30° to right.

Plate 4.6 - Photo of block of red-to-blue weathering chlorite-diopside-garnet rock, showing sharp contacts, at east end of Perovskite Knob. Hammer handle is on chlorite-diopside-garnet rock, head on enclosing red-to-green weathering serpentinite rock, block dips 60° left.

Plate 4.7 - Photomicrograph of M2 garnet vein in sample 688-6 from Perovskite Knob. M2 Ti-garnet is birefringent, sector twinned, and compositionally zoned. Fans of yellow, M2 chlorite grow out from vein wall below birefringent garnet. Wallrock of vein occupies left half of photo; it consists mainly of M1 chlorite, some of which shows anomalous blue interference colors. Opaque minerals in upper left include deep red M1 garnet and magnetite. Crossed nicols. Field of view 2 mm.

nearly continuous with an offset below the east end of the knob which separates the east and west summit blocks higher up. At the NW corner of the knob the exposed contact ends abruptly at a large talus pile. On the south side of the knob only one small outcropping of the chlorite-diopside-garnet rock was found, near the base of a digger pine.

At the present erosion level, the lower boundary of the chlorite-diopside-garnet rock is not exposed. The exposed portion, however, including its upper contact, bears strong resemblance in mineralogy and bulk composition to the slab of chlorite-diopside-garnet rock at the 34-50 locality. In contrast to the occurrence at 34-50, an outer zone of diopside-rich rock has not developed at Perovskite Knob. It is nevertheless proposed here that this contact between chlorite-diopside-garnet rock and overlying serpentinite is the outer boundary of a block consisting of chlorite-diopside-garnet rock. Shearing along this contact during emplacement of the serpentinite has resulted in the slickensided "dragon skin" rock on the less-competent serpentine side of the contact. The exposed cap rock at 34-50 corresponds to the dragon skin rock at Perovskite Knob. The antigorite rock at Perovskite Knob has no counterpart at 34-50: if once present, it has been eroded, an interpretation consistent with the poor, crumbly condition of the 34-50 towers compared with the high relief at Perovskite Knob.

At the extreme eastern (uphill) end of Perovskite Knob the contact between chlorite-diopside-garnet rock and overlying dragon skin includes an angular block of chlorite-diopside-garnet rock surrounded by sheared serpentine rock. This 2 meter high angular block is about 30 cm. wide, lies in sub vertical orientation, and superficially resembles a dike (Plate 4.6). Close examination of the block shows that it is not a dike, but an intact block of massive, fine grained chlorite-diopside-garnet rock. The contacts between the chlorite-diopside-garnet block and the surrounding serpentine are sharp; there are no visible

textural gradients across the block. This block is interpreted as an irregular portion of the otherwise generally planar contact of underlying chlorite-diopside-garnet rock.

The blue-grey chlorite-diopside-garnet rock at Perovskite Knob does not exhibit the strong foliation observed at the 34-50 locality. It is massive to weakly foliated, and is cut by parallel vertical veins and fractures that strike northeast. These fractures are part of the late stage northeast trending features shown in **Figure 4.1**. The fractures contain museum quality mineral specimens of garnet, vesuvianite (idocrase), and perovskite (**Table 4.4**).

Extensive blasting by mineral collectors has occurred at Perovskite Knob. This is a mixed blessing for the geologist. Some excellent mineral specimens were exposed by the blasting but geologic relations were obscured by talus. The only rattlesnake observed within the serpentinite during the course of this study was found in the talus pile at Perovskite Knob by the author's daughter in the summer of 1990.

The mineralogy of the chlorite-diopside-garnet rock at Perovskite Knob is rich and varied; this is a famous collecting locality. Phases encountered in the course of this study include: chlorite, diopside, titaniferous garnet, andradite garnet, magnetite, perovskite, vesuvianite (idocrase), titanite (sphene), apatite, zirconolite, pyrolusite, chalcopyrite, and the secondary minerals calcite and hydromagnesite. Other minerals have been found at this locality; the reader is referred to Coleman (1986) for a more complete list. The titaniferous garnets from Perovskite Knob and other nearby localities are of particular interest both mineralogically and petrologically; they are discussed further in Chapter 5.

Chlorite at Perovskite Knob occurs in more than one generation, as at the 34-50 locality. The first generation of chlorite defines the weak foliation of the rock. A few grains of this M1 chlorite show a blue anomalous interference color in thin section. The M2 chlorite is

associated with vein-filling M2 garnet, and is locally found in millimeter-sized hexagonal plates coating the walls of veins. In thin section the M2 chlorite is displayed as blades arranged in the shape of a fan, attached to the vein wall (**Plate 4.7**). The M2 chlorite is more magnesian than the first generation. **Table 4.3** shows chlorite compositions at Perovskite Knob. Comparison with **Table 4.2** shows that Perovskite Knob chlorites have a higher Fe content than 34-50 central zone chlorites. However, chlorite 688-8C.7 in **Table 4.3** is second generation; it is magnesian, comparable to chlorites from the outer zone at 34-50. This observation suggests that some of the chlorite in the outer zone of 34-50 may be of the M2 generation.

M1 diopside at Perovskite Knob occurs chiefly as isolated equant matrix grains, unlike at 34-50 where there are diopside-dominated domains. The overall abundance of diopside at Perovskite Knob is significantly lower than at 34-50, reflecting a different bulk composition. The diopside at Perovskite Knob is also somewhat more Fe-rich than at 34-50 (**Table 4.1**).

D. The Melanite Mine

This locality is a low and deeply weathered exposure of yellow-weathering chlorite-diopside-garnet rock, lying high on the north side of Hill 4857 above the streambed of the south fork of the San Benito River (which forks just upstream from the Gem Mine). The outcrop lies straight downhill via a pair of rough roads from the EPA gate at the northwest corner of the Atlas Mine site. The coordinates are 36°19'.88N, 120°36'.02W; the elevation is about 4700 ft. (1433 m.). The Melanite Mine may be also be approached on foot from below, by ascending a gully from a road which traverses the north slope of Hill 4857. This locality was unknown at the time of Coleman's work in the 1950s.

Unlike 34-50 and Perovskite Knob, the Melanite Mine is not protected by resistant cap rock, which accounts for its low and generally unimpressive appearance (**Plate 4.8**). The locality might be overlooked altogether were it not for abundant drusy crystals of black Ti-rich M2 garnets coating vein surfaces: mineral collectors have blasted the outcrop with dynamite, leaving a large talus pile with easily gathered grab samples.

The outcrop is a low bench of yellow-weathering, chlorite-diopside-garnet rock about 1 m. high and 15 m. wide. The bench is flanked on both sides by green-weathering serpentine rock. Here, as at many other New Idria localities, contact relations are best seen from a few meters away, as subtle color contrasts between adjacent rock types. At the south end of the bench a backhoe excavation leading up the hill a short distance has exposed the green-weathering serpentine rock at the south end of the outcrop. Evidently mineral collectors wished to see if a buried portion of the outcrop could be uncovered; as a result the contact at the edge of the chlorite-diopside-garnet rock is now exposed. **Figure 4.6** shows in schematic form the essential rock types at the Melanite Mine: comparison with **Figures 4.2** and **4.3** shows the same progression of rock types as those seen at the 34-50 locality and Perovskite Knob. The Melanite Mine is accordingly interpreted as a 15 m. wide slab of chlorite-diopside-garnet rock, bounded on both sides by sheared serpentinite rock. The thickness of this slab cannot be determined from the existing exposure.

Like the 34-50 locality, the central zone of chlorite-diopside-garnet rock here contains both chlorite-rich and diopside-rich domains. The chlorite-rich domains are moderately well foliated with M1 chlorite defining the foliation. The diopside-rich domains are massive to weakly foliated. The abundance of M1 garnets is somewhat greater in the diopside-rich domains. The exposed face of chlorite-diopside-garnet rock in the central zone also contains irregular regions of serpentinite, making the field relations very confusing at the Melanite Mine. These serpentinite regions appear to be artifacts of blasting and may

Plate 4.8 - View of the Melanite Mine, consisting of a slab of yellow-weathering chlorite-diopside-garnet rock above talus slope, enclosed by green-weathering serpentinite. Total width of slab 15 m. Contact of slab with serpentinite visible by color change, one third of distance from left side of photo.

Figure 4.6 - Schematic diagram of Melanite Mine tabular outcrop, showing mineralogical variation from left to right. The progression of rock types is similar to that of 34-50 (Figure 4.3) but rotated 90°.

Figure 4.6 - Schematic of Melanite Mine

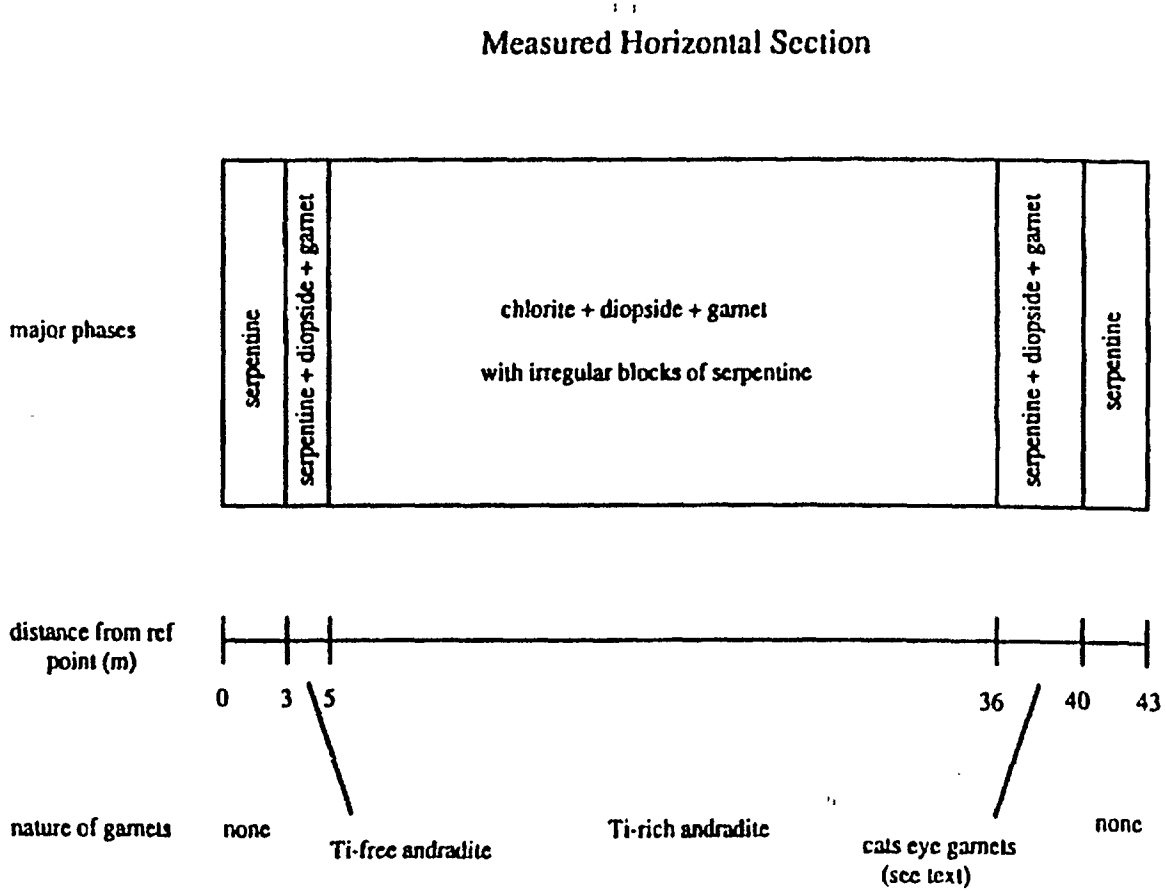

Plate 4.9 - Photomicrograph of "cat's eye" garnets with black, Ti-rich cores and yellow, Ti-poor rims. These garnets have been found in the lateral transition zone at the Melanite Mine. Field of view 0.3 mm. Photo by Dan Behnke.

therefore represent part of an irregular contact surface at the margin of the chlorite-diopside-garnet slab. Weathering at this outcrop makes an exact interpretation of the contact relations problematical.

The mineralogy at the Melanite Mine is quite simple compared with Perovskite Knob; the great variety of accessory phases there is absent at the Melanite Mine. In the left hand or southern transitional zone between the central zone and the serpentinite, patches of M2 diopside whiskers about 5 mm. long are found coating serpentinite, giving the rock a fuzzy appearance. In the central zone Ti-rich M2 garnets coat vein walls. These garnets are jet black and of generally uniform size, under 1 mm. At the right hand or northern transitional zone, some remarkable "cat's eye" garnets were found, as indicated in **Figure 4.6.** These small (< 1 mm.) andradite garnets have black, Ti-rich cores, and yellow, Ti-free rims. The compositional zoning is abrupt and extreme, as seen in **Plate 4.9.** The diopside-rich substrate on which the garnets lie has a porous or spongy texture, suggesting high fluid flux. These euhedral M2 garnets formed in the altered rind of the relatively Ti-rich central zone. Aqueous fluids from which the garnets precipitated during the M2 event were able to mobilize Ti on a scale of about one meter, the width of the rind. Outside this rind only Ti-free garnets were found, due to the greater mobility of Ca under M2 conditions. The interpretation of these cat's eye garnets is also discussed in Chapter 6, as an example of Ti mobility in aqueous fluids. Müntener & Hermann (1994) have reported similar garnets from Val Malenco, Italy.

E. Discussion of Chlorite Compositions

Table 4.2 and **Table 4.3** give compositions of chlorite from the 34-50 and Perovskite Knob localities respectively. All compositions are ordinary metamorphic chlorites; they fall into the categories of clinochlore, pycnochlorite, and penninite in the nomenclature of Hey

(1954). Figure 4.7 shows these compositions in the system Al_2O_3-FeO-MgO projected through SiO_2 and H_2O. Examination of Table 4.2, 4.3 and Figure 4.7 shows a considerable compositional range for New Idria chlorites, particularly in Fe/Mg ratio and in Al content. Much of this variation may be explained by the exchange vectors $Al_2Mg_{-1}Si_{-1}$ (Tk) and $FeMg_{-1}$ (Fm). Additionally, substitution of ferric iron via $Fe^{3+}Al_{-1}$ (Fa) probably takes place, but in this study ferrous/ferric ratios were not determined. Figure 4.8 plots the progress along the Tk exchange vector against the ratio Fe/(Fe+Mg), in order to show strong covariance of Fe and Al. Laird (1988) demonstrated that in mafic and ultramafic rocks, a strong positive correlation exists between progress along the Tk vector in chlorite and metamorphic grade. I therefore conclude from Figure 4.8 that the M1 chlorites record higher grade conditions than the M2, and that the M1 chlorites generally did not recrystallize during the M2 event.

In both Figure 4.7 and Figure 4.8 the data points for M2 chlorites are distinguished from M1. The M2 chlorites are more magnesian and less aluminous than the M1. The Fe-Mg ratio in chlorite reflects the local bulk composition of the rock (Maruyama et al., 1986). As noted before, all New Idria chlorites are less magnesian than coexisting diopside, which is an exception to the general rule that chlorites tend to be more magnesian than coexisting mafic minerals. Using the thermochemical data of Helgeson et al. (1978) in the model system FMASH, I find that at sub-greenschist conditions, the assemblage Fe-chlorite (daphnite) + diopside is stable relative to Mg-chlorite (clinochlore) + hedenbergite, which is consistent with the field observations at New Idria.

F. Discussion of Bulk Compositions

Bulk compositions of the chlorite-diopside-garnet rocks are very similar to pyroxenites from other ultramafic rocks world wide. Table 4.5 shows representative bulk

Figure 4.7 - Chlorite compositions projected into the system MgO-(Fe+MnO)-Al_2O_3 system. M1 and M2 chlorites form distinct groups as shown.

Figure 4.7 - Compositional Variation in Chlorite

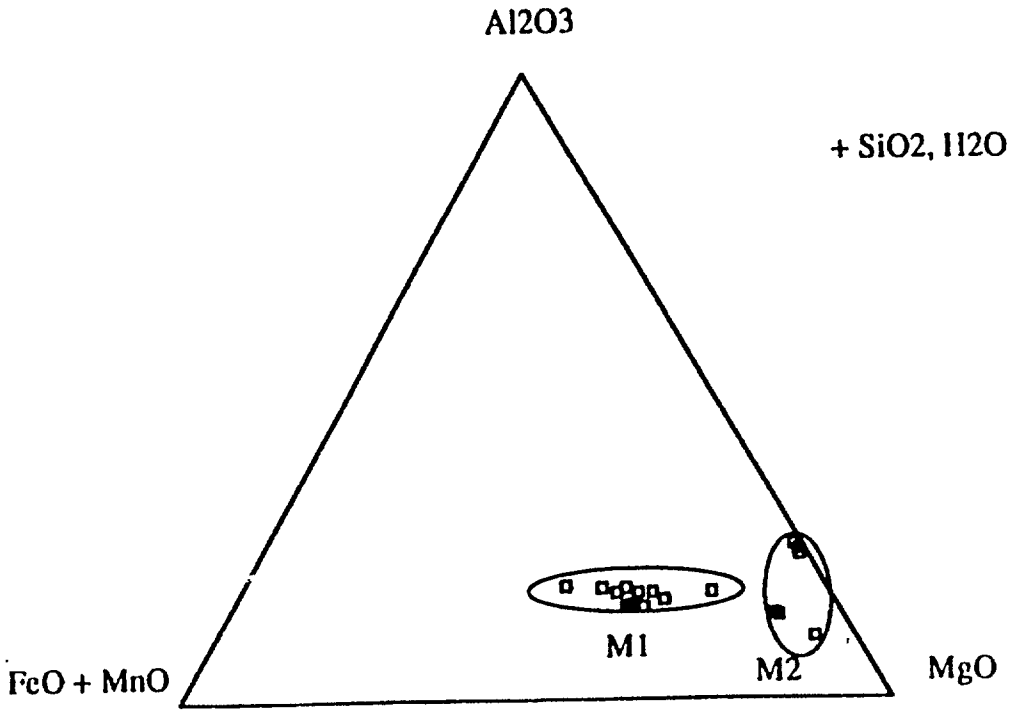

Figure 4.8 - Tschermak variation in chlorites plotted against Fe/(Fe+Mg), showing covariance. M1 chlorites record higher grade conditions than M2 (Laird, 1988).

Figure 4.8 Tschermak Variation in Chlorite

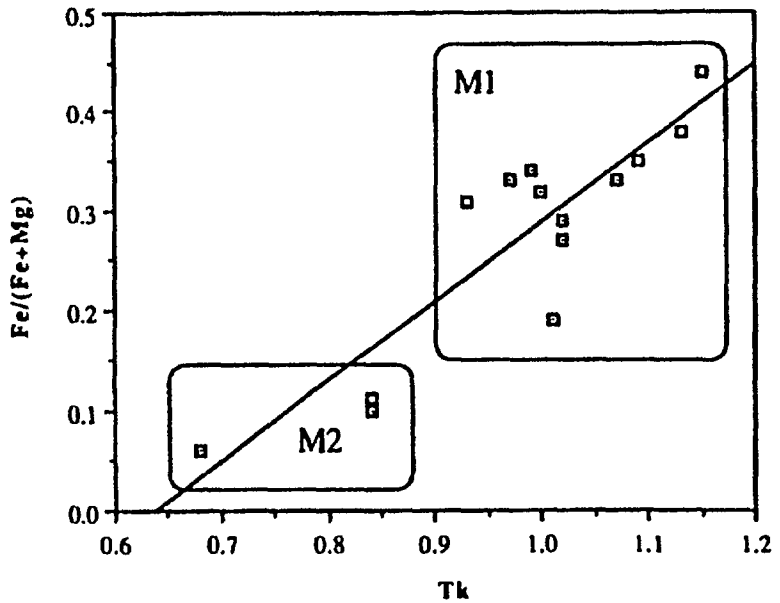

compositions of chlorite-diopside-garnet rocks, along with pyroxenites from other localities and with New Idria Serpentinite sample 989-45 for comparison. The bulk compositions of the chlorite-diopside-garnet rocks vary over a considerable range: Al, Ca, and the ratio Mg/Si show the largest excursions. The variability in the New Idria samples is partly explained by the nature of rock samples chosen for analysis: chlorite-diopside-garnet rock containing chlorite and diopside in all proportions is found at New Idria; ensuring that a given sample is "representative" is difficult.

Some trace element data are shown in **Table 4.5** for the samples in this study and for the comparison samples. The trace element concentrations for the chlorite-diopside-garnet rocks fall within the normal range for pyroxenites; both are different from the depleted 989-45 sample, which is a serpentinized harzburgite.

Table 4.6 recalculates the analyses from **Table 4.5** using the spinel norm method described in **Chapter 3. Figure 4.9** shows the analyses from **Table 4.6** projected into the ultramafic ternary system ol-opx-cpx (see also figure **Figure 3.3**). The projection is through spinel and minor components, e.g. TiO_2. A similar projection through garnet or anorthite would slightly affect the plotted positions by moving all points incrementally away from the Cpx vertex, but the effect would be small, and the equivalent rock types would not change. The shaded oval outlines the area of serpentinite bulk compositions from **Figure 3.4**: these lie in the dunite to harzburgite fields. All of the data points plotted in **Figure 4.9** lie in the pyroxenite field: most fall within the olivine websterite category. The dotted line in **Figure 4.9** represents the locus of compositions along a mixing line between two end members: pure chlorite and pure diopside, using actual mineral compositions from the 34-50 locality. All compositions with the exception of the pure chlorite sample lie in the pyroxenite portion of composition space; the pure chlorite end member lies along the ol-opx join. The open triangle symbol that lies nearly on the dotted

line represents a model composition used for thermodynamic calculations in the following section.

G. Models for the Origin of Chlorite-Diopside-Garnet Rocks

1. Metasomatism

Coleman (1957) referred to the chlorite-diopside-garnet rocks of New Idria as *metasomatic chlorite-rich rocks*, and proposed that they were formed by metasomatic alteration of ordinary serpentine rock. He proposed a process of alteration of serpentine rock to one containing chlorite, diopside and garnet, by fluids importing Ca, Al, Ti, and Fe while exporting Mg and Si to the surrounding environment. He proposed that the metasomatic fluids were hydrothermal fluids related to the intrusion of some small intrusive syenite bodies 1-2 km. distant. The main reason for this hypothesis was to explain the extreme enrichment of Ti in the "metasomatic" rocks (more than four orders of magnitude). He suggested that breakdown of Ti-rich amphibole in the intrusives could have contributed aqueous Ti complexes to the hydrothermal fluids. However, kilometer scale movement of Ti-rich hydrothermal fluids is problematical given current understanding of the very limited mobility of Ti in crustal rocks (see Chapter 7, also Van Baalen, 1993).

Ti (and Al) complexes in aqueous fluids at low temperatures have such low concentrations that the required advection of these elements could be accomplished only by massive fluxes of fluids infiltrating through a well developed subterranean plumbing system. At New Idria, however, there is no evidence of a large scale system of fluid conduits and vein systems. On the contrary, the chlorite-diopside-garnet blocks are relatively small, isolated from one another, and show no obvious spatial relationships to each other. No evidence of veins connecting blocks has been found. Furthermore, close examination of serpentinite

rock at the contact with the syenite intrusive shows no sign of metasomatic alteration. The contact instead appears to be relatively dry and baked, with an aureole containing in turn olivine, antigorite, and lizardite/chrysotile at increasing distances from the contact. This succession of mineral zones in the aureole represents successively lower peak temperatures within an essentially isochemical system. On the syenite side of the contact, however, there is in places a rind of albitite or chloritized amphibole with titanite (sphene) that suggests deuteric alteration. Formation of titanite (sphene) as a breakdown product of Ti-amphibole suggests that Ti may have been conserved rather than exported during this process.

The penetratively foliated textures of the chlorite-diopside-garnet rocks manifest powerful shear during the crystallization of the chlorite. Serpentine rock in the area, while generally sheared and crudely foliated, never shows this penetrative foliation. This observation suggests that the development of penetrative foliation predates entrainment of the blocks.

2. Isochemical Metamorphism

All of these problems with the metasomatism hypothesis are solved by a simpler proposal adopted here, that the chlorite-diopside-garnet rocks represent nearly isochemically metamorphosed blocks of a pyroxenite bulk composition that are included within the larger serpentinite body; these are not the lherzolite veins of Chapter 3. Only water is required as an open system component. This interpretation is suggested by the field relations and rock textures, by comparison of bulk compositions, and finally by analogy with similar rocks from other localities that do not have the same local geology as New Idria.

If the blocks are indeed metapyroxenites, the question of the origin of the blocks must be addressed; there are several possibilities. It is possible that the metapyroxenite blocks are

tectonic inclusions from an unknown source entrained within the serpentinite; tectonic inclusions of a variety of other rock types are present. It is also possible that the metapyroxenite blocks might be primary igneous features or even have a cognate origin with the depleted dunites and harzburgites. They may represent cumulate layers from passing basaltic melts, or crosscutting veins and dikes; this possibility might be investigated with a trace element study if it could be shown that trace element patterns persist through serpentinization. The mirror symmetry displayed at the 34-50 locality suggests but does not prove an origin as a multiple injection dike. Other, less-altered ophiolitic slices in the Coast Ranges, e.g. Elder Creek in Tehama County, have meter-scale veins and dikes of clinopyroxenite (Rynearson, 1946; Shervais & Beaman, 1994). The present random orientation of the blocks may well result from boudinage or other tectonic dismemberment of dikes followed by block rotation during the diapiric ascent of the New Idria Serpentinite.

3. Whole Rock Reactions

If the chlorite-diopside-garnet rocks are derived from pyroxenites, then it should be possible to write whole-rock reactions relating the two rock types. These whole-rock reactions in turn must be linear combinations of the component reactions. Since the Ti-garnets, magnetite and chromite are only accessory minerals to the rock-forming minerals chlorite and diopside, we are justified in ignoring them at first. This simplification allows us to initially employ the model system CaO-MgO-Al_2O_3-SiO_2-H_2O (CMASH).

A representative model composition in CMASH for a pyroxenite is $10MgO + 2CaO + Al_2O_3 + 9SiO_2 + 6H_2O$. Under upper mantle conditions this composition (ignoring the water) would exist as a mixture of olivine + orthopyroxene + clinopyroxene + spinel.

Figure 4.9 - Chlorite-diopside-garnet bulk compositions in the ultramafic ternary (see Figure 3.3 for field boundaries). Explanation of symbols: filled squares, chlorite-diopside-garnet rocks from New Idria; filled triangle, chlorite-diopside-garnet rock from Val Malenco (Müntener, 1994); filled circle, pyroxenite sample 66SAL-1 from Hawaii; open triangle, model composition used for calculations (see text). Dotted line is locus of points containing mixtures of chlorite and diopside, from 0% to 100% diopside. Shaded oval is region of serpentinite bulk compositions from dunite to harzburgite (see Figure 3.4).

Figure 4.9 - Chlorite-Diopside-Garnet Bulk Compositions

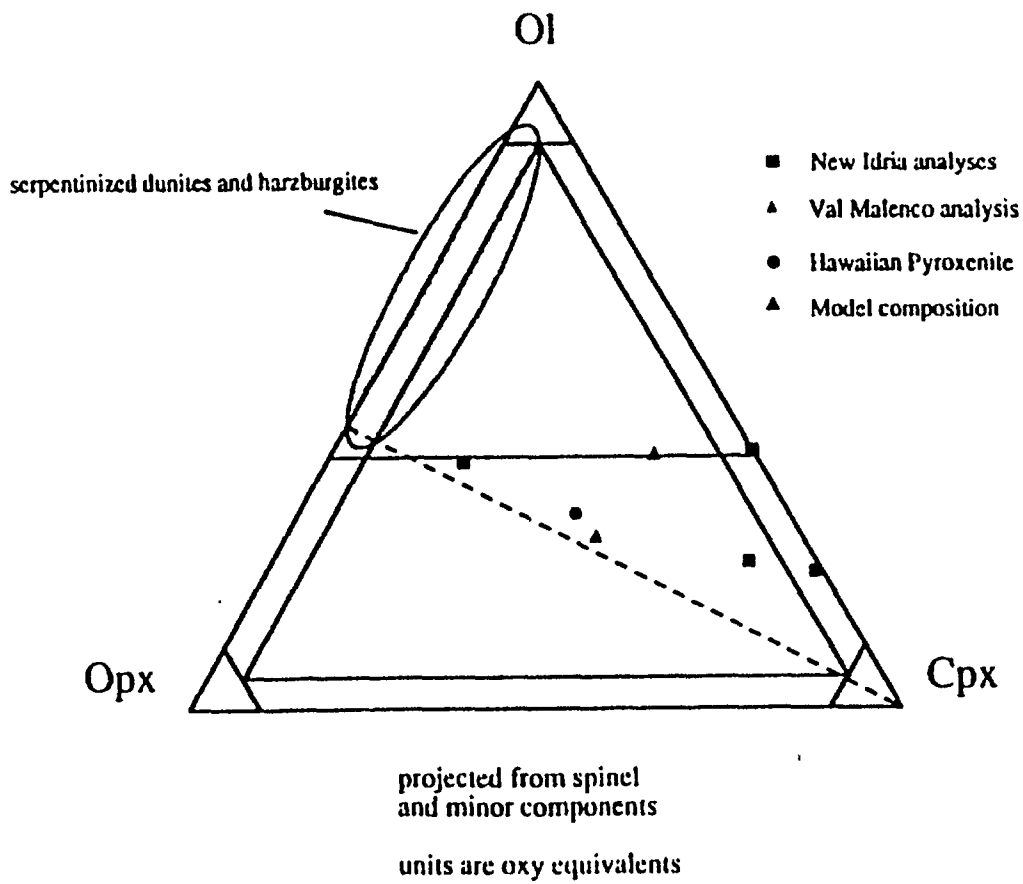

Figure 4.10 - Equivalent mineral assemblages for composition shown, P-T conditions generally increasing from top of table to bottom.

Figure 4.10 - Arrangements of $10MgO + 2CaO + Al_2O_3 + 9SiO_2 + 6H_2O$

$$\underset{\text{chlorite}}{Mg_5Al_2Si_3O_{10}(OH)_8} + \underset{\text{serpentine}}{Mg_3Si_2O_5(OH)_4} + \underset{\text{diopside}}{2CaMgSi_2O_6}$$

$$\underset{\text{plag}}{CaAl_2Si_2O_8} + \underset{\text{Cpx}}{CaMgSi_2O_6} + \underset{\text{olivine}}{4Mg_2SiO_4} + \underset{\text{Opx}}{MgSiO_3} \qquad (+6H_2O)$$

$$\underset{\text{spinel}}{MgAl_2O_4} + \underset{\text{Cpx}}{2CaMgSi_2O_6} + \underset{\text{olivine}}{2Mg_2SiO_4} + \underset{\text{Opx}}{3MgSiO_3} \qquad (+6H_2O)$$

$$\underset{\text{garnet}}{CaMg_2Al_2Si_3O_{12}} + \underset{\text{Cpx}}{CaMgSi_2O_6} + \underset{\text{olivine}}{3Mg_2SiO_4} + \underset{\text{Opx}}{MgSiO_3} \qquad (+6H_2O)$$

$$\underset{\text{Cpx}}{2CaMgSi_2O_6} + \underset{\text{olivine}}{3Mg_2SiO_4} + \underset{\text{Opx}}{3MgSiO_3} + \underset{\text{Tk}}{Al_2Mg_{-1}Si_{-1}} \qquad (+6H_2O)$$

Recast in terms of New Idria minerals, this composition is equivalent to a mixture of chlorite + serpentine + diopside. The composition corresponds to the open triangle symbol in **Figure 4.9**. This point falls within the pyroxenite (olivine websterite) field, and lies near the Hawaiian reference sample. **Figure 4.10** shows the equivalent mineralogical arrangements of this model composition expressed in terms of anhydrous mantle minerals. Whole rock reactions therefore relate the phase assemblages in successive lines. The equivalence of the anhydrous phase assemblages in **Figure 4.10** and the metamorphic reactions connecting them were demonstrated by Thompson using the concepts of modal space and reaction space (Thompson, 1991, 1982). At New Idria, there is no reason to prefer one of these upper mantle assemblages over another; for present purposes they will be considered equivalent. In other words, the conclusions drawn here do not depend on the starting mantle mineralogy.

4. Component Reactions

Chapter 3 showed how the serpentinization of dunites and harzburgites results in a mixture of serpentine + brucite as the low-temperature assemblage. The modal proportions of serpentine and brucite are determined by the modal proportions of olivine and Opx in the parent rock, i.e. by the Mg/Si ratio. This traditional, simplistic model of serpentinization is limited by the MSH model system.

a. Conservation of Al

While a serpentine phase is produced during hydration of these rocks, chlorite appears as the characteristic aluminous phase; chlorite is apparently stable relative to aluminous serpentine. The reaction that relates lizardite to chlorite involves the Tschermak substitution:

$$2Mg_3Si_2O_5(OH)_4 + Al_2Mg_{-1}Si_{-1} = Mg_5Al_2Si_3O_{10}(OH)_8$$

lizardite Tk clinochlore

O'Hanley et al. (1989) briefly considered the issue of Al partitioning between aluminous lizardite and clinochlore but did not resolve the relative roles of these minerals during serpentinization. The relative stabilities of the 7Å phases such as aluminous serpentine and amesite versus the 14Å chlorites are not well understood. Recently Bailey[1] et al. (1995) described dozyite, a 1:1 regular interstratification of serpentine and chlorite.

The component reaction relating plagioclase and chlorite in CMASH is straightforward:

$$CaAl_2Si_2O_8 + 3Mg_2SiO_4 + 4H_2O = Mg_5Al_2Si_3O_{10}(OH)_8 + CaMgSi_2O_6$$

anorthite forsterite chlorite diopside

This reaction shows that, in the presence of olivine and water, the aluminum in plagioclase is conserved as the aluminum in chlorite. Note also that this reaction has diopside as a product, resulting in an *increase* of modal pyroxene during hydration! However, serpentinization of Opx will decrease modal pyroxene, so that the abundance of total pyroxene in the hydrated rock will depend on the Cpx/Opx ratio in the anhydrous assemblage.

Spinel or pyrope garnet may be related to chlorite with analogous reactions in which aluminum is conserved.

[1] This paper was published posthumously; Sturges Bailey passed away November 30, 1994.

Figure 4.11 - Univariant reactions in a portion of the CMASH system relevant to serpentinized peridotites and pyroxenites. Note that chlorite coexists with all of the low-temperature assemblages. Tremolite appears and diopside disappears at low amphibolite grade. Complex reactions at upper amphibolite grade omitted - see Evans (1977) for further details.. Calculations using TWQ2S code of Berman (1991).

Figure 4.11 - Univariant Curves in the CMASH System

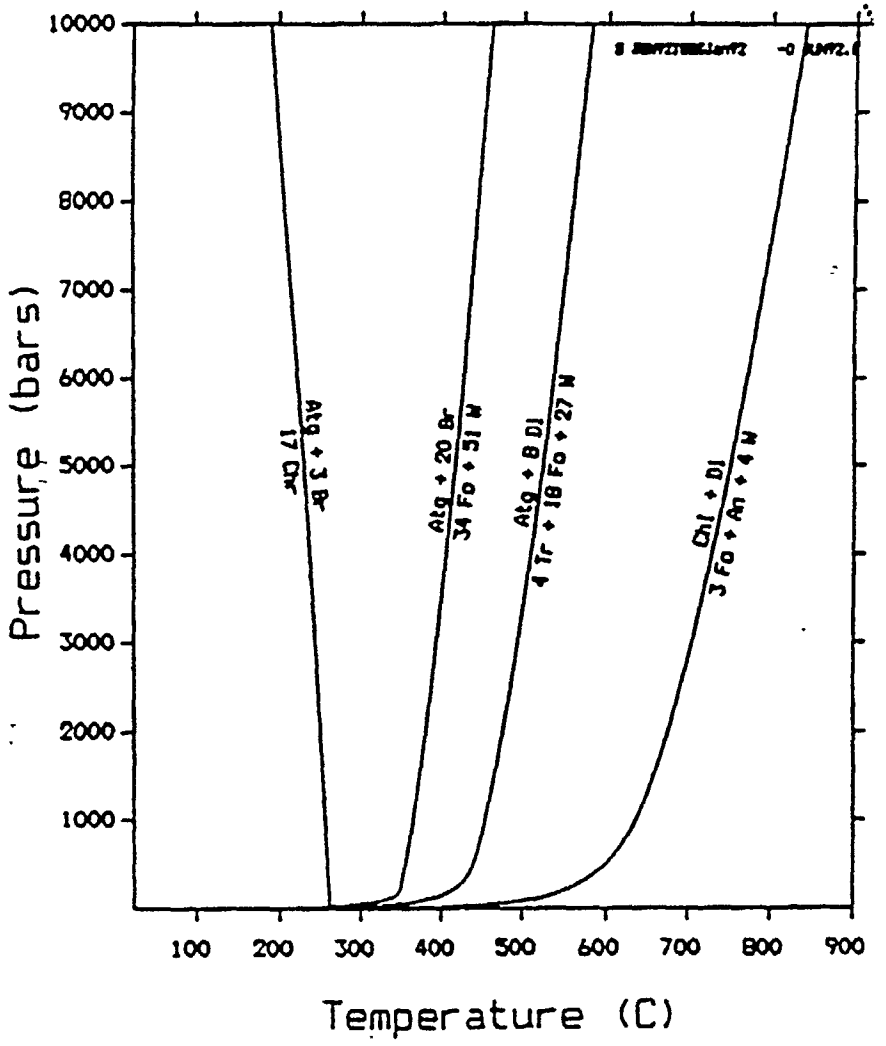

Figure 4.11 shows some of the key metamorphic reactions in CMASH involving serpentine, chlorite, and the accompanying calcic minerals. In this figure, chlorite is stable over nearly the entire diagram; its breakdown reactions at high temperatures have been omitted. According to Trommsdorff & Evans (1974), chlorite undergoes a continuous reaction at upper amphibolite grade during Alpine-style metamorphism, producing green spinel. Breakdown curves for dissociation of chlorite at high temperatures have been also been investigated experimentally by Cho & Fawcett (1986), Jenkins & Chernosky, (1986) and Staudigel & Schreyer (1977). Some experiments have produced cordierite as a product of chlorite breakdown, but cordierite is only found in metamorphosed ultramafic rocks under high-temperature low-pressure conditions. The New Idria rocks have not experienced high grade metamorphism; the rocks have remained well within the stability field of chlorite.

b. The Role of Ca

During low temperature hydration of fertile ultramafic rocks, diopside appears as the characteristic calcic phase, because there are no calcic chlorites. It is at first surprising that diopside, not tremolite is the stable low temperature product of the hydration of fertile ultramafic rocks. This behavior distinguishes diopside in ultramafic compositions from diopside in siliceous dolomites. **Figure 4.11** shows that tremolite forms by prograde metamorphism of diopside + antigorite at temperatures in excess of 400°C. Evans & Trommsdorff (1970) showed in chemographic form the mineral assemblages encountered by progressive metamorphism of rocks of this bulk composition. At high temperatures tremolite breaks down and diopside reappears. Thus in this bulk composition diopside has not one but *two* stability fields. Although a full discussion of the stabilities of these minerals is beyond the scope of this study, it is relevant that the stability of tremolite at low

temperatures is enhanced by a high activity of CO_2 in the metamorphic fluids - at New Idria the serpentinizing fluids were probably low in CO_2, as was shown in Chapter 3.

Another important observation is that Ca is frequently lost to the rock body during serpentinization, so that the bulk composition of the serpentinite is lower in Ca than the precursor ultramafic rocks. The Ca is contained in aqueous fluids; the fluids associated with active serpentinization have high pH and are generally saturated or supersaturated with respect to $Ca(OH)_2$ (Coleman, 1977; Barnes & O'Neil, 1972). On the other hand, streamwaters draining completely serpentinized bodies such as New Idria are low in Ca; instead they are enriched in Mg^{2+} and HCO_3^- (ibid).

c. The Roles of Fe and Ti

Thus far we have focused on the rock forming minerals and used CMASH as a model system. Consideration of metamorphic Ti-garnet and magnetite requires us to include Fe and Ti in the discussion, and thus expand our model system to CFTMASH. Chapter 3 discussed the stability of magnetite during serpentinization. The formation of andradite garnet is probably due to component reactions involving the hedenbergite component of Cpx (Taylor & Liou, 1978):

$$9CaFeSi_2O_6 + 2O_2 = 3Ca_3Fe_2Si_3O_{12} + Fe_3O_4 + 9SiO_2$$

or

$$9CaFeSi_2O_6 + 4H_2O = 3Ca_3Fe_2Si_3O_{12} + Fe_3O_4 + 9SiO_2 + 4H_2$$

Hd Adr Mag

In these reactions the SiO_2 component does not appear as free quartz; rather, its effect is equivalent to a decrease in the Ol/Opx ratio and a change in the amounts of modal chlorite, serpentine and brucite produced during serpentinization. As noted in Chapter 3, the presence of awaruite (FeNi) and other phases characteristic of relatively reducing conditions demonstrates that serpentinization may occur at very low oxygen fugacities. Peretti et al. (1992) demonstrated that andradite garnet occurs in serpentinites in conjunction with these reduced phases. The formation of Ti-garnet probably occurs in reactions similar to those above, in which a Ti component of the precursor Cpx, (expressed as the exchange vector $TiFe_{-1}$), enters the garnet phase. See Chapter 5 for a discussion of Ti-garnets and the exchange vector $TiFe_{-1}$.

$$9CaFeSi_2O_6 + 3TiFe_{-1} + 4H_2O = 3Ca_3TiFeSi_3O_{12} + Fe_3O_4 + 9SiO_2 + 4H_2$$

Hd Ti-Adr

I. Serpentinization of Fertile Rocks

Traditional discussions of serpentinization imply, without generally stating, that the starting material was a mixture of olivine and Opx, i.e. a dunite or a harzburgite. The reactions usually written are expressed in MSH. This simplification is justified, because the majority of exposed serpentinites world-wide appear to be hydrated dunites and harzburgites. However, ultramafic rocks in nature frequently have more complex, fertile compositions, and so a more general view of serpentinization is needed. The hydration of fertile lherzolites and pyroxenites is more complex than that of their depleted cousins because of the presence of the elements Ca and Al. As before, Fe and Ti may initially be ignored. The addition of CO_2 as a component in the serpentinizing fluids would affect the phase relations discussed here, mainly by the addition of magnesite, and changes in the stability

fields of talc and tremolite. A full discussion of the effects of CO_2 in serpentinizing fluids is beyond the scope of this discussion; the reader is referred to Sanford (1981).

For bulk compositions that can be expressed as points within the triangles of **Figure 4.9** or **Figure 3.3**, i.e. a mixture of Ol + Opx + Cpx with minor Spl, the low-temperature hydrated equivalent can be represented by a point in the tetrahedron brucite-talc-diopside-clinochlore, (Brc-Tlc-Di-Chl) as shown in **Figure 4.12a**. Only compositions more silicic than a 1:1 ratio of Ol:Opx will plot to the right of the shaded plane Ctl-Di-Chl in **Figure 4.12a**. Such compositions will have talc and possibly tremolite as part of their low-temperature assemblage; as noted in Chapter 3, such compositions are extremely rare: they include olivine orthopyroxenites, orthopyroxenites, and websterites. More typical serpentinized peridotites and pyroxenites, however, will lie in the reduced tetrahedron brucite-chrysotile-chlorite-diopside. At New Idria, the depleted rocks are a mixture of chrysotile and brucite; they lie on the basal edge of the tetrahedron. The chlorite-diopside-garnet rocks lie inside the reduced tetrahedron close to the Di-Chl join.

Ca loss during serpentinization would cause the bulk composition to migrate away from the diopside vertex but remain inside the tetrahedron. The presence of CO_2 in the serpentinizing fluids will result in the low-temperature assemblage talc + magnesite instead of serpentine. Talc and diopside do not coexist at low temperatures, but are replaced by tremolite, as discussed in Chapter 3. The resulting phase assemblage of Chl + Tr + Tlc + Mgs lies in the shaded plane Tlc-Tr-Chl of **Figure 4.12a**, provided that the figure is redefined so as to project from Mgs.

As a general rule, Fe and Mg follow separate geochemical pathways during hydration of fertile mantle rocks; Ti partitions into andradite garnet. The minerals in the hydrated assemblage accommodate Fe and Mg to different degrees, resulting in a greater *number* of

Figure 4.12a - Phase relations in the system brucite-diopside-talc-chlorite at 200°C, 1 kb, projected through water. Compositions with Ol-Opx ratio > 1 lie behind shaded plane passing through Ctl-Di-Chl. Compositions with Ol-Opx ratio < 1 may contain Tr as part of low -T assemblage, indicated by smaller shaded plane Ctl-Tr-Chl. Abbreviations are Ctl:chrysotile, Brc:brucite, Di:diopside, Tlc:talc, Chl:chlorite, Tr:tremolite.

Figure 4.12a - Phase Relations in the System Brc-Tlc-Chl-Di

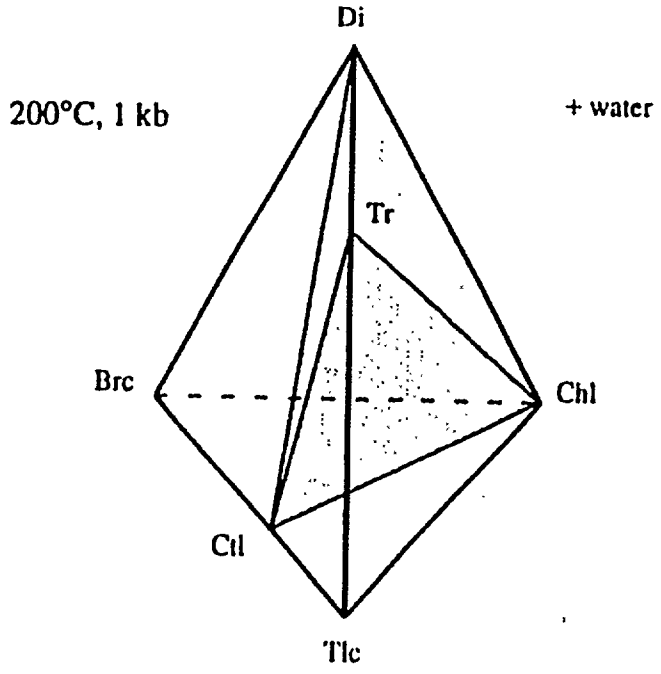

Figure 4.12b - Major element partitioning during serpentinization of fertile peridotites and pyroxenites. Chlorite is the characteristic aluminous phase when Al-exchange capacity of lizardite is exceeded (see text).

Figure 4.12b - Major Element Partitioning During Serpentinization

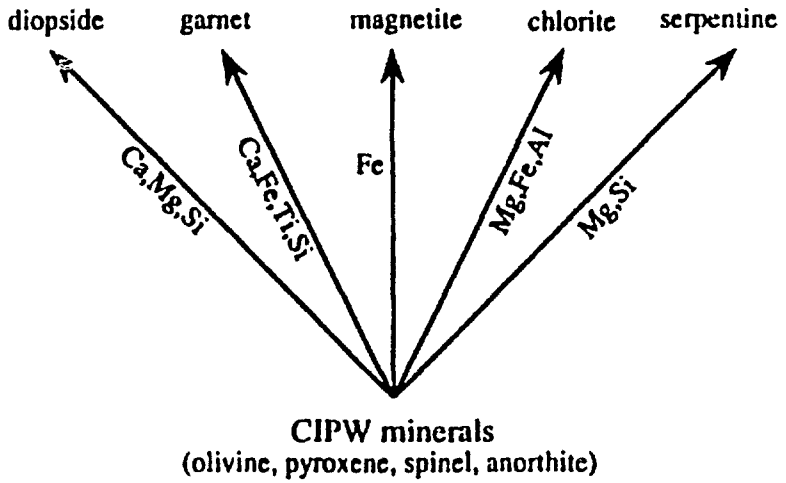

Figure 4.12c - Prograde metamorphism in a portion of CMASH. Topological changes in phase relations correspond to univariant reactions in Figure 4.11. Abbreviations as in Figure 4.11.

Figure 4.12c - Prograde Metamorphism in a Portion of CMASH

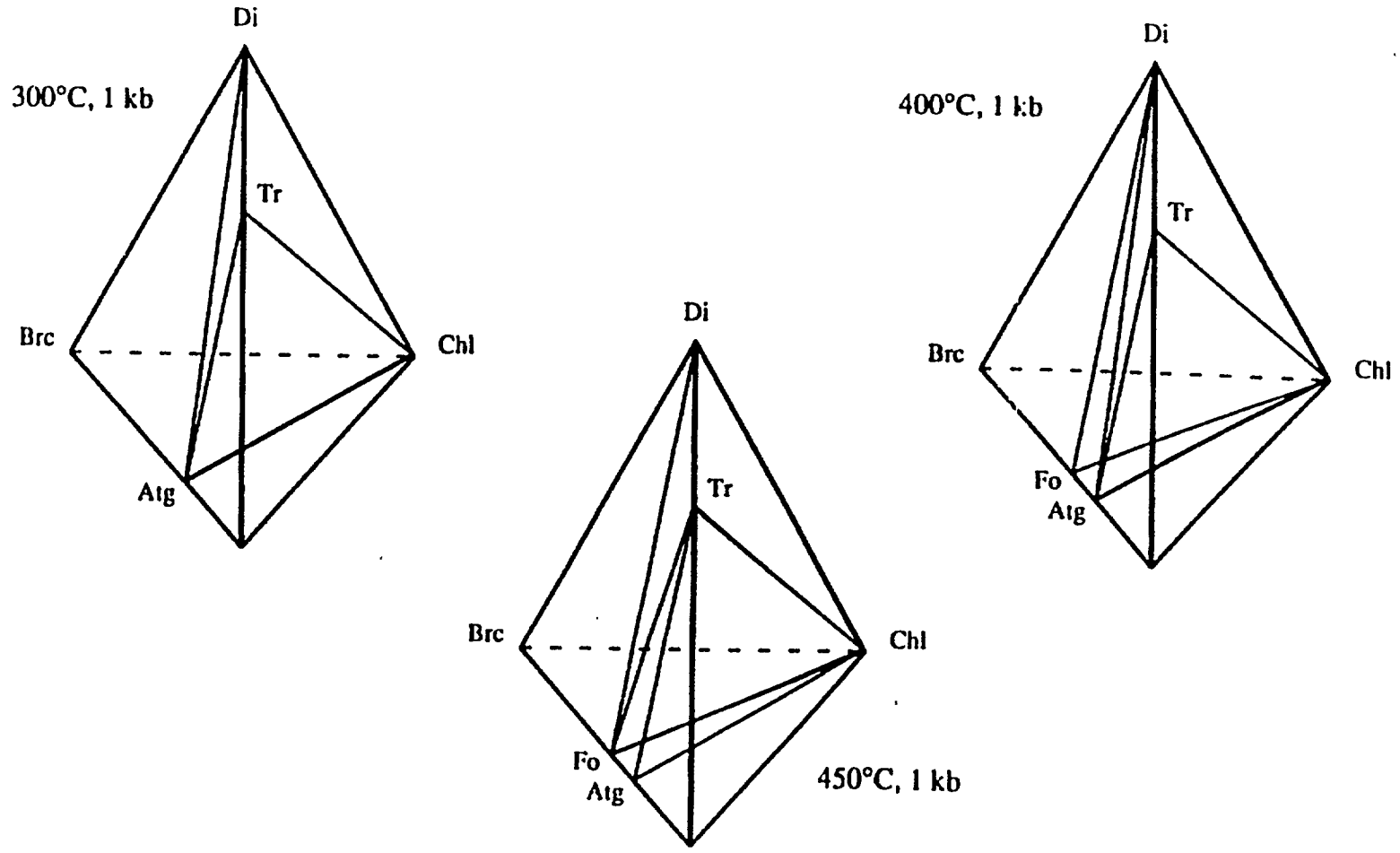

minerals. This greater number in turn reduces the thermodynamic variance of the assemblage according to the phase rule, when compared with the anhydrous assemblage. The forsterite component of olivine, the enstatite component of Opx and the diopside component of Cpx reappear in the hydrated assemblage in the form of chlorite, serpentine ± brucite and diopside. The fayalite component of olivine, the ferrosilite component of Opx and the hedenbergite component of Cpx reappear in the hydrated assemblage as chlorite, andradite garnet, magnetite and possibly brucite.

Because the distribution coefficients for the elements in the hydrated assemblage differ from those in the anhydrous assemblage, element redistribution takes place during serpentinization. This partitioning is summarized in **Figure 4.12b**. This figure shows in schematic form the chemical pathways for major elements and Ti. The modal abundance of the hydrous product phases depends on the exchange capacity (e.g. for Tk) of the hydrous minerals, and on the starting composition.

Prograde metamorphism of the low temperature phase assemblages of **Figure 4.12a** produces a series of reactions that change the topology within the tetrahedron. These reactions are shown in **Figure 4.11** and in the topological changes in **Figure 4.12c**. A more extended discussion of prograde metamorphism of alpine serpentinites is contained in Evans (1977) and in earlier papers by Evans and Trommsdorff. One of the important conclusions of this study is that the work of Trommsdorff and Evans in the Alps is also applicable to the evolution of the New Idria Serpentinite.

I. Temperatures of M1 and M2 Metamorphism

The above discussion using model systems shows that the phase assemblage chlorite + diopside + Ti-garnet ± magnetite can be derived from the low-temperature hydration of an

ultramafic precursor of pyroxenite composition. This event is defined as the M1 event. The phase assemblages found at New Idria suggest that greenschist or blueschist facies conditions accompanied this event. The blocks containing these phases are enclosed within chrysotile-lizardite host rock, which is also stable under low greenschist and blueschist conditions. Chlorite compositions discussed earlier (see **Figure 4.8**) show that the M1 event represents a higher metamorphic grade than the M2.

Since the M2 mineralogy is the same as the M1, the phase assemblage must have been stable under the conditions of M1 and M2. In an effort to learn more about the conditions of M2 metamorphism, a fluid inclusion study was undertaken, using fluid inclusions in M2 garnets. The results of the study were that homogenization temperatures averaged 235°C, suggesting that trapping temperatures during M2 metamorphism were below 400°C, well within the greenschist facies. Details of this study are described below in Section VI.

J. About Rodingites

The chlorite-diopside-garnet rocks at New Idria bear a superficial resemblance to a coarse grained rock type known as rodingite. Rodingites are metasomatic calc-silicate rock bodies associated with certain serpentinites, such as the one at Belvidere Mt., Vermont. The characteristic minerals of rodingites are hydrogrossular, idocrase, diopside, and chlorite.

Rodingites were first described at exposures along the Roding River in the Dun Mt. ultramafic complex, New Zealand (Bell et al.,1911). Mafic dikes were intruded into the ultramafite prior to serpentinization, so that when serpentinization occurred, chemical potential gradients and incompatible mineral assemblages provided the driving force for metasomatic exchange of Ca (out of the ultramafite) and Si (into the ultramafite), producing

the characteristic suite of calc-silicate minerals. The term rodingite has since been used more generally (e.g. Coleman, 1977) to describe metasomatic rinds that form during serpentinization, by reactions either with intrusive dikes or siliceous country rock.

Figure 4.13 shows on an ACF diagram the bulk compositions of chlorite-diopside-garnet rock from **Table 4.6** compared with the rodingite field from Coleman (1977). While the New Idria rocks plot near a tie line between chlorite and diopside, the rodingite field sits astride the grossular-diopside join.

The chlorite-diopside-garnet rocks of New Idria did not form as rodingites because the bulk composition of both the metapyroxenite blocks and the enclosing serpentinite were *both* silica-poor. Chlorite, diopside and titaniferous andradite garnets are all stable phases in association with serpentine minerals. There is no regional scale rodingite rind at the boundary of the New Idria Serpentinite because the emplacement into the country rock postdated serpentinization.

One possible exception to this conclusion is the small rock body of locality 990-1 (see **Figure 1.3**), at which the rock contains both vesuvianite and grossular garnet, the characteristic rodingite minerals. The bulk composition of this outcrop is unknown, but could lie in the rodingite field.

K. Chlorite-Diopside-Garnet Rocks from Other Localities

Chlorite-diopside-Ti garnet rocks are not abundant on land; pyroxenites are seldom exposed at the earth's surface and their metamorphic products, chlorite-diopside-garnet rock, weather and erode rapidly. In Val Malenco, Italy, however, chlorite-diopside-garnet rocks with mineral compositions similar to those of New Idria are found in altered

pyroxenite blocks contained in the Malenco serpentinite (Müntener, & Hermann, 1994). This serpentinite, one of the alpine ophiolites, lies structurally below the Austroalpine Margna nappe and above the Penninic Suretta nappe, and is one of the largest exposed serpentinites in the Alps.

The Ti-rich melanite and schorlomite garnets were found first at the Forcella Fellaria locality, associated with a metamorphosed clinopyroxenite layer. However, field work in the summer of 1994 uncovered several other similar localities in the Malenco serpentinite (Müntener, 1994, pers. comm.). Unlike at New Idria, the metapyroxenites at Malenco may turn out to be continuous enough to extract structural information about the serpentinite. Val Malenco is also widely known for the green *demantoid* variety of andradite garnet. These Ti-free garnets are widespread at Val Malenco, but are not associated with chlorite-diopside-garnet rocks. At New Idria, similar demantoid garnets are found at the Green Fire Mine and other localities. See Chapter 5 for a discussion of garnet compositions.

Two other occurrences of Ti-garnets are noteworthy: Switzer et al. (1971) describe Ti-garnets from serpentinized peridotites in the Mid-Atlantic Ridge near 43°N. The garnets are hosted by chlorite-diopside rock. The authors compared this discovery to the New Idria occurrence, which at the time was the only known example of this garnet paragenesis. The authors also speculated that, unless their dredge sample was extremely unusual, there may be much more chlorite-diopside-garnet rock in the submarine environment than previously realized. Still another interesting occurrence of Ti-garnet is in the Sangabawa District of Japan, described by Onuki et al., (1981). This metamorphic occurrence is in rock described as "olivine clinopyroxenite" that is included within a serpentinite in the paired metamorphic belts of Honshu.

Figure 4.13 - Bulk compositions of chlorite-diopside-garnet rocks compared with Rodingite field of Coleman (1977).

Figure 4.13 - Chlorite-Diopside-Garnet Rocks versus Rodingites

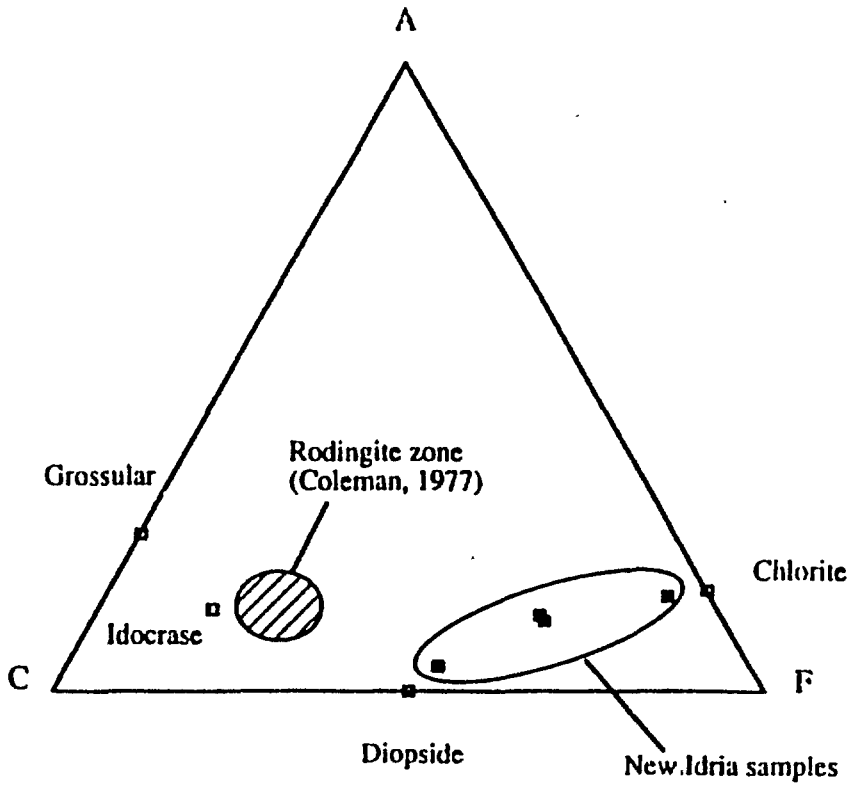

IV. Mafic Schists and Greenstones

A. General Statement

These blocks of grey-green to blue, massive to penetratively foliated mafic schists and greenstone are irregularly distributed throughout the New Idria Serpentinite. **Figure 4.14** shows the distribution of the larger blocks, here labelled simply "tectonic inclusions". Louderback & Blasdale (1909) and Coleman (1957) proposed that these blocks were Franciscan rocks entrained within the serpentinite during emplacement. The bulk compositions and mineralogies of the blocks are very similar to Franciscan rocks found throughout the Coast Ranges (e.g. Ernst, 1965). No blocks of Great Valley sandstones and shales have been found within the serpentinite. All of the blocks have sheared contacts and are relatively resistant to weathering, and are therefore ridge formers. The sizes of the blocks vary from kilometer scale to meter scale. The largest of these blocks forms the southwestern boundary of the oval serpentinite massif itself; this large marginal flake of Franciscan rock lies in fault contact with the serpentinite on one side and the younger Great Valley rocks on the other, as shown in **Figure 1.2.** Other marginal Franciscan blocks are found along the New Idria Thrust Fault which marks the northeastern margin of the serpentinite (**Plate 1.1**). Some physical mechanisms for emplacement of tectonic blocks in serpentinites were described by Barriga et al. (1992).

Table 4.7 compares representative bulk compositions of some of the tectonic blocks of mafic schist and greenstone from New Idria (columns 1-3) with Franciscan rocks (columns 4-6). The samples in columns 1-2 are from the Gem Mine locality described below; column 3 is from a jadeite-bearing locality in Clear Creek described by Coleman (1961). Examination of these analyses shows that all of these rocks are relatively high in silica and

soda compared with the the other types of tectonic blocks and with the bulk serpentinite. All of the analyses are also relatively low in alumina and lime; two are peralkaline with acmite in the norm. All of the analyses therefore would plot near the F vertex in a classical ACF diagram (not shown).

As with the other types of tectonic blocks, the mafic schists and greenstones have experienced at least one episode of pre-entrainment M1 metamorphism. M2 metamorphism is manifest by mineralized veins that crosscut the M1 foliation.

B. Jadeite-bearing Blocks

Tectonic blocks of albite-crossite schist that contain jadeite are found in the Clear Creek Valley at the northern end of the District. The blocks are easily found at a distance by looking for the oak trees which they support, in contrast to the digger pines of surrounding serpentine soils. Coleman (1961) described the mineralogy and petrology of these mafic schists. He interpreted these blocks as desilicated keratophyres (Na-rich silicic volcanics) of the Franciscan Formation. Some of the blocks contain white, near end-member jadeite in pods and in crosscutting veins. The jadeite formed in veins that crosscut the M1 foliation, but it is difficult to say whether the jadeite formed pre- or post-entrainment of the blocks. Coleman developed a model for the origin of jadeite at low temperature and moderate pressure.

The effect of M2 metamorphism on these jadeite-bearing blocks is manifest in the development of late stage zeolites and pectolite in the veins and pods. The reader is referred to Coleman (1961) for further details on the development of jadeite in the tectonic blocks of the Clear Creek Valley.

Figure 4.14 - Distribution of some tectonic blocks in the New Idria Serpentinite Modified from Eckel & Myers (1946), Coleman (1961).

Figure 4.14 - Tectonic Inclusions in the New Idria Serpentinite

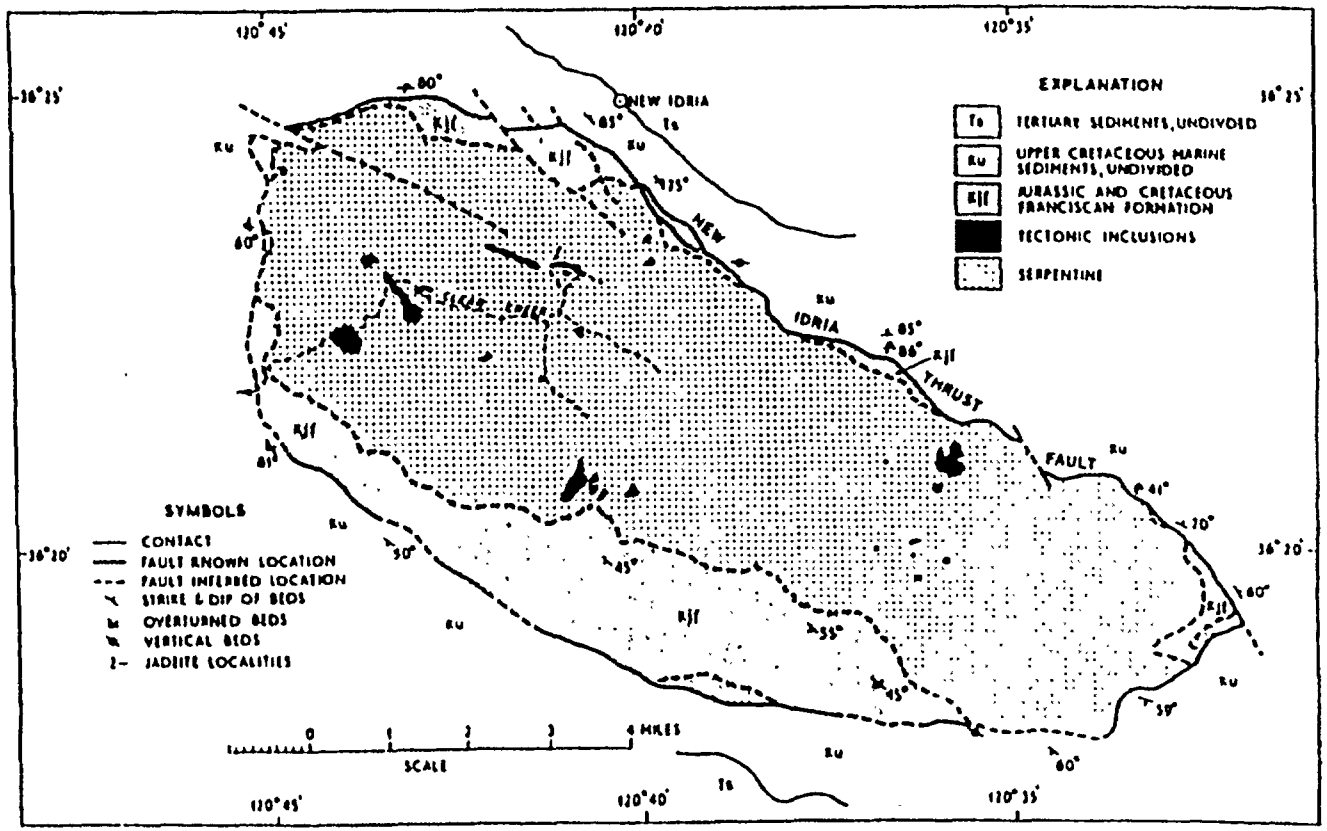

Geology from Eckel & Myers, 1946, Coleman, 1961, This study

Table 4.7 and Table 8 in Coleman (1961) show that, as a group, the jadeite-bearing blocks have low Ti contents, averaging 0.5 wt. % TiO_2. This geochemical characteristic is used to distinguish these blocks from those with more normal Franciscan values of 1-3 wt. % described next.

C. Blocks Containing Benitoite, Neptunite, and Joaquinite

Blocks of mafic schist and greenstone that contain up to 2 wt. % TiO_2 are exposed in the vicinity of the Gem Mine in the southern part of the District, at the Victor Claim in the Clear Creek Valley, and on the east summit of Santa Rita Peak. The blocks of mafic schist contain blue amphiboles (crossite, glaucophane) and are compositionally similar to Franciscan blueschists; they are interpreted as altered blueschists. Blocks of greenstone contain albite, chlorite, and non-jadeitic pyroxene; they are interpreted as Franciscan metagreywackes and metavolcanics. Mineralized M2 veins crosscut the M1 foliation of the mafic schists.

1. The Gem Mine

The Gem Mine is located near the headwaters of the San Benito River on the western flank of Santa Rita Peak. The coordinates are 36°19.90' N, 120°36.71' W. The open cut mine is reached by one of several poorly maintained roads that may require four wheel drive vehicles, especially in wet weather. The Gem Mine is a patented claim located on private property and permission from the owners is required in order to visit the mine. Mr. Elvis "Buzz" Gray of Missoula, Montana, and Mr. William Forrest of Fresno, California, control access to the property at this time. Wise & Gill (1977) reviewed the history and development of the Gem Mine, which has operated under several names, including

Benitoite Gem mine, Benitoite mine, Gem Mine, Dallas Benitoite mine, Dallas Gem mine and Sapphire mine.

This famous locality is best known as the site of the 1906 discovery of benitoite ($BaTiSi_3O_9$), a blue mineral that is now the state gemstone of California (Louderback & Blasdale, 1907). Neptunite ($Na_2KLi(Fe,Mg,Mn)_2Ti_2O_2Si_8O_{22}$, the second reported occurrence) and joaquinite ($Ba_2NaCe_2Fe(Ti,Nb)_2Si_8O_{26}(OH,F)\cdot H_2O$, a new mineral) from the mine were described along with benitoite by Louderback & Blasdale (1909). All of these minerals are strongly peralkaline. Laird & Albee (1972) discussed the composition and physical properties of benitoite, neptunite and joaquinite. Wise et al., (1977) described jonesite, another new mineral from this locality. Wise & Gill (1977) described the minerals of the Gem Mine and concurred with Coleman on their probable metasomatic origin. **Plate 4.10** shows in thin section the assemblage of benitoite and neptunite in a gangue of zeolite, primarily natrolite with minor thomsonite.

Figure 4.15 shows a sketch map and cross section of the Gem Mine, redrawn after Coleman (1957) and Wise & Gill (1977). The main feature of the map is an oval, northwest trending body of mafic schist and greenstone that is embedded in the surrounding serpentinite. This oval body contains two parts: greenstone to the north and mafic schist to the south. The mineralized zone lies in a brecciated zone along the contact between the two parts. The excavated working area of the Gem Mine lies in the mafic schist of the footwall, where veins and fractures contain the ore minerals. The greenstone of the hanging wall forms a 10 m. high cliff on the north side of the mine. Barren mafic schist forms a low cliff to the south. At the eastern end of the mafic schist body are some small, spheroidal bodies of altered gabbro that contain labradorite feldspar.

Plate 4.10 - Photomicrograph of sample 688-H from the Gem Mine, containing benitoite (high relief trigonal mineral) and neptunite (orange bladed mineral) in a gangue of polycrystalline natrolite. Crossed nicols. Field of view 2 mm.

Figure 4.15 - Geological map and cross section of Gem Mine, redrawn after Coleman (1957), Wise & Gill (1977).

Figure 4.15 - Geologic Map and Cross Section of the Gem Mine

Redrawn after Coleman (1957), Wise & Gill (1977)

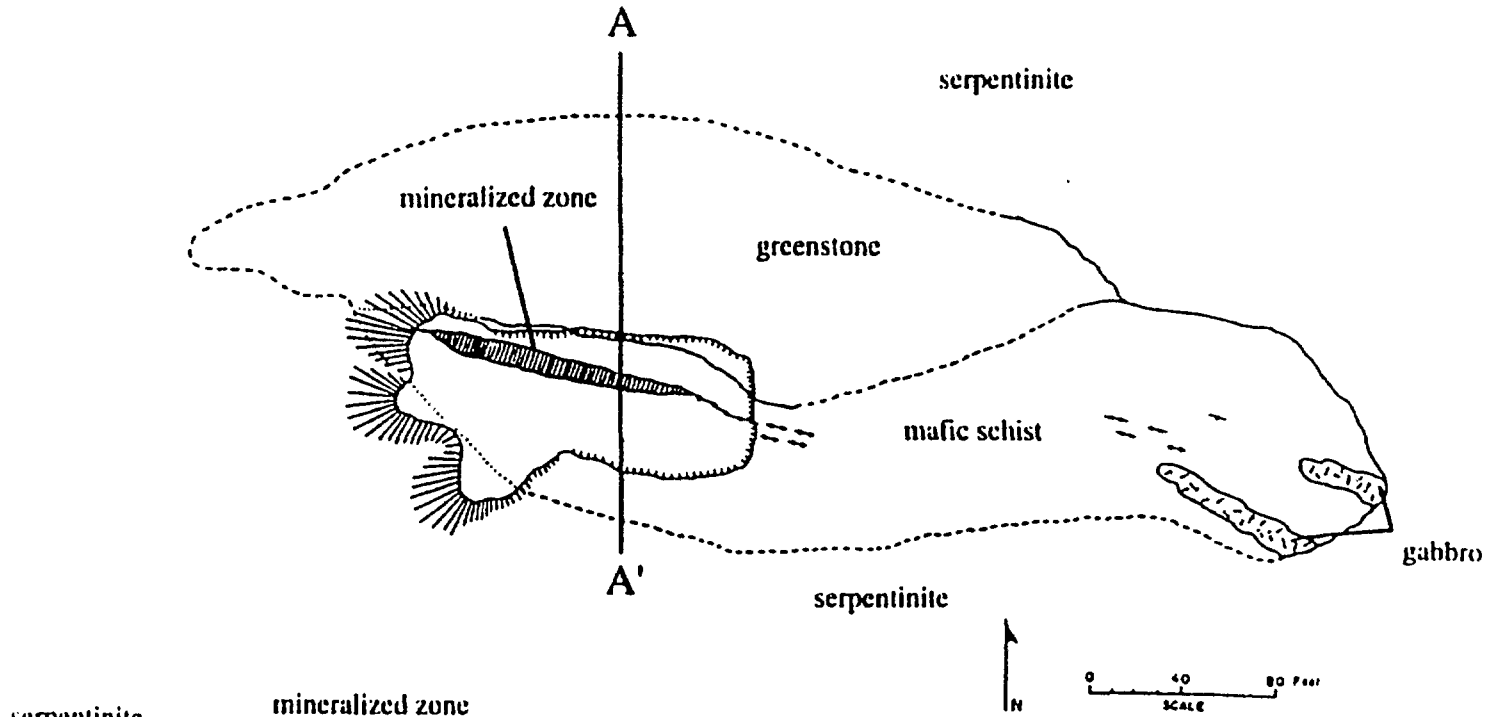

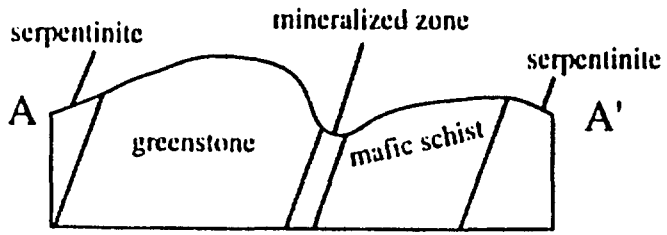

The original geologic relations at the Gem Mine have been largely obscured by decades of mining. For this reason, the original field descriptions by Louderback are of paramount importance. Louderback and Blasdale (1909) reported that the brecciated and mineralized zone was 520 ft. long and about 400 ft. wide in its widest part. Within that zone, the benitoite-bearing rocks were only 64 ft. wide and 400 ft. long, with the abundance of benitoite decreasing to the west. Benitoite was only found at the surface for 230 ft. of the 400 ft. Louderback also noted that the greenstone diminished in abundance to the west. The general nature of the mineralized zone was, from the center outward, drusy cavities containing benitoite, neptunite and natrolite deposited concurrently, next white, relatively pure natrolite, then bluish natrolite containing abundant amphibole needles, and finally the altered wall rock in which cavities filled with amphiboles in a felty texture suggested the leaching out of the feldspathic components of the wall rock. Outside the mineralized zone, albite rather than natrolite was the characteristic sodic aluminosilicate mineral.

Louderback also suggested that the mineralized zone was the locus of deformation and faulting, together with development of northwest striking foliation in the footwall blueschist. Post-mineralization transverse (i.e. northeast-trending) veins were also noted. Finally, he noted that brecciation of the serpentinite rock extended to the east of the mineralized zone, in the same direction. He gave the orientation of the outcrop as 300°, with a dip averaging 70°N.

As noted above, the greenstone and mafic schist at the Gem Mine are interpreted as Franciscan rock entrained within the serpentinite. A large block of Franciscan rock containing a contact between greenstone and mafic schist may have been caught up with the serpentinite during emplacement. Alternatively, a block of Franciscan greenstone and a block of Franciscan mafic schist may have been separately entrained but moved to their present adjacent positions by tectonic movements during ascent of the diapir. Relative

movement between the two blocks would help to explain the brecciated zone along the contact.

The greenstone of the hanging wall consists of two distinct types: the relationship between these types is obscure. The first type is a fine grained, massive, light brown-weathering, green granular rock composed of albite, chlorite, green pumpellyite, a non-sodic pyroxene, stilpnomelane, titanite (sphene), barite, and zircon. This greenstone is crosscut by veins containing albite and chlorite. Table 4.7 (column 1) contains a bulk analysis of this rock. The second greenstone is a massive, grey-weathering, dark green rock composed of albite, chlorite, a pyroxene near aegirine (acmite), stilpnomelane, and strongly corroded opaques. Limonite stains some of the albite orange. The bulk composition of this second greenstone was not determined in this study, but is probably higher in soda than the first greenstone, as suggested by sodic pyroxene. The second greenstone may also have a higher pressure M1 metamorphic history. Both greenstones are relatively resistant to weathering so that the northern portion of the Gem Mine claim is a positive weathering ridge on the western slope of Santa Rita Peak.

The altered mafic schist of the footwall, along the contact with greenstone, is a light to medium blue, brecciated rock containing actinolite, crossite, natrolite, albite, that is crosscut by zeolite veins (natrolite ± thomsonite) containing benitoite, neptunite, joaquinite, jonesite and several accessory minerals, including apatite, gypsum, a member of the zoisite group and several copper sulfides: djurleite (this study; Wise & Gill, 1977) digenite, covellite (Wise & Gill, 1977), and possibly chalcocite (Louderback & Blasdale, 1909). The copper sulfides are in turn surrounded with alteration haloes of chrysocolla. The productive zone of the mine is quite narrow, being restricted to the brecciated zone immediately adjacent to the contact. A 1914 photo at the Gem Mine (Bradley, 1938)

showed that there were underground workings starting from an adit, but presently all work takes place in the open cut.

The unaltered, barren mafic schist of the footwall is grey-blue, moderately resistant, massive to weakly foliated, actinolite-crossite-albite schist. In the more massive samples the actinolite occurs in randomly oriented blades and bundles, and is more abundant than crossite. In more foliated samples the amphiboles, especially crossite, take on a preferred orientation. Accessory stilpnomelane is present, together with unidentified opaques. Unaltered mafic schist (but not greenstone) crops out along the road that curves around the west end of the Gem Mine.

2. The Victor Claim

The Victor Claim consists of some weathered outcrops of mafic schist in and above an unnamed stream that forms a tributary to Clear Creek in the northern portion of the District. The coordinates are 36° 22.17' N, 120°42.22' W. The mineralogy of the Victor Claim was described by Millage (1982): small colorless grains of benitoite have been formed here, probably by reactions similar to the one below. Neptunite also occurs, but at much lower abundance than at the Gem Mine. As pointed out by Millage, the benitoite at Victor Claim is hosted in albite rather than natrolite. This may have been due to relatively lower activity of silica. Slight modifications to the benitoite-generating reaction proposed below would be required if albite were to be a product rather than a reactant.

During this study the Victor Claim was visited only once, and its mineralogy was not studied in detail. Whether Franciscan greenstone is present at the Victor Claim is unknown; Millage (1981) did not mention this rock type. The extent of hydrothermal wallrock alteration appeared to be much less than that at the Gem Mine. One notable

feature of the locality not mentioned by Millage was the occurrence of a nearby mercury mine. In general, the mercury mines at New Idria are found along the periphery of the serpentinite, not deep within the serpentinite as in this case. It is possible that the mercury mine and the Victor Claim both lie along a throughgoing fault that is suggested by the Jennings & Strand (1958) map The southerly continuation of this fault, that lies parallel to the New Idria Thrust Fault, also coincides with the linear array of syenite intrusives discussed in Chapter 1 (**Figure 1.2, Plate 1.1**). It is suggested here that this fault provided a conduit for circulating fluids during the M2 metamorphic event, and may have been responsible for the mineralization at the Victor Claim and and the adjacent mercury mine.

3. Other Benitoite Localities

There is another benitoite occurrence at an undisclosed locality within the New Idria Serpentinite, according to Wise & Gill (1977). Outside of the New Idria District, benitoite is extremely rare. Grains of benitoite have been found in drill cores elsewhere in California, in Eocene sands of Texas, and in Belgian sands (Roberts et al., 1990). If the mechanism proposed below for the formation of benitoite is correct, then there may well be additional undiscovered benitoite localities. A promising place to look would be in the vicinity of tectonic blocks in serpentinites, especially at a contact between two different tectonic blocks.

4. The Formation of Benitoite

One of the enduring mysteries of the New Idria District has been the origin of the rare mineral benitoite, $BaTiSi_3O_9$. Coleman (1957) hypothesized that benitoite formed by metasomatic alteration of the Franciscan rocks at the Gem Mine, as a result of fluids

associated with syenite intrusions 1 km or more distant. This hypothesis was analogous to that for the formation of chlorite-diopside-garnet rocks from ordinary serpentinite, as described in the previous section.

An alternative hypothesis is proposed here, that benitoite at the Gem Mine formed by metamorphism of the contact between the hanging wall greenstone and footwall mafic schist, in the presence of Na-rich, low silica fluids. Mineralized drusy cavities and extensive development of vein systems certainly suggest hydrothermal mineralization at the Gem Mine, but the chemical components needed to produce benitoite and probably the other exotic minerals are available in the adjacent wall rocks. Therefore there is no need to advect Ti, Al, and other components from a great distance. Ordinary brines associated with M2 metamorphism probably produced local mobility of the all the required chemical components of benitoite and other minerals. The pockets of felty amphiboles that are found throughout the brecciated zone and altered wall rock suggest that sodic feldspar was leached out of this rock and redeposited in the veins as natrolite ± thomsonite, with attendant loss of silica to the environment. Natrolite must have precipitated from a fluid with low silica activity. A hypothesis for origin of the hydrothermal fluids is described in Chapter 7.

By assuming the end member formulas for required minerals, we have the following simplified component reaction:

$$\text{barite} + \text{titanite} + \text{albite} + \text{chlorite} + H_2O =$$
$$\text{benitoite} + \text{actinolite} + \text{clinozoisite} + \text{natrolite} + SO_2(aq).$$

The actual whole rock reaction that took place in the presence of hydrothermal fluids is likely to be different that this reaction, particularly in the specific aqueous species present.

There is also no guarantee that the system was closed except for water. Extensive wall rock alteration in the mineralized zone suggests large volumes of fluid have passed through. However, all of the reactant phases in this equation are hanging wall phases; all of the product phases occur in the footwall. The above reaction is not unique: other similar reactions could be constructed, e.g. by substituting thomsonite for clinozoisite as a product. In all of these reactions, however, the Ba required to produce benitoite can be found in barite, a rather common mineral in Franciscan rocks. Likewise, the required Ti can be found in (titanite (sphene).

Louderback & Blasdale (1909) commented on the absence of barite or any other apparent source of barium in their original report. Only with the advent of the electron microprobe did it become possible to recognize the relatively abundant, micron-sized grains of this mineral. A mass balance of the Ba budget for these rocks shows that the abundance of benitoite is consistent with the abundance of barite in the surrounding rocks. **Table 4.7** shows the amount of Ba to be 100-200 ppm, which compares with 150 ppm in the Catalina greenstone. Assuming that all of the Ba is incorporated in benitoite after the above reaction, the amount of benitoite should be approximately 0.01 wt. % in the mineralized zone, or 1 part in 10,000. The actual amount of benitoite present is well under this amount. A similar mass balance of the Ti budget shows adequate titanium to account for abundance of the Ti-bearing minerals such as benitoite and neptunite.

The temperature and pressure of formation of benitoite are not well constrained. Millage (1982) suggested that the upper stability limit of benitoite is about 600°C. If benitoite and natrolite formed concurrently, then the conditions must have been within the stability field of natrolite, which is limited to about 250°C at 1 bar (Peacor, 1973). Wise & Gill (1977) argued that the presence of djurleite as a companion phase placed a constraint on the temperature of formation of benitoite. The upper limit of stability of djurleite is about 95°C.

However, as pointed out by Ulrich Petersen (pers. comm., 1992), the copper sulfide minerals readily recrystallize and invert to other forms with falling temperatures, unlike most silicates. This means that the crystals that are now djurleite could have originally formed as digenite or another high-temperature sulfide. Therefore, the implied constraint on the temperature of formation of benitoite at or below 100°C should not be considered a reliable limit. Fluid inclusion evidence from garnets in nearby tectonic blocks suggests that M2 metamorphism may have occurred at about 300°C; similar temperatures may have occurred at the Gem Mine at the same time.

5. The Formation of Neptunite

The veins that contain benitoite also contain neptunite, a rare peralkaline mineral associated with alkalic rocks. A simplified formula for neptunite is $Na_2KLi(Fe,Mg,Mn)_2Ti_2Si_8O_{24}$. Neptunite has both igneous and metamorphic parageneses. The New Idria occurrence is considered to be metamorphic, and is similar to an Australian occurrence of neptunite in a tectonic block included in the Woodsreef Serpentinite (Slansky & Glen, 1982). Neptunite is hosted by albite, rather than natrolite, in the Australian occurrence.

At New Idria, textural relations suggest that benitoite, neptunite and natrolite crystallized at the same time. The abundance of neptunite is everywhere greater than that of benitoite. Neptunite probably is produced by a reaction similar to that for benitoite formation, that involves hanging wall and footwall phases. Neptunite contains potash as an essential constituent and Mn as a significant impurity. Bulk analyses of the wall rock (Table 4.7) show sufficient K and Mn to account for the amount of neptunite present.

6. The Ages of Benitoite and Neptunite

In an effort to understand the timing of M2 metamorphism at New Idria, a reconnaissance study of the age of crystallization of the benitoite-neptunite crystals was undertaken. The minerals are assumed to have crystallized simultaneously. Using Rb/Sr dating techniques on samples from this study, Marvin Lanphere of the USGS constructed a two-point isochron of a mineral pair, yielding an age of 11.96 Ma. With a two point isochron no reliable error estimate is possible, so the benitoite-neptunite age should be considered preliminary. A further attempt to date the neptunite crystals using $^{40}Ar/^{39}Ar$ technique is currently underway. However, this preliminary age agrees well with the 12.4 ±0.8 Ma age of the New Idria Syenite, mentioned in Chapter 1. The interpretation of this Miocene age of mineralization is discussed in Chapter 7.

7. The Formation of Natrolite

The abundance of natrolite as a gangue mineral at the Gem Mine is much greater than any of the exotic Ti-bearing minerals. Natrolite can form at relatively low temperatures by hydration of albite in a low silica environment, i.e.

$$2\cdot\text{albite} + 8H_2O = \text{natrolite} + 3SiO_2(aq)$$

The excess silica is readily absorbed by the surrounding serpentinite and does not appear as free quartz. This reaction probably accounts for the natrolite veins found on the east summit of Santa Rita Peak, which is another tectonic block of mafic schist. Benitoite has not been found at this locality, although Coleman (1957) reported joaquinite.

V. Antigorite Knockers

A. General Statement

Resistant knobs or knockers of red-weathering, dark green rock stand in high relief against the crumbly rock which otherwise characterizes the District. These knobs consist almost entirely of dense, tough antigorite with a sugary texture. Prominent examples occur on the main (west) summit of Santa Rita Peak, on the west side of San Carlos Peak, and on the top of Perovskite Knob. The antigorite knobs may be sheared or mylonitized as at Santa Rita Peak, with recrystallization of antigorite within the mylonite zone. Where exposed, the contacts of these blocks are strongly sheared. Some knobs are crosscut by veins of yellow andradite garnet, as at Santa Rita Peak and at San Carlos Peak. The knobs probably represent prograde metamorphism of pre-existing chrysotile and lizardite to form antigorite. Alternatively, they may record primary serpentinization of peridotite at a high temperature (see Chapter 3). In either case, these knobs have a thermal history separate in part from that of the bulk serpentinite, and must be older than the immediately surrounding serpentinite.

B. Santa Rita Peak

The summit of Santa Rita Peak (1574 m) is the most prominent topographic landmark in the New Idria District (**Plate 4.11**). The peak, unnamed at the time, was used as a geographic landmark by Arnold & Anderson (1908). Along with wooded San Benito Mt. 5 km. north, the summit of Santa Rita Peak forms the highest portion of the Diablo Range. Santa Rita Peak has two summits separated by a saddle; the craggy western summit is the higher of the two. A microwave communications tower maintained by Chevron Oil stands on the saddle; the gravel road to the tower is generally well graded and provides ready

access to the summit region. The upper slopes of Santa Rita Peak are treeless, due to recurring forest fires. Access to outcrops on the mountain is hindered only by occasionally dense chapparal. One of the few sources of potable water within the District, Agua Buena Spring, lies on the south slope of the peak.

The western summit of Santa Rita Peak is a large, resistant knob of red-weathering antigorite. The antigorite has a non-pseudomorphic, interpenetrating texture. This texture is typical of prograde serpentine - antigorite - replacing earlier lizardite and chrysotile (Wicks & Whittaker, 1977; Wicks & O'Hanley, 1988). The immediately adjacent rock, separated by sheared contacts, consists of the normal lizardite and chrysotile that characterize the District. Portions of the summit knob are sheared and mylonitized; shear planes strike 060° and dip 35SE, roughly perpendicular to the regional structure. Plate 4.12 shows this brecciated zone. Presence of antigorite in this block, together with its absence in adjacent rock, shows that the thermal history of Santa Rita Peak differs from the bulk serpentinite. Santa Rita Peak must be older than the adjacent serpentinite, and probably represents a remnant of an earlier serpentinization event. A stable isotope study of the antigorite block might help to clarify its relationship to the bulk serpentinite.

The antigorite is crosscut locally by veins of yellow M2 andradite garnet, and has a dark green, almost black color due to disseminated and locally comminuted particles of magnetite and chromite. The veins of yellow andradite garnet are known by their varietal name, topazolite; many garnets contain fluid inclusions. At Santa Rita Peak these garnets are not uniformly distributed through the rock, but are concentrated in a band a few meters above the mylonite zone.

The relationship and timing of the formation of the garnet veins to the development of the mylonite zone deserves study; both events postdate crystallization of the antigorite block

Plate 4.11 - Santa Rita Peak (1574 m.), with its blocky summit, dominates the southern portion of the New Idria landscape. The summit is a red-weathering antigorite knocker. Gem Mine visible as brown scar on lower slope of peak, KCAC Mine as large open pit area near left side of photo. Photo from Condon Peak.

Plate 4.12 - Antigorite mylonite zone at summit of Santa Rita Peak.

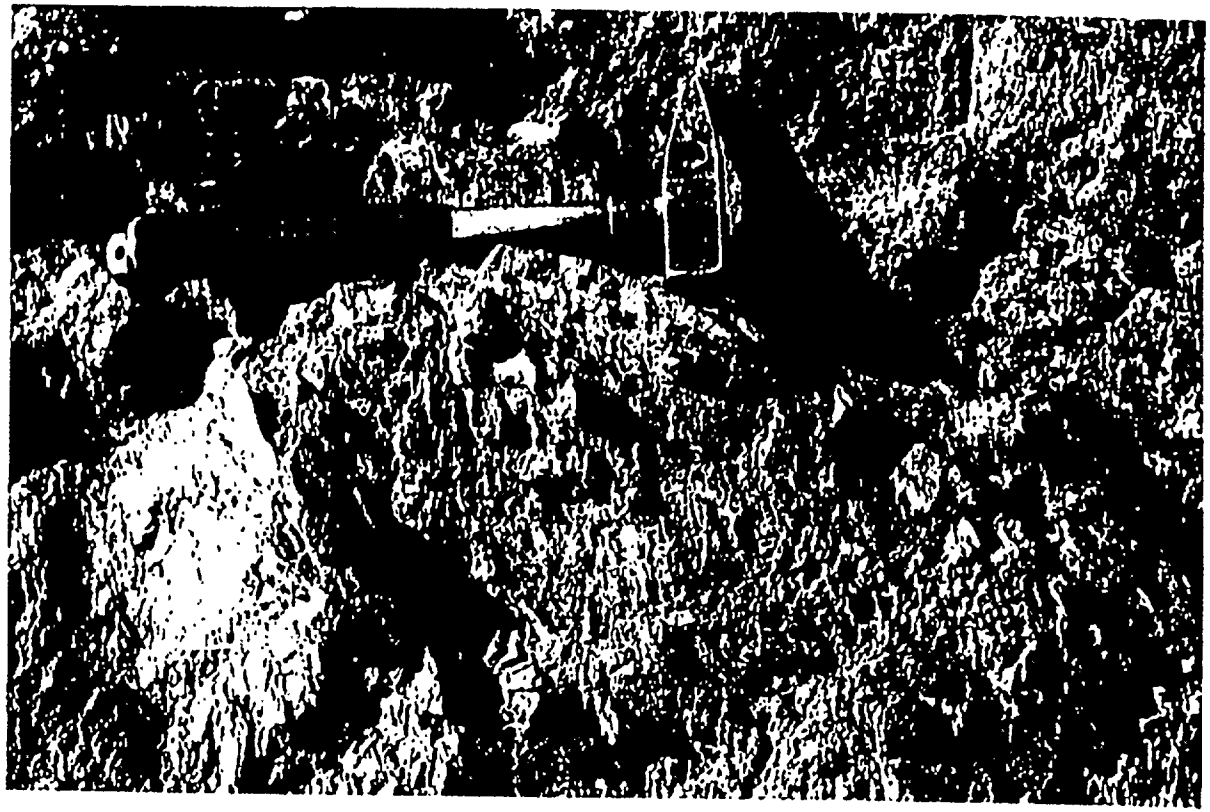

and are assigned to the M2 event. The author is indebted to David O'Hanley for pointing out the significance of this mylonite zone on a 1991 field trip.

Some of the chromite grains in the antigorite at Santa Rita Peak are surrounded by alteration haloes of kammererite that crosscut the antigorite fabric; this alteration is also assigned to the M2 event and is discussed in Chapter 3.

The eastern summit of Santa Rita Peak is held up by mafic schist crosscut by natrolite veins (see preceding section); this summit is interpreted as a separate tectonic block unrelated to the antigorite of the west summit.

C. San Carlos Peak

A prominent knob on the west side of San Carlos Peak in the northern part of the District has rock very similar to that of Santa Rita Peak: antigorite crosscut by veins of yellow garnet. It may be significant that both this knob and Santa Rita Peak lie close to the eastern margin of the serpentinite and the New Idria Thrust Fault.

D. Perovskite Knob

Perovskite Knob is described in the section on chlorite-diopside-garnet rocks (see Figure 4.4, 4.5). The summit of Perovskite Knob consists of massive antigorite, but without the veins of yellow garnet. There are also faint northeast-trending shear planes crosscutting the antigorite, that may represent a poorly developed mylonite zone. Perovskite Knob is here interpreted as an antigorite knob welded to a tectonic block of chlorite-diopside-garnet rock. This physical juxtaposition may be a clue to the origin of both types of tectonic block.

VI. Fluid Inclusion Constraints on M2 metamorphism

The garnets of Santa Rita Peak contain fluid inclusions of a type similar to those in garnets of the chlorite-diopside-garnet rocks described earlier. In an effort to learn more about the conditions of M2 metamorphism, a fluid inclusion study was undertaken.

Primary, pseudosecondary, and secondary fluid inclusions, as defined by Roedder (1984) are present. The inclusions are irregular in shape and vary from 5 to 30 μm. in size. The majority of the inclusions are in the 5-10μm range. The euhedral garnet crystals hosting these inclusions range in size from 1-10 mm; the anhedral vein-filling garnets occupy veins typically 5-10 mm in width. The size and abundance of fluid inclusions in the garnets correlate negatively with the Ti content of the garnets and positively with their Fe-content. Except for the smallest, inclusions are of the two-phase aqueous type; no daughter crystals were observed. No evidence for CO_2 in the inclusions was found, as expected from the experimental stability studies of low temperature andradites by Taylor and Liou (1978). Microthermometric measurements on 31 two-phase inclusions showed homogenization temperatures averaging 255°C. Chapter 1 derived an upper limit of 3 kb for Miocene deuteric alteration of the New Idria syenite at the present erosion level. If this alteration occurred at the same time and at the same depth as the formation of M2 garnets, as proposed in Chapter 7, then the 3 kb upper limit also applies to the garnets. If the maximum pressure of M2 metamorphism was 3 kb, then the maximum inclusion trapping temperature was ≤ 400°C. Internal reflections and the dark color of Ti-bearing garnets in thin section made melting temperature measurements especially difficult, but measurements on large inclusions showed T_m (ice) = -3.5 to -2.0°C, indicating that the salinity was equivalent to 3-5 wt. % NaCl (Roedder, 1984).

Figure 4.16 - Fluid inclusion homogenization temperatures from M2 garnets. Mean is 235°C. See text for details.

Figure 4.16 - Fluid Inclusion Homogenization Temperatures

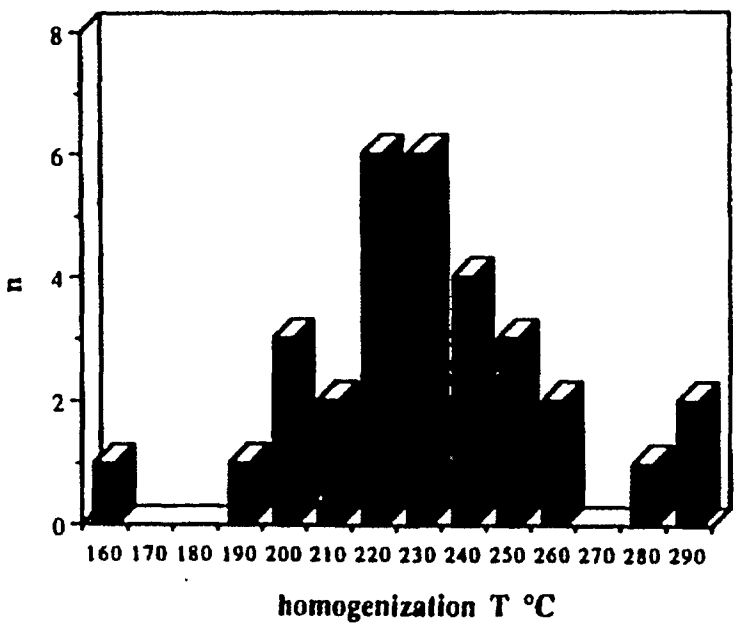

Figure 4.17 - Fluid inclusion temperatures of final melting from M2 garnets. Salinity equivalent to 3-5 wt.% NaCl.

Figure 4.17 - Fluid Inclusion Melting Temperatures

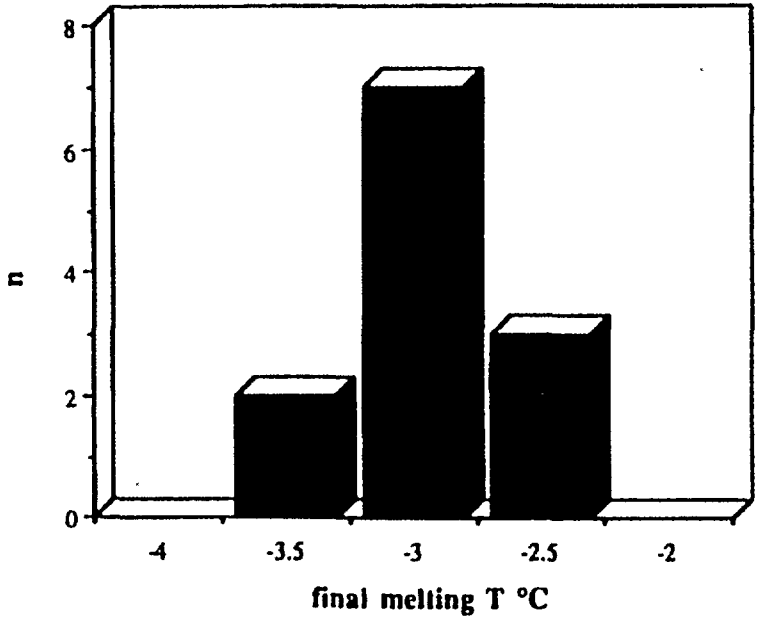

Except for one sample, no clathrate formation was observed. In this sample, from Santa Rita Peak, a reconnaissance study using Raman spectroscopy in the laboratory of Prof. Jill D. Pasteris, Washington University, showed the presence of a small amount of methane (approx 0.5 bars). Re-examination of this sample on the fluid inclusion stage showed the possibility of formation of methane clathrates. The significance of the presence of methane is unknown, but suggests that low oxygen fugacity prevailed during M2 metamorphism.

Figure 4.16 and **Figure 4.17** show histograms for homogenization and final melting temperatures respectively. The only phases in this study found to contain fluid inclusions were the M2 garnets, which occur as anhedral and euhedral vein filling crystals. At Santa Rita Peak the compositions of the garnets are near end-member andradite; in chlorite-diopside-garnet rocks the garnets are titaniferous andradites. There were no systematic differences in properties between the Santa Rita Peak garnets and those of the chlorite-diopside-garnet rocks. This similarity supports the proposal that M2 metamorphism affected the region with similar temperatures over a broad area.

VII. Conclusions

1. Three types of tectonic blocks are recognized in the New Idria Serpentinite: chlorite-diopside-garnet rocks, mafic schists, and antigorite knockers.

2. All types of tectonic blocks show evidence of two metamorphic events, here defined as M1 and M2. M1 metamorphism is associated with the development of penetrative foliation in the chlorite-diopside-garnet rocks and the mafic schists, and the interpenetrating fabric of the antigorite blocks. Some of the M1 metamorphism must have been of the high-pressure blueschist type. M1 metamorphism occurred prior to entrainment

of the blocks, and may have been a multi-stage event. M2 metamorphism is post-entrainment of the blocks and is associated with the development of tension cracks and veins that crosscut the M1 foliation in chlorite-diopside-garnet blocks and mafic schists, and with crosscutting garnet veins in the antigorite knockers.

3. The 34-50 locality consists of four rock towers each 2 m. high. Each tower is capped by dark green, sheared but relatively resistant serpentine, under which lies a slab of light green to white, chlorite-diopside-garnet rock dipping gently to the east. The towers are apparently the eroded remnants of a once-continuous slab of chlorite-diopside-garnet rock preserved under resistant serpentine cap rock.

4. M1 chlorite defines the foliation in the chlorite-rich central zone of 34-50. M1 chlorite in the outer, diopside-rich zones is more magnesian than chlorite from the central zone. M1 diopside is more magnesian than coexisting chlorite, in both central and outer zones. M1 garnet occurs in foliation-parallel veins and blebs.

5. At 34-50 shearing is manifest in the central zone by strong foliation of the dominant Fe-rich M1 chlorite, and in the outer zone by fracturing and recrystallization of M1 diopside. These observations show that the M1 metamorphism was synkinematic.

6. The M1 fabric at 34-50 is crosscut by veins interpreted as tension cracks. These veins are filled with M2 garnet, diopside, and minor chlorite. The M2 minerals in the veins have beautifully preserved delicate textures with no sign of post-mineralization deformation. Therefore the M2 mineralization was postkinematic.

7. The Perovskite Knob locality consists of resistant serpentine cap rock overlying a slab of chlorite-diopside-garnet rock that dips gently to the south. The summit of

Perovskite Knob consists of the same tough antigorite rock that is found at the summit of Santa Rita Peak.

8. In contrast to 34-50, the chlorite-diopside-garnet rock at Perovskite knob is only weakly foliated, determined by M1 chlorite. M2 chlorite is found in millimeter-sized euhedral crystals coating vein walls in places. M2 chlorite is more magnesian than M1 chlorite. M1 diopside is more magnesian than coexisting M1 chlorite.

9. The Melanite Mine locality consists of a 15 m. wide slab of chlorite-diopside-garnet rock bounded laterally by serpentine rock. There is no resistant cap rock and the exposure is poor.

10. M2 "cats eye" garnets in the lateral transition zone at the Melanite Mine show evidence for meter-scale Ti mobility. Cores of Ti-rich garnet overgrown by Ti-poor garnet are found only in the lateral transition zone. These are interpreted as the result of Ti-bearing fluids moving out of the Ti-rich chlorite-diopside-garnet rock into Ti-free serpentinite rock.

11. Bulk compositions of the chlorite-diopside-garnet rocks are different from the bulk serpentinite but are very similar to pyroxenites from other ultramafic rocks world-wide. The trace element concentrations for the chlorite-diopside-garnet rocks fall within the normal range for pyroxenites; both are different from a serpentinized harzburgite sample.

12. Using the "spinel norm" calculation the chlorite-diopside-garnet rocks are shown to be the metamorphosed equivalents of olivine websterites.

13. Low solubilities of Ti oxide minerals, lack of a well-developed vein system between chlorite-diopside-garnet blocks, lack of penetrative foliation in serpentine rock adjacent to foliated chlorite-rich rocks, and lack of apparent Ti-metasomatism at the margin of the igneous intrusives all argue against formation of chlorite-diopside-garnet rock by metasomatic alteration of ordinary serpentine rock by fluids from igneous intrusives.

14. Bulk compositional similarities, the observation of M1 and M2 metamorphism, rock textures, and existence of chlorite-diopside-garnet rocks from other localities argue for essentially isochemical metamorphism of blocks of pyroxenite to produce the chlorite-diopside-garnet rocks at New Idria.

15. It is possible that the metapyroxenite blocks are tectonic inclusions from an unknown source entrained within the serpentinite: tectonic inclusions of a variety of other rock types are present. It is also possible that the metapyroxenite blocks might be primary igneous features or even have a cognate origin with the depleted dunites and harzburgites. They may represent cumulate layers or crosscutting veins and dikes. The present random orientation of the blocks may well result from boudinage or other tectonic dismemberment of dikes followed by block rotation during the diapiric ascent of the New Idria Serpentinite.

16. An analysis using model systems shows that the phase assemblage chlorite + diopside + Ti-garnet ± magnetite can be derived from the low-temperature hydration of an ultramafic precursor of pyroxenite composition. The phase assemblages found at New Idria suggest that greenschist or blueschist facies conditions accompanied this hydration. The stability of this phase assemblage is at present the only control on the temperature of M1 metamorphism. However, comparison of M1 and M2 chlorite compositions shows that the M1 event was of higher metamorphic grade than the M2.

17. A study of fluid inclusions in M2 minerals showed that homogenization temperatures averaged 235°C, suggesting that trapping temperatures during M2 metamorphism were below 400°C. No quantitative pressure estimate was obtained from this study.

18. Models for serpentinization are frequently expressed in the MSH system. A more general model for serpentinization of fertile ultramafic rocks in the system CMASH and CFTMASH is proposed here. The resulting phases all lie inside the brucite-talc-diopside-chlorite tetrahedron. Ca is considered a mobile component during serpentinization; Al, Fe and Ti are conserved.

19. Chlorite-diopside-garnet rocks at New Idria are shown not to be Rodingites.

20. Chlorite + diopside + Ti-garnet rocks are now known from three localities outside the New Idria District: Val Malenco, Italy; Sangabawa District, Japan; Mid-Atlantic Ridge at 43°N. All parageneses are in serpentinized ultramafic rocks.

21. Greenstone and mafic schist at the Gem Mine are interpreted as Franciscan rock entrained within the serpentinite. The mineralized zone that contains benitoite lies along or near the contact between these two rock types.

22. It is here proposed that benitoite has formed by an essentially isochemical reaction involving barite, titanite, albite and chlorite as reactants and benitoite, actinolite, clinozoisite thomsonite and natrolite as products. Neptunite probably has formed by a similar reaction.

23. A preliminary determination of the age of benitoite and neptunite has been made using the Rb-Sr method and a two-point isochron. The age is estimated to be 11.96 Ma.

No error bar is available, however. This age should be compared with the age of the New Idria Syenite, 12.4 ± 0.8 Ma reported in Chapter 1. A further attempt to date neptunite crystals using $^{40}Ar/^{39}Ar$ technique is currently underway.

24. Knockers of dense, tough antigorite with a sugary texture form resistant, positive-weathering knobs in the District. These knockers may be sheared or mylonitized as at Santa Rita Peak, with recrystallization of antigorite within the mylonite zone. Locally, the knockers are crosscut by veins of M2 garnet that contain fluid inclusions. Some of the fluid inclusions contain methane. The knockers have a thermal history separate in part from that of the bulk serpentinite, and must be older than the immediately surrounding serpentinite.

Table 4.1 - Diopside compositions at 34-50 locality and Perovskite Knob									Note: Total Fe as FeO*	
Number ->	1	2	3	4	5	6	7	8	9	10
Sample ->	990-22.2	990-16.5	990-16.7	990-16.10	990-16.11	990-16.15	990-16.16	990-16.17	688-6	688-6
locality ->	34-50	34-50	34-50	34-50	34-50	34-50	34-50	34-50	PK	PK
SiO2	53.97	55.43	54.33	54.93	54.69	54.76	53.43	54.25	53.17	52.94
TiO2	0.01	0.02	0.01	0.02	0.01	0.04	0.03	0.02	0.00	0.02
Al2O3	0.28	0.41	1.12	0.40	0.33	0.60	1.83	0.64	0.49	0.53
Cr2O3	0.11	0.00	0.00	0.00	0.02	0.04	0.02	0.14	0.13	0.14
FeO*	3.50	2.53	2.38	2.24	2.52	2.95	2.78	2.36	5.10	5.28
MnO	0.30	0.10	0.07	0.11	0.09	0.18	0.12	0.11	0.84	0.82
MgO	16.17	17.20	16.45	17.02	17.35	17.04	16.52	17.03	15.75	15.52
CaO	25.15	25.01	24.49	24.03	24.68	24.46	24.51	24.14	24.64	24.49
Na2O	0.14	0.28	0.72	0.26	0.20	0.29	0.26	0.34	n.d.	n.d.
Total	99.63	100.98	99.57	99.01	99.89	100.36	99.50	99.03	100.12	99.74
Si	1.99	2.00	1.99	2.01	1.99	1.99	1.96	1.99	1.97	0.98
Ti	0.00	0.00	0.00	0.00	0.00	0.00	0.00	0.00	0.00	0.00
Al	0.01	0.02	0.05	0.02	0.01	0.03	0.08	0.03	0.02	0.01
Cr	0.00	0.00	0.00	0.00	0.00	0.00	0.00	0.00	0.00	0.00
Fe*	0.11	0.08	0.07	0.07	0.08	0.09	0.09	0.07	0.16	0.16
Mn	0.01	0.00	0.00	0.00	0.00	0.01	0.00	0.00	0.03	0.03
Mg	0.89	0.92	0.90	0.93	0.94	0.92	0.90	0.93	0.87	0.87
Ca	0.99	0.97	0.96	0.94	0.96	0.95	0.96	0.95	0.98	0.98
Na	0.01	0.02	0.05	0.02	0.01	0.02	0.02	0.02	0.00	0.00
Total	4.01	4.00	4.02	3.99	4.01	4.01	4.01	4.00	4.02	3.03
Wo	0.50	0.49	0.50	0.49	0.49	0.48	0.49	0.49	0.49	0.49
En	0.45	0.47	0.46	0.48	0.48	0.47	0.46	0.48	0.43	0.43
Fs	0.05	0.04	0.04	0.04	0.04	0.05	0.04	0.04	0.08	0.08
Xmg	0.90	0.92	0.92	0.93	0.92	0.91	0.91	0.93	0 84	0 84

Table 4.1

Table 4.2 - Chlorite compositions at 34-50 locality					
Sample ->	990-22.1	990-22.3	990-22.4	990-16.6	990-16.9
locality ->	central	central	central	outer	outer
SiO2	28.37	28.12	27.91	32.66	32.71
TiO2	0.02	0.02	0.01	0.00	0.00
Al2O3	18.12	18.66	18.52	14.39	14.68
Cr2O3	0.26	0.17	0.24	n.d.	n.d.
FeO*	16.58	17.10	16.87	6.55	6.96
MnO	0.19	0.21	0.20	0.07	0.04
MgO	22.74	22.20	22.25	32.57	31.99
CaO	0.02	0.02	0.08	0.03	0.05
Na2O	0.02	0.01	0.02	0.00	0.00
K2O	n.d.	n.d.	n.d.	0.01	0.01
H2O diff	13.68	13.49	13.90	13.72	13.56
Total	100.00	100.00	100.00	100.00	100.00
AFM space:					
Al	0.18	0.19	0.19	0.14	0.14
Fe+Mn	0.24	0.25	0.24	0.09	0.09
Mg	0.58	0.56	0.57	0.78	0.77
Xmg	0.71	0.70	0.70	0.90	0.89
notes:	total Fe expressed as FeO*				
	H2O determined by difference				
	Xmg is Mg/(Mg+Fe) mole fraction				

Table 4.2

Table 4.3 - Chlorite compositions at Perovskite Knob										
Sample ->	688-4.3	688-4A.1	688-4A.2	688-4A.7	688-4A.8	688-4A.10	688-4A.11	688-8C.3	688-8C.5	688-8C.7
locality ->	PK	PK	PK	PK	PK	PK	PK	PK	PK	PK
SiO2	27.69	28.25	29.14	29.18	30.34	30.04	28.72	29.54	29.96	34.69
TiO2	0.07	0.01	0.03	0.05	0.04	0.03	0.03	0.22	0.05	0.02
Al2O3	17.85	17.39	16.20	16.96	17.55	17.71	18.03	15.24	14.92	10.83
Cr2O3	n.d.	n.d.	n.d.	n.d.	n.d.	n.d.	n.d.	n.d.	n.d.	0.42
FeO*	21.48	20.26	16.05	17.92	11.25	17.10	18.88	19.62	18.59	4.09
MnO	0.46	0.53	0.45	0.50	0.55	0.61	0.46	0.45	0.38	0.18
MgO	19.78	20.92	23.87	21.72	26.90	23.26	21.11	22.06	22.78	35.79
CaO	0.14	0.02	0.23	0.10	0.11	0.09	0.09	0.33	0.21	0.10
Na2O	0.03	0.03	0.09	0.02	0.02	0.02	0.01	0.02	0.00	ND
K2O	0.00	0.00	0.01	0.00	0.01	0.01	0.02	0.07	0.00	ND
H2O diff	12.50	12.59	13.93	13.55	13.23	11.13	12.65	12.45	13.11	13.88
Total	100.00	100.00	100.00	100.00	100.00	100.00	100.00	100.00	100.00	100.00
AFM space:										
Al	0.18	0.17	0.16	0.17	0.17	0.17	0.18	0.15	0.15	0.10
Fe+Mn	0.31	0.30	0.23	0.27	0.16	0.25	0.28	0.29	0.27	0.06
Mg	0.51	0.53	0.60	0.56	0.66	0.58	0.54	0.56	0.58	0.84
Xmg	0.62	0.64	0.72	0.68	0.80	0.70	0.66	0.66	0.68	0.94
notes:	total Fe expressed as FeO*									
	H2O determined by difference									
	Xmg is Mg/(Mg+Fe) mole fraction									

Table 4.3

Table 4.4 - Miscellaneous Mineral Compositions			
Sample ->	688-8C	688-5	990-3
phase ->	Titanite	Perovskite	Vesuvianite
SiO2	30.00	0.02	36.10
TiO2	38.27	58.23	1.34
ZrO2	n.d.	n.d.	n.d.
Al2O3	1.29	n.d.	15.78
Cr2O3	0.07	n.d.	n.d.
Fe2O3*	n.d.	n.d.	2.44
FeO*	0.63	0.23	n.d.
MnO	0.04	0.00	0.11
MgO	0.04	0.01	2.05
CaO	27.97	40.89	35.89
Na2O	n.d.	n.d.	0.02
Nb2O5	n.d.	0.19	0.00
Ce2O3	n.d.	0.10	0.13
La2O3	n.d.	0.00	0.02
Y2O3	n.d.	0.02	0.00
H2O(diff)	n.d.	n.d.	6.11
Total	98.31	99.68	100.00
Si	1.00	0.00	8.87
Ti	0.95	1.00	0.25
Zr	0.00	0.00	0.00
Al	0.05	0.00	4.57
Cr	0.00	0.00	0.00
Fe*	0.02	0.00	0.45
Mn	0.00	0.00	0.02
Mg	0.00	0.00	0.75
Ca	0.99	1.00	9.44
Na	0.00	0.00	0.02
Nb	0.00	0.00	0.00
Ce	0.00	0.00	0.02
La	0.00	0.00	0.00
Y	0.00	0.00	0.00
Total	3.01	2.00	24.39
Total Fe expressed as either FeO* or Fe2O3*, as shown			

Table 4.5 - Representative Bulk Compositions for Chlorite-Diopside Rocks								
Sample ->	990-22	1091-67	890-12	RGC-34-50	66SAL-1	Peretti	989-45	model comp
lithology ->	Chl-Di	Chl-Di	Chl-Di	Chl-Di	Websterite	Pyroxenite	harzburgite	Chl-Di
location ->	34-50	34-50	PK	34-50	Hawaii	Val Malenco	New Idria	New Idria
SiO2	39.39	45.35	36.22	36.96	44.82	45.61	47.89	45.86
TiO2	1.25	1.39	0.66	2.02	0.52	0.18	0.00	0.00
Al2O3	11.82	4.14	16.37	11.42	8.21	4.20	1.45	11.12
Fe2O3*	14.56	11.02	11.81	16.37	10.12	8.55	6.44	0.00
MnO	0.21	0.26	0.26	0.29	0.19	0.14	0.16	0.00
MgO	19.24	15.47	30.00	19.67	26.53	30.55	43.83	30.77
CaO	12.81	21.26	3.57	13.14	8.12	10.75	0.06	12.23
Na2O	0.21	0.20	0.11	0.09	0.89	0.00	0.16	0.00
K2O	0.00	0.01	0.00	0.05	0.03	0.00	0.00	0.00
P2O5	0.00	0.09	0.02	0.00	nd	0.02	0.00	0.03
Total	99.49	99.17	99.01	100.00	99.43	100.00	100.00	100.00
Anhydrous analyses; all Fe expressed as Fe2O3								
In analysis RGC-34-50, Fe2O3 recalculated from FeO=9.76, Fe2O3=4.52; also H2O+=6.88, H2O-=0.39								
In analysis 5, Fe2O3 recalculated from FeO=7.91, Fe2O3=2.07; also Cr2O3=0.20; NiO=0.20								
Trace (ppm)	990-22	1091-67	890-12	RGC-34-50	Hawaii	Val Malenco	989-45	model
Nb	10.89	12.42	1.29	n.d.	n.a.	<4	0.00	n.a.
Zr	198.37	198.25	50.46	n.d.	n.a.	<10	4.28	n.a.
Sr	44.73	125.55	1.68	n.d.	n.a.	<15	1.75	n.a.
Zn	211.13	104.58	134.07	n.d.	n.a.	19.00	55.38	n.a.
Ni	850.85	722.39	1083.27	n.d.	2000	3327.00	2171.52	n.a.
Cr	1023.11	799.67	1418.00	n.d.	2000	853.00	2304.95	n.a.
V	167.89	138.01	136.35	n.d.	n.a.	64.00	24.00	n.a.
Ce	56.96	49.93	2.31	n.d.	n.a.	n.d.	0.51	n.a.
Ba	5.49	47.20	3.86	n.d.	n.a.	<10	32.45	n.a.
La	27.04	22.80	0.15	n.d.	n.a.	n.d.	1.14	n.a.

Table 4.5

Table 4.6 - Spinel Norm Calculations for Chlorite-Diopside Compositions at High Pressures

Oxide	Weight %	GFW	M-Prop.	Ap	Ilm	Or	Jd	Wo	Sp	Di	En	Ol	Totals	(FeMg)	
sample	990-22														Y =
SiO2	40.18	60.090	0.669			0.000	0.014	0.000		0.466	0.066	0.123	0.669		0.669
TiO2	1.27	79.700	0.016		0.016								0.016		
Al2O3	12.05	101.940	0.118			0.000	0.004		0.115	0.000			0.118		Si excess
Cr2O3	0.00	152.020	0.000										0.000		0.001
Fe2O3	0.00	159.700	0.000										0.000		
FeO	13.36	71.850	0.189										0.000	28%	Ol trial
MnO	0.22	70.940	(in FeO ^)		0.016				0.115	0.233	0.066	0.246	0.676	0.676	0.123
MgO	19.63	40.320	0.487										0.000	72%	
CaO	13.07	56.080	0.233	0.000				0.000		0.233			0.233		Tk in Cpx
Na2O	0.22	61.980	0.004				0.004						0.004		0.000
K2O	0.00	94.200	0.000			0.000							0.000		
P2O5	0.00	141.850	0.000	0.000									0.000		
H2O	0.00	18.016	0.000										0.000		
Totals	100.00														
Oxy Equivalents				0.000	0.048	0.000	0.042	0.000	0.459	1.398	0.198	0.492	2.638		
Est Mode				0.0	1.8	0.0	1.6	0.0	17.4	53.0	7.5	18.7	100.0		
Ol-Opx-Cpx coordinates										66.9	9.5	23.6	100.0		
Mol proportion										0.233	0.066	0.492	0.791		
Mol Fraction norm to 1.0										29.46	8.35	62.19	100		

Table 4.6 folio 1

Oxide	Weight %	GFW	M-Prop.	Ap	Ilm	Or	Jd	Wo	Sp	Di	En	Ol	Totals	(FeMg)	
sample	1091-67														Y =
SiO2	46.24	60.090	0.769			0.001	0.013	0.130		0.509	0.008	0.109	0.769		0.769
TiO2	1.42	79.700	0.018		0.018								0.018		
Al2O3	4.23	101.940	0.041			0.000	0.003		0.038	0.000			0.041		Si excess
Cr2O3	0.00	152.020	0.000										0.000		0.000
Fe2O3	0.00	159.700	0.000										0.000		
FeO	10.11	71.850	0.144										0.000	27%	Ol trial
MnO	0.26	70.940	(in FeO *)		0.018				0.038	0.254	0.008	0.218	0.535	0.535	0.109
MgO	15.77	40.320	0.391										0.000	73%	
CaO	21.68	56.080	0.387	0.002				0.130		0.254			0.387		Tk in Cpx
Na2O	0.20	61.980	0.003				0.003						0.003		0.000
K2O	0.01	94.200	0.000			0.000							0.000		
P2O5	0.09	141.850	0.001	0.001									0.001		
H2O	0.00	18.016	0.000										0.000		
Totals	100.00														
Oxy Equivalents				0.005	0.053	0.002	0.039	0.390	0.152	1.526	0.023	0.435	2.626		
Est Mode				0.2	2.0	0.1	1.5	14.8	5.8	58.1	0.9	16.6	100.0		
Ol-Opx-Cpx coordinates										76.9	1.2	21.9	100.0		
Mol proportion										0.254	0.008	0.435	0.697		
Mol Fraction norm to 1.0										36.48	1.10	62.42	100		

Table 4.6 folio 2

Oxide	Weight %	GFW	M-Prop.	Ap	Ilm	Or	Jd	Wo	Sp	Di	En	Ol	Totals	(Fe/Mg)	
sample	890-12														Y =
SiO2	37.02	60.090	0.616			0.000	0.008	0.000		0.129	0.280	0.200	0.617		0.617
TiO2	0.67	79.700	0.008		0.008								0.008		
Al2O3	16.74	101.940	0.164			0.000	0.002		0.162	0.000			0.164		Si excess
Cr2O3	0.00	152.020	0.000										0.000		0.001
Fe2O3	0.00	159.700	0.000										0.000		
FeO	10.86	71.850	0.155										0.000	17%	Ol trial
MnO	0.26	70.940	(in FeO ^)		0.008				0.162	0.065	0.280	0.400	0.916	0.916	0.200
MgO	30.67	40.320	0.761										0.000	83%	
CaO	3.64	56.080	0.065	0.000				0.000		0.065			0.065		Tk in Cpx
Na2O	0.12	61.980	0.002				0.002						0.002		0.000
K2O	0.00	94.200	0.000			0.000							0.000		
P2O5	0.02	141.850	0.000	0.000									0.000		
H2O	0.00	18.016	0.000										0.000		
Totals	100.00														
Oxy Equivalents				0.001	0.025	0.000	0.023	0.000	0.649	0.388	0.840	0.800	2.726		
Est Mode				0.0	0.9	0.0	0.8	0.0	23.8	14.2	30.8	29.3	100.0		
Ol-Opx-Cpx coordinates										19.1	41.4	39.4	100.0		
Mol proportion										0.065	0.280	0.800	1.145		
Mol Fraction norm to 1.0										5.65	24.47	69.88	100		

Table 4.6 folio 3

Oxide	Weight %	GFW	M-Prop.	Ap	Ilm	Or	Jd	Wo	Sp	Di	En	Ol	Totals	(FeMg)	
sample	RGC-34-50														Y =
SiO2	37.57	60.090	0.625			0.003	0.006	0.055		0.366	0.002	0.193	0.625		0.625
TiO2	2.06	79.700	0.026		0.026								0.026		
Al2O3	11.61	101.940	0.114			0.001	0.001		0.112	0.000			0.114		Si excess
Cr2O3	0.00	152.020	0.000										0.000		0.000
Fe2O3	0.00	159.700	0.000										0.000		
FeO	14.98	71.850	0.213										0.000	30%	Ol trial
MnO	0.29	70.940	(in FeO ^)		0.026				0.112	0.183	0.002	0.386	0.708	0.708	0.193
MgO	19.99	40.320	0.496										0.000	70%	
CaO	13.35	56.080	0.238	0.000				0.055		0.183			0.238		Tk in Cpx
Na2O	0.09	61.980	0.001				0.001						0.001		0.000
K2O	0.05	94.200	0.001			0.001							0.001		
P2O5	0.00	141.850	0.000	0.000									0.000		
H2O	0.00	18.016	0.000										0.000		
Totals	100.00														
Oxy Equivalents				0.000	0.077	0.009	0.017	0.165	0.448	1.099	0.005	0.772	2.592		
Est Mode				0.0	3.0	0.4	0.6	6.4	17.3	42.4	0.2	29.8	100.0		
Ol-Opx-Cpx coordinates										58.6	0.2	41.2	100.0		
Mol proportion										0.183	0.002	0.772	0.957		
Mol Fraction norm to 1.0										19.14	0.16	80.69	100		

Table 4.6 folio 4

Oxide	Weight %	GFW	M·Prop.	Ap	Ilm	Or	Jd	Wo	Sp	Di	En	Ol	Totals	(FeMg)	
sample	66SAL-1														Y =
SiO2	45.54	60.090	0.758			0.002	0.058	0.000		0.294	0.227	0.176	0.758		0.758
TiO2	0.53	79.700	0.007		0.007								0.007		
Al2O3	8.34	101.940	0.082			0.000	0.015		0.067	0.000			0.082		Si excess
Cr2O3	0.00	152.020	0.000										0.000		0.000
Fe2O3	0.00	159.700	0.000										0.000		
FeO	9.25	71.850	0.131										0.000	16%	Ol trial
MnO	0.19	70.940	(in FeO ^)		0.007				0.067	0.147	0.227	0.352	0.800	0.800	0.176
MgO	26.96	40.320	0.669										0.000	84%	
CaO	8.25	56.080	0.147	0.000				0.000		0.147			0.147		Tk in Cpx
Na2O	0.90	61.980	0.015				0.015						0.015		0.000
K2O	0.03	94.200	0.000			0.000							0.000		
P2O5	0.00	141.850	0.000	0.000									0.000		
H2O	0.00	18.016	0.000										0.000		
Totals	100.00														
Oxy Equivalents				0.000	0.020	0.005	0.175	0.000	0.268	0.883	0.682	0.704	2.737		
Est Mode				0.0	0.7	0.2	6.4	0.0	9.8	32.3	24.9	25.7	100.0		
Ol-Opx-Cpx coordinates										38.9	30.1	31.0	100.0		
Mol proportion										0.147	0.227	0.704	1.079		
Mol Fraction norm to 1.0										13.64	21.08	65.28	100		

Table 4.6 folio 5

Oxide	Weight %	GPW	M-Prop.	Ap	Ilm	Or	Jd	Wo	Sp	Di	En	Ol	Totals	(Fe/Mg)	
sample	Peretti														Y =
SiO2	46.02	60.090	0.766			0.000	0.000	0.000		0.387	0.121	0.258	0.766		0.766
TiO2	0.19	79.700	0.002		0.002								0.002		
Al2O3	4.24	101.940	0.042			0.000	0.000		0.042	0.000			0.042		Si excess
Cr2O3	0.00	152.020	0.000										0.000		0.000
Fe2O3	0.00	159.700	0.000										0.000		
FeO	7.76	71.850	0.110										0.000	13%	Ol trial
MnO	0.14	70.940	(in FeO ^)		0.002				0.042	0.193	0.121	0.516	0.874	0.874	0.258
MgO	30.82	40.320	0.764										0.000	87%	
CaO	10.84	56.080	0.193	0.000				0.000		0.193			0.193		Tk in Cpx
Na2O	0.00	61.980	0.000				0.000						0.000		0.000
K2O	0.00	94.200	0.000			0.000							0.000		
P2O5	0.00	141.850	0.000	0.000									0.000		
H2O	0.00	18.016	0.000										0.000		
Totals	100.00														
Oxy Equivalents				0.000	0.007	0.000	0.000	0.000	0.166	1.160	0.364	1.032	2.729		
Est Mode				0.0	0.3	0.0	0.0	0.0	6.1	42.5	13.3	37.8	100.0		
Ol-Opx-Cpx coordinates										45.4	14.2	40.4	100.0		
Mol proportion										0.193	0.121	1.032	1.346		
Mol Fraction norm to 1.0										14.36	9.00	76.64	100		

Table 4.6 folio 6

Oxide	Weight %	GFW	M-Prop.	Ap	Ilm	Or	Jd	Wo	Sp	Di	En	Ol	Totals	(FeMg)	
sample	model														Y =
SiO2	46.70	60.090	0.777			0.000	0.000	0.000		0.345	0.258	0.173	0.777		0.777
TiO2	0.00	79.700	0.000		0.000								0.000		
Al2O3	8.80	101.940	0.086			0.000	0.000		0.086	0.000			0.086		Si excess
Cr2O3	0.00	152.020	0.000										0.000		0.000
Fe2O3	0.00	159.700	0.000										0.000		
FeO	0.00	71.850	0.000										0.000	0%	Ol trial
MnO	0.00	70.940	(in FeO ^)		0.000				0.086	0.173	0.258	0.346	0.863	0.863	0.173
MgO	34.82	40.320	0.863										0.000	100%	
CaO	9.68	56.080	0.173	0.000				0.000		0.173			0.173		Tk in Cpx
Na2O	0.00	61.980	0.000				0.000						0.000		0.000
K2O	0.00	94.200	0.000			0.000							0.000		
P2O5	0.00	141.850	0.000	0.000									0.000		
H2O	0.00	18.016	0.000										0.000		
Totals	100.00														
Oxy Equivalents				0.000	0.000	0.000	0.000	0.000	0.345	1.036	0.775	0.692	2.849		
Est Mode				0.0	0.0	0.0	0.0	0.0	12.1	36.4	27.2	24.3	100.0		
Ol-Opx-Cpx coordinates										41.4	31.0	27.6	100.0		
Mol proportion										0.173	0.258	0.692	1.123		
Mol Fraction norm to 1.0										15.38	23.01	61.61	100		

Table 4.6 folio 7

Oxide	Weight %	GFW	M-Prop.	Ap	Ilm	Or	Jd	Wo	Sp	Di	En	Ol	Totals	(FeMg)	
sample	Di 100														Y =
SiO2	54.34	60.090	0.904			0.000	0.019	0.000		0.872	0.008	0.005	0.904		0.904
TiO2	0.03	79.700	0.000		0.000								0.000		
Al2O3	1.02	101.940	0.010			0.000	0.005		0.005	0.000			0.010	Si excess	
Cr2O3	0.07	152.020	0.000										0.000		0.000
Fe2O3	0.00	159.700	0.000										0.000		
FeO	2.71	71.850	0.040										0.000	9%	Ol trial
MnO	0.14	70.940	(in FeO ^)		0.000				0.005	0.436	0.008	0.010	0.459	0.459	0.005
MgO	18.92	40.320	0.420										0.000	91%	
CaO	24.46	56.080	0.436	0.000				0.000		0.436			0.436	Tk in Cpx	
Na2O	0.30	61.980	0.005				0.005						0.005		0.000
K2O	0.00	94.200	0.000			0.000							0.000		
P2O5	0.00	141.850	0.000	0.000									0.000		
H2O	0.00	18.016	0.000										0.000		
Totals	100.00														
Oxy Equivalents				0.000	0.001	0.000	0.058	0.000	0.021	2.617	0.023	0.020	2.740		
Est Mode				0.0	0.0	0.0	2.1	0.0	0.8	95.5	0.8	0.7	100.0		
Ol-Opx-Cpx coordinates										98.4	0.9	0.8	100.0		
Mol proportion										0.436	0.008	0.020	0.464		
Mol Fraction norm to 1.0										94.03	1.65	4.31	100		

Table 4.6 folio 8

Oxide	Weight %	GFW	M·Prop.	Ap	Ilm	Or	Jd	Wo	Sp	Di	En	Ol	Totals	(FeMg)	
sample	Di 60														Y =
SiO2	50.95	60.090	0.848			0.000	0.016	0.000		0.698	0.082	0.052	0.848		0.848
TiO2	0.02	79.700	0.000		0.000								0.000		
Al2O3	4.30	101.940	0.042			0.000	0.004		0.038	0.000			0.042		Si excess
Cr2O3	0.06	152.020	0.000										0.000		0.000
Fe2O3	0.00	159.700	0.000										0.000		
FeO	3.83	71.850	0.055										0.000	10%	Ol trial
MnO	0.13	70.940	(in FeO ^)		0.000				0.038	0.349	0.082	0.104	0.574	0.574	0.052
MgO	20.90	40.320	0.518										0.000	90%	
CaO	19.56	56.080	0.349	0.000				0.000		0.349			0.349		Tk in Cpx
Na2O	0.24	61.980	0.004				0.004						0.004		0.000
K2O	0.00	94.200	0.000			0.000							0.000		
P2O5	0.00	141.850	0.000	0.000									0.000		
H2O	0.00	18.016	0.000										0.000		
Totals	100.00														
Oxy Equivalents				0.000	0.001	0.001	0.047	0.000	0.153	2.093	0.246	0.208	2.749		
Est Mode				0.0	0.0	0.0	1.7	0.0	5.8	76.1	9.0	7.6	100.0		
Ol-Opx-Cpx coordinates										82.2	9.7	8.2	100.0		
Mol proportion										0.349	0.082	0.208	0.639		
Mol Fraction norm to 1.0										54.59	12.85	32.55	100		

Table 4.6 folio 9

Oxide	Weight %	GFW	M-Prop.	Ap	Ilm	Or	Jd	Wo	Sp	Di	En	Ol	Totals	(Fe/Mg)	
sample	Di 60														Y =
SiO2	47.56	60.090	0.792			0.001	0.012	0.000		0.523	0.158	0.098	0.792		0.792
TiO2	0.02	79.700	0.000		0.000								0.000		
Al2O3	7.57	101.940	0.074			0.000	0.003		0.071	0.000			0.074		Si excess
Cr2O3	0.04	152.020	0.000										0.000		0.000
Fe2O3	0.00	159.700	0.000										0.000		
FeO	4.95	71.850	0.071										0.000	10%	Ol trial
MnO	0.12	70.940	(in FeO ^)		0.000				0.071	0.262	0.158	0.196	0.687	0.687	0.098
MgO	24.88	40.320	0.617										0.000	90%	
CaO	14.67	56.080	0.262	0.000				0.000		0.262			0.262		Tk in Cpx
Na2O	0.18	61.980	0.003				0.003						0.003		0.000
K2O	0.01	94.200	0.000			0.000							0.000		
P2O5	0.00	141.850	0.000	0.000									0.000		
H2O	0.00	18.016	0.000										0.000		
Totals	100.00														
Oxy Equivalents				0.000	0.001	0.002	0.035	0.000	0.285	1.570	0.475	0.392	2.759		
Est Mode				0.0	0.0	0.1	1.3	0.0	10.3	56.9	17.2	14.2	100.0		
Ol-Opx-Cpx coordinates										64.4	19.5	16.1	100.0		
Mol proportion										0.262	0.158	0.392	0.812		
Mol Fraction norm to 1.0										32.22	19.50	48.28	100		

Table 4.6 folio 10

Oxide	Weight %	GFW	M-Prop.	Ap	Ilm	Or	Jd	Wo	Sp	Di	En	Ol	Totals	(Fe/Mg)	
sample	Di 40														Y =
SiO2	44.18	60.090	0.735			0.001	0.008	0.000		0.349	0.232	0.145	0.735		0.735
TiO2	0.01	79.700	0.000		0.000								0.000		
Al2O3	10.84	101.940	0.106			0.000	0.002		0.104	0.000			0.106		Si excess
Cr2O3	0.03	152.020	0.000										0.000		0.000
Fe2O3	0.00	159.700	0.000										0.000		
FeO	6.07	71.850	0.086										0.000	11%	Ol trial
MnO	0.11	70.940	(in FeO ^)		0.000				0.104	0.175	0.232	0.290	0.801	0.801	0.145
MgO	28.84	40.320	0.715										0.000	89%	
CaO	9.79	56.080	0.175	0.000				0.000		0.175			0.175		Tk in Cpx
Na2O	0.12	61.980	0.002				0.002						0.002		0.000
K2O	0.01	94.200	0.000			0.000							0.000		
P2O5	0.00	141.850	0.000	0.000									0.000		
H2O	0.00	18.016	0.000										0.000		
Totals	100.00														
Oxy Equivalents				0.000	0.000	0.002	0.023	0.000	0.417	1.047	0.697	0.580	2.767		
Est Mode				0.0	0.0	0.1	0.8	0.0	15.1	37.9	25.2	21.0	100.0		
Ol-Opx-Cpx coordinates										45.1	30.0	25.0	100.0		
Mol proportion										0.175	0.232	0.580	0.987		
Mol Fraction norm to 1.0										17.69	23.54	58.77	100		

Table 4.6 folio 11

Oxide	Weight %	GFW	M·Prop.	Ap	Ilm	Or	Jd	Wo	Sp	Di	En	Ol	Totals	(Fe/Mg)	
sample	Di 20														Y =
SiO2	40.81	60.090	0.679			0.001	0.004	0.000		0.175	0.308	0.191	0.679		0.679
TiO2	0.01	79.700	0.000		0.000								0.000		
Al2O3	14.10	101.940	0.138			0.000	0.001		0.137	0.000			0.138	Si excess	
Cr2O3	0.01	152.020	0.000										0.000		0.000
Fe2O3	0.00	159.700	0.000										0.000		
FeO	7.18	71.850	0.101										0.000	11%	Ol trial
MnO	0.09	70.940	(in FeO ^)		0.000				0.137	0.088	0.308	0.382	0.915	0.915	0.191
MgO	32.80	40.320	0.814										0.000	89%	
CaO	4.91	56.080	0.088	0.000				0.000		0.088			0.088	Tk in Cpx	
Na2O	0.06	61.980	0.001				0.001						0.001		0.000
K2O	0.02	94.200	0.000			0.000							0.000		
P2O5	0.00	141.850	0.000	0.000									0.000		
H2O	0.00	18.016	0.000										0.000		
Totals	100.00														
Oxy Equivalents				0.000	0.000	0.003	0.012	0.000	0.549	0.526	0.924	0.764	2.778		
Est Mode				0.0	0.0	0.1	0.4	0.0	19.7	18.9	33.3	27.5	100.0		
Ol-Opx-Cpx coordinates										23.8	41.7	34.5	100.0		
Mol proportion										0.088	0.308	0.764	1.160		
Mol Fraction norm to 1.0										7.56	26.56	65.88	100		

Table 4.6 folio 12

Oxide	Weight %	GFW	M·Prop.	Ap	Ilm	Or	Jd	Wo	Sp	Di	En	Ol	Totals	(FeMg)	
sample	Di 0														Y =
SiO2	37.44	60.090	0.623			0.001	0.000	0.000		0.002	0.382	0.238	0.623		0.623
TiO2	0.00	79.700	0.000		0.000								0.000		
Al2O3	17.35	101.940	0.170			0.000	0.000		0.170	0.000			0.170		Si excess
Cr2O3	0.00	152.020	0.000										0.000		0.000
Fe2O3	0.00	159.700	0.000										0.000		
FeO	8.30	71.850	0.117										0.000	11%	Ol Trial
MnO	0.08	70.940	(in FeO ^)		0.000				0.170	0.001	0.382	0.476	1.028	1.028	0.238
MgO	36.76	40.320	0.912										0.000	89%	
CaO	0.05	56.080	0.001	0.000				0.000		0.001			0.001		Tk in Cpx
Na2O	0.00	61.980	0.000				0.000						0.000		0.000
K2O	0.02	94.200	0.000			0.000							0.000		
P2O5	0.00	141.850	0.000	0.000									0.000		
H2O	0.00	18.016	0.000										0.000		
Totals	100.00														
Oxy Equivalents				0.000	0.000	0.004	0.000	0.000	0.680	0.005	1.145	0.952	2.785		
Est Mode				0.0	0.0	0.1	0.0	0.0	24.4	0.2	41.1	34.2	100.0		
Ol-Opx-Cpx coordinates										0.2	54.5	45.3	100.0		
Mol proportion										0.001	0.382	0.952	1.334		
Mol Fraction norm to 1.0										0.06	28.59	71.35	100		

Table 4.6 folio 13

Table 4.7 - Representative Bulk Compositions for Mafic Schists and Greenstones

	1	2	3	4	5	6
Sample ->	990-89	1190-15	Coleman	Ernst	Ernst	Sorensen
lithology ->	greenstone	mafic schist	mafic schist	blueschist	greenstone	greenstone
location ->	New Idria	New Idria	New Idria	Pacheco	Pacheco	Catalina
SiO2	51.48	53.61	65.47	57.29	49.22	50.40
TiO2	2.09	1.46	0.50	1.04	3.40	1.20
Al2O3	13.52	11.70	15.96	14.58	12.87	15.70
Fe2O3*	12.79	11.14	1.62	7.92	4.94	n.d.
FeO*	n.d.	n.d.	1.82	5.10	12.05	9.70
MnO	0.23	0.70	0.10	0.21	0.27	0.17
MgO	6.46	8.64	1.72	6.15	4.94	7.70
CaO	6.95	3.98	2.32	1.88	8.55	11.80
Na2O	6.25	7.97	9.90	5.42	3.09	1.80
K2O	0.07	0.48	0.53	0.42	0.31	0.86
P2O5	0.18	0.13	0.07	n.d.	0.36	n.d.
Total	100.02	99.80	100.00	100.00	100.00	99.33
All analyses are anhydrous: analyses with 100% totals have been normalized to 100%						
Fe2O3* and FeO* indicate total Fe for those samples lacking separate determinations for Fe						
Trace (ppm)						
Nb	3.25	8.58	n.d.	n.d.	n.d.	n.d.
Zr	137.31	67.49	130	n.d.	n.d.	n.d.
Sr	29.10	86.92	300	n.d.	n.d.	68.00
Zn	107.25	142.70	n.d.	n.d.	n.d.	88.20
Ni	99.20	323.63	26	n.d.	n.d.	n.d.
Cr	107.03	412.70	66	n.d.	n.d.	471.00
V	366.25	128.70	n.d.	n.d.	n.d.	n.d.
Ce	19.54	10.73	n.d.	n.d.	n.d.	5.29
Ba	116.44	212.37	2500	n.d.	n.d.	148.00
La	4.33	1.26	n.d.	n.d.	n.d	1.28

Table 4.7 folio 1

Table 4.7 - CIPW Normative Minerals for Mafic Schists and Greenstones						
	1	2	3	4	5	6
Sample ->	990-89	1190-15	Coleman	Ernst	Ernst	Sorensen
lithology ->	greenstone	mafic schist	mafic schist	blueschist	greenstone	greenstone
location ->	New Idria	New Idria	New Idria	Franciscan	Franciscan	Catalina
Quartz			0.81	10.28	3.76	4.29
Corundum				1.79		
Orthoclase	0.41	2.84	3.13	2.48	1.83	5.08
Albite	48.10	43.90	79.14	45.86	26.15	15.23
Acmite		8.75	4.08			
Anorthite	8.63			9.33	20.33	32.22
Nepheline	2.59	7.37				
Diopside	19.47	15.08	8.99		16.35	20.78
Hypersthene			2.44	16.81	17.12	12.17
Olivine	6.50	14.55				
Magnetite	9.28	3.69	0.31	11.48	7.16	7.82
Ilmenite	3.97	2.77	0.95	1.98	6.46	2.28
Apatite	0.43	0.31	0.17		0.85	
Total	99.39	99.26	100.01	100.01	100.02	99.87
References: Coleman sample from Coleman (1961), Ernst samples from Ernst (1965)						
Sorensen Sample from Sorensen (1986)						

Chapter 5

Compositions and Mineral Associations of Garnets from the New Idria Serpentinite

Chapter 5 - Compositions and Mineral Associations of Garnets from the New Idria Serpentinite

Chapter 5 - Compositions and Mineral Associations of Garnets from the New Idria Serpentinite

I. Introduction

The purpose of this chapter is to present and discuss approximately 300 electron microprobe analyses of Ti-garnets from the New Idria District. Analyses of coexisting minerals, principally chlorite and diopside, are given in Chapter 4. The garnet compositions are shown in the Schorlomite-Andradite-Grossular (SAG) projection; compositional variations of the garnets are explored using exchange vectors.

Garnets from the New Idria serpentinite in San Benito and Fresno Counties, California are widely known for their unusual colors and titanium-rich compositions. Most of the New Idria garnets are calcic and belong to the andradite clan with end-member formula ($Ca_3Fe_2^{3+}Si_3O_{12}$). Titanium substitution occurs principally along the exchange vector $TiFe_{-1}$, making these garnets Ti-andradites. Some of the garnets are also hydrous and vary along the hydrogarnet exchange vector H_4Si_{-1}. Some of the garnets are Ti-grossulars, a portion of composition space not previously explored. Compositional variation in these garnets occurs along the vector $TiFe^{2+}Al_{-2}$. This study presents approximately 300 electron microprobe analyses of garnets from the New Idria District, together with analyses of coexisting minerals, principally chlorite and diopside. The mean TiO_2 content of the garnets in this study is 5 wt. %. One of the garnets contains 15.62 wt. % TiO_2, which corresponds to approximately one Ti atom per formula unit, i.e. the schorlomite end member.

Most New Idria garnets are hosted in tectonic blocks of chlorite-diopside-garnet rocks that are interpreted as metapyroxenites entrained by the serpentinite. These garnets occur in two generations assigned to metamorphic events M1 and M2 (see Chapter 4). At one locality, near end-member grossular, end-member andradite, and Ti-andradite coexist in a single rock. Some yellow, Ti-free andradites occur in tectonic blocks of massive antigorite. Outside of the tectonic blocks, widespread but minor uvarovitic garnet is found as an alteration product of the ubiquitous chromite grains in the serpentinite. These garnets are discussed separately, in Chapter 3. Uvarovitic garnet inside tectonic blocks may also be titaniferous, however.

The colors and varietal names of andradite garnets found at New Idria range from light green (demantoid) to yellow (topazolite), through brown (unnamed) to black (melanite and schorlomite). Uvarovitic garnets are emerald green. There is a general correlation between garnet color and composition that is a useful field guide at New Idria, although not necessarily applicable elsewhere.

Many, but not all garnets of the New Idria district are strongly anisotropic, sector twinned, and zoned. Cation ordering on the octahedral sites has been cited as a principal cause of anisotropy in garnets that reduces the cubic symmetry to tetragonal or even triclinic (e.g. Akizuki, 1984; Griffin et.al., 1990; Kingma & Downs, 1989). Recent spectroscopic work by Lager et al. (1989) has demonstrated the presence of (OH) groups in New Idria garnets. If these (OH) groups enter the garnet structure through the hydrogarnet substitution, they may also contribute to anisotropy. Sector twinning and zoning are most frequently observed in vein-filling garnets at New Idria; these garnets generally have Ti-rich cores and Ti-poor rims, but sometimes the zoning pattern is reversed. The appearance of these garnets is suggestive of skarn deposits, e.g. Harris & Einaudi (1982), although the New Idria occurrences are not associated with skarns.

II. Geological Setting of the New Idria District

The term *New Idria District*, referred to in this study simply as *the District*, was first used by Becker to describe the general region encompassing the historic mercury mines at New Idria, California (Becker, 1888). The most remarkable feature of the District is an oval, 23 by 8 km, fault bounded, serpentinite massif flanked by steeply dipping, locally overturned, sedimentary and metamorphic rocks of the Jurassic-Cretaceous Franciscan and the Cretaceous to Pliocene Great Valley Sequence of California.

The New Idria Serpentinite is a part of the Coast Range Ophiolite in California (Hopson et al., 1981). Its emplacement within the Franciscan Formation is related to subduction of the Farallon plate in the Jurassic. The tectonic setting of the ophiolite was a forearc basin lying between the Sierra Nevada volcanic arc to the east and a trench-subduction complex to the west, represented by the Franciscan Formation (Bartow, 1990). A piece of oceanic crust or underlying mantle was obducted onto the North American continent, later to rise through the Franciscan Formation as a serpentinite diapir. Emplacement of the New Idria Serpentinite as a diapir within the Franciscan has resulted in a piercement structure or tectonic window, lying just east of the San Andreas fault system northeast of Parkfield. Further details about the geological environment of the District can be found in Chapter 1.

III. Titaniferous Garnets

Titaniferous andradites have been recognized as a unique variety of garnet for over a century. Tschermak (1885) mentioned Ti-rich garnets from serpentinites and alkaline igneous rocks in the Alps, and recognized them as members of the andradite clan. The nature of the exchange vectors that incorporate Ti in garnet, and the valence state of Ti in

garnet, have led to an extensive literature on this subject (e.g. Kühberger et al., 1989; Huggins et al., 1977a,b; Dowty, 1969; Huckenholz, 1969; Howie & Wooley, 1968; Isaacs, T., 1968; Ito & Frondel, 1967; Piners, 1894). Garnets with more than about 1 wt % TiO_2 in their analyses are strongly colored: black in hand sample and deep red in thin section. The nature of the electronic absorption that leads to this coloration has led to much speculation. Current theories include the possibility of electron hopping between Ti and Fe-occupied sites, making the actual valence state of Ti and Fe indeterminate. The possible presence of Ti^{3+} cations in garnet is still hotly debated. Studies by Huggins et al. (1977a) and Dowty (1969) used Mossbauer spectroscopy in an attempt to determine site occupancy of cations in the garnet structure. Dowty (1969) doubted the occurrence of Ti^{3+} in garnet; Kühberger et al. (1989) reached the opposite conclusion. The limitations of these studies are that, due to the techniques employed, only indirect evidence is available regarding the valence state of Ti; model-dependent assumptions must be made. The presence or absence of Ti^{3+} can be deduced from assumptions about crystal chemical preferences and charge balance combined with measurements of the site occupancy and valence state of Fe. Waychunas (1987) attempted a direct measurement of the valence state of Ti in silicate minerals using synchrotron radiation and XANES spectroscopy. He concluded that while Ti^{3+} in terrestrial minerals cannot be completely ruled out, its concentration must be very low. Further studies using a brighter synchrotron source and EXAFS spectroscopic techniques might resolve this question in a direct manner. Therefore, I conclude at the present time that presence of Ti^{3+} in garnets has not been completely ruled out, but is only supported by indirect and equivocal evidence.

The stability field of andradite garnets and the location in P-T space of univariant reactions involving Ti-garnet have been investigated by Taylor & Liou (1972), Huckenholz (1969), Huckenholz et al. (1976) and others in synthesis experiments. The evidence from these studies and from natural occurrences in metamorphic and igneous rocks is that both

andradites and Ti-andradites are stable from about 300°C up to, and including, igneous temperatures. None of the studies has delimited the stability field of the Ti-rich varieties explicitly, but there is a positive dependency on oxygen fugacity (Huckenholz et al., 1976). Virgo et al. (1976) suggested that Ti and Al stabilize Fe^{3+} in andradite, allowing these andradites to persist as stable phases at lower oxygen fugacities than otherwise possible.

The paragenesis of Ti-rich garnets is largely restricted to alkaline igneous rocks and serpentinites. Apparently, low silica activity and peralkaline bulk compositions favor Ti-garnet, provided that Ti is available. Saturating Ti minerals, e.g. rutile, perovskite, titanite and ilmenite, appear in extremely Ti-rich bulk compositions. While all of these minerals occur at New Idria, they are very rare.

Other localities that have Ti-garnets associated with serpentinites include the Sangabawa District of Japan (Onuki et al., 1981), and some of the Alpine serpentinites. Recently, Müntener & Hermann (1994) have described an occurrence of Ti-garnets in the Malenco serpentinite in the Italian Alps. Their paragenesis in chlorite-diopside host rocks appears to be very similar to the New Idria occurrences; comparative studies among these localities are underway. The Malenco Ti-garnets are not associated with igneous intrusives. Switzer et al., (1971) reported an oceanic occurrence of Ti-garnet hosted by chlorite-diopside rock in a dredge sample of serpentinized peridotite from the Mid-Atlantic Ridge near 43° N.

IV. Titaniferous Garnets at New Idria:

The occurrence of Ti-garnets at New Idria is restricted to host rocks found in isolated tectonic blocks consisting of chlorite, diopside, garnet, and accessory minerals. These blocks are interpreted as metapyroxenites. The nature and origin of these blocks is described in Chapter 4.

Garnet in the blocks occurs in two generations: an early (M1) generation of foliation-parallel blebs, stringers, and isolated grains, and a late (M2) generation of subhedral to euhedral vein-filling crystals. The second generation M2 garnets, which fill crosscutting veins and form drusy coatings on the walls of cavities, have received the most attention by mineral collectors because of their relatively large size (up to 1 cm) and the relative abundance of gem and museum-quality specimens.

The first generation M1 garnets are anhedral to subhedral; the individual grains are usually too small to be seen with a hand lens: using SEM, isolated garnets of micron size can be found. Typically the garnets have a light to deep red color in thin section and are isotropic; they tend to form elongate, polycrystalline aggregates up to 5 mm. long. The M1 garnets are principally found in chlorite-rich domains of the host rock, so that the garnets coexist with abundant chlorite and minor diopside, along with accessory minerals.

Second generation M2 garnets are much larger (up to cm. size), are generally euhedral to subhedral, and are commonly, though not universally, anisotropic. They are generally deep red in thin section. These garnets coexist with diopside whiskers that are affixed to vein walls, and with chlorite that sometimes forms fan-shaped bundles.

V. The SAG Projection

Titaniferous garnets may best be considered as "improved" andradite and grossular garnets, in which Ti substitutes for Fe and Al respectively. A convenient projection for this portion of composition space is the SAG projection, using the ternary components schorlomite ($Ca_3TiFe^{2+}Si_3O_{12}$), andradite ($Ca_3Fe_2^{3+}Si_3O_{12}$) and grossular ($Ca_3Al_2Si_3O_{12}$), projected

through pyralspite and all other components. The transformation equations for this projection, using atom fractions of Ti, Fe and Al respectively, are as follows:

$$S = \frac{2Ti}{Ti+Fe+Al} \qquad A = \frac{(Fe-Ti)}{Ti+Fe+Al} \qquad G = \frac{Al}{Ti+Fe+Al}$$

Using the wt. % of TiO_2, Fe_2O_3, and Al_2O_3 provides a more convenient form of the transformation equations:

$$S = \frac{\frac{2TiO_2}{79.90}}{\frac{TiO_2}{79.90} + \frac{2Fe_2O_3}{159.70} + \frac{2Al_2O_3}{101.94}}$$

$$A = \frac{\frac{2Fe_2O_3}{159.70} + \frac{TiO_2}{79.90}}{\frac{TiO_2}{79.90} + \frac{2Fe_2O_3}{159.70} + \frac{2Al_2O_3}{101.94}}$$

$$G = \frac{\frac{2Al_2O_3}{101.94}}{\frac{TiO_2}{79.90} + \frac{2Fe_2O_3}{159.70} + \frac{2Al_2O_3}{101.94}}$$

VI. Compositions of New Idria Garnets

Figure 5.1 shows 300 electron microprobe analyses of garnets from New Idria in the SAG projection. All but one of the garnet analyses in this study plot within the triangle defined by these components. One Ti-rich analysis plots just outside the triangle beyond the S vertex. Compositional variation along the three binaries S-A, A-G and S-G can be expressed by the exchange vectors $TiFe_{-1}$, $AlFe_{-1}$, and $TiFeAl_{-2}$ respectively.

Due to the strongly zoned nature of the majority of New Idria garnets, each analysis in Figure 5.1 represents the composition at a specific point in a garnet crystal; compositions are not averaged. In the majority of cases New Idria garnets were found to be zoned, with Ti-rich cores and Ti-poor rims. This was particularly true in vein-filling subhedral garnets, suggesting that the composition of fluids in the veins evolved from Ti-rich to Ti-poor, as reported in Van Baalen & Zbinden, (1989). Some exceptions to the normal zoning patterns were observed: some garnets varied from Ti-poor to Ti-rich and back to Ti-poor in a traverse from core to rim.

In **Figure 5.1**, most of the analyses are relatively low in Al and plot near the S-A join. These garnets are interpreted as modified andradites. The exchange vector $TiFe_{-1}$ relates compositions along the S-A join to the andradite composition. $TiFe_{-1}$ substitution may be achieved by more than one crystal chemical process: the vector is equivalent to either or both of the vectors $TiFe^{2+}Fe^{3+}_{-2}$ and $Ti^{3+}Fe^{3+}_{-1}$. As noted previously, the $Ti^{3+}Fe^{3+}_{-1}$ vector is considered the less likely of the two, but until the proper spectroscopic studies are completed, the debate will rage on. In this study using microprobe analytical techniques it was not possible to distinguish between these two possibilities; for present purposes the vector $TiFe_{-1}$ is used.

Table 5.1 and 5.2 present the garnet analyses plotted in **Figure 5.1.** The data are divided into two groups: those analyses with totals between 99.00 - 100.99 wt. % are considered preferred analyses; they are given in **Table 5.1.** Those analyses with low totals of 97.00-98.99 wt. % are given in **Table 5.2.** It is likely that most of the analyses in Table 5.2 represent garnets with a significant hydrogarnet component, making them hydroandradites and titanohydroandradites. In this study analytic determination of the

hydrogarnet component was not possible. However, recent spectroscopic work by Lager et al. (1989) has demonstrated the presence of (OH) groups in New Idria garnets.

In routine garnet analyses in this study, the major elements measured are those shown in Table 5.1. However, each garnet sample was examined for major impurities using EDS analysis, with a detection limit of approximately 1 wt. %. A representative garnet sample was also analyzed using the WDS technique for the presence of V, Zr, Sn, P, Na, and REE. All of these elements were below the detection limits of approximately 0.01 wt %. Cr, however, was found to occur in significant amounts in some samples.

In an effort to understand the uncertainty of garnet compositions measured in this study, a working standard was chosen early in the study. This standard was a point in a relatively homogeneous portion of a Ti-rich hydrogarnet; this point was repeatedly analyzed for consistency during the course of the study. The composition of the working standard in wt. %, with 1 σ errors, was thereby determined to be:

Oxide	Wt. %	± 1 σ
SiO_2	33.55	0.29
TiO_2	5.56	0.13
Al_2O_3	0.73	0.02
Cr_2O_3	0.01	0.01
Fe_2O_3*	23.29	0.20
MnO	0.16	0.03
MgO	0.48	0.02
CaO	33.65	0.18
Totals	97.44	0.29

Figure 5.1 - Compositions of 300 garnets from New Idria in ternary system schorlomite-andradite-grossular (SAG), projected from pyralspite and all other components. See text for details of projection. Dotted line is along apparent compositional trend shown by a significant number of analyses.

Figure 5.1 - Compositions of New Idria Garnets

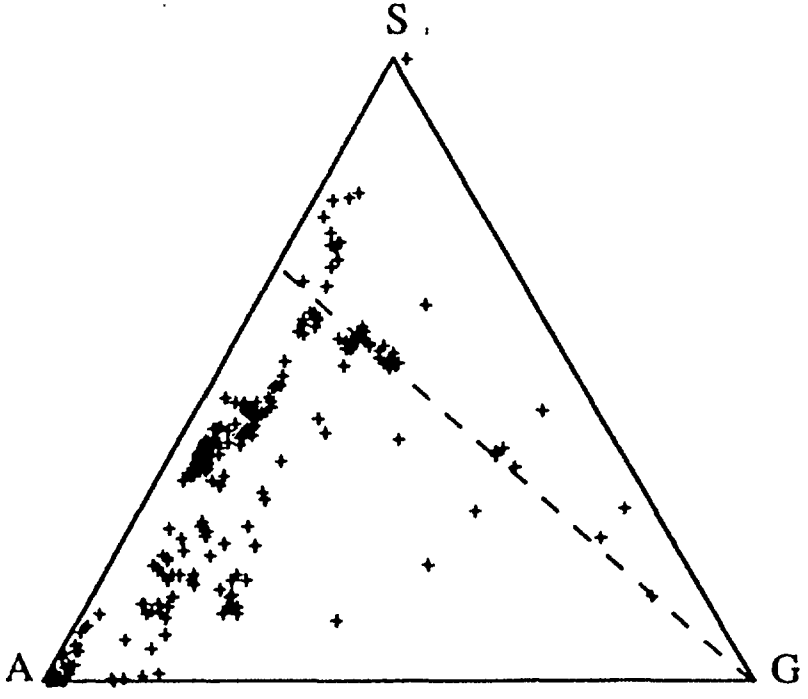

300 Analyses

S - schorlomite
A - andradite
G - grossular

Using the site preference rules of Huggins et al. (1977), who found that tetrahedral site preference was in the sequence Al > Fe > Ti, and with normalization to 12 oxygens, this well-determined composition is equivalent to an anhydrous structural formula of:

$$Ca_{3.00\pm.02}(Ti_{0.36\pm.01}Fe_{1.45\pm.01}Mn_{0.01}Mg_{0.06}Ca_{0.09})(Si_{2.88\pm.02}Al_{0.07}Fe_{0.05})$$

In this formulation the tetrahedral sites and the 8-coordinated sites sum to the ideal number of 3.0; the octahedral cations sum to 1.98. Error estimates are shown for major elements; errors for Mn,Mg and Al are approximately ± 0.002. Note that the analysis appears to be Si-deficient and to have excess Ca. As been noted by most other workers, Ti-garnets world-wide are commonly subsilicic, i.e. they have < 3 Si pfu, and supercalcic, i.e.they have > 3 Ca pfu. This compositional feature is apparently real and not an artifact of the analytical techniques used.

The chief source of random variability in microprobe analyses is the counting statistics in the detectors on the spectrometers. The working standards used for the microprobe at Harvard have also been analyzed using wet chemistry in order to constrain systematic errors. In this study no other significant sources of error were found, i.e. no error terms other than counting statistics were required to explain the variability in the analyses.

The mean compositions of the garnets in **Tables 5.1** (totals ≥ 99%) and **Table 5.2** (< 99%) are given in the final column of each table and are listed below for convenience. A comparison of the two groups shows that the garnets in the second group are slightly lower in Si and Ca; noticeably higher in Ti and Al; noticeably lower in Fe, and higher in the trace constituents Cr and Mg. Mn as a trace constituent is the same in both groups. I therefore conclude that the garnets of the first group are essentially Ti-andradites, with only minor

amounts of other components, while the garnets of the second group vary more broadly in composition space.

Oxide	Table 5.1	Table 5.2
SiO_2	34.47	34.01
TiO_2	4.40	5.73
Al_2O_3	1.85	2.85
Cr_2O_3	0.06	0.15
Fe_2O_3*	24.08	20.75
MnO	0.15	0.15
MgO	0.27	0.70
CaO	34.21	34.06
Totals	99.50	98.40

The lower Si contents of the garnets in the second group correlate in a general way with lower analysis totals, but a plot (not shown) of Si wt. % versus analysis totals shows considerable scatter. Therefore, the simple hypothesis that low analysis totals are mainly due to the hydrogarnet substitution does not fully explain the compositional complexity in these garnets.

VII. Compositions of Ti-garnets from Other Localities

Figure 5.2 presents analyses of Ti-garnets from other localities for comparison with the New Idria samples. The Onuki et al. (1981) data are from the Sangabawa district of Japan; the Hermann & Müntener (1991) data are from Val Malenco, Italy. In both cases the garnets are found in serpentinites. The Switzer et al. (1971) samples are from

Figure 5.2 - Compositions of garnets from other localities for comparison with Figure 5.1. Symbols as noted in figure.

Figure 5.2 - Other Garnet Compositions

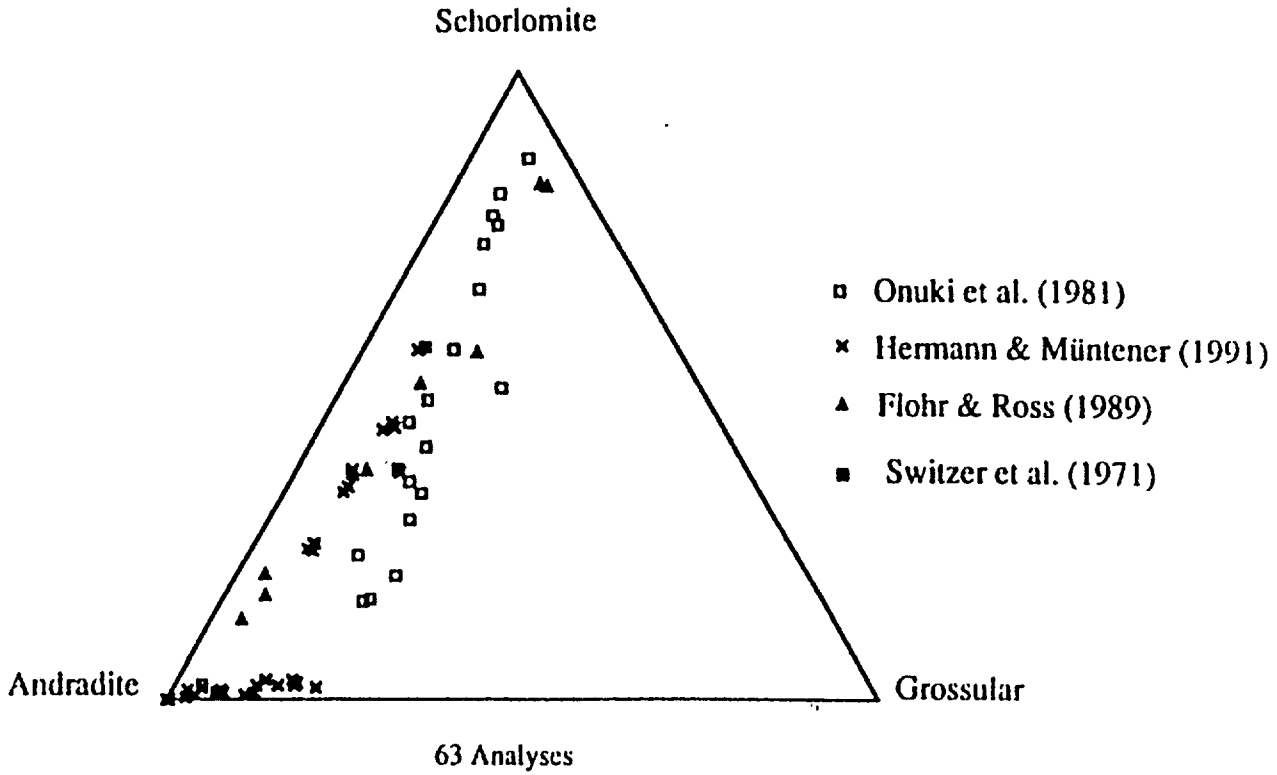

63 Analyses

Figure 5.3 - Microprobe traverse of an M2 garnet vein in sample 989-65a. Early Ti-rich garnet grew along vein walls; late Ti-poor garnet filled vein center.

Figure 5.3 - Garnet Vein Traverse

Sample 989-65a

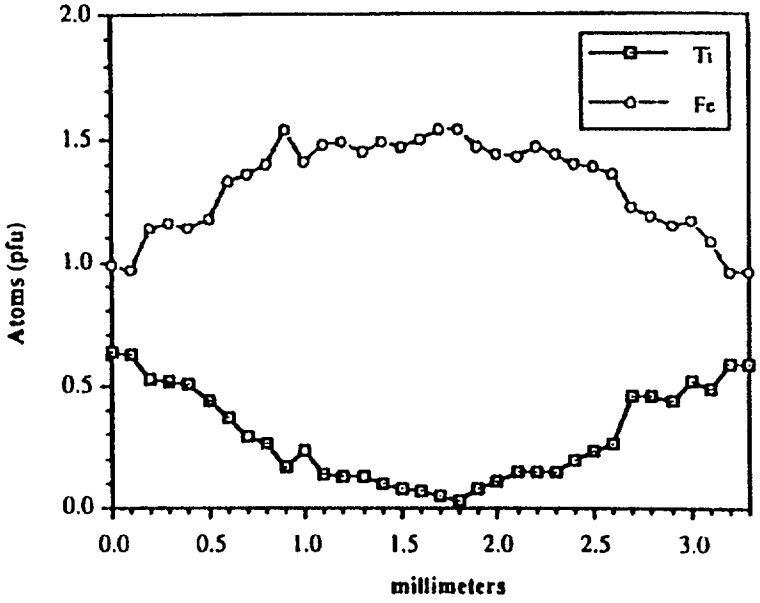

Figure 5.4 - Fe-Ti exchange in same garnet traverse as Figure 5.3. Good inverse correlation argues for progress along $TiFe._1$ vector (see text for discussion of $TiFe._1$).

Figure 5.4 - Fe-Ti Exchange in Sample 989-65a

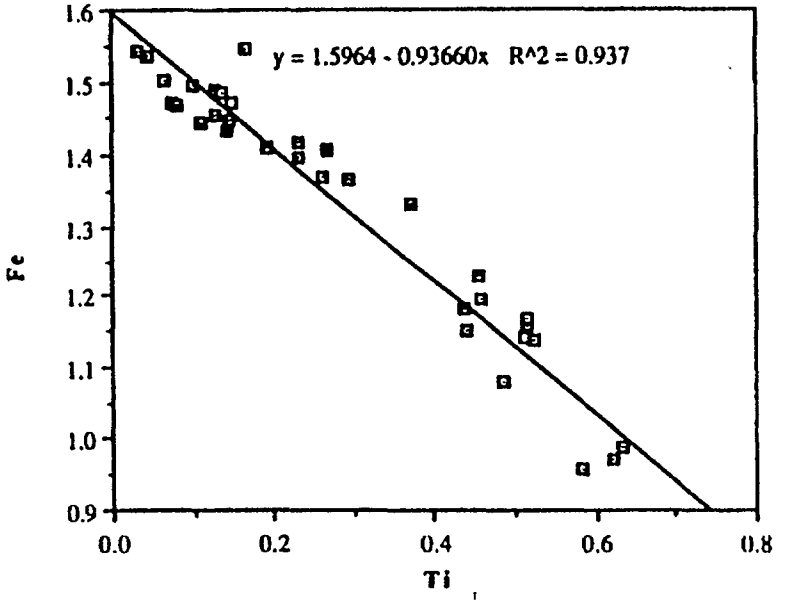

Figure 5.5 - (Fe+Al)-Ti exchange, compare with Figure 5.4. Improved fit shows that nearly all compositional variation can be explained by progress along $AlFe_{-1}$ exchange vector combined with $FeTi_{-1}$. Minor tetrahedral Fe and Al is also likely.

Figure 5.5 - (Fe+Al) - Ti Exchange in Sample 989-65a

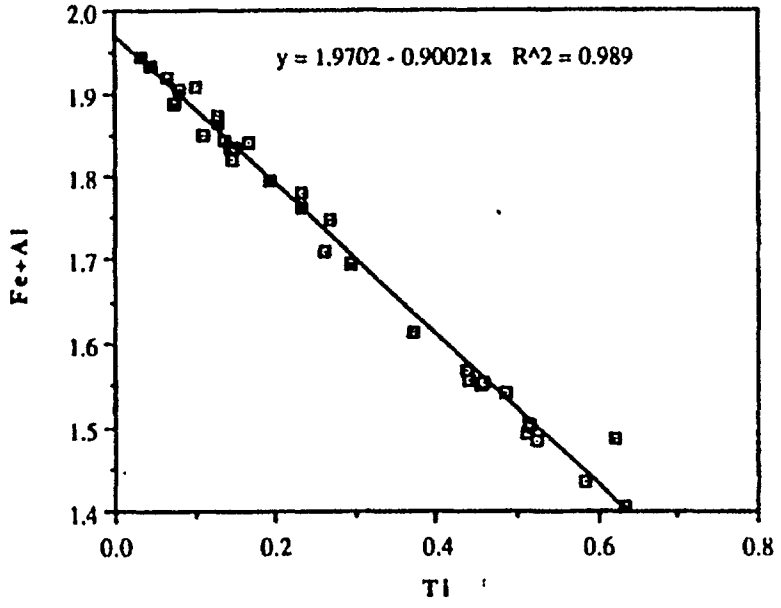

Plate 5.1 - Photo of M2 garnet vein crosscutting M1 chlorite-diopside-garnet rock, sample 989-65a. Garnet in veins is black and Ti-rich at edge, but yellow and Ti-poor in center of veins, showing that fluids precipitating garnet evolved from Ti-rich to Ti-poor compositions. Width of sample 3 cm.

serpentinized peridotite dredged from the Mid-Atlantic Ridge near 43° N. Ti-andradites also have an igneous paragenesis, in association with alkalic rocks such as nepheline syenites. The Flohr & Ross (1989) data are from Magnet Cove, Arkansas, USA, where the garnets have an igneous origin.

Figure 5.2 shows that the trends of the Onuki et al. (1981) and the Flohr & Ross (1989) analyses are roughly parallel to the S-A join at relatively constant G. One of the Onuki samples is somewhat enriched in Al (4.75 wt.% Al_2O_3). The Hermann & Müntener (1991) samples fall into two groups: a low-Ti group that lies along the S-G join and a Ti-enriched group that lies near the S-A join at low and constant Al.

I therefore conclude that the dominant exchange vector for the garnets in Figure 5.2 is along $FeTi_{-1}$, with variation along $AlFe_{-1}$ for some of the Hermann & Müntener samples.

Comparison of Figures 5.1 and 5.2 shows that the New Idria garnets very over a much wider compositional range than the garnets from other localities. This is particularly noticeable in the Al contents: some New Idria garnets are quite aluminous. Figure 5.1 also shows that some compositions lie along a trend that projects to the G-vertex. Less obvious is the observation that some garnets in Figure 5.2 also lie along this same trend. This trend is shown as a dotted line in Figure 5.1; the intersection along the S-A join is at about $S_{68}A_{32}$. The exchange vector that defines this trend is a weighted sum of the two vectors $TiFe_{-1}$ and $TiFeAl_{-2}$.

VIII. Some Crystal Chemical Considerations

Examination of Table 5.1 and 5.2 shows that most analyses have less than 3 Si cations per formula unit (pfu), and more than 3 Ca cations pfu. The New Idria garnets are

therefore similar to many other reported titaniferous garnets in that they are *subsilicic* and *supercalcic*. From a crystal chemical standpoint the subsilicic compositions can be explained by proposing that some tetrahedral sites are occupied by Al, Fe^{3+}, and even Ti^{4+}. Huggins et al. (1977a) discussed tetrahedral occupancy in titaniferous garnets and concluded that the order of preference for these cations is Al > Fe > Ti. The occurrence of more than 3 Ca cations pfu apparently requires some Ca in the octahedral sites. Müntener & Hermann (1994) suggested that the apparent Ca excess in Ti-andradites may be an artifact of the water free cation normalization, for those garnets containing a significant hydrogarnet component. However, in this study even garnets with analysis totals close to 100% (**Table 5.1**) and which therefore should have a low hydrogarnet component, appear to be supercalcic. I therefore conclude that the excess Ca is real, and may be explained by the larger octahedral site in andradite as compared to the other common garnets. According to Smyth & Bish (1988), the mean bond distance and polyhedral volume respectively in the relatively large octahedral site of andradite are 2.024Å and 11.046$Å^2$, compared with 1.924Å and 9.491$Å^2$ in grossular and 1.887Å and 8.937$Å^2$ in pyrope. However, it should be noted that the 8-coordinated site in andradite measures 2.433Å and 24.55$Å^2$ respectively, which is very much larger than the octahedral site.

IX. Exchange Vectors

In an attempt to understand the nature of Ti-Al-Fe exchange in these garnets, detailed studies of individual crystals were undertaken. **Figure 5.3** presents the results of a microprobe traverse across a garnet vein in sample 989-65A (**Plate 5.1**). The garnet vein crosscuts the foliation in a chlorite-diopside-garnet rock, and the garnets are considered to be M2. The garnets with the greatest Ti contents occur along the walls of the vein and grew earlier than the low-Ti andradites that fill the center of the vein. Whiskers of diopside attached to the vein walls are enveloped by garnet that continued to precipitate in the

absence of diopside. The inverse correlation of Ti and Fe in this traverse is striking. Figure 5.4 plots Fe-Ti exchange in the vein garnet; the inverse correlation is good and supports the the suggestion of a simple substitution of Ti for Fe, according to the exchange vector $TiFe_{-1}$. However, particularly for the low Ti-garnets the scatter in Figure 5.4 is noticeable and the Fe content at zero Ti is not two Fe atoms pfu. In these garnets an Fe-Al exchange also appears to be significant. Figure 5.5 plots Ti versus Fe+Al; the anticorrelation is further improved and the intercept is nearly 2. This figure also argues for minor, but noticeable, amounts of tetrahedral Fe and Al, possibly via vectors similar to $Ti\ ^{iv}Al\ ^{vi}Al_{-1}Si_{-1}$ and $Ti\ ^{iv}Fe\ ^{vi}Fe_{-1}Si_{-1}$, which are both equivalent to $TiSi_{-1}$.

X. A Three-Garnet Rock

In the course of this study a minor outcrop designated 990-1, in a stream gully south of the Gem Mine, was found to consist of chlorite-diopside-garnet rock with very aluminous garnets. This locality may be the same as Coleman's outcrop 92-52, although the description given by Coleman (1957) described a much larger outcrop than presently exists at 990-1. Garnets from the 990-1 locality have unusual parageneses and compositions. Figure 5.6 shows garnet analyses from this locality in the SAG projection. The compositions fall into two groups, a "normal" group and an aluminous group.

Plate 5.2 shows a backscatter electron micrograph of a sample from 990-1. In the upper portion of this photo, left of center, is a composite garnet grain containing at least three generations of garnet. The central portion in medium grey is an aluminous garnet with the composition given in Table 5.2 column 97. This earliest generation was apparently fractured, and the pieces were overgrown by a Ti-rich garnet that appears light grey in the photo (Table 5.2 column 101). Later the entire grain was overgrown by near end-member andradite that shows as white in the photo (Table 5.1 column 152). These three

compositions are the vertices of the dashed triangle in Figure 5.6. The three generations of garnet meet at two points as shown in Plate 5.2.

The host rock at the 990-1 locality is strongly foliated. The garnet textures suggest brecciation or mylonitization, and the garnets appear to have grown in a succession of equilibrium states (each garnet generation appears homogeneous). Therefore we may not conclude on the strength of this evidence that the three garnet compositions are in equilibrium with each other. The assignment of the garnets to an M1 or an M2 event is ambiguous in this sample. Apparently, the latest generation of garnet precipitated from fluids percolating through the brecciated rock,and acted as a crack-filling material that welded the rock into a dense, tough mass.

The 990-1 samples also contain REE-enriched titanite (sphene) and zircon as accessory minerals.

XI. Compositions of Minerals Coexisting with Garnet

Chapter 4 deals with chlorite-diopside-garnet rocks which are the host rock for the garnets described in this chapter. It was suggested in Chapter 4 that the ultimate source of Ti for the Ti-bearing garnets was a fertile ultramafic rock of pyroxenite composition. In such a rock Ti would have been present in Cpx and spinel. It was also suggested in Chapter 4 that the garnet-forming reactions involved the breakdown of the hedenbergite component of clinopyroxene, resulting in production of garnet, magnetite and free silica, probably SiO_2(aq). It was shown further that these reactions may have taken place under conditions of very low oxygen fugacity. The presence of small amounts of methane in fluid inclusions from the garnets of Santa Rita Peak also implies low oxygen fugacity during M2 metamorphism. Understanding the formation of the minerals in these rocks requires

Figure 5.6 - Garnet compositions in chlorite-diopside-garnet sample 990-1, projection as in Figure 5.1. Open squares are all garnet compositions. Dashed triangle with filled squares at vertices outlines compositions of three coexisiting garnets shown in Plate 5.2.

Figure 5.6 - Garnet Compositions in Sample 990-1

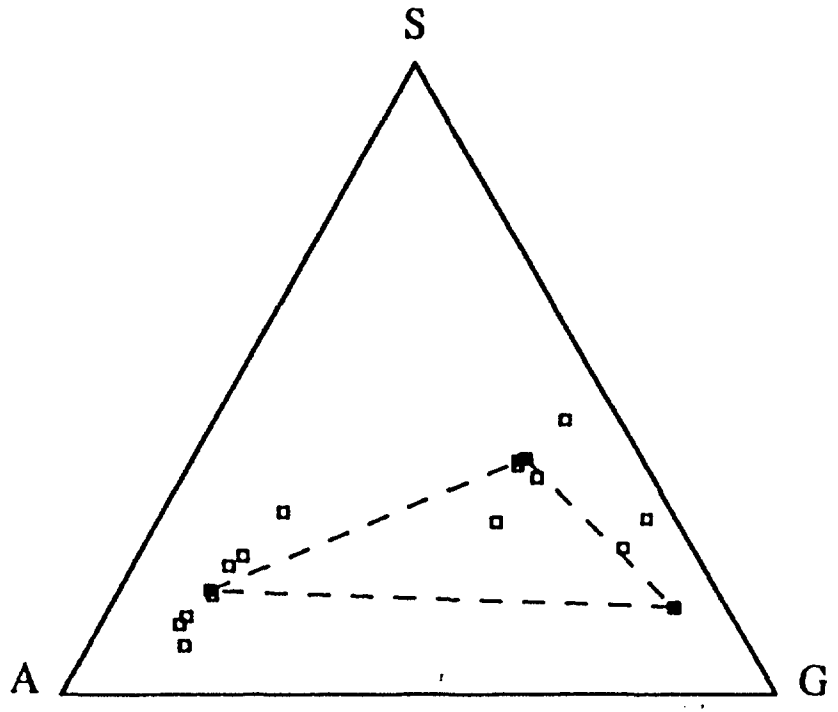

Plate 5.2 - Backscatter electron photomicrograph of sample from 990-1 locality. Three generations of garnet comprise the large grain in center. Earliest garnet (dark grey) is grossular; second generation (medium grey) is Ti-andradite; third generation (white) is Ti-free andradite. Field of view 25 µm.

knowledge of the compositions of coexisting minerals. The reader is referred to Tables 4.1, 4.2, 4.3, 5.1 and 5.2 for some of these compositions.

One New Idria sample used in this study was 92453, from the collection of the Harvard Mineralogical Museum. This sample, from an unknown location at New Idria, contains some M2 veins of homogeneous garnet coexisting with homogeneous diopside. The table below gives the mean compositions of 22 garnet and 8 diopside analyses respectively.

Oxide	garnet	diopside
SiO_2	33.74	53.09
TiO_2	8.31	0.03
Al_2O_3	3.71	0.36
Cr_2O_3	0.03	0.05
Fe_2O_3*	17.85	n.d.
FeO*	n.d.	8.18
MnO	0.18	0.40
MgO	0.27	13.33
CaO	34.68	24.63
Na_2O	n.d.	0.12
Totals	98.76	100.20

XII. The Colors of New Idria Garnets

New Idria andradite garnets occur in a variety of hues, including yellows, reds, greens, browns, and black. The colors of garnets and other minerals relate broadly to their chemical composition, both major and trace elements. The exact mechanisms are a controversial subject, and it is not the intention of this study to discuss detailed mechanisms. It is instead shown here that the colors of andradites relate in a logical manner to major element chemistry. The relationships are a useful field guide at New

Idria, but may not be universally applicable. Table 5.3 shows averaged chemical analyses for groups of garnets with a specified color.

One color series relates to the relative proportions of Ti and Fe. Groups 1-5 in Table 5.3 show increasing Ti content and decreasing Fe content, in accordance with progress along the $TiFe_{-1}$ exchange vector. Garnets with TiO_2 < 0.05 wt % (Group 1) are light green; they take the the varietal name of *demantoid*. Garnets with TiO_2 between 0.05 and 1 0 wt % (Group 2) are honey yellow, with the varietal name of *topazolite*. This group is the most widespread at New Idria. Increasing TiO_2 contents cause the color to darken: yellow-brown (Group 3) garnets have TiO_2 from about 1.0 to 2.0 wt. %. Garnets with 2.0 to 3.5 wt. % TiO_2 (Group 4) have a characteristic dull brown color, which may also be related to the greater Mn content of this group: MnO is up to ten times higher in Group 4 than in other garnets in Groups 1-5. There are two archaic varietal names for brown, manganoan andradites: *allochroite* and *polyadelphite*. Garnets with TiO_2 greater than 3.5 wt. % and low Al_2O_3 (Group 5) are a brilliant jet black: there are two varietal names used for this group, *melanite* and *schorlomite*. The distinction between melanite (under 5 wt % TiO_2), and schorlomite (> 5 wt % TiO_2.is arbitrary and based on TiO_2 content, not color. At New Idria this study shows that some garnets that chemically are in the melanite group are not in fact black, suggesting that the term melanite needs revising or abandoning.

Some New Idria garnets do not fit into the above simple color progression. Chromiferous garnets, Group 6 in Table 5.3, are emerald green and almost always anhedral. These garnets have a significant uvarovite component, and should be called chromian andradites. Aluminous garnets, Group 7 in Table 5.3, are a distinctive cinnamon brown and are frequently euhedral. These garnets have a significant

grossular component, although many are also high-Ti: these should be called titaniferous grossulars.

The determination of the exact electronic configurations responsible for the observed colors is not a goal of this study. The major color progression correlates well with progress along the $TiFe_{-1}$ exchange vector. Ti^{4+} should have no direct effect on mineral color, since it has no *3d* electrons with absorption in the visible spectrum. However, if the vector $TiFe_{-1}$ is equivalent to $TiFe^{2+}Fe^{3+}_{-2}$ then the coloring may be due to the presence of Fe^{2+} or to electron hopping between Fe and Ti ions in adjacent sites. If the vector $TiFe_{-1}$ is equivalent to $Ti^{3+}Fe^{3+}_{-1}$ then the presence of Ti^{3+}, with one *3d* electron, might have an impact on color. As discussed earlier, this possibility is considered doubtful. Elevated Mn contents are known to be related empirically to brown coloration in garnets, as evidenced by the varietal names for these types. The emerald green color of the chromian garnets is well established, as is the cinnamon color of grossular. It is interesting and perhaps relevant to note that the elevated Ti content of Group 7 garnets has no apparent effect on their color, giving further weight to the suggestion that Ti *per se* has no great coloration effect. New Idria garnets form an excellent data set for future spectroscopic studies of mineral colors.

XIII. Conclusions

1. 300 electron microprobe analyses of garnets from the New Idria District are presented. Analyses of coexisting minerals, principally chlorite and diopside, are given in Chapter 4.

2. Most of the New Idria garnets are calcic and belong to the andradite clan. Many, but not all garnets of the New Idria district are strongly anisotropic, sector twinned, and zoned. Titanium substitution occurs principally along the exchange vector $TiFe_{-1}$, making these garnets Ti-andradites. Some of the garnets are also hydrous and vary along the hydrogarnet exchange vector H_4Si_{-1}. Some of the garnets are Ti-grossulars, a portion of composition space not previously explored. Compositional variation in these garnets occurs along the vector $TiFe^{2+}Al_{-2}$. The mean TiO_2 content of the garnets in this study is 5 wt. %. One of the garnets contains 15.62 wt. % TiO_2, which corresponds to approximately one Ti atom per formula unit, i.e. the schorlomite end member.

3. At the present time that presence of Ti^{3+} in garnets has not been completely ruled out, but is only supported by indirect and equivocal evidence. $TiFe_{-1}$ substitution may be achieved by more than one crystal chemical process: the vector is equivalent to either or both of the vectors $TiFe^{2+}Fe^{3+}_{-2}$ and $Ti^{3+}Fe^{3+}_{-1}$. The $Ti^{3+}Fe^{3+}_{-1}$ vector is considered the less likely of the two, but until the proper EXAFS studies are completed, the debate will rage on. In this study using microprobe analytical techniques it was not possible to distinguish between these two possibilities and $TiFe_{-1}$ is used to describe compositional variations in garnets.

4. A representative garnet sample was also analyzed using the WDS technique for the presence of V, Zr, Sn, P, Na, and REE. All of these elements were below the detection limits of approximately 0.01 wt %.

5. Most New Idria garnets are hosted in tectonic blocks of chlorite-diopside-garnet rocks that are interpreted as metapyroxenites entrained by the serpentinite. The ultimate

source of the Ti in the Ti-garnets is from these pyroxenites. The garnets occur in two generations assigned to metamorphic events M1 and M2.

6. Most analyses have less than 3 Si cations per formula unit (pfu), and more than 3 Ca cations pfu. The New Idria garnets are therefore similar to many other reported titaniferous garnets in that they are *subsilicic* and *supercalcic*.

7. One sample contains three coexisting garnets. The garnet textures suggest brecciation or mylonitization and the garnets appear to have grown in a succession of equilibrium states (each garnet generation appears homogeneous).

8. New Idria andradite garnets occur in a variety of hues, including yellows, reds, greens, browns, and black. The colors of garnets and other minerals relate broadly to chemical composition, both major and trace elements. The principal color series is from yellow to black, correlating with progress along the $TiFe_{-1}$ exchange vector. Chromian garnets are emerald green, grossular garnets are cinnamon.

9. Ti^{4+} should have no direct effect on mineral color since it has no *3d* electrons with absorption in the visible spectrum. However, if the vector $TiFe_{-1}$ is equivalent to $TiFe^{2+}Fe^{3+}_{-2}$ then the coloring may be due to the presence of Fe^{2+} or to electron hopping between Fe and Ti ions in adjacent sites.

Table 5.1 - Preferred Garnet Analyses, Totals 99.00-101.04 wt. %												
Number ->	1	2	3	4	5	6	7	8	9	10	11	12
Sample -->	92453	92453	92453	92453	92453	92453	92453	92453	92453	92453	92453	92453
SiO2	34.86	34.03	34.04	33.91	34.10	35.01	34.03	35.73	35.12	33.79	35.07	33.66
TiO2	3.83	8.62	8.78	7.41	6.74	3.02	6.79	2.71	2.69	8.75	3.13	8.77
Al2O3	1.12	3.97	2.94	1.78	1.32	1.56	1.58	1.93	1.65	3.28	1.52	3.33
Cr2O3	0.03	0.02	0.03	0.00	0.01	0.02	0.00	0.00	0.00	0.02	0.01	0.03
Fe2O3*	25.46	17.18	18.51	20.91	22.06	25.60	22.08	25.24	25.52	18.27	25.62	18.10
MnO	0.26	0.18	0.14	0.08	0.08	0.07	0.07	0.08	0.06	0.14	0.08	0.17
MgO	0.09	0.26	0.27	0.44	0.29	0.19	0.34	0.25	0.18	0.28	0.21	0.30
CaO	33.88	34.78	34.62	34.64	34.39	34.16	34.25	34.05	34.00	34.77	34.06	34.66
Totals	99.52	99.05	99.33	99.16	99.00	99.63	99.14	100.00	99.22	99.31	99.70	99.02
Cations												
Si	2.93	2.81	2.82	2.83	2.86	2.93	2.85	2.97	2.95	2.80	2.94	2.79
Ti	0.24	0.54	0.55	0.47	0.43	0.19	0.43	0.17	0.17	0.54	0.20	0.55
Al	0.11	0.39	0.29	0.18	0.13	0.15	0.16	0.19	0.16	0.32	0.15	0.33
Cr	0.00	0.00	0.00	0.00	0.00	0.00	0.00	0.00	0.00	0.00	0.00	0.00
Fe*	1.61	1.07	1.15	1.32	1.39	1.61	1.39	1.58	1.61	1.14	1.61	1.13
Mn	0.02	0.01	0.01	0.01	0.01	0.00	0.00	0.01	0.00	0.01	0.01	0.01
Mg	0.01	0.03	0.03	0.05	0.04	0.02	0.04	0.03	0.02	0.03	0.03	0.04
Ca	3.05	3.08	3.07	3.10	3.09	3.07	3.07	3.03	3.06	3.08	3.06	3.08
Totals	7.97	7.93	7.92	7.95	7.95	7.99	7.95	7.98	7.99	7.93	7.98	7.93
Notes: all Fe expressed as Fe2O3												
Notes: cations calculated on basis of 12 oxygens												

Table 5.1

Number ->	13	14	15	16	17	18	19	20	21	22	23	24
Sample -->	92453	92453	688-4A	688-6	688-6	688-6	688-6	688-6	688-6	688-6	688-6	688-6
SiO2	33.57	33.66	36.81	34.39	34.55	34.09	34.14	33.70	33.97	34.22	33.51	34.08
TiO2	8.62	8.58	3.08	5.48	5.29	5.53	5.49	6.54	6.28	5.91	5.84	6.13
Al2O3	3.34	3.48	9.34	0.80	0.87	0.89	1.05	1.33	1.23	1.20	0.94	0.80
Cr2O3	0.02	0.03	0.13	0.03	0.02	0.03	0.02	0.03	0.05	0.05	0.03	0.04
Fe2O3*	18.31	18.02	14.97	24.47	25.06	24.42	24.40	22.78	22.94	23.70	24.47	24.82
MnO	0.18	0.15	0.21	0.20	0.16	0.20	0.15	0.20	0.22	0.20	0.18	0.21
MgO	0.33	0.31	0.32	0.47	0.45	0.41	0.40	0.33	0.30	0.29	0.32	0.36
CaO	34.67	34.91	35.12	34.33	34.34	34.27	34.26	34.31	34.44	34.32	34.36	34.18
Totals	99.03	99.13	99.97	100.18	100.74	99.85	99.93	99.22	99.42	99.98	99.67	100.63
Cations												
Si	2.79	2.79	2.94	2.87	2.87	2.86	2.86	2.83	2.85	2.86	2.82	2.84
Ti	0.54	0.53	0.19	0.34	0.33	0.35	0.35	0.41	0.40	0.37	0.37	0.38
Al	0.33	0.34	0.88	0.08	0.09	0.09	0.10	0.13	0.12	0.12	0.09	0.08
Cr	0.00	0.00	0.01	0.00	0.00	0.00	0.00	0.00	0.00	0.00	0.00	0.00
Fe*	1.14	1.12	0.90	1.54	1.57	1.54	1.54	1.44	1.45	1.49	1.55	1.55
Mn	0.01	0.01	0.01	0.01	0.01	0.01	0.01	0.01	0.02	0.01	0.01	0.01
Mg	0.04	0.04	0.04	0.06	0.06	0.05	0.05	0.04	0.04	0.04	0.04	0.04
Ca	3.09	3.10	3.01	3.07	3.06	3.08	3.07	3.09	3.10	3.07	3.10	3.05
Totals	7.94	7.94	7.98	7.98	7.97	7.98	7.98	7.97	7.97	7.96	7.99	7.96
Notes: all Fe expressed as Fe2O3												
Notes: cations calculated on basis of 12 oxygens												

Table 5.1 Folio 2

Table 5.1

Number ->	25	26	27	28	29	30	31	32	33	34	35	36
Sample -->	688-6	688-6	688-6	688-6	688-6	688-6	688-6	688-6	688-6	688-6	688-6	688-6
SiO2	34.08	34.13	33.72	33.95	33.81	33.82	34.00	33.96	34.01	33.54	33.08	33.93
TiO2	5.72	6.03	7.29	6.32	7.04	6.34	6.18	6.57	6.57	6.98	7.63	7.23
Al2O3	0.81	0.97	0.65	0.94	1.54	1.70	1.75	1.90	1.83	1.88	1.83	1.85
Cr2O3	0.06	0.05	0.05	0.04	0.04	0.04	0.03	0.01	0.05	0.04	0.03	0.04
Fe2O3*	24.53	24.22	23.41	23.26	21.81	22.40	22.69	22.44	22.40	22.26	21.65	21.39
MnO	0.15	0.14	0.18	0.20	0.20	0.17	0.19	0.15	0.16	0.21	0.20	0.17
MgO	0.34	0.33	0.40	0.37	0.35	0.32	0.28	0.29	0.28	0.28	0.29	0.29
CaO	34.24	34.36	34.43	34.36	34.58	34.67	34.57	34.52	34.30	34.23	34.28	34.52
Totals	99.92	100.23	100.12	99.46	99.37	99.46	99.70	99.85	99.59	99.43	99.00	99.42
Cations												
Si	2.85	2.85	2.82	2.85	2.83	2.83	2.84	2.83	2.84	2.81	2.78	2.83
Ti	0.36	0.38	0.46	0.40	0.44	0.40	0.39	0.41	0.41	0.44	0.48	0.45
Al	0.08	0.10	0.06	0.09	0.15	0.17	0.17	0.19	0.18	0.19	0.18	0.18
Cr	0.00	0.00	0.00	0.00	0.00	0.00	0.00	0.00	0.00	0.00	0.00	0.00
Fe*	1.55	1.52	1.47	1.47	1.37	1.41	1.43	1.41	1.41	1.40	1.37	1.34
Mn	0.01	0.01	0.01	0.01	0.01	0.01	0.01	0.01	0.01	0.01	0.01	0.01
Mg	0.04	0.04	0.05	0.05	0.04	0.04	0.03	0.04	0.03	0.03	0.04	0.04
Ca	3.07	3.07	3.08	3.09	3.10	3.11	3.09	3.08	3.07	3.07	3.09	3.09
Totals	7.97	7.97	7.96	7.97	7.96	7.98	7.97	7.96	7.95	7.96	7.96	7.95
Notes: all Fe expressed as Fe2O3												
Notes: cations calculated on basis of 12 oxygens												

Table 5.1

Number ->	37	38	39	40	41	42	43	44	45	46	47	48
Sample -->	688-6	688-6	688-6	688-6	688-6	688-6	688-6	688-6	688-6	688-6	688-6	688-6
SiO2	33.63	32.95	32.80	32.96	33.20	33.07	32.66	32.86	32.32	34.17	34.18	33.79
TiO2	8.25	9.15	9.30	8.95	9.31	10.05	10.61	11.19	11.52	5.41	5.38	5.99
Al2O3	1.75	1.68	1.65	1.87	1.97	1.76	1.55	1.41	1.05	0.85	0.84	0.78
Cr2O3	0.06	0.06	0.05	0.02	0.04	0.05	0.02	0.03	0.01	0.00	0.00	0.00
Fe2O3*	21.10	20.18	20.05	20.12	19.41	18.85	18.89	18.74	18.88	24.15	23.98	23.96
MnO	0.20	0.22	0.22	0.20	0.20	0.20	0.18	0.21	0.18	0.22	0.27	0.26
MgO	0.29	0.33	0.32	0.33	0.33	0.37	0.38	0.46	0.47	0.51	0.52	0.52
CaO	34.38	34.49	34.74	34.55	34.78	34.89	34.99	34.76	34.70	33.94	34.04	33.82
Totals	99.66	99.06	99.20	99.01	99.25	99.24	99.29	99.66	99.15	99.26	99.21	99.12
Cations												
Si	2.60	2.76	2.75	2.76	2.77	2.76	2.73	2.73	2.71	2.88	2.88	2.85
Ti	0.52	0.58	0.59	0.56	0.58	0.63	0.67	0.70	0.73	0.34	0.34	0.38
Al	0.17	0.17	0.16	0.18	0.19	0.17	0.15	0.14	0.10	0.08	0.08	0.08
Cr	0.00	0.00	0.00	0.00	0.00	0.00	0.00	0.00	0.00	0.00	0.00	0.00
Fe*	1.32	1.27	1.27	1.27	1.22	1.18	1.19	1.17	1.19	1.53	1.52	1.52
Mn	0.01	0.02	0.02	0.01	0.01	0.01	0.01	0.01	0.01	0.02	0.02	0.02
Mg	0.04	0.04	0.04	0.04	0.04	0.05	0.05	0.06	0.06	0.06	0.07	0.07
Ca	3.07	3.10	3.12	3.10	3.11	3.12	3.13	3.10	3.12	3.06	3.07	3.06
Totals	7.93	7.94	7.95	7.94	7.94	7.93	7.93	7.91	7.92	7.97	7.98	7.97
Notes: all Fe expressed as Fe2O3												
Notes: cations calculated on basis of 12 oxygens												

Table 5.1

Number ->	49	50	51	52	53	54	55	56	57	58	59	60
Sample -->	688-6	688-6	688-6	688-6	688-6	688-6	688-6	688-6	688-6	688-6	688-6	688-6
SiO2	34.32	34.02	34.24	33.70	33.91	33.65	33.83	34.06	34.03	33.96	34.05	33.96
TiO2	5.00	5.18	5.10	6.03	6.09	5.96	5.87	5.72	5.71	5.26	5.63	5.49
Al2O3	0.76	0.77	0.85	0.78	0.76	0.77	0.77	0.85	0.84	0.85	0.78	0.89
Cr2O3	0.00	0.00	0.00	0.00	0.02	0.00	0.00	0.00	0.01	0.00	0.00	0.00
Fe2O3*	24.78	24.54	24.38	24.36	24.07	24.59	24.02	24.09	23.74	24.49	23.79	24.29
MnO	0.19	0.23	0.27	0.26	0.27	0.28	0.27	0.27	0.24	0.19	0.24	0.23
MgO	0.53	0.53	0.54	0.54	0.53	0.53	0.50	0.47	0.47	0.46	0.51	0.50
CaO	33.92	34.04	33.96	33.93	33.77	33.87	33.87	34.04	34.00	33.99	34.05	33.93
Totals	99.49	99.31	99.34	99.61	99.40	99.65	99.12	99.50	99.04	99.19	99.05	99.29
Cations												
Si	2.88	2.87	2.88	2.83	2.85	2.83	2.85	2.86	2.87	2.86	2.87	2.86
Ti	0.32	0.33	0.32	0.38	0.39	0.38	0.37	0.36	0.36	0.33	0.36	0.35
Al	0.08	0.08	0.08	0.08	0.08	0.08	0.08	0.08	0.08	0.08	0.08	0.09
Cr	0.00	0.00	0.00	0.00	0.00	0.00	0.00	0.00	0.00	0.00	0.00	0.00
Fe*	1.57	1.56	1.54	1.54	1.52	1.56	1.53	1.52	1.51	1.55	1.51	1.54
Mn	0.01	0.02	0.02	0.02	0.02	0.02	0.02	0.02	0.02	0.01	0.02	0.02
Mg	0.07	0.07	0.07	0.07	0.07	0.07	0.06	0.06	0.06	0.06	0.06	0.06
Ca	3.05	3.07	3.06	3.06	3.04	3.05	3.06	3.06	3.07	3.07	3.08	3.06
Totals	7.98	7.99	7.98	7.98	7.96	7.98	7.97	7.97	7.97	7.98	7.98	7.98

Notes: all Fe expressed as Fe2O3

Notes: cations calculated on basis of 12 oxygens

Table 5.1

Number ->	61	62	63	64	65	66	67	68	69	70	71	72
Sample -->	688-6	688-6	688-6	688-6	688-6	688-6	688-6	688-6	688-6	688-6	688-6	688-6
SiO2	34.20	34.52	34.50	34.10	34.04	33.82	34.24	34.06	34.29	34.39	33.92	34.13
TiO2	5.29	5.58	5.21	5.34	6.13	6.12	5.37	5.90	5.54	5.45	5.51	5.61
Al2O3	0.93	0.94	0.96	1.09	1.42	1.14	1.03	1.00	1.01	1.12	1.15	1.13
Cr2O3	0.00	0.00	0.00	0.00	0.00	0.00	0.00	0.00	0.00	0.00	0.00	0.00
Fe2O3*	24.37	24.32	24.70	24.59	23.40	23.89	24.01	23.73	24.22	23.60	24.01	23.77
MnO	0.28	0.24	0.25	0.30	0.28	0.26	0.26	0.24	0.26	0.27	0.23	0.20
MgO	0.48	0.52	0.44	0.42	0.32	0.37	0.35	0.39	0.36	0.45	0.46	0.41
CaO	33.98	33.94	33.89	33.80	33.96	33.94	33.99	33.96	33.83	34.05	33.89	33.88
Totals	99.53	100.05	99.94	99.63	99.57	99.55	99.25	99.28	99.52	99.34	99.17	99.13
Cations												
Si	2.87	2.88	2.88	2.86	2.85	2.84	2.88	2.86	2.88	2.89	2.86	2.87
Ti	0.33	0.35	0.33	0.34	0.39	0.39	0.34	0.37	0.35	0.34	0.35	0.36
Al	0.09	0.09	0.09	0.11	0.14	0.11	0.10	0.10	0.10	0.11	0.11	0.11
Cr	0.00	0.00	0.00	0.00	0.00	0.00	0.00	0.00	0.00	0.00	0.00	0.00
Fe*	1.54	1.53	1.55	1.55	1.47	1.51	1.52	1.50	1.53	1.49	1.52	1.51
Mn	0.02	0.02	0.02	0.02	0.02	0.02	0.02	0.02	0.02	0.02	0.02	0.01
Mg	0.06	0.06	0.05	0.05	0.04	0.05	0.04	0.05	0.05	0.06	0.06	0.05
Ca	3.06	3.03	3.03	3.04	3.05	3.05	3.06	3.06	3.04	3.06	3.06	3.05
Totals	7.98	7.96	7.97	7.97	7.96	7.96	7.97	7.96	7.96	7.97	7.98	7.96
Notes: all Fe expressed as Fe2O3												
Notes: cations calculated on basis of 12 oxygens												

Table 5.1 Folio 6

Table 5.1

Number ->	73	74	75	76	77	78	79	80	81	82	83	84
Sample -->	688-6	688-6	688-6	688-6	688-6	688-6	688-7	688-7	688-7	688-7	688-7	688-7
SiO2	34.64	34.56	34.05	33.95	34.16	33.18	35.21	35.20	35.08	34.75	35.44	35.50
TiO2	5.48	5.00	6.34	6.86	6.97	10.73	0.73	0.02	0.18	0.59	0.00	0.19
Al2O3	1.12	1.88	2.02	2.00	1.96	1.64	0.41	0.22	0.17	0.17	0.25	0.22
Cr2O3	0.02	0.00	0.00	0.00	0.00	0.00	0.04	0.32	0.65	0.60	0.05	0.06
Fe2O3*	23.71	23.88	22.45	21.69	21.04	18.46	28.72	30.17	29.38	29.74	30.55	31.32
MnO	0.27	0.25	0.23	0.23	0.26	0.29	0.08	0.01	0.03	0.04	0.05	0.03
MgO	0.44	0.33	0.32	0.35	0.32	0.46	0.30	0.03	0.09	0.06	0.03	0.05
CaO	33.96	34.01	34.19	34.00	34.37	34.34	33.57	33.38	33.50	33.31	33.42	33.45
Totals	99.63	99.91	99.60	99.08	99.08	99.09	99.05	99.35	99.07	99.25	99.79	100.81
Cations												
Si	2.90	2.88	2.84	2.84	2.86	2.77	2.99	2.99	2.99	2.96	3.00	2.98
Ti	0.34	0.31	0.40	0.43	0.44	0.67	0.05	0.00	0.01	0.04	0.00	0.01
Al	0.11	0.18	0.20	0.20	0.19	0.16	0.04	0.02	0.02	0.02	0.02	0.02
Cr	0.00	0.00	0.00	0.00	0.00	0.00	0.00	0.02	0.04	0.04	0.00	0.00
Fe*	1.49	1.50	1.41	1.37	1.32	1.16	1.84	1.93	1.89	1.91	1.95	1.98
Mn	0.02	0.02	0.02	0.02	0.02	0.02	0.01	0.00	0.00	0.00	0.00	0.00
Mg	0.05	0.04	0.04	0.04	0.04	0.06	0.04	0.00	0.01	0.01	0.00	0.01
Ca	3.04	3.04	3.06	3.05	3.08	3.07	3.06	3.04	3.06	3.04	3.03	3.01
Totals	7.96	7.97	7.96	7.95	7.95	7.90	8.02	8.02	8.02	8.02	8.01	8.01

Notes: all Fe expressed as Fe2O3

Notes: cations calculated on basis of 12 oxygens

Table 5.1

Number ->	85	86	87	88	89	90	91	92	93	94	95	96
Sample -->	688-7	688-7	688-7	688-7	688-7	688-7	688-7	688-7	688-7	688-7	688-7	688-7
SiO2	34.68	34.76	34.49	34.94	34.54	35.23	35.52	35.36	35.38	35.41	35.49	34.94
TiO2	0.07	0.02	0.05	0.06	0.03	0.69	0.01	0.03	0.25	0.09	0.00	0.05
Al2O3	0.17	0.18	0.20	0.15	0.18	0.14	0.21	0.19	0.16	0.20	0.25	0.20
Cr2O3	0.11	0.14	0.23	0.17	0.19	0.52	0.08	0.09	0.36	0.12	0.06	0.12
Fe2O3*	30.65	30.22	30.60	30.37	30.69	28.83	30.15	30.10	29.97	30.19	30.41	30.96
MnO	0.04	0.05	0.05	0.00	0.02	0.03	0.00	0.04	0.03	0.00	0.01	0.03
MgO	0.07	0.11	0.06	0.06	0.11	0.06	0.09	0.05	0.06	0.48	0.04	0.06
CaO	33.35	33.54	33.47	33.43	33.42	33.70	33.32	33.55	33.42	33.15	33.43	33.37
Totals	99.14	99.00	99.15	99.18	99.18	99.20	99.38	99.41	99.62	99.64	99.70	99.74
Cations												
Si	2.96	2.97	2.95	2.98	2.95	3.00	3.01	3.00	3.00	3.00	3.01	2.97
Ti	0.00	0.00	0.00	0.00	0.00	0.04	0.00	0.00	0.02	0.01	0.00	0.00
Al	0.02	0.02	0.02	0.02	0.02	0.01	0.02	0.02	0.02	0.02	0.02	0.02
Cr	0.01	0.01	0.02	0.01	0.01	0.03	0.01	0.01	0.02	0.01	0.00	0.01
Fe*	1.97	1.95	1.97	1.95	1.98	1.84	1.93	1.92	1.91	1.92	1.94	1.98
Mn	0.00	0.00	0.00	0.00	0.00	0.00	0.00	0.00	0.00	0.00	0.00	0.00
Mg	0.01	0.01	0.01	0.01	0.01	0.01	0.01	0.01	0.01	0.06	0.01	0.01
Ca	3.05	3.07	3.07	3.06	3.06	3.07	3.03	3.05	3.03	3.01	3.03	3.04
Totals	8.03	8.04	8.04	8.03	8.04	8.01	8.01	8.02	8.01	8.02	8.01	8.03
Notes: all Fe expressed as Fe2O3												
Notes: cations calculated on basis of 12 oxygens												

Table 5.1

Number ->	97	98	99	100	101	102	103	104	105	106	107	108
Sample -->	688-7	688-7	688-7	688-7	688-7	688-7	688-7	688-7A	688-8	688-8	688-8	688-8
SiO2	35.60	35.43	35.19	35.05	35.42	35.73	36.87	35.13	34.08	33.46	33.95	33.98
TiO2	0.03	0.02	0.02	0.01	0.02	0.00	0.00	1.22	6.33	7.07	6.38	6.16
Al2O3	0.23	0.20	0.19	0.23	0.21	0.14	0.41	0.22	0.92	1.24	1.85	1.68
Cr2O3	0.51	0.15	0.12	0.17	0.13	0.21	0.30	0.07	0.03	0.04	0.05	0.04
Fe2O3*	29.64	30.44	30.83	31.19	30.84	30.48	29.79	28.95	23.11	22.38	22.13	22.62
MnO	0.03	0.00	0.00	0.06	0.05	0.04	0.00	0.01	0.18	0.20	0.19	0.21
MgO	0.77	0.02	0.14	0.04	0.05	0.04	0.89	0.30	0.37	0.36	0.31	0.30
CaO	32.95	33.57	33.39	33.30	33.35	33.56	32.78	33.60	34.01	34.27	34.18	34.10
Totals	99.76	99.82	99.88	100.05	100.07	100.20	101.04	99.50	99.01	99.03	99.04	99.08
Cations												
Si	3.00	3.00	2.98	2.97	2.99	3.01	3.05	2.97	2.87	2.82	2.85	2.85
Ti	0.00	0.00	0.00	0.00	0.00	0.00	0.00	0.08	0.40	0.45	0.40	0.39
Al	0.02	0.02	0.02	0.02	0.02	0.01	0.04	0.02	0.09	0.12	0.18	0.17
Cr	0.03	0.01	0.01	0.01	0.01	0.01	0.02	0.00	0.00	0.00	0.00	0.00
Fe*	1.88	1.94	1.97	1.99	1.96	1.93	1.86	1.84	1.46	1.42	1.40	1.43
Mn	0.00	0.00	0.00	0.00	0.00	0.00	0.00	0.00	0.01	0.01	0.01	0.01
Mg	0.10	0.00	0.02	0.01	0.01	0.01	0.11	0.04	0.05	0.05	0.04	0.04
Ca	2.98	3.04	3.03	3.02	3.02	3.03	2.91	3.05	3.07	3.09	3.07	3.07
Totals	8.02	8.02	8.02	8.02	8.01	8.01	7.99	8.01	7.95	7.96	7.96	7.96
Notes: all Fe expressed as Fe2O3												
Notes: cations calculated on basis of 12 oxygens												

Table 5.1

Number ->	109	110	111	112	113	114	115	116	117	118	119	120
Sample -->	688-8	688-8	688-8	688-8	688-8	688-8	688-8	688-8	989-65A	989-65A	989-65A	989-65A
SiO2	33.77	34.05	33.62	33.49	33.96	33.79	34.04	34.31	33.48	33.53	33.49	34.28
TiO2	6.26	6.14	5.78	7.05	6.03	7.00	5.11	5.21	8.22	8.24	8.40	4.70
Al2O3	1.69	1.72	1.34	1.19	1.80	0.93	1.60	1.80	3.51	3.53	5.14	3.33
Cr2O3	0.04	0.08	0.06	0.05	0.04	0.05	0.04	0.05	0.01	0.00	0.02	0.01
Fe2O3*	22.53	22.51	23.80	22.78	22.78	22.67	24.01	23.40	18.49	18.57	16.29	21.74
MnO	0.20	0.14	0.17	0.22	0.18	0.23	0.17	0.19	0.14	0.13	0.18	0.08
MgO	0.31	0.32	0.32	0.35	0.29	0.37	0.30	0.30	0.18	0.21	0.17	0.16
CaO	34.37	34.22	34.20	34.21	34.37	34.43	34.28	34.36	34.98	34.81	35.30	34.74
Totals	99.17	99.17	99.30	99.34	99.44	99.47	99.54	99.62	99.01	99.01	99.01	99.05
Cations												
Si	2.84	2.85	2.83	2.81	2.84	2.83	2.86	2.87	2.78	2.79	2.76	2.86
Ti	0.40	0.39	0.37	0.45	0.38	0.44	0.32	0.33	0.51	0.52	0.52	0.30
Al	0.17	0.17	0.13	0.12	0.18	0.09	0.16	0.18	0.34	0.35	0.50	0.33
Cr	0.00	0.01	0.00	0.00	0.00	0.00	0.00	0.00	0.00	0.00	0.00	0 00
Fe*	1.42	1.42	1.51	1.44	1.44	1.43	1.52	1.47	1.16	1.16	1.01	1.37
Mn	0.01	0.01	0.01	0.02	0.01	0.02	0.01	0.01	0.01	0.01	0.01	0.01
Mg	0.04	0.04	0.04	0.04	0.04	0.05	0.04	0.04	0.02	0.03	0.02	0.02
Ca	3.09	3.07	3.09	3.08	3.08	3.09	3.08	3.08	3.12	3.10	3.12	3.11
Totals	7.97	7.96	7.98	7.96	7.97	7.96	7.98	7.98	7.95	7.94	7.96	7.99
Notes: all Fe expressed as Fe2O3												
Notes: cations calculated on basis of 12 oxygens												

Table 5.1

Number ->	121	122	123	124	125	126	127	128	129	130	131	132
Sample -->	989-65A	989-65A	989-65A	989-65A	989-65A	989-65A	989-65A	989-65A	989-65A	989-65A	989-65A	989-65A
SiO2	34.14	33.63	34.19	34.84	35.21	33.67	35.21	35.15	34.91	34.64	35.34	35.30
TiO2	6.78	7.77	3.70	3.46	1.94	7.27	1.05	1.94	3.10	2.68	1.78	2.27
Al2O3	3.67	4.75	3.66	3.82	3.96	3.29	4.26	4.17	3.94	3.75	4.16	3.99
Cr2O3	0.02	0.00	0.03	0.00	0.02	0.02	0.01	0.02	0.02	0.03	0.00	0.01
Fe2O3*	19.49	17.36	22.53	22.04	23.36	19.60	23.91	23.23	22.53	23.52	23.08	23.29
MnO	0.14	0.16	0.12	0.12	0.11	0.12	0.12	0.08	0.07	0.13	0.10	0.13
MgO	0.17	0.12	0.13	0.14	0.09	0.23	0.07	0.13	0.10	0.14	0.11	0.11
CaO	34.68	35.32	34.81	34.77	34.53	35.06	34.68	34.71	34.77	34.59	34.93	34.43
Totals	99.08	99.11	99.17	99.18	99.21	99.26	99.32	99.43	99.44	99.47	99.51	99.54
Cations												
Si	2.83	2.78	2.86	2.90	2.93	2.80	2.94	2.92	2.90	2.89	2.94	2.93
Ti	0.42	0.48	0.23	0.22	0.12	0.45	0.07	0.12	0.19	0.17	0.11	0.14
Al	0.36	0.46	0.36	0.38	0.39	0.32	0.42	0.41	0.39	0.37	0.41	0.39
Cr	0.00	0.00	0.00	0.00	0.00	0.00	0.00	0.00	0.00	0.00	0.00	0.00
Fe*	1.22	1.08	1.42	1.38	1.47	1.23	1.50	1.45	1.41	1.48	1.44	1.46
Mn	0.01	0.01	0.01	0.01	0.01	0.01	0.01	0.01	0.00	0.01	0.01	0.01
Mg	0.02	0.01	0.02	0.02	0.01	0.03	0.01	0.02	0.01	0.02	0.01	0.01
Ca	3.09	3.13	3.12	3.10	3.08	3.13	3.10	3.09	3.10	3.09	3.11	3.06
Totals	7.95	7.96	8.02	8.00	8.02	7.97	8.04	8.02	8.01	8.02	8.03	8.00

Notes: all Fe expressed as Fe2O3

Notes: cations calculated on basis of 12 oxygens

Table 5.1

Number ->	133	134	135	136	137	138	139	140	141	142	143	144
Sample -->	989-65A	989-65A	989-65A	989-65A	989-65A	989-65A	989-65A	989-65A	989-65A	989-65A	989-65A	989-65A
SiO2	34.89	35.63	35.42	35.15	35.25	34.84	34.81	35.12	35.81	35.60	35.27	35.71
TiO2	2.37	0.55	1.27	1.98	2.19	3.72	2.65	2.04	1.19	2.34	2.22	1.77
Al2O3	3.69	4.11	4.44	4.37	3.90	3.74	3.00	3.91	4.25	3.84	3.68	4.47
Cr2O3	0.04	0.00	0.03	0.00	0.03	0.01	0.04	0.01	0.01	0.01	0.00	0.02
Fe2O3*	23.49	24.64	23.56	23.32	23.40	22.38	24.63	23.86	23.68	23.28	23.79	23.28
MnO	0.10	0.13	0.10	0.12	0.10	0.10	0.09	0.09	0.11	0.08	0.12	0.12
MgO	0.11	0.05	0.11	0.10	0.13	0.13	0.11	0.07	0.08	0.10	0.10	0.10
CaO	34.88	34.55	34.81	34.69	34.73	34.87	34.48	34.75	34.78	34.73	34.79	34.66
Totals	99.57	99.67	99.73	99.74	99.74	99.79	99.82	99.86	99.92	99.98	99.98	100.12
Cations												
Si	2.91	2.96	2.94	2.91	2.92	2.89	2.90	2.91	2.96	2.94	2.92	2.94
Ti	0.15	0.03	0.08	0.12	0.14	0.23	0.17	0.13	0.07	0.15	0.14	0.11
Al	0.36	0.40	0.43	0.43	0.38	0.37	0.29	0.38	0.41	0.37	0.36	0.43
Cr	0.00	0.00	0.00	0.00	0.00	0.00	0.00	0.00	0.00	0.00	0.00	0.00
Fe*	1.47	1.54	1.47	1.45	1.46	1.40	1.55	1.49	1.47	1.45	1.48	1.44
Mn	0.01	0.01	0.01	0.01	0.01	0.01	0.01	0.01	0.01	0.01	0.01	0.01
Mg	0.01	0.01	0.01	0.01	0.02	0.02	0.01	0.01	0.01	0.01	0.01	0.01
Ca	3.11	3.08	3.09	3.08	3.09	3.10	3.08	3.09	3.08	3.07	3.09	3.06
Totals	8.03	8.03	8.03	8.02	8.02	8.00	8.01	8.02	8.02	8.00	8.02	8.01
Notes: all Fe expressed as Fe2O3												
Notes: cations calculated on basis of 12 oxygens												

Table 5.1

Number ->	145	146	147	148	149	150	151	152	153	154	155	156
Sample -->	989-65A	989-65A	989-65A	989-65A	990-1	990-1	990-1	990-1	990-1	GT-A	GT-A	GT-A
SiO2	35.55	35.38	35.95	35.67	35.47	35.26	35.01	35.52	35.37	34.90	35.35	35.81
TiO2	2.04	1.62	0.71	1.77	5.68	1.88	1.72	2.52	2.50	1.74	0.85	0.43
Al2O3	4.21	4.25	4.06	4.02	10.49	2.24	2.14	2.51	2.68	1.83	2.47	0.44
Cr2O3	0.02	0.01	0.00	0.03	0.08	0.03	0.07	0.02	0.04	0.56	0.07	0.00
Fe2O3*	23.45	24.04	24.76	23.89	11.17	25.11	25.53	24.30	24.78	25.62	26.26	28.86
MnO	0.11	0.12	0.13	0.09	0.31	0.14	0.12	0.10	0.08	0.00	0.05	0.05
MgO	0.08	0.08	0.07	0.09	0.06	0.21	0.20	0.20	0.18	0.32	0.22	0.20
CaO	34.69	34.69	34.64	34.82	35.80	34.25	34.39	34.46	34.42	34.07	33.92	33.44
Totals	100.15	100.19	100.32	100.38	99.06	99.13	99.18	99.64	100.04	99.04	99.19	99.23
Cations												
Si	2.93	2.92	2.97	2.94	2.85	2.96	2.95	2.96	2.94	2.94	2.97	3.03
Ti	0.13	0.10	0.04	0.11	0.34	0.12	0.11	0.16	0.16	0.11	0.05	0.03
Al	0.41	0.41	0.39	0.39	0.99	0.22	0.21	0.25	0.26	0.18	0.24	0.04
Cr	0.00	0.00	0.00	0.00	0.01	0.00	0.00	0.00	0.00	0.04	0.00	0.00
Fe*	1.46	1.49	1.54	1.48	0.67	1.59	1.62	1.52	1.55	1.63	1.66	1.84
Mn	0.01	0.01	0.01	0.01	0.02	0.01	0.01	0.01	0.01	0.00	0.00	0.00
Mg	0.01	0.01	0.01	0.01	0.01	0.03	0.03	0.02	0.02	0.04	0.03	0.03
Ca	3.07	3.07	3.06	3.07	3.08	3.08	3.10	3.08	3.06	3.08	3.05	3.03
Totals	8.01	8.02	8.02	8.01	7.97	8.01	8.03	8.00	8.00	8.02	8.02	8.00

Notes: all Fe expressed as Fe2O3

Notes: cations calculated on basis of 12 oxygens

								Table 5.1
Number ->	157	158	159	160	161	162		Means
Sample -->	GT-A	GT-A	GT-A	GT-B	GT-B	GT-B		99-100%
SiO2	35.09	35.49	35.64	34.63	34.83	35.47		34.47
TiO2	0.96	1.05	0.04	3.11	2.70	0.87		4.40
Al2O3	0.28	1.60	0.42	1.35	2.16	0.35		1.85
Cr2O3	0.00	0.03	0.02	0.00	0.03	0.03		0.06
Fe2O3*	28.91	27.41	30.14	25.51	25.28	29.21		24.08
MnO	0.05	0.07	0.04	0.17	0.17	0.03		0.15
MgO	0.28	0.22	0.03	0.44	0.33	0.29		0.27
CaO	33.78	33.96	33.62	33.97	34.10	33.66		34.21
Totals	99.34	99.83	99.94	99.17	99.60	99.92		99.50
Cations								
Si	2.98	2.98	3.01	2.92	2.92	2.99		2.89
Ti	0.06	0.07	0.00	0.20	0.17	0.06		0.28
Al	0.03	0.16	0.04	0.13	0.21	0.03		0.18
Cr	0.00	0.00	0.00	0.00	0.00	0.00		0.00
Fe*	1.85	1.73	1.91	1.62	1.59	1.85		1.52
Mn	0.00	0.00	0.00	0.01	0.01	0.00		0.01
Mg	0.04	0.03	0.00	0.06	0.04	0.04		0.03
Ca	3.07	3.05	3.04	3.07	3.06	3.04		3.07
Totals	8.02	8.01	8.01	8.01	8.01	8.01		7.98
Notes: all Fe expressed as Fe2O3								
Notes: cations calculated on basis of 12 oxygens								

Table 5.2 - Additional New Idria Garnet Analyses, Totals 97.00-98.99 wt. %												
Number ->	1	2	3	4	5	6	7	8	9	10	11	12
Sample -->	92453	92453	92453	92453	92453	92453	92453	92453	92453	92453	92453	92453
SiO2	33.30	33.71	33.86	33.65	33.78	33.61	33.90	33.97	33.49	34.05	33.49	33.60
TiO2	8.30	8.59	8.15	8.10	8.59	8.48	8.45	6.02	9.08	8.27	9.01	7.49
Al2O3	4.42	3.90	4.79	4.86	4.31	4.31	4.77	0.89	3.44	4.74	3.55	1.84
Cr2O3	0.03	0.03	0.03	0.01	0.02	0.04	0.01	0.03	0.00	0.02	0.00	0.07
Fe2O3*	16.79	16.97	16.11	16.48	16.46	16.59	16.08	23.22	17.44	16.32	17.53	21.11
MnO	0.21	0.18	0.23	0.20	0.20	0.23	0.22	0.08	0.17	0.18	0.18	0.20
MgO	0.25	0.27	0.22	0.21	0.29	0.31	0.24	0.21	0.39	0.24	0.38	0.27
CaO	34.66	34.54	34.84	34.77	34.69	34.79	34.80	34.14	34.55	34.82	34.50	34.12
Totals	98.01	98.19	98.23	98.28	98.33	98.36	98.48	98.55	98.57	98.63	98.64	98.70
Cations												
Si	2.79	2.81	2.81	2.80	2.81	2.79	2.81	2.88	2.79	2.81	2.79	2.82
Ti	0.52	0.54	0.51	0.51	0.54	0.53	0.53	0.38	0.57	0.51	0.56	0.47
Al	0.44	0.38	0.47	0.48	0.42	0.42	0.47	0.09	0.34	0.46	0.35	0.18
Cr	0.00	0.00	0.00	0.00	0.00	0.00	0.00	0.00	0.00	0.00	0.00	0.00
Fe*	1.06	1.06	1.01	1.03	1.03	1.04	1.00	1.48	1.09	1.02	1.10	1.34
Mn	0.01	0.01	0.02	0.01	0.01	0.02	0.02	0.01	0.01	0.01	0.01	0.01
Mg	0.03	0.03	0.03	0.03	0.04	0.04	0.03	0.03	0.05	0.03	0.05	0.03
Ca	3.10	3.08	3.10	3.10	3.09	3.10	3.09	3.10	3.08	3.08	3.07	3.07
Totals	7.95	7.93	7.94	7.94	7.93	7.94	7.93	7.96	7.93	7.93	7.93	7.94
Notes: all Fe expressed as Fe2O3												
Notes: cations calculated on basis of 12 oxygens												

Table 5.2

Number ->	13	14	15	16	17	18	19	20	21	22	23	24
Sample -->	92453	92453	92453	92453	92453	92453	92453	92453	688-4	688-4	688-4A	688-6
SiO2	33.79	33.58	33.57	33.40	33.57	33.45	33.41	33.52	32.51	32.32	33.70	33.57
TiO2	8.29	8.80	8.71	8.64	9.02	8.85	8.89	9.03	11.37	11.89	6.22	5.48
Al2O3	4.68	3.54	3.22	3.48	3.59	3.47	3.67	3.53	0.49	0.51	6.29	0.71
Cr2O3	0.02	0.00	0.01	0.02	0.04	0.02	0.01	0.00	0.07	0.03	0.16	0.01
Fe2O3*	16.68	17.79	18.20	17.94	17.46	17.96	17.70	17.75	18.31	18.11	15.99	23.04
MnO	0.19	0.11	0.15	0.19	0.13	0.14	0.14	0.16	0.28	0.35	0.22	0.12
MgO	0.24	0.32	0.28	0.31	0.30	0.34	0.32	0.37	0.71	0.77	0.04	0.50
CaO	34.87	34.67	34.67	34.86	34.76	34.65	34.79	34.55	33.84	33.71	34.77	33.66
Totals	98.76	98.80	98.82	98.85	98.87	98.87	98.92	98.93	97.59	97.69	97.40	97.10
Cations												
Si	2.80	2.79	2.79	2.78	2.79	2.78	2.77	2.78	2.76	2.74	2.82	2.89
Ti	0.52	0.55	0.55	0.54	0.56	0.55	0.56	0.56	0.73	0.76	0.39	0.35
Al	0.46	0.35	0.32	0.34	0.35	0.34	0.36	0.35	0.05	0.05	0.62	0.07
Cr	0.00	0.00	0.00	0.00	0.00	0.00	0.00	0.00	0.00	0.00	0.01	0.00
Fe*	1.04	1.11	1.14	1.12	1.09	1.12	1.11	1.11	1.17	1.16	1.01	1.49
Mn	0.01	0.01	0.01	0.01	0.01	0.01	0.01	0.01	0.02	0.03	0.02	0.01
Mg	0.03	0.04	0.03	0.04	0.04	0.04	0.04	0.05	0.09	0.10	0.00	0.06
Ca	3.09	3.09	3.09	3.11	3.09	3.09	3.09	3.07	3.08	3.06	3.11	3.10
Totals	7.94	7.93	7.93	7.95	7.93	7.93	7.94	7.93	7.90	7.90	7.98	7.98

Notes: all Fe expressed as Fe2O3

Notes: cations calculated on basis of 12 oxygens

Table 5.2 Folio 2

Table 5.2

Number ->	25	26	27	28	29	30	31	32	33	34	35	36
Sample -->	688-6	688-6	688-6	688-6	688-6	688-6	688-6	688-6	688-6	688-6	688-6	688-6
SiO2	33.76	33.09	33.28	33.88	33.35	33.66	32.72	33.63	33.72	33.75	33.72	33.68
TiO2	5.48	7.42	5.58	5.38	5.84	5.51	9.28	7.64	6.24	5.52	6.37	6.91
Al2O3	0.73	1.92	0.73	0.76	0.70	0.73	1.66	1.88	0.82	0.75	1.86	2.01
Cr2O3	0.00	0.00	0.00	0.03	0.01	0.00	0.06	0.00	0.02	0.04	0.05	0.02
Fe2O3*	23.15	20.64	23.45	23.41	23.31	23.40	19.41	20.43	22.97	23.39	21.70	21.11
MnO	0.15	0.10	0.13	0.21	0.16	0.18	0.19	0.11	0.20	0.18	0.17	0.15
MgO	0.48	0.30	0.50	0.49	0.49	0.46	0.35	0.28	0.38	0.49	0.27	0.27
CaO	33.48	33.90	33.74	33.36	33.67	33.61	34.26	33.96	33.66	33.94	34.13	34.12
Totals	97.22	97.38	97.42	97.53	97.54	97.55	97.93	97.94	98.01	98.08	98.26	98.27
Cations												
Si	2.90	2.82	2.86	2.90	2.86	2.88	2.77	2.84	2.87	2.88	2.85	2.84
Ti	0.35	0.48	0.36	0.35	0.38	0.35	0.59	0.49	0.40	0.35	0.40	0.44
Al	0.07	0.19	0.07	0.08	0.07	0.07	0.17	0.19	0.08	0.08	0.19	0.20
Cr	0.00	0.00	0.00	0.00	0.00	0.00	0.00	0.00	0.00	0.00	0.00	0.00
Fe*	1.49	1.32	1.52	1.51	1.50	1.51	1.24	1.30	1.47	1.50	1.38	1.34
Mn	0.01	0.01	0.01	0.02	0.01	0.01	0.01	0.01	0.01	0.01	0.01	0.01
Mg	0.06	0.04	0.06	0.06	0.06	0.06	0.04	0.04	0.05	0.06	0.03	0.03
Ca	3.08	3.09	3.10	3.06	3.09	3.08	3.11	3.07	3.07	3.10	3.09	3.08
Totals	7.97	7.95	7.99	7.96	7.98	7.97	7.93	7.93	7.95	7.98	7.96	7.95

Notes: all Fe expressed as Fe2O3

Notes: cations calculated on basis of 12 oxygens

Table 5.2

Number ->	37	38	39	40	41	42	43	44	45	46	47	48
Sample -->	688-6	688-6	688-6	688-6	688-6	688-6	688-6	688-6	688-6	688-6	688-6	688-6
SiO2	33.69	32.33	32.35	33.79	33.46	33.79	32.61	33.67	33.91	33.50	33.25	33.18
TiO2	6.36	11.23	12.19	5.23	9.12	5.47	12.33	6.29	5.34	6.70	9.42	8.88
Al2O3	0.93	1.46	0.98	1.20	1.99	0.88	1.15	0.77	1.25	1.82	1.84	1.68
Cr2O3	0.00	0.02	0.13	0.04	0.00	0.00	0.02	0.01	0.00	0.05	0.00	0.03
Fe2O3*	22.94	18.37	17.63	23.63	19.17	24.04	17.35	23.24	23.89	22.12	19.43	20.05
MnO	0.26	0.27	0.22	0.16	0.26	0.25	0.27	0.27	0.26	0.17	0.24	0.24
MgO	0.42	0.46	0.66	0.36	0.36	0.49	0.71	0.51	0.41	0.28	0.36	0.33
CaO	33.82	34.35	34.36	34.22	34.33	33.80	34.31	34.02	33.76	34.21	34.33	34.48
Totals	98.43	98.49	98.52	98.63	98.68	98.72	98.75	98.78	98.82	98.85	98.86	98.87
Cations												
Si	2.86	2.72	2.72	2.86	2.80	2.86	2.73	2.85	2.86	2.82	2.78	2.78
Ti	0.41	0.71	0.77	0.33	0.57	0.35	0.78	0.40	0.34	0.42	0.59	0.56
Al	0.09	0.14	0.10	0.12	0.20	0.09	0.11	0.08	0.12	0.18	0.18	0.17
Cr	0.00	0.00	0.01	0.00	0.00	0.00	0.00	0.00	0.00	0.00	0.00	0.00
Fe*	1.46	1.16	1.11	1.51	1.21	1.53	1.09	1.48	1.52	1.40	1.22	1.27
Mn	0.02	0.02	0.02	0.01	0.02	0.02	0.02	0.02	0.02	0.01	0.02	0.02
Mg	0.05	0.06	0.08	0.05	0.04	0.06	0.09	0.06	0.05	0.04	0.04	0.04
Ca	3.07	3.10	3.09	3.11	3.08	3.07	3.08	3.08	3.06	3.09	3.08	3.10
Totals	7.96	7.91	7.90	7.99	7.92	7.98	7.89	7.97	7.97	7.96	7.92	7.94

Notes: all Fe expressed as Fe2O3

Notes: cations calculated on basis of 12 oxygens

Table 5.2

Number ->	49	50	51	52	53	54	55	56	57	58	59	60
Sample -->	688-6	688-6	688-6	688-6	688-6	688-7	688-7	688-7	688-7	688-7	688-7	688-7
SiO2	33.56	34.02	33.85	32.72	32.41	37.54	34.97	37.68	34.38	34.75	35.04	35.20
TiO2	6.71	5.45	5.35	11.21	11.30	0.01	1.34	0.00	0.01	0.02	0.75	0.73
Al2O3	1.79	0.82	0.81	1.22	1.38	0.33	0.34	0.41	0.18	0.17	0.46	0.39
Cr2O3	0.01	0.00	0.00	0.00	0.06	0.06	0.17	0.14	0.08	0.14	0.07	0.02
Fe2O3*	22.20	24.00	24.55	18.90	18.55	20.00	27.54	20.86	29.70	29.44	28.61	28.65
MnO	0.17	0.23	0.27	0.27	0.21	0.03	0.06	0.04	0.04	0.03	0.12	0.06
MgO	0.28	0.46	0.48	0.48	0.43	17.05	0.34	19.20	0.13	0.25	0.26	0.27
CaO	34.16	33.90	33.64	34.15	34.64	22.59	33.13	19.63	33.53	33.48	33.17	33.25
Totals	98.88	98.88	98.93	98.96	98.98	97.60	97.89	97.97	98.05	98.28	98.48	98.58
Cations												
Si	2.82	2.88	2.86	2.74	2.72	3.04	3.00	3.02	2.97	2.99	2.99	3.00
Ti	0.42	0.35	0.34	0.71	0.71	0.00	0.09	0.00	0.00	0.00	0.05	0.05
Al	0.18	0.08	0.08	0.12	0.14	0.03	0.03	0.04	0.02	0.02	0.05	0.04
Cr	0.00	0.00	0.00	0.00	0.00	0.00	0.01	0.01	0.01	0.01	0.00	0.00
Fe*	1.41	1.53	1.56	1.19	1.17	1.22	1.78	1.26	1.93	1.91	1.84	1.84
Mn	0.01	0.02	0.02	0.02	0.01	0.00	0.00	0.00	0.00	0.00	0.01	0.00
Mg	0.04	0.06	0.06	0.06	0.05	2.06	0.04	2.30	0.02	0.03	0.03	0.03
Ca	3.08	3.07	3.05	3.06	3.11	1.96	3.04	1.69	3.10	3.09	3.04	3.04
Totals	7.96	7.97	7.98	7.90	7.92	8.33	8.00	8.32	8.05	8.04	8.01	8.01

Notes: all Fe expressed as Fe2O3

Notes: cations calculated on basis of 12 oxygens

Table 5.2

Number ->	61	62	63	64	65	66	67	68	69	70	71	72
Sample -->	688-7	688-7	688-7	688-7	688-7	688-7A	688-8	688-8	688-8	688-8	688-8	688-8
SiO2	34.27	35.17	34.89	36.58	34.71	35.40	33.81	33.72	33.77	33.40	33.84	33.54
TiO2	0.05	1.32	0.03	0.00	0.02	0.35	6.31	6.13	6.32	6.75	6.21	6.95
Al2O3	0.18	0.31	0.17	0.27	0.16	0.37	1.84	1.72	1.71	1.87	1.73	1.55
Cr2O3	0.19	0.19	0.12	0.05	0.11	0.03	0.06	0.05	0.04	0.03	0.03	0.04
Fe2O3*	30.63	28.21	30.09	26.62	30.36	28.88	22.37	22.49	22.09	21.77	22.46	22.26
MnO	0.03	0.05	0.01	0.02	0.01	0.08	0.18	0.15	0.18	0.15	0.18	0.21
MgO	0.07	0.34	0.28	5.38	0.07	0.23	0.26	0.30	0.32	0.28	0.29	0.34
CaO	33.44	33.31	33.32	29.99	33.55	33.57	33.83	34.19	34.36	34.52	34.17	34.06
Totals	98.85	98.90	98.91	98.92	98.99	98.90	98.66	98.75	98.77	98.78	98.92	98.95
Cations												
Si	2.94	2.99	2.98	3.05	2.97	3.01	2.85	2.84	2.84	2.81	2.85	2.82
Ti	0.00	0.08	0.00	0.00	0.00	0.02	0.40	0.39	0.40	0.43	0.39	0.44
Al	0.02	0.03	0.02	0.03	0.02	0.04	0.18	0.17	0.17	0.19	0.17	0.15
Cr	0.01	0.01	0.01	0.00	0.01	0.00	0.00	0.00	0.00	0.00	0.00	0.00
Fe*	1.98	1.80	1.94	1.67	1.96	1.85	1.42	1.43	1.40	1.38	1.42	1.41
Mn	0.00	0.00	0.00	0.00	0.00	0.01	0.01	0.01	0.01	0.01	0.01	0.01
Mg	0.01	0.04	0.04	0.67	0.01	0.03	0.03	0.04	0.04	0.04	0.04	0.04
Ca	3.08	3.03	3.05	2.68	3.08	3.06	3.05	3.09	3.10	3.12	3.08	3.07
Totals	8.05	8.00	8.03	8.10	8.04	8.02	7.95	7.97	7.97	7.97	7.96	7.96
Notes: all Fe expressed as Fe2O3												
Notes: cations calculated on basis of 12 oxygens												

Table 5.2

Number ->	73	74	75	76	77	78	79	80	81	82	83	84
Sample -->	688-8	688-8C	688-8C	989-65A	989-65A	989-65A	989-65A	989-65A	989-65A	989-65A	989-65A	989-65A
SiO2	33.40	31.45	34.78	32.54	33.05	32.43	32.96	33.23	33.38	33.59	33.89	33.36
TiO2	6.88	15.62	8.97	9.75	9.29	10.09	8.29	8.92	8.27	7.01	6.33	7.29
Al2O3	1.49	0.59	0.85	4.94	4.85	4.22	3.50	3.41	4.75	4.13	4.03	3.65
Cr2O3	0.06	0.27	0.61	0.02	0.03	0.04	0.03	0.03	0.00	0.04	0.03	0.00
Fe2O3*	22.46	15.33	17.63	14.79	15.27	15.69	17.99	17.62	16.54	16.29	19.08	18.98
MnO	0.22	0.26	0.27	0.18	0.16	0.15	0.13	0.17	0.13	0.20	0.16	0.13
MgO	0.35	1.41	3.08	0.14	0.12	0.15	0.20	0.23	0.13	0.15	0.15	0.17
CaO	34.11	32.24	31.97	35.24	35.12	35.25	34.98	34.70	35.20	35.05	34.87	35.01
Totals	98.97	97.18	98.16	97.60	97.89	98.02	98.09	98.31	98.38	98.46	98.54	98.59
Cations												
Si	2.81	2.66	2.89	2.72	2.76	2.71	2.77	2.78	2.78	2.81	2.83	2.79
Ti	0.44	0.99	0.56	0.61	0.58	0.64	0.52	0.56	0.52	0.44	0.40	0.46
Al	0.15	0.06	0.08	0.49	0.48	0.42	0.35	0.34	0.47	0.41	0.40	0.36
Cr	0.00	0.02	0.04	0.00	0.00	0.00	0.00	0.00	0.00	0.00	0.00	0.00
Fe*	1.42	0.98	1.10	0.93	0.96	0.99	1.14	1.11	1.04	1.15	1.20	1.19
Mn	0.02	0.02	0.02	0.01	0.01	0.01	0.01	0.01	0.01	0.01	0.01	0.01
Mg	0.04	0.18	0.38	0.02	0.01	0.02	0.03	0.03	0.02	0.02	0.02	0.02
Ca	3.08	2.92	2.85	3.16	3.14	3.16	3.15	3.11	3.14	3.14	3.12	3.14
Totals	7.96	7.82	7.93	7.95	7.94	7.95	7.96	7.94	7.96	7.97	7.97	7.97

Notes: all Fe expressed as Fe2O3

Notes: cations calculated on basis of 12 oxygens

Table 5.2

Number ->	85	86	87	88	89	90	91	92	93	94	95	96
Sample -->	989-65A	989-65A	989-65A	989-65A	989-65A	989-65A	989-65A	989-65A	989-65A	989-65A	989-65A	989-65A
SiO2	33.70	34.31	33.42	33.15	34.48	33.77	33.41	32.73	33.60	35.04	33.82	34.08
TiO2	4.23	4.17	8.14	8.20	2.70	6.97	5.71	10.02	8.36	2.27	5.92	4.78
Al2O3	3.44	3.45	3.60	3.42	3.78	3.93	3.27	5.30	4.44	4.07	2.85	3.17
Cr2O3	0.02	0.01	0.03	0.05	0.03	0.01	0.01	0.07	0.05	0.02	0.02	0.02
Fe2O3*	22.21	21.70	18.18	18.57	22.90	18.85	21.34	15.61	16.90	22.84	21.13	21.87
MnO	0.11	0.12	0.14	0.18	0.08	0.17	0.09	0.13	0.13	0.11	0.10	0.11
MgO	0.13	0.13	0.21	0.17	0.14	0.14	0.13	0.18	0.13	0.10	0.20	0.18
CaO	34.76	34.81	35.00	34.97	34.66	34.99	34.91	34.85	35.27	34.48	34.92	34.76
Totals	98.60	98.70	98.71	98.71	98.78	98.84	98.87	98.88	98.88	98.94	98.96	98.96
Cations												
Si	2.84	2.88	2.79	2.77	2.89	2.81	2.80	2.70	2.78	2.93	2.83	2.85
Ti	0.27	0.26	0.51	0.52	0.17	0.44	0.36	0.62	0.52	0.14	0.37	0.30
Al	0.34	0.34	0.35	0.34	0.37	0.39	0.32	0.52	0.43	0.40	0.28	0.31
Cr	0.00	0.00	0.00	0.00	0.00	0.00	0.00	0.00	0.00	0.00	0.00	0.00
Fe*	1.41	1.37	1.14	1.17	1.45	1.18	1.35	0.97	1.05	1.44	1.33	1.38
Mn	0.01	0.01	0.01	0.01	0.01	0.01	0.01	0.01	0.01	0.01	0.01	0.01
Mg	0.02	0.02	0.03	0.02	0.02	0.02	0.02	0.02	0.02	0.01	0.02	0.02
Ca	3.14	3.13	3.13	3.13	3.12	3.12	3.14	3.08	3.13	3.09	3.13	3.12
Totals	8.02	8.00	7.96	7.96	8.03	7.97	8.00	7.93	7.95	8.01	7.99	8.00
Notes: all Fe expressed as Fe2O3												
Notes: cations calculated on basis of 12 oxygens												

Table 5.2 Folio 8

Table 5.2

Number ->	97	98	99	100	101	102	103	104	105	106	107	108
Sample -->	990-1	990-1	990-1	990-1	990-1	990-1	990-1	990-1	990-1	990-1	990-1	990-1
SiO2	36.76	36.30	36.41	33.69	34.51	34.70	34.56	34.23	35.50	34.95	35.07	34.74
TiO2	2.13	4.19	3.70	4.53	6.10	5.92	7.28	1.19	4.49	6.11	3.41	3.19
Al2O3	15.43	13.14	13.72	3.35	9.67	9.55	10.40	2.66	9.87	9.60	2.86	2.66
Cr2O3	0.01	0.17	0.00	0.13	0.18	0.23	0.12	0.03	0.21	0.16	0.05	0.13
Fe2O3*	4.42	5.46	6.83	21.40	11.45	11.80	9.85	25.57	12.71	11.97	22.93	23.73
MnO	0.20	0.15	0.09	0.13	0.26	0.29	0.27	0.06	0.44	0.31	0.09	0.07
MgO	2.34	2.79	1.48	0.25	0.08	0.08	0.08	0.32	0.06	0.07	0.19	0.22
CaO	35.78	35.09	35.55	34.34	35.69	35.69	35.80	34.35	35.47	35.63	34.21	34.19
Totals	97.06	97.29	97.80	97.82	97.93	98.25	98.36	98.40	98.75	98.80	98.81	98.92
Cations												
Si	2.92	2.90	2.90	2.85	2.82	2.83	2.79	2.91	2.87	2.83	2.94	2.92
Ti	0.13	0.25	0.22	0.29	0.37	0.36	0.44	0.08	0.27	0.37	0.21	0.20
Al	1.45	1.24	1.29	0.33	0.93	0.92	0.99	0.27	0.94	0.92	0.28	0.26
Cr	0.00	0.01	0.00	0.01	0.01	0.01	0.01	0.00	0.01	0.01	0.00	0.01
Fe*	0.26	0.33	0.41	1.36	0.70	0.72	0.60	1.64	0.77	0.73	1.45	1.50
Mn	0.01	0.01	0.01	0.01	0.02	0.02	0.02	0.00	0.03	0.02	0.01	0.00
Mg	0.28	0.33	0.18	0.03	0.01	0.01	0.01	0.04	0.01	0.01	0.02	0.03
Ca	3.05	3.00	3.03	3.12	3.12	3.11	3.10	3.13	3.08	3.09	3.07	3.08
Totals	8.10	8.06	8.03	8.01	7.99	7.99	7.96	8.06	7.99	7.97	7.98	8.00

Notes: all Fe expressed as Fe2O3

Notes: cations calculated on basis of 12 oxygens

Table 5.2

Number ->	109	110	111	112	113	114	115	116	117	118	119	120
Sample -->	GT-A	GT-A	GT-A	GT-A	GT-A	GT-A	GT-A	GT-A	GT-A	GT-A	GT-A	GT-A
SiO2	33.60	33.50	33.79	34.55	35.32	35.29	34.90	35.00	35.35	34.86	35.11	35.01
TiO2	0.03	0.01	0.03	2.78	2.05	0.40	1.93	0.01	1.70	2.35	1.98	1.95
Al2O3	2.14	1.95	1.85	1.18	3.21	0.55	1.54	0.37	1.73	1.69	2.90	1.95
Cr2O3	0.00	0.00	0.00	0.02	5.41	0.01	0.00	0.01	0.00	2.12	4.46	0.01
Fe2O3*	27.09	27.56	27.54	24.80	17.60	28.36	26.12	29.70	25.59	23.31	19.63	25.47
MnO	0.00	0.00	0.00	0.02	0.01	0.05	0.04	0.03	0.05	0.04	0.00	0.04
MgO	0.18	0.53	0.18	0.47	0.43	0.19	0.35	0.01	0.37	0.32	0.40	0.34
CaO	34.06	33.86	34.26	34.22	34.24	33.60	33.65	33.46	33.90	34.17	34.40	34.14
Totals	97.09	97.40	97.65	98.06	98.26	98.46	98.52	98.59	98.69	98.86	98.87	98.90
Cations												
Si	2.91	2.90	2.92	2.95	2.96	3.01	2.96	3.00	2.98	2.94	2.94	2.95
Ti	0.00	0.00	0.00	0.18	0.13	0.03	0.12	0.00	0.11	0.15	0.12	0.12
Al	0.22	0.20	0.19	0.12	0.32	0.06	0.15	0.04	0.17	0.17	0.29	0.19
Cr	0.00	0.00	0.00	0.00	0.36	0.00	0.00	0.00	0.00	0.14	0.30	0.00
Fe*	1.77	1.80	1.79	1.59	1.11	1.82	1.67	1.91	1.63	1.48	1.24	1.62
Mn	0.00	0.00	0.00	0.00	0.00	0.00	0.00	0.00	0.00	0.00	0.00	0.00
Mg	0.02	0.07	0.02	0.06	0.05	0.02	0.04	0.00	0.05	0.04	0.05	0.04
Ca	3.16	3.14	3.17	3.13	3.08	3.07	3.06	3.07	3.07	3.09	3.09	3.09
Totals	8.09	8.10	8.09	8.02	8.01	8.02	8.01	8.03	8.01	8.01	8.02	8.02
Notes: all Fe expressed as Fe2O3												
Notes: cations calculated on basis of 12 oxygens												

Table 5.2

Number ->	121	122	123	124	125	126	127	128	129	130	131	132
Sample -->	GT-A	GT-A	GT-A	GT-B	GT-B	GT-B	GT-B	GT-B	GT-B	GT-B	GT-B	GT-B
SiO2	35.41	35.27	35.42	34.67	33.17	32.89	34.10	34.48	34.24	35.09	34.16	34.88
TiO2	0.20	1.55	0.03	1.54	3.96	8.61	3.48	3.67	3.98	2.08	3.27	1.67
Al2O3	0.58	2.32	0.31	7.16	3.38	2.00	1.54	2.17	1.91	2.15	1.81	0.43
Cr2O3	0.00	0.41	0.03	0.03	0.11	0.01	0.00	0.00	0.01	0.01	0.00	0.02
Fe2O3*	28.75	25.07	29.45	18.16	22.58	18.56	24.45	23.26	23.73	24.34	24.57	27.39
MnO	0.09	0.04	0.00	0.14	0.19	0.06	0.17	0.17	0.20	0.17	0.16	0.02
MgO	0.16	0.22	0.01	0.96	0.33	0.88	0.35	0.34	0.34	0.45	0.39	0.35
CaO	33.72	34.06	33.74	34.58	33.52	34.50	33.84	34.05	33.94	34.07	34.00	33.66
Totals	98.90	98.93	98.99	97.23	97.23	97.51	97.93	98.13	98.35	98.36	98.36	98.41
Cations												
Si	3.01	2.97	3.02	2.90	2.83	2.79	2.91	2.92	2.90	2.97	2.90	2.98
Ti	0.01	0.10	0.00	0.10	0.25	0.55	0.22	0.23	0.25	0.13	0.21	0.11
Al	0.06	0.23	0.03	0.71	0.34	0.20	0.15	0.22	0.19	0.21	0.18	0.04
Cr	0.00	0.03	0.00	0.00	0.01	0.00	0.00	0.00	0.00	0.00	0.00	0.00
Fe*	1.84	1.59	1.89	1.14	1.45	1.18	1.57	1.48	1.51	1.55	1.57	1.76
Mn	0.01	0.00	0.00	0.01	0.01	0.00	0.01	0.01	0.01	0.01	0.01	0.00
Mg	0.02	0.03	0.00	0.12	0.04	0.11	0.04	0.04	0.04	0.06	0.05	0.04
Ca	3.07	3.07	3.08	3.10	3.07	3.13	3.09	3.09	3.08	3.09	3.09	3.08
Totals	8.03	8.01	8.02	8.08	8.01	7.97	8.01	8.00	7.99	8.02	8.01	8.01

Notes: all Fe expressed as Fe2O3

Notes: cations calculated on basis of 12 oxygens

								Table 5.2
Number ->	133	134	135	136	137	138		Means
Sample -->	GT-B	GT-B	GT-B	GT-B	GT-B	GT-B		97-98%
SiO2	34.67	34.54	34.68	34.26	34.95	35.14		34.01
TiO2	3.83	2.78	2.68	3.65	1.96	0.20		5.73
Al2O3	1.93	1.35	2.50	2.26	1.48	3.08		2.85
Cr2O3	0.01	0.00	0.03	0.00	0.02	0.09		0.15
Fe2O3*	23.70	25.53	24.13	23.99	26.40	25.81		20.75
MnO	0.16	0.14	0.18	0.16	0.04	0.04		0.15
MgO	0.35	0.41	0.41	0.34	0.38	0.17		0.70
CaO	33.96	33.89	34.04	34.13	33.67	34.42		34.06
Totals	98.61	98.64	98.65	98.79	98.91	98.96		98.40
Cations								Cations
Si	2.92	2.93	2.92	2.89	2.95	2.96		2.86
Ti	0.24	0.18	0.17	0.23	0.12	0.01		0.36
Al	0.19	0.13	0.25	0.22	0.15	0.31		0.28
Cr	0.00	0.00	0.00	0.00	0.00	0.01		0.01
Fe*	1.50	1.63	1.53	1.52	1.68	1.64		1.32
Mn	0.01	0.01	0.01	0.01	0.00	0.00		0.01
Mg	0.04	0.05	0.05	0.04	0.05	0.02		0.09
Ca	3.07	3.08	3.08	3.08	3.05	3.11		3.07
Totals	7.99	8.01	8.02	8.01	8.01	8.05		7.98
Notes: all Fe expressed as Fe2O3								
Notes: cations calculated on basis of 12 oxygens								

Table 5.3 - Mean Compositions and Colors for 51 New Idria Garnets										
Group	SiO2	TiO2	Al2O3	Cr2O3	Fe2O3	MnO	MgO	CaO	Total	Color
1	33.63	0.02	1.98	0.00	27.40	0.00	0.30	34.06	97.39	light green
2	35.43	0.19	0.45	0.01	29.21	0.04	0.10	33.60	99.02	honey yellow
3	35.10	1.69	1.66	0.88	25.25	0.03	0.33	33.97	98.92	yellow-brown
4	34.40	3.27	2.04	0.02	24.26	0.17	0.37	33.96	98.49	brown
5	33.70	7.36	1.55	0.01	20.89	0.07	0.49	34.43	98.50	black
6	34.97	0.09	0.09	8.11	21.40	0.05	0.31	33.49	98.50	emerald green
7	35.91	4.37	13.18	0.04	7.03	0.19	1.30	35.71	97.74	cinnamon

Chapter 6

Titanium Mobility in Metamorphic Systems

Note: This chapter appeared in its entirety as an article in *Chemical Geology*, V. 110, pp. 233-249, 1993. For this reason the section numbering in this chapter differs from the other chapters.

Chapter 6 - Titanium Mobility in Metamorphic Systems

Chapter 6 - Titanium Mobility in Metamorphic Systems

Abstract

Titanium is a dispersed lithophile element commonly regarded as chemically immobile at sub-magmatic temperatures. However, a growing number of field studies demonstrate that Ti is somewhat mobile in certain environments. This review examines the current state of knowledge concerning the mobility of titanium during alteration and metamorphism of crustal rocks. Also considered are relevant Ti-oxide solubility data from experiments and determinations of Ti concentrations in natural waters.

Where Ti mobility is well documented, its length scale is ≤ 10 m. However, Ti may move greater distances in deep crustal shear zones. The solubility of Ti-oxides in geologic fluids is strongly temperature dependent. Under low to medium grade metamorphic conditions Ti mobility is limited by the low solubility of Ti-oxides in the associated fluids. Under eclogite conditions Ti mobility is probably limited not by Ti-oxide solubility (which reaches 1% [Ti]) but by restricted fluid flow in low permeability rocks.

1. Introduction

Titanium, a dispersed lithophile element, is the ninth most abundant element in the earth's crust: estimated TiO_2 concentration in the earth's crust is 0.9 wt. % (Mason & Moore, 1982); in the average shale 0.80 wt. % (Ronov et al., 1992). Oxides of Ti have low solubilites in aqueous fluids under most geologic conditions, and Ti is commonly regarded as chemically immobile at sub-magmatic temperatures, i.e. in sedimentary and metamorphic environments.

Titanium is incompatible in most igneous processes, with excess Ti usually incorporated in oxides or titanite (sphene). However, when the activity of water is high, biopyriboles may form, containing up to 10 wt. % TiO_2. In silica-deficient or peralkaline magmas, other Ti phases may form, including schorlomite garnet, perovskite, neptunite, zirconolite, and other rare Ti minerals.

The term high field strength element, or HFSE, has appeared in the petrologic literature in recent years as a shorthand notation for a group of chemical elements with broadly similar properties. Titanium is the most abundant member of this group. Elements frequently cited as members of the HFSE group are Ti, Zr, Hf, Nb, Ta, plus occasionally Th. Early mentions of the term HFSE include Reagan & Meijer, (1984) and Stebbins et al., (1984).

An older, and much preferable, term for element field strength is ionic potential, originally defined by Cartledge (1928) as the numeric ratio of ionic charge to ionic radius (in Å). This preferable term not only has historical precedence, but avoids awkward questions of just *where* in the electric field of an ion its field strength is to be measured. Barth (1952) noted empirically that the numeric value of ionic potential divides the chemical elements into three groups, based on the solubilities of many of their compounds in water:

(1) Elements whose most frequently observed ions have an ionic potential less than 3 (e.g. Na^{+}) have highly soluble oxides and hydroxides.

(2) Those with an ionic potential between 3 and 12 (e.g. Ti^{4+}) hydrolize easily in solution, and their hydroxides and oxides are only sparingly soluble. The HFSE fall into this group.

(3) Elements whose most frequently observed ions have an ionic potential greater than 12 (e.g. P^{5+}) form soluble oxyacids in solution.

1.1 Element mobility

Element mobility directly addresses the question of the "circulation of the elements in nature", in the sense intended by Goldschmidt (1954). Furthermore, for the petrologist, mobility directly addresses the question of open-system versus closed-system behavior. The definition of mobility used in this paper is this: *An element is considered mobile if measurable changes in its concentration relative to a specified reference frame occur during a particular process.* A chemist might object that all elements are mobile to a degree, but our definition says that if mobility is too small to be measured then we will call the element *immobile*. Ordinarily one relies upon the concentrations of elements relative to each other in mass balance calculations, and makes arguments that at least one element is immobile - and thereby constitutes a reference frame. Since certain elements are believed to be immobile during most petrologic processes, the concentrations of these elements are often used, without specific proof, as the basis of a reference frame for determining the mobility of other elements. Al, Ti, Zr, Hf, Cr, Ce^{4+}, are often used in this sense. The use of one or more immobile elements as a reference frame lies at the heart of a number of useful methods for analyzing mass balance in petrologic processes. Examples include Pearce element ratios (Pearce, 1968), isocon diagrams (Grant, 1986), and the rock cell (Barth, 1952).

1.1.1 Length scales

The length scale of titanium mobility in metamorphic environments is poorly understood. Sorting out what is known about this subject is best done by considering the characteristic length scale of such mobility. The strongest case for significant Ti mobility is the appearance of Ti-bearing phases in a rock otherwise devoid of TiO_2, when these phases are limited to a

Figure 6.1 - Idealized cross section showing advection of Ti across boundary layer between Ti-rich Rock Type 1 (e.g.1.0% TiO_2) and Ti-free Rock Type 2 (e.g. 0.0% TiO_2). Segment AB is Type 1, with boundary at B. CD is Type 2. BC is boundary layer, with phase assemblage typical of Type 2, but with introduced Ti-bearing phases. The length scale of Ti transport is the distance BC. Ti concentration profile shown in lower portion of figure.

Figure 6.1 - Advection of Ti Across a Boundary Layer

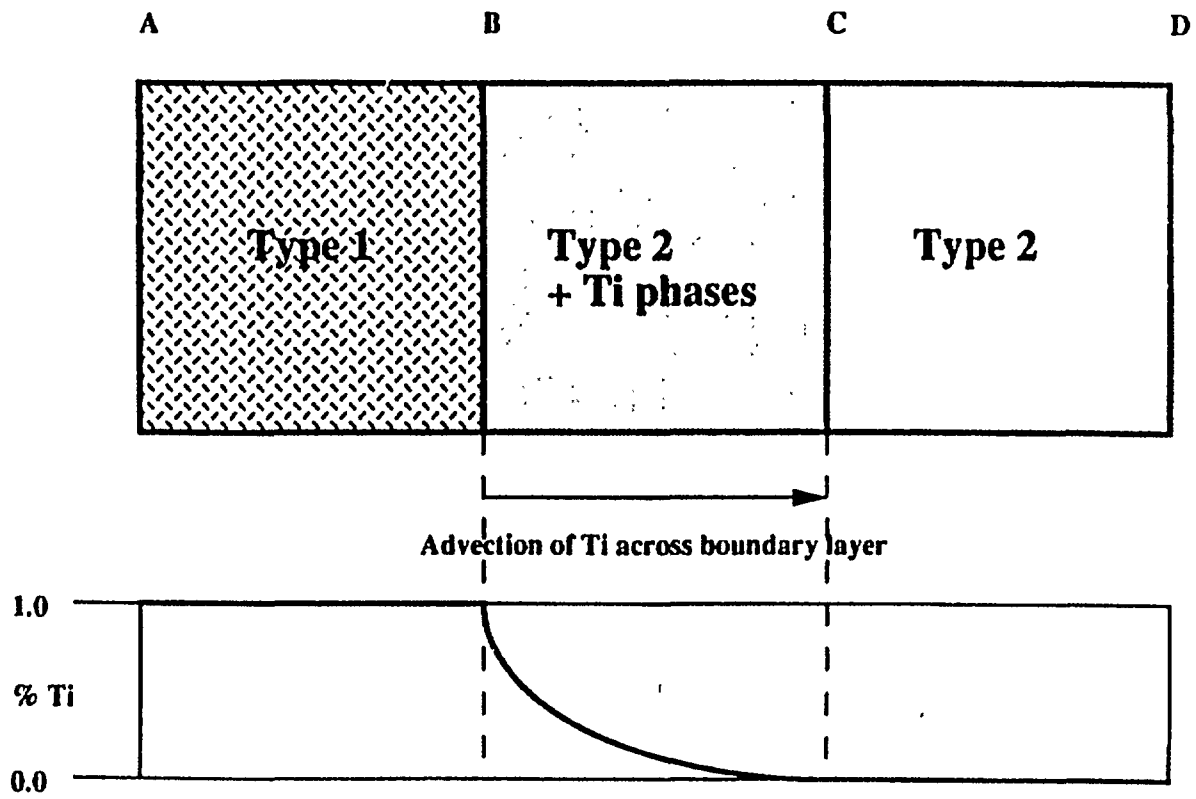

boundary layer and where textural evidence shows advection across this boundary layer. Figure 6.1 illustrates this concept in an idealized manner.

1.1.2 Mobility in fluids

Experimental and field studies to date have concentrated on aqueous fluids as the principal vehicle for titanium mobility. The Ti concentration in most geologic fluids is controlled by the solubility of Ti-oxides. Titanium mobility resulting from fluid transport during metamorphic and metasomatic processes involves the dissolution of solids, fluid transport, and precipitation. Each of these three stages is an important topic in its own right, but here the emphasis is on the net effects of these processes, rather than the details of their mechanisms. Whether intergranular fluids differ from free fluids in their ability to tranport titanium is unknown.

1.1.3 Solid state diffusion

Solid state diffusion may be important as a transport mechanism for certain elements, but there is no evidence supporting diffusive transport of titanium beyond the dimensions of single crystals in the metamorphic environment. No studies known to this author have reported monomineralic zones of titanium-saturated minerals created by the sort of diffusive processes modeled by Thompson (1959), in which chemical potential gradients are the driving forces. Diffusion kinetics are well discussed by Mueller (1966). Mueller concludes that lattice diffusion is ineffective as a vehicle for element mobility except on a very short length scale, although he suggests that diffusion in a differential stress field may contribute to the formation of gneissic banding. He also makes the simple observation that components with low solubilities in fluids are likely to have limited mobility. It will be shown below that the converse of this statement is not necessarily true.

2. Experimental data and Ti concentrations in natural waters

2.1 Measurements of Ti in natural waters

Numerous studies confirm the essential immobility of titanium during weathering and diagenesis (e.g. Piotrowski et al., 1989, Patterson, 1971, Hoppe, 1941). The concentration of Ti in natural waters is very low, except under extremes of pH or at high P-T conditions. The few recent determinations of Ti concentrations in natural waters at low temperatures are summarized in **Table 6.1.** These data show appreciable Ti concentrations (a few ppm) at pH 12 (Kranov, 1973) and pH < 2 (White et al., 1963), but low concentrations (ppb or lower) in the near-neutral pH range most often found in natural waters. The absence of studies reporting significant aqueous Ti in the near-neutral pH range in natural waters is consistent with low solubility of TiO_2 in these fluids. No direct measurements of Ti concentration have been made in natural waters at high P-T conditions.

2.2 Low Temperature Experimental Data

Experimental data for TiO_2 solubility are sparse, and a number of experiments have been made under geologically unrealistic conditions. **Table 6.2** summarizes the best available measurements from several studies; the data are organized in terms of increasing temperature. Nabivanets & Lukachina (1964), in a series of experiments apparently never repeated, showed constant TiO_2 solubility of about 0.1 ppm TiO_2 between pH 4-7, at 18°C and 1 bar, in 0.1M perchlorate solutions. If these results were applicable in natural systems, then we would expect to see much higher concentrations of Ti in natural waters in the near-neutral pH range than shown in **Table 6.1.** Other experiments have explored the effect of pH on TiO_2 solubility: Babko et al. (1962) and Liberti et al. (1963) demonstrated that TiO_2 solubility at pH < 2.5 has a steep inverse relationship with pH, rising to 72 ppm TiO_2 at pH 1.3. These results support the existence of a dipositive mononuclear Ti

hydroxyl complex in this pH range, as discussed below. Other experiments (e.g. Bright & Readey, 1987, and Barsukova et al. 1979) have explored the effect of possible fluoride complexing on the solubility of TiO_2. Their results support the idea that fluoride complexes (probably TiF_6^{2-}) significantly enhance TiO_2 solubility at high fluoride concentrations (0.5-2.1M F^- or 1-4 wt. % fluoride). Extrapolation of these results to the concentrations of fluoride normally found in natural waters (1-10 ppm) suggests that TiO_2 solubility may not be significantly enhanced by fluoride complexing in natural waters. At hydrothermal temperatures, Schuiling & Vink, (1967) reported 1-2 ppm dissolved Ti at 200-300°C and 15-80 bars[1]. These investigators also showed that anatase is more soluble than rutile, in keeping with its more positive ΔG_f^0. Agapova et al., (1979) investigated the possible role of sulfate and carbonate complexes of Ti; neither of these complexing agents increased the solubility of rutile beyond the values of Schuiling and Vink under the same P-T conditions. The same is true for chloride complexing; since Ti concentrations do not increase with chloride concentration, we conclude that Ti-chloride complexes are not of major importance. Ayers & Watson (1993), in experiments discussed below, found an inverse relationship between chloride concentration and rutile solubility, probably due to the decrease in the activity of water.

It should be pointed out that in all of these experiments, the surface properties of the solid phase and sample preparation methods of the materials used may have had a significant effect on the observed solubility. Bright and Ready (1987), for example, describe the surface properties of their materials in great detail, and conclude that the kinetics of dissolution are substantially controlled by surface reactions. The solubility of well

[1]Note the mistake in the literature concerning the Schuiling & Vink (1967) results: there is an apparent typographical error in a paper by Vasil'ev et.al. (1974), which recalculates the molality of the Schuiling & Vink data (1.33 and 1.57 ppm) as 2.78×10^{-8} and 3.28×10^{-8} mol/kg respectively, instead of the correct values of 2.78×10^{-5} and 3.28×10^{-5} mol/kg. This error has been propagated in the literature. The correct values are shown in Table 2.

crystallized rutile may be lower than that of amorphous starting materials produced in the laboratory, described as TiO_2(activated) or TiO_2(hydrous).

These low temperature experimental data are shown in **Figure 6.2a**, together with natural waters data in **Figure 6.2b** to facilitate comparison. The regression lines from **Figure 6.2a**, defining a solubility curve, are redrawn in **Figure 6.2b**. In **Figure 6.2b**, the measurement of White (1963) at low pH is the only measurement which falls on the solubility curve for rutile. The data of Skrabal et al. (1992) and Orians et al. (1990), who report Ti concentrations in estuaries and the open ocean respectively, indicate that these waters are undersaturated with respect to rutile.

2.3 High Temperature Experimental Data

The solubility of rutile in water increases by several orders of magnitude with increasing P and T. As shown in **Table 6.2**, Ayers & Watson (1991, 1993) reported rutile solubility in water to be about 1% at 1100°C from 10 to 21 kb. These experiments also showed increasing rutile solubility with temperature at a fixed pressure, and slightly decreasing solubility with pressure at a fixed temperature, in the interval 800°-1200°C and 10-30kb. In these experiments, adding CO_2, NaCl, and HF to the fluid each decreased rutile solubility. Schneider & Eggler (1987) found approximately 0.02 wt. % TiO_2 dissolved in water at 750°C and 15 kb in their experiments with amphibole breakdown reactions. Phillipot and Selverstone (1991) reported rutile daughter crystals in moderately saline fluid inclusions from eclogites, which were trapped at 550°C and 10-11 kbar. A rough estimate of the concentration of Ti required to produce these daughter crystals is 0.05-0.5 wt. % TiO_2 at the time of trapping. This estimate is generally consistent with the experimental data. **Figure 6.3** shows rutile solubility data as a function of temperature. Solubility data at pH < 2.5 or high fluoride concentrations have been omitted. **Figure 6.3** is a projection

Figure 6.2a - Total dissolved Ti vs pH from experiments at 1 bar, 18-25°C. Data points and references listed in Table 6-2.

Figure 6.2a - Solubility of Ti Oxides

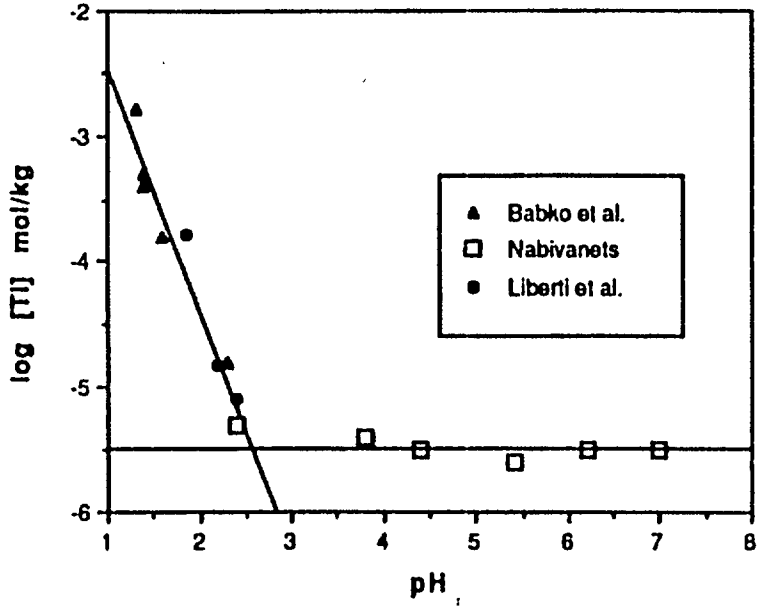

Figure 6.2b - Ti concentrations in natural waters, 1-400 bars, 25-300°C. Data points and references listed in Table 1. TiO_2 solubility curve from Figure 6-2a shows poor fit to data.

Figure 6.2b - Ti Concentrations in Natural Waters

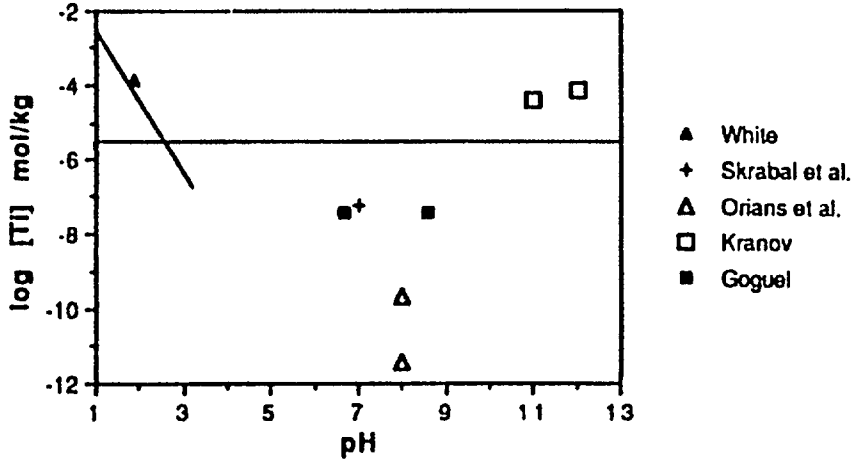

Figure 6.3 - Experimental TiO_2 solubility in dilute, near neutral pH solutions as a function of temperature. See Table 6.2 for fluid chemistry and references. Apparent linear trend due to projection from P-T-X space onto T-X plane. Experimental pressures labelled.

Figure 6.3 - Solubility of Ti Oxides as a Function of Temperature

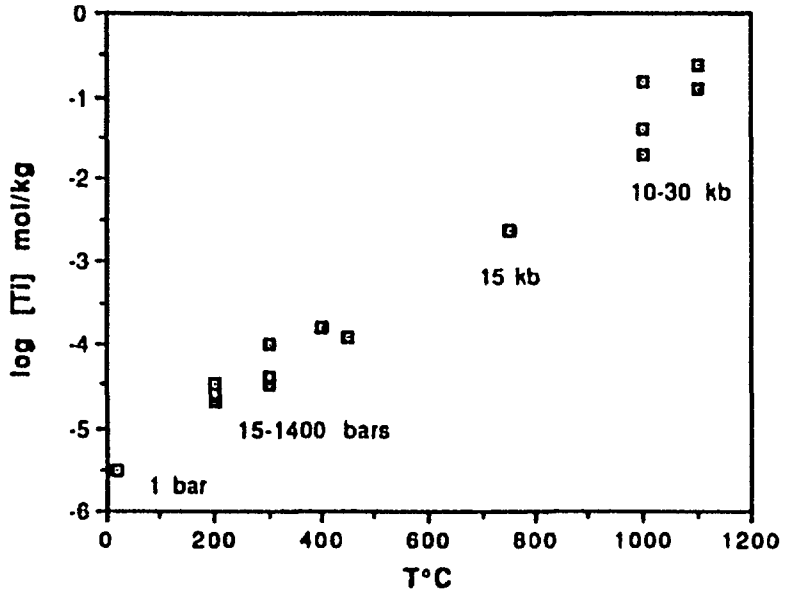

from P-T-X space onto the T-X plane. There is an essentially linear relationship between between T and log [Ti] in this projection.

2.4 Comparing the effects of Temperature and Pressure

Consideration of **Figure 6.3** raises the question of the relative importance of temperature versus pressure in explaining the large (3-4 orders of magnitude) increase in rutile solubility from low grade (greenschist) to high grade (eclogite) conditions. The fluid density in each of the experiments in **Figure 6.3** varies between 0.7 and 1.2 g/cm^3. We therefore suggest that the solubility of rutile in supercritical water is essentially *temperature* dependent, with the proviso that the fluid density remains high enough to show liquid-like, rather than vapor-like properties. The Ayers & Watson (1993) experiments showed an inverse relationship of rutile solubility and pressure at a constant temperature, making it difficult to argue that increasing pressure is the essential control on rutile solubility. If rutile solubility were essentially pressure dependent, then one would expect to encounter evidence of high rutile mobility under blueschist conditions. Unfortunately no experiments have reported rutile solubility data under blueschist conditions, but neither have any field studies of blueschists noted significant Ti mobility. Under high T, low P (volcanic) conditions, in which the fluid phase has low density and vapor-like properties, the ability of water to transport dissolved substances is generally very low, and one would expect insignificant rutile solubility.

2.5 Speciation of Titanium in Aqueous Fluids

Ti complexes in geologic fluids remain a subject of great dispute. Ti as a small, highly charged cation hydrolizes easily, and does not appear as the Ti^{4+} ion except possibly at extremely low pH. Below pH 2.5, titanium is probably present as a dipositive mononuclear complex, either TiO^{2+} or $Ti(OH)_2^{2+}$, a conclusion supported by good

experimental evidence (Babko et al., 1962; Liberti et al., 1963). In the pH range 3-7, some experimental evidence (Nabivanets & Lukachina, 1964) supports the presence of a neutral complex. Baes & Mesmer (1986) accepted this evidence and supposed that the neutral species was either $Ti(OH)_4^0$ or $TiO(OH)_2^0$. Schmets et al., (1966), however, proposed that above pH 5.6 a negatively charged complex $HTiO_3^-$ becomes dominant; if true this would enhance rutile solubility in strongly alkaline waters. Schmets et al. also described the phase $TiO(OH)_2$ as a white solid, not an aqueous species: this solid may be the substance referred to in the literature as TiO_2(activated) or TiO_2(hydrous), which is known to have a higher solubility than well-crystallized rutile or anatase. Clearly, further experiments are needed.

Although there is little agreement about titanium speciation in water, theoretical speciation calculations using the correlation methods of Helgeson et al. (1981) show promise. Recent calculations using these methods (e.g. Willis et al. 1990) have proposed a variety of hydroxyl complexes (including some with trivalent titanium) at hydrothermal temperatures over a range of Eh-pH values, but experimental data confirming these predictions are not yet available. Most workers agree that if the fluoride activity is high in solution, then fluoride species such as TiF_6^{2-} are present. This means that high fluoride activity may be a sufficient, but not a necessary, condition for mobilizing Ti in natural waters. As noted earlier, sulfate, carbonate, and chloride complexes appear to be of minor importance in geological fluids. In the sedimentary environment, organic complexes of Ti may be significant (e.g. Skrabal et al., 1992, Milnes & Fitzpatrick, 1989).

3. Titanium mobility observed in low grade metamorphic rocks

3.1 Alteration of silicate minerals

If all the silicate minerals in a rock are TiO_2 saturated, then one or more of the saturating phases rutile, titanite (sphene), ilmenite or rarely, perovskite appear. Otherwise, titanium substitutes as a minor or trace element in silicate minerals, especially in the biopyriboles. In terrestrial silicates, Ti is almost invariably found in the +4 valence state, occupying octahedral sites where it substitutes for Al, Mg, and Fe. The distribution of Ti among silicate minerals may change as a function of metamorphic grade (Guidotti et al., 1977).

Alteration or breakdown reactions of biopyriboles, which may release Ti, are of particular interest. A common breakdown reaction occurs during retrograde metamorphism of Ti-rich biotite, producing chlorite intergrown with masses of fine rutile with preferred orientation in chlorite crystals. **Plate 6.1** shows an example of the products of this reaction in a pelitic schist. Based on petrographic examination of the progressive replacement of biotite by chlorite and exsolved rutile, one can say that the Ti in the rutile crystals came from the preexisting biotite, and has moved at most a millimeter. By contrast, potassium apparently was highly mobile in this environment, as shown by the near-total lack of white mica or other sinks for the potassium released during the biotite breakdown reaction.

3.1.1 Hydrothermal Rutile

In hydrothermal systems Ti is generally conserved; the occurrence of ore grade deposits of hydrothermal rutile is readily explained by reactions of the type proposed by Force, (1991):

silicate + sulfur = silicate + rutile + pyrite
(Ti-rich) (Ti-free)

Analogous reactions involving CO_2 or O_2 as volatiles in place of sulfur yield carbonates and/or oxides. **Plate 6.2** illustrates this type of occurrence in a hydrothermal rutile vein

from the Titanium Corp. of America mine at Magnet Cove, Arkansas. According to Force (pers.commun., 1992), the length scale of Ti transport in typical hydrothermal systems is very short, perhaps millimeters in the case of the large deposits at Bingham, Utah. Leucoxene, a finely divided material consisting of Ti-oxides, also results from a breakdown reaction of ilmenite in hydrothermal environments (e.g. Conrad, 1990).

3.2 New Idria, California

Titanium has been mobilized on a meter scale at New Idria, California, USA (Van Baalen, 1991, Van Baalen & Zbinden, 1989). The New Idria district is a fault-bounded, diapirically emplaced serpentinite body roughly 20 km long, which is considered to be part of the Coast Range ophiolite (Hopson et al., 1981). The serpentinite body consists mainly of highly sheared and crumbly fragments of serpentine minerals (Mumpton & Thompson, 1975). It also contains numerous tectonic inclusions of various lithologies, with a size range from 1 to 1500 meters (Coleman, 1986). Some of these tectonic blocks, particularly those at the southern end of the district, contain titanium-bearing minerals, including schorlomite garnets, as well as perovskite, titanite (sphene), benitoite, and neptunite. Schorlomite garnets contain > 5 wt. % TiO_2 : schorlomite garnets at New Idria have TiO_2 contents as much as 16 wt. %. These high-Ti minerals are only found within the tectonic blocks or in alteration rinds surrounding the blocks. Some small intrusive stocks of syenite are associated spatially with the blocks containing these minerals. Most of the Ti minerals are euhedral to subhedral and have vein-filling textures. The veins crosscut all other fabrics in the rock, and probably formed as tension cracks during uplift of the massif. A fluid inclusion study indicated that the garnets grew in low salinity fluids at temperatures around 300°C (Van Baalen, 1991). Other than in association with these tectonic blocks, the New Idria serpentinite shows a total absence of Ti minerals, and whole-rock analyses of the serpentinite show consistently low levels of titanium (<1 ppm Ti by XRF analysis, this study).

Plate 6.1 - Exsolution of rutile needles from chlorite that has formed after titanium-rich biotite during retrograde metamorphism of a pelitic schist. Note that the orientation of the rutile appears to be crystallographically controlled within the chlorite crystal. Field of view 2 mm. Sample PJ-11E courtesy of J. Selverstone.

Plate 6.2 - Vein of hydrothermal rutile in a porous matrix of K-feldspar, calcite and pyrite. Sample from Titanium Corporation of America pit, Magnet Cove, Arkansas. Width of sample 5 cm.

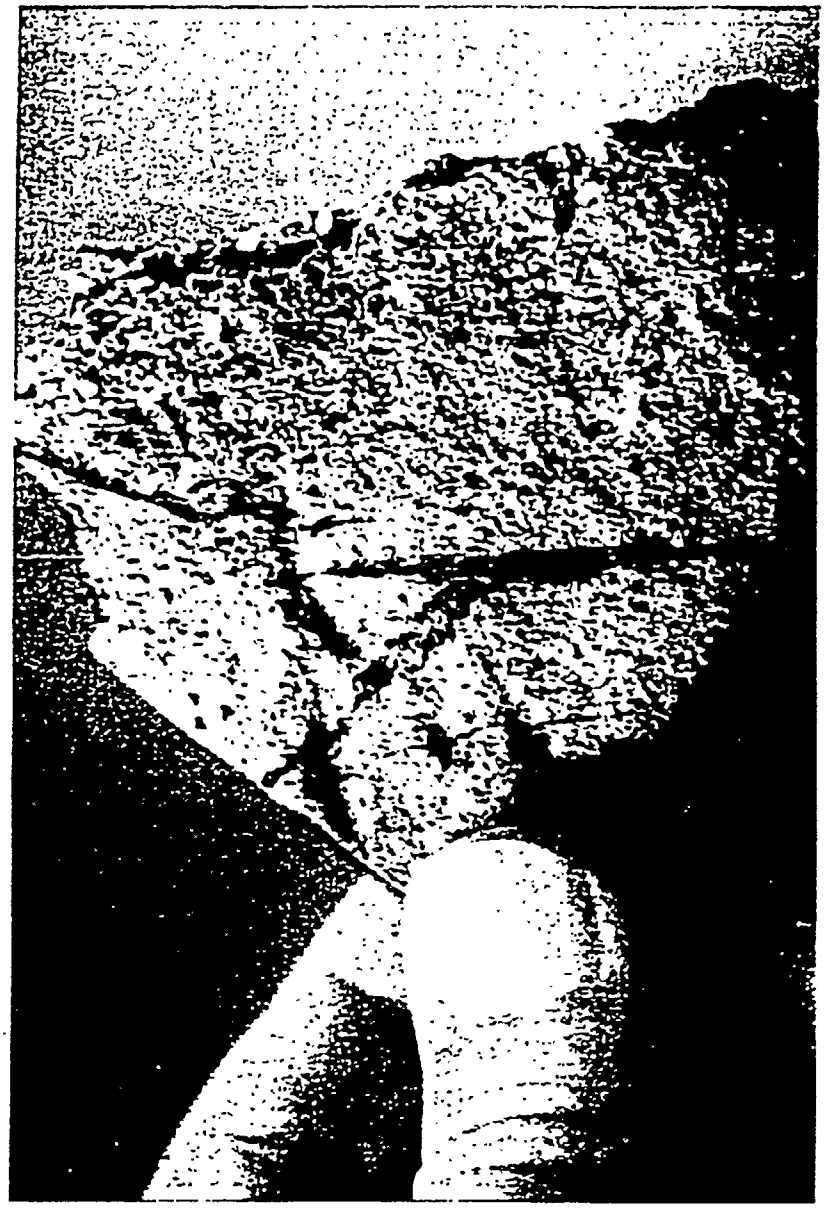

Minerals limited to the altered rinds of a tectonic block are well displayed at the Melanite Mine, located in the New Idria district. Here, a tectonic block crops out at the surface as a north-south trending cliff ca. 2 m high and 15 m wide. Near the north and south ends of the cliff one finds boundary layers of the type described in **Figure 6.1.** The phase assemblage within the block, "rock type 1", consists of chlorite + diopside ± schorlomite garnet. The phase assemblage outside the block, "rock type 2", consists of serpentine ± andradite garnet (Ti-free). At the Melanite Mine, "rock type 2" extends for at least several hundred meters, so that distance CD is effectively infinite. The boundary layer BC, about 1 meter in width, consists of serpentine plus a remarkable garnet, which has a schorlomite core overgrown with andradite, as shown in **Plate 4.9** in Chapter 4. Garnets of this type are limited to the north and south boundary layers at this locality, and found nowhere else in the region.

The garnets in this boundary layer document titanium mobility on a length scale of 1 meter. Fluids containing dissolved Ti moved through the tectonic block, precipitating schorlomite garnets within the block and in its boundary layer, under greenschist facies conditions. Both pervasive flow through the rock and channelized flow through the veins occurred. Titaniferous garnets are only found within the tectonic block or its boundary layer, but fluids outside the tectonic block precipitated Ti-free andradite garnet over an area much larger than the zone of titanium mineralization. Elsewhere within the New Idria district there are numerous additional instances of Ti mobility: these are always related to the tectonic blocks and their margins. There are no fluoride minerals at New Idria; this suggests that fluoride complexing was not a major factor in Ti mobility there.

3.3 Sierra Blanca, Texas

Titanium has been mobilized on a 4 meter scale at Sierra Blanca, in the Trans Pecos region of West Texas, USA. At Sierra Blanca, mildly peraluminous and rare-metal-enriched Oligocene

rhyolites have formed a series of laccoliths which intrude and dome up the Buda limestone of mid-Cretaceous age (Rubin et al., 1989). Fluorspar occurs along the rhyolite-limestone contact, and both Be and Ti mineralization are hosted by this fluorspar. Since much of the exposure is subsurface, Rubin et al. relied on samples taken from drill cores, bulldozer cuts, and an adit intersecting the contact.

Mineralization is extensive at Sierra Blanca, and rutile is merely an accessory phase. The mineralization extends several meters into the limestone, the distance controlled in part by the dip of the contact. Rubin et al. do not give full chemical analyses of the altered and unaltered limestone, but they do give trace element analyses, which show a relative enrichment of Ti by one order of magnitude 4 m from the contact. It is interesting to note that all of the titanium group elements, also Al and Y, are enriched by about this same factor.

Sierra Blanca thus shows mobility of titanium on a length scale of a few meters, in an environment where the activity of fluoride was high, as demonstrated by the presence of extensive fluorite deposits. The temperature of mineralization is estimated by Rubin et al. to have been 250°-400°C. The pressure is not stated, but is assumed to be low (J. Rubin, pers. commun., 1991). Unlike at New Idria, fluoride complexing with Ti in the hydrothermal solutions seems possible at Sierra Blanca.

3.4 Adamello, Italy

Titanium and zirconium have been mobilized on a scale of 10 meters at Valle di Breguzzo, Italy, at the margin of the Adamello batholith. Adamello, located in northern Italy in the Provincia di Trento, 50 km south of the borders with Austria and Switzerland, is the largest Tertiary igneous complex in the Alps. Along the eastern margin of the batholith, an intrusive contact of tonalite against dolomite is exposed in the Valle di Breguzzo. According to Gieré

(1990, 1992), veins containing Ti minerals extend up to 10 meters from the contact into the dolomite, which has been contact metamorphosed to marble. Similar veins have been observed by this author at Val Dâone, which is also located on the eastern contact of Adamello. Gieré observed four distinct mineralogical zones in the veins at Valle di Breguzzo, with sharp boundaries separating them. Several Ti and Zr-bearing minerals occur there, including rutile, titanite (sphene), zirconolite, geikelite, and titanian clinohumite. Whole rock analyses of the unaltered dolomite show negligible Ti and Zr (< 0.08% Ti and < 16 ppm Zr) (Gieré, 1990). Textural features show that the Ti and Zr in the vein minerals were advected from the tonalite. Whole rock Nd-isotope data for the veins and for the tonalite suggest Nd-isotopic equilibrium between the vein-forming fluid and the intrusive tonalite (Gieré, 1992).

The Ti and Zr-bearing minerals were formed as fluids associated with the intrusive tonalite penetrated the dolomite wallrock. These fluids carried Ti and Zr. The length scale of transport for both Ti and Zr was about 10 meters along the veins, but only a few centimeters perpendicular to the vein walls. Pressure and temperature estimates for these veins are 550°-600°C and 2 Kb, with high activities of CO_2, H_2S, and F^-, the latter suggested by the abundance of idiomorphic fluor-apatite as an accessory mineral in the veins (Gieré, 1992). As at Sierra Blanca, but unlike at New Idria, fluoride complexing potentially enhanced Ti mobility.

3.5 Magnet Cove, Arkansas

Titanium mobility on more than one length scale has occurred at Magnet Cove, Arkansas, USA. The Magnet Cove district is in the west central part of Arkansas, and contains several remarkable mineralogical and petrological localities associated with the intrusion in the Cretaceous of a series of nepheline syenites and carbonatites into Paleozoic sedimentary

rocks (Erickson & Blade, 1963). These intrusions form a series of concentric ring dikes 5 km in diameter. The intruded country rocks consist mainly of shales and a slightly metamorphosed chert unit known as the Arkansas Novaculite.

There are two examples of titanium mobility at Magnet Cove of interest here: one is the hydrothermal rutile at the mine of the Titanium Corporation of America, which is interpreted as a hydrothermal alteration of a phonolite. Whole rock analyses of the altered phonolite show 2-3% TiO_2, which is similar to that of the unaltered phonolites in the vicinity. Titanium in the unaltered phonolite is concentrated in titanite (sphene) and ilmenite. The simplest interpretation is that the rutile deposit is an in-situ accumulation of the breakdown products of the titanite (sphene) and ilmenite.

The brookite deposits in and around the Christy pit on the east side of the Magnet Cove complex are, however, a different matter. At the Christy pit, and at the nearby Moses Hill locality, euhedral brookite is found intergrown with quartz crystals filling veins and vugs in the novaculite (quartzite) unit a few hundred meters beyond the eastern margin of the igneous complex. Willis et al., (1991) report in a fluid inclusion study that these quartz crystals formed at temperatures of 300-500°C. Unaltered, pure novaculite has an extremely low Ti content, < 0.008 % (Erickson & Blade, 1963). It has been suggested (Williams, 1891, Willis et al., 1990) that the brookite crystals were precipitated from hydrothermal fluids[2], which caused the breakdown of igneous Ti minerals (melanite garnet and perovskite) in the nepheline syenite 300 meters away, and transported Ti in solution to the place where brookite was preciptated. This is certainly a possibility, which if true would demonstrate that Ti moved for a distance of a few hundred meters. Another possibility worth investigating is that

[2]Williams (1891) stated "The most plausible theory to account for the transformation of this element (titanium) from its original condition ... in the syenite, to that of brookite ... is that it was dissolved by the hot water and steam under pressure ... and was recrystallized."

the source of the Ti is in the Missouri Mt. Shale, which underlies the novaculite. The Missouri Mt. Shale, contains about 0.5 wt % TiO_2,. The contact between the novaculite and this shale crops out in the wall of the Christy pit. It is possible that the shale is the source of Ti for the brookite, and that Ti was leached out by hydrothermal fluids and transported only a few meters to the site of the brookite deposits. If this hypothesis turns out to be correct, then Ti mobility is still demonstrated at the Christy pit, but on a length scale of a few meters rather than hundreds of meters.

3.6 The Alpine Clefts

The Alpine Clefts refer to a large number of mineralized cavities or vugs, located throughout the Western and Central Alps (Niggli, 1940). Many clefts are filled with euhedral, often museum quality, mineral specimens. These minerals include titanite (sphene), rutile, and other Ti-bearing phases; the environment of deposition suggests precipitation from Ti-bearing fluids. The metamorphic conditions were estimated by Poty et al. (1974) to have been 340-505°C and 2.5-3 kb. Titanium was mobilized in metamorphic fluids probably released by dewatering reactions in the Alpine nappes during the Miocene. The length scale of Ti mobility in the vicinity of the clefts is uncertain, and has not been specifically studied. These clefts represent an intermediate case between the low pressure environments described above, and the high pressure examples to follow.

4. Titanium mobility observed in high grade metamorphic rocks

The systematic depletion of Ti relative to major elements and REE in island arc basalts (IAB) is well established (e.g. Perfit et al., 1980). Ryerson & Watson (1987) showed that the Ti depletion must be a characteristic of the IAB source region. One mechanism for depletion of the source region might be leaching of Ti by aqueous fluids, which then transport Ti out of

the source region, presumably to be precipitated elsewhere, e.g. Ayers & Watson (1993). Direct evidence from subduction zones comes in two forms: one is the study of volcanic products above subduction zones; the other is the study of metamorphic rocks, especially blueschists and eclogites, which have experienced subduction zone conditions. The experimental evidence suggests that significant Ti could be present in fluids under eclogite conditions. But high solubility of rutile does not necessarily imply effective transport of Ti.

4.1 Monviso, France

Philippot & Selverstone, (1991), in a study of eclogites from Monviso, France, in the western Alps, report evidence for high Ti concentration in fluids associated with these rocks. Monviso lies in the French-Italian Western Alps, and is thought to be a part of the Neotethys basin separating the South Alpine plate from the European plate. The unaltered eclogitic rocks are preserved within a horizon of metagabbros which contain 10 x 1 m boudins associated with a shear zone. The boudins contain shear fractures, tension gashes and dilatant fractures. Philippot & Selverstone (1991) estimate the P-T conditions during the metamorphism of these rocks to have been 500 ± 50°C and at least 10-11 kbar.

Omphacitic pyroxenes in the veins and shear fractures contain fluid inclusions. These contain several daughter crystals, including rutile, titanite (sphene), and baddeleyite. The presence of these crystals indicates that the concentration of Ti and Zr was significant in the brines from which the omphacites grew. As noted earlier, a rough estimate by this author of the concentration of Ti and Zr required to produce these daughter crystals is 0.05-0.5 wt % for both Ti and Zr, at the time of trapping. Decrepitiation of the inclusions on heating frustrated attempts to redissolve the daughter minerals.

Rutile and titanite (sphene) are found in both the veins and the mylonites. The authors suggest that the veins were caused by hydraulic fracturing during reduction of the bulk rock permeability due to dynamic recrystallization. If so, the titanium required to precipitate rutile and titanite (sphene) in the veins need not have been advected from a great distance. Selverstone (pers. commun., 1992) believes that the length scale of Ti migration in these rocks is at most a few centimeters. Philippot & Selverstone also point out that the crack seal geometry of the veins suggests that fluid flow occurred in pulses, and that the minerals in the veins probably grew during opening of the veins as a result of these pulses.

At Monviso the solubility of rutile was probably significant, yet transport of Ti seems to have been limited to a centimeter scale due to the limited movement of metamorphic fluids in these low permeability rocks.

4.2 Santa Catalina Island, California

A second locality which sheds some light on titanium mobility under high P-T conditions is Santa Catalina Island, California, USA. The Catalina Schist, exposed on that island, is interpreted as a fossil subduction zone in which three distinct tectonic units are preserved: amphibolite-, greenschist-, and blueschist-facies rocks (Sorensen, 1986, 1988). Tectonic blocks of various sizes included in the amphibolite unit were metamorphosed under high P and T conditions, and developed centimeter scale reaction rims or "rinds" (Sorensen & Grossman, 1989). These authors estimate the P-T conditions during formation of these rinds to have been 11 kbar and 640-750°C. The tectonic blocks of interest to the present discussion are described by Sorensen & Grossman as "non-migmatitic blocks with rinds". These blocks contain rutile, and the rinds contain rutile and titanite (sphene). The matrix between the blocks is described as meta-ultramafic. Whole rock analyses for all rock types

are given: the TiO_2 content of the blocks, rinds, and matrix are 1.4-2.5%, 0.2-2.4%, and 0.03-0.18% respectively.

During metamorphism of these blocks under eclogite conditions, Ti migrated from the inner edges of the rinds towards the outer. Ti moved some 5-15 cm, the width of the rinds. This is a rather small distance, considering the significant concentration of Ti expected in metamorphic fluids at 700°C and 11 kbar. It is possible that there was not much fluid circulation in this system. However, Bebout & Barton (1989) found evidence for massive fluid flux in a shear zone, and have proposed a model involving channelized flow along the top of the subducted slab. Bebout & Barton documented extensive mobility of major elements, including Al and the alkalis, but did not present any evidence for significant mobility of titanium. The documented Ti mobility of 5-15 cm probably represents a minimum value, and further work at this locality may well furnish evidence for movement of Ti for greater distances. This example, as well as the next, suggests the importance of fluids in deep crustal shear zones.

4.3 Tauern Window, Austria

A third locality which sheds light on the mobility of titanium in high grade rocks is at the Stillup Tal, in the west central portion of the Tauern Window, Austria. At this locality, ductile shearing of a granodiorite transformed this rock into a SiO_2-undersaturated staurolite schist at approximately 550°C and 11 kbar (Selverstone et al., 1991). Using the "conventional wisdom", the authors used Al and Zr as the basis of an immobile reference frame during the shearing event. Relative to this reference frame, Ti, Fe, and Mg were added while Si, Ca, and Sr were removed, and there was a 60% volume loss. Alteration profiles show that fluid flow was channelized in the shear zone and did not significantly penetrate the wallrock to a distance of more than 1 meter.

Unfortunately for the purposes of the present paper, no information is preserved on the length scale of the presumed Ti mobility at Stillup Tal. Since the Ti concentration in the fluids was probably high during metamorphism in this area, a significant quantity of Ti may well have come from a considerable distance. The assumption that Zr was immobile in this case may be questioned, given the experimental evidence on zircon solubility (Ayers & Watson, 1991) and the fluid inclusion evidence from Monviso. More probably, *both* Ti and Zr were mobile, perhaps to varying degrees.

5. Conclusions

1. The total body of experimental data for the solubility of Ti-oxides is rather thin; many of the experiments have been performed under geologically unrealistic conditions.

2. It is likely that the concentration of Ti in geologic fluids is limited by the solubility of Ti-oxides. TiO_2 occurs in several forms, including the crystalline polymorphs and a metastable hydrated phase which has a greater solubility than the well-crystallized oxide. The rate of dissolution of these phases depends on their surface properties.

3. The solubility of TiO_2 is pH dependent. At pH < 2.5, a hydroxyl complex, either TiO^{2+} or $Ti(OH)_2^{2+}$, is the dominant Ti species in solution. The nature of the dominant Ti complex in solutions at pH > 2.5 is in dispute. In much of the literature it is assumed that a neutral hydroxyl complex, either $Ti(OH)_4^0$ or $TiO(OH)_2^0$, is the dominant species. Chloride complexing is probably not important, and a high chloride activity may even decrease rutile solubility by lowering the activity of water. Experiments with other complexing agents show that they do not play a major role in the concentration of Ti in most geologic fluids.

4. TiO_2 solubility increases with temperature to about 1 wt. % near 1000°C. The solubility of rutile in supercritical water is much more a function of temperature than of pressure, in fluids of density ≥ 0.7 g/cm^3.

5. Titanium mobility on a length scale of meters has been demonstrated in low grade metamorphic rocks related spatially to shallow intrusives. Studies of eclogite facies rocks have demonstrated Ti mobility on a length scale of only a few centimeters in spite of the much greater concentration of Ti expected in fluids under these conditions. There are no reports of extensive Ti mobility under blueschist conditions. Studies of mantle xenoliths (e.g. Haggerty, 1987) suggest Ti mobility and mantle metasomatism, but the evidence is not yet clearcut: a full discussion of that field is beyond the scope of this paper.

6. Evidence regarding Ti mobility in deep crustal shear zones is somewhat equivocal, but these zones must play a major role in Ti movement if significant quantities of Ti are leached from island arc basalt (IAB) source regions. Ryerson & Watson (1987) suggested that the IAB source region has been depleted in these elements, due possibly to a previous episode of partial melting, or to removal of Ti-group elements through interaction with aqueous fluids. If the removal is by aqueous fluids, then the scale of this process must be large. To date, study of metamorphic rocks has not been able to document such a large scale process.

Table 6.1 - Tl concentrations in natural waters						
reported value	[Tl] mol/kg	log [Tl]		environment	fluid chemistry	reference
0.2 nM/l	2.0e-10	-9.7		estuary - saltwater end	see note a	Skrabal et.al., 1992
67 nM/l	6.7e-08	-7.2		estuary - freshwater end	see note a	Skrabal et.al., 1992
4 pM/l	4.0e-12	-11.4		ocean surface waters	see note b	Orians et.al., 1990
200 pM/l	2.0e-10	-9.7		ocean bottom waters	see note b	Orians et.al., 1990
5.4 ppm	1.1e-04	-3.9		hot spring	see note c	White et.al., 1963
2 ppm	4.2e-05	-4.4		mine waters	see note d	Kranov, 1973
4 ppm	8.4e-05	-4.1		mine waters	see note d	Kranov, 1973
2 ppb	4.0e-08	-7.4		geothermal well	see note e	Goguel, 1988
note a: [Tl] variable; upper, lower limits shown; est. pH 7 at freshwater end, pH 8 at saltwater end						
note b: est. pH 8						
note c: T 60°C, pH 1.86, in acid sulfate hot spring, Uzon volcano						
note d: pH 11-12 reported, Lovozero and Pamir localities						
note e: T 250°-300°C, PCO2 = 0.1-10 bars, pH est 7.6						

Table 6.2 - Experimental Ti-oxide solubility data								
ppm Ti	[Ti] mol/kg	log [Ti]	P (bars)	T °C	mineral	fluid	study	
0.1	3.1e-06	-5.5	1	18	TiO2(act)	see note a	Nabivanets & Lukachina 1964	
71.8	1.5e-03	-2.8	1	25	TiO2(act)	see note b	Babko et.al., 1962	
0.7	1.5e-05	-4.8	1	25	TiO2(act)	see note b	Babko et al., 1962	
0.4	7.9e-06	-5.1	1	25	n/a	see note c	Liberti et al., 1963	
2000	4.2e-02	-1.4	1	95	anatase	see note d	Bright & Readey, 1987	
1.7	3.5e-05	-4.5	15	200	anatase	see note e	Schuiling & Vink, 1967	
1.3	2.8e-05	-4.6	15	200	rutile	see note e	Schuiling & Vink, 1967	
1.0	2.1e-05	-4.7	100	200	rutile	see note f	Agapova et al., 1979	
2.1	4.3e-05	-4.4	83	300	anatase	see note e	Schuiling & Vink, 1967	
1.6	3.3e-05	-4.5	83	300	rutile	see note e	Schuiling & Vink, 1967	
5.0	1.0e-04	-4.0	100	300	rutile	see note f	Agapova et al., 1979	
7.7	1.6e-04	-3.8	1000	400	rutile	see note g	Barsukova et.al. 1979	
239	5.0e-03	-2.3	1000	400	rutile	see note g	Barsukova et.al. 1979	
6.7	1.4e-04	-3.9	1400	450	rutile	see note g	Barsukova et.al. 1979	
245	5.1e-03	-2.3	1400	450	rutile	see note g	Barsukova et.al. 1979	
185	2.3e-03	-2.6	15000	750	see note h	pure H2O	Schneider & Eggler, 1987	
14150	1.8e-01	-0.8	10000	1000	rutile	pure H2O	Ayers & Watson, 1993 - see note i	
3300	4.1e-02	-1.4	21000	1000	rutile	pure H2O	Ayers & Watson, 1993	
1500	1.9e-02	-1.7	29300	1000	rutile	pure H2O	Ayers & Watson, 1993	
19000	2.4e-01	-0.6	10000	1100	rutile	pure H2O	Ayers & Watson, 1993	
10475	1.3e-01	-0.9	21000	1100	rutile	pure H2O	Ayers & Watson, 1993 - see note i	

note a: fluid chemistry given as 0.1M NaClO4, pH varied from 4.4-7.0: [Ti] essentially constant, mean value tabulated

note b: fluid chemistry given as 0.1 M NaCl, 5 measurements between pH 1.3-2.3: upper & lower values listed here

note c: organic reagent of Ti in perchloric acid: 3 measurements between pH 1.9-2.4: value tabulated is at pH 2.4

note d: fluid chemistry given as 0.5 M HF 0.5 M HCl

note e: fluid chemistry given as 1 M NaCl, pH not specified (est 5.5-6.0)

note f: fluid chemistry given as pH 7.2, $\Sigma CO2 = 1.0$, $\Sigma H2S = 0.3$, $\Sigma SO4 = 0.01$ mol/kg

note g: fluid chemistry given as pH 8-9, [F-] varied from 0.3 to 2.1 M, by adding KF: [Ti] increases with [F-]

note h: starting materials prepared from a mixture of natural materials, including kaersutite - see ref. for details

note i: tabulated figures are means of several runs at stated conditions

Chapter 7

Discussion and Conclusions

Chapter 7 - Discussion and Conclusions

Chapter 7 - Discussion and Conclusions

Opening Statement

In this chapter I attempt to assemble all of the facts and ideas of the preceding chapters and combine them into a larger picture. This chapter is organized around 8 major themes; detailed conclusions from the earlier chapters are discussed in the context of these themes. The themes are arranged from the specific to the general.

The mineralogy and petrology of the New Idria Serpentinite are seen to be complex, yet not without parallels in other Alpine serpentinites and ultramafic bodies. The bulk composition and relict textures in the serpentinite suggest that the ultramafic protolith was a peridotite consisting of dunite and harzburgite, together with minor lherzolite and pyroxenite. The very high degree of alteration and weathering has obscured much of the evidence at New Idria, but there remain telltale signs of the evolution of this body in the form of relict minerals and rock textures.

I. Minerals and Mineral Associations

At least five generations of minerals are present in the New Idria Serpentinite. These generations represent an overall time progression; they record one or more stages in the evolution of the serpentinite. The minerals of these generations may appear in more than one rock type, but their occurrence is consistent with their relative timing.

- **Relict Igneous Minerals:** such minerals are scarce, but are occasionally preserved as unserpentinized cores of grains in serpentinite rock. Olivine, orthopyroxene, clinopyroxene and chromite are locally preserved. Chromite is unique in that it appears to be relatively unaffected by serpentinization.

- **Serpentine Minerals:** the serpentine minerals and related oxides and hydroxides form the host rock of the District, which comprises over 90% of all rock types present. New Idria differs from most other serpentinites in that it is chrysotile-dominated. Lizardite, antigorite, brucite and magnetite all occur in lesser quantities. However, serpentine recrystallization generally limits our ability to see through more than two serpentinization events.

- **Metamorphic Minerals of the Tectonic blocks:** mineral associations in these tectonic inclusions are a valuable source of information about the metamorphic processes to which these rocks were subjected, and indirectly, about the nature of the protoliths. Each block type records an M1 and an M2 metamorphic event. The M1 generation of minerals appears to predate entrainment of the tectonic blocks, but M1 metamorphism itself may have been a multi-stage event for some of the tectonic blocks. The M2 mineral generation postdates block entrainment; the minerals for which the District is best known, benitoite and Ti-garnet, belong to this generation.

- **Intrusive Igneous Minerals:** late intrusions of an amphibole soda syenite have a unique mineralogy. A small contact aureole about the best exposed of these intrusions documents the intrusive event. The original igneous minerals are preserved, but minerals resulting from deuteric alteration are also found.

- Surface Alteration Minerals: these are chiefly carbonates of various types, that record the interaction of meteoric waters with the rocks of the serpentinite. These minerals appear primarily in fully serpentinized igneous rocks, but are also found in the metamorphic rocks of tectonic inclusions. Calcite, magnesite and hydromagnesite are the most abundant of the alteration minerals.

Table 7.1 summarizes these points in the form of a correlation chart. Each column represents a distinct rock type at New Idria. Within each column, the relative timing of mineral generations proceeds from oldest to youngest. In a few cases it is possible to correlate mineral generations across rock types; the shaded bar in the Miocene suggests that all of these mineral generations record Miocene events, as discussed below.

A. Serpentine

1. The phase relations among the serpentine minerals are difficult to show schematically, and are not completely understood. In general, lizardite and chrysotile are the low temperature serpentine minerals; antigorite is the high temperature phase. Lizardite and antigorite are the high pressure phases. The most up-to-date discussion of this issue is in Wicks & O'Hanley (1988).

2. Antigorite, chrysotile and lizardite are no longer considered to be polymorphs: they are not chemically identical (O'Hanley et al., 1989). Each mineral occupies a compositional range, and these ranges partially overlap.

3. According to O'Hanley et al. (1989), a_{H_2O} affects the formation of lizardite versus chrysotile. Molecular water in the halloysite structure might correspond to (thus far

undetected) water in the chrysotile structure. If true, this would lead to a hypothetical chrysotile formula of $Mg_3Si_2O_5(OH)_4 \cdot nH_2O$., where $0 \leq n \leq 1$.

4. In antigorite, the Si-O-Si bonds at the points where the tetrahedral sheets invert are responsible for the tough, resistant nature of antigorite compared with lizardite or chrysotile, in which the adjacent layers are held together by weak bonds involving hydrogen. Antigorite is a member of a polysomatic series between lizardite and talc (e.g. Otten, 1993; Sanford, 1978; Thompson, 1978). The conventional antigorite formula is equivalent to 15 Liz + 1 Tlc. If the wavelength of the modulation were to decrease the structure would become increasingly talc-like, while if the wavelength were to increase the structure would become increasingly lizardite-like.

5. Fe and Al are the principal compositional variants in serpentine. Compositional variation occurs along the three exchange vectors $Al_2Mg_{-1}Si_{-1}$(Tk); $FeMg_{-1}$; $Fe^{3+}Al_{-1}$. The dioctahedral vacancy substitution $[]Al_2Mg_{-3}$ is not known to occur in serpentine. Trace amounts of Ca, Na, and K reported in serpentine analyses may represent mixtures mixtures of other silicates with serpentine in the analyzed samples.

6. At New Idria, the dominant phase assemblage of chrysotile + brucite indicates an Mg/Si ratio between forsterite and enstatite, serpentinizing fluids low in CO_2, and a low temperature equilibrium (<250°C). Antigorite knockers described in Chapter 4 record a higher temperature. On the basis of trace occurrences of josephinite, I conclude that the environment during serpentinization was relatively reducing.

B. Olivine, Pyroxene and Chromite

1. Relict olivine, orthopyroxene and clinopyroxene are locally preserved in lherzolite veins, in the cores of serpentine grains. Their compositions are related by the inequality:

$$X_{Mg}^{Cpx} \geq X_{Mg}^{Opx} \geq X_{Mg}^{Ol}$$

2. Accessory chromite includes two groups, a primary group and an altered group. The primary group includes chromites with appreciable contents of Cr, Fe, Mg, and Al, but only trace amounts of Ti, Mn, Ni, and Zn. The compositions are typical of chromites from Alpine-type ultramafic bodies worldwide, and are properly named *ferroan magnesiochromites*.

3. The altered group of chromites occurs in rocks which have clearly undergone post-serpentinization metamorphism. Altered chromites are frequently found rimmed by the chromian chlorite kammererite; this chlorite overprints the surrounding serpentine fabric in these rocks. Altered chromites are cryptically zoned, with Cr-rich cores and Cr-poor rims.

C. Chlorite and Diopside

1. Evidence for Fe-Mg partitioning (X_{Mg}) between coexisting minerals is preserved in the serpentinite and in tectonic blocks. A surprising observation is that, for these bulk compositions, chlorite appears to be more Fe-rich than the coexisting Cpx, an exception to the normal rule that chlorite is less Fe-rich than a coexisting mafic mineral. In this study, the following relationships were established:

$$X_{Mg}^{Ol(ig)} > X_{Mg}^{Ol(met)}$$

$$X_{Mg}^{Cpx(ig)} > X_{Mg}^{Cpx(met)}$$

$$X_{Mg}^{Cpx} > X_{Mg}^{Chl}$$

$$X_{Mg}^{Chl(M2)} > X_{Mg}^{Chl(M1)}$$

2. Under the prevailing metamorphic conditions, chlorite was the only phase that could accommodate significant amounts of Al in addition to Fe and Mg. Differences in chlorite compositions reflect differences in bulk compositions from one block to another. However, based on the relatively Fe and Al-rich nature of the M1 chlorite compared to the M2 chlorite *within a single tectonic block*, I conclude that the M1 event occurred at a higher metamorphic grade than the M2 (Laird, 1988).

D. Garnets

1. Most of the New Idria garnets are calcic and belong to the andradite clan. Many, but not all garnets of the New Idria district are strongly anisotropic, sector twinned, and zoned. Titanium substitution occurs principally along the exchange vector $TiFe_{-1}$, making these garnets titaniferous andradites. Some of the garnets are also hydrous and vary along the hydrogarnet exchange vector H_4Si_{-1}. A few of the garnets are Ti-grossulars, and occupy a portion of composition space not previously explored. Compositional variation in these garnets occurs along the vector $TiFe^{2+}Al_{-2}$. The mean TiO_2 content of the garnets in this study is 5 wt. %. One of the garnets contains 15.62 wt. % TiO_2, which corresponds to approximately one Ti atom per formula unit, i.e. the schorlomite end member.

2. Most analyses have less than 3 Si cations per formula unit (pfu), and more than 3 Ca cations pfu. The New Idria garnets are therefore similar to many other reported titaniferous garnets in that they are *subsilicic* and *supercalcic*.

3. At the present time that presence of Ti^{3+} in garnets has not been completely ruled out, but is only supported by indirect and equivocal evidence. $TiFe_{-1}$ substitution may be achieved by more than one crystal chemical process: the vector is equivalent to either or both of the vectors $TiFe^{2+}Fe^{3+}_{-2}$ and $Ti^{3+}Fe^{3+}_{-1}$. The $Ti^{3+}Fe^{3+}_{-1}$ vector is considered the less likely of the two, but until the proper EXAFS studies are completed, the debate will rage on. In this study using microprobe analytical techniques it was not possible to distinguish between these two possibilities and $TiFe_{-1}$ is used to describe compositional variations in garnets.

4. New Idria andradite garnets occur in a variety of hues, including yellows, reds, greens, browns, and black. The colors of garnets and other minerals relate broadly to chemical composition, both major and trace elements. The principal color series is from yellow to black, correlating well with progress along the $TiFe_{-1}$ exchange vector. Chromian garnets are emerald green, grossular garnets are cinnamon colored. Garnets containing both Ti and Mn are a dull brown color.

5. Andradite garnets containing up to 38 mole % uvarovite component are found in slabby serpentinized harzburgite blocks. These garnets are anhedral, emerald green, and often associated with relict chromite grains. Chromian andradites are very rare: these are believed to be the first chromian andradites reported from the United States.

E. Sodic Amphibole

1. A blue amphibole was found in veins within antigorite serpentinite near the western margin of the New Idria serpentinite. The amphibole has a partially filled A-site and appears to lie approximately one-third of the distance between a winchite and eckermannite; the paragenesis is a new one. An approximate formula for this amphibole is:

$$(Na,K)_{0.31}(Na,Ca,Fe^{2+})_2(Mg,Fe^{3+},Fe^{2+},Al,Cr,Mn,Ti)_5Si_{8.00}O_{22}(OH,Cl,F)_2$$

II. Tectonic Blocks

1. Three types of tectonic blocks are recognized in the New Idria Serpentinite: chlorite-diopside-garnet rocks, mafic schists, and antigorite knockers.

2. All types of tectonic blocks show evidence of two metamorphic events, here defined as M1 and M2. M1 metamorphism is associated with the development of penetrative foliation in the chlorite-diopside-garnet rocks and the mafic schists, and the interpenetrating fabric of the antigorite blocks. M2 metamorphism is associated with the development of tension cracks and veins that crosscut the M1 foliation in chlorite-diopside-garnet blocks and mafic schists, and with crosscutting garnet veins in the antigorite knockers.

3. Shearing during M1 metamorphism is manifest by penetrative foliation of the dominant Fe-rich M1 chlorite, and by bending, fracturing and recrystallization of M1 diopside and garnet. These observations show that the M1 metamorphism was synkinematic.

4. The M1 fabric is crosscut by veins interpreted as tension cracks. These veins are filled with M2 garnet, diopside, and minor chlorite. The M2 minerals in the veins have beautifully preserved delicate textures without post-mineralization deformation. Therefore the M2 mineralization was postkinematic.

5. A study of fluid inclusions in M2 minerals showed that homogenization temperatures averaged 235°C. Measurements of melting temperatures showed that Tm(ice) = -3.5° to -2.0°C, indicating that the salinity was equivalent to 3-5 wt. % NaCl. Assuming that the pressure of M2 metamorphism did not exceed 3 kb (see Section III), the trapping temperatures were at or below 400°C.

6. The bulk compositions of the chlorite-diopside-garnet rocks differ from that of the bulk serpentinite, but are very similar to those of pyroxenites from other ultramafic rocks world- wide. The trace element concentrations of the chlorite-diopside-garnet rocks fall within the normal range for pyroxenites; the concentrations are different from those of a serpentinized harzburgite sample from New Idria.

7. The chlorite-diopside-garnet rocks are shown, by means of a "spinel norm" calculation, to be the metamorphosed equivalents of olivine websterites.

8. The phase assemblage chlorite + diopside + Ti-garnet ± magnetite can be derived from the low-temperature hydration of an ultramafic precursor of pyroxenite composition. The phase assemblages found at New Idria suggest that greenschist or blueschist facies conditions accompanied this hydration. The stability of this phase assemblage is at present the only control on the temperature of M1 metamorphism.

9. The chlorite-diopside-garnet rocks of New Idria did not form as rodingites because the bulk composition of both the metapyroxenite blocks and the enclosing serpentinite were *both* silica-poor. Chlorite, diopside and titaniferous andradite garnets are all stable phases in association with serpentine minerals. There is no regional scale rodingite rind at the boundary of the New Idria Serpentinite because the emplacement into the country rock postdated serpentinization.

10. Low solubilities of Ti oxides, lack of a well-developed vein system connecting chlorite-diopside-garnet blocks, lack of penetrative foliation in serpentine rock adjacent to foliated chlorite-rich rocks, and lack of apparent Ti-metasomatism at the margin of the igneous intrusives all argue against formation of chlorite-diopside-garnet rock by the metasomatic alteration of ordinary serpentine rock by fluids from igneous intrusives.

11. Bulk compositional similarities, the observation of M1 and M2 metamorphism, rock textures, and the existence of chlorite-diopside-garnet rocks in other localities argue for essentially isochemical metamorphism of blocks of pyroxenite to produce the chlorite-diopside-garnet rocks at New Idria.

12. It is possible that the meta-pyroxenite blocks are tectonic inclusions from an unknown source entrained within the serpentinite: tectonic inclusions of a variety of other rock types are present. It is also possible that the meta-pyroxenite blocks were primary igneous features or even that they have a cognate origin with the depleted dunites and harzburgites. They may represent cumulate layers or crosscutting veins and dikes. The mirror symmetry observed at the 34-50 locality suggests, but does not prove, an origin as a multiple injection dike. The present random orientation of the blocks may well be the result of boudinage or other tectonic dismemberment of dikes followed by block rotation during the diapiric ascent of the New Idria Serpentinite.

13. Chlorite + diopside + Ti-garnet rocks are now known from three localities outside the New Idria District: Val Malenco, Italy; Sangabawa District, Japan; Mid-Atlantic Ridge at 43°N. All of these parageneses are in serpentinized ultramafic rocks.

14. Greenstone and mafic schist at the Gem Mine are interpreted as Franciscan rocks entrained by the serpentinite. The mineralized zone that contains benitoite lies along or near the contact between these two rock types.

15. It is proposed here that benitoite at the Gem Mine formed by metamorphism of the contact between the hanging wall greenstone and footwall mafic schist, in the presence of Na-rich, low silica fluids. Mineralized drusy cavities and extensive development of vein systems suggest hydrothermal mineralization at the Gem Mine, but the chemical components needed to produce benitoite and probably the other exotic minerals are available in the adjacent wall rocks. Therefore there is no need to advect Ti, Ba and other components from a great distance. Ordinary brines associated with M2 metamorphism probably produced local mobility of the all the required chemical components of benitoite and other minerals.

16. A preliminary determination of the age of benitoite and neptunite has been made using the Rb-Sr method and a two-point isochron. The age is estimated to be 11.96 Ma. (error bar not available). This age should be compared with the age of the New Idria Syenite, 12.4 ± 0.8 Ma reported in Section III. A further attempt to date neptunite crystals using $^{40}Ar/^{39}Ar$ technique is currently underway.

17. Knockers of dense, tough antigorite with a sugary texture form resistant, positive-weathering knobs in the District. These knockers may be sheared or mylonitized as at

Santa Rita Peak, with recrystallization of antigorite within the mylonite zone. Locally, the knockers are crosscut by veins of M2 garnet that contain fluid inclusions. Some of the fluid inclusions contain methane. The knockers have a thermal history separate in part from that of the bulk serpentinite, and must be older than the immediately surrounding serpentinite.

III. Intrusive Rocks

1. The New Idria Serpentinite contains small syenite stocks of Miocene age, here collectively named the New Idria Syenite. The syenite is shown to have an intrusive relationship with the surrounding serpentinite. In the contact aureole around the intrusive syenite, prograde olivine replaces antigorite. The aureole grades outwards to a mixture of chrysotile and lizardite.

2. The New Idria Syenite is a soda syenite, composed primarily of sodic feldspar and kaersutite amphibole. The amphibole is very coarse grained in places, with crystals up to 30 cm. long. Elsewhere the rock is fine-grained with only millimeter-sized amphibole crystals.

3. The age of the New Idria Syenite has been determined by Marvin Lanphere (USGS) to be 12.4 ± 0.8 Ma, using the $^{40}Ar/^{39}Ar$ total fusion technique on an amphibole mineral separate from the syenite.

4. The occurrence of the prehnite-zoisite pair in deuterically altered syenite provides a pressure estimate at the time of alteration. The stability fields of prehnite and zoisite overlap only between 1 and 3 kb and between 250° and 280°C (Frey et al., 1991).

Therefore the outcrop presently at the surface lay at a depth of 3.5 to 10 km. at the time of alteration, assuming an average density of 2.8 g/cm^3 for the rock formerly overlying the outcrop. This is the only quantitative pressure estimate obtained during the course of this study, although blueschist minerals described in Chapter 4 provide a general estimate.

5. If the 12.4 Ma age of the syenite is close to the time of deuteric alteration, which is reasonable for a small intrusion, then the unroofing rate since the late Miocene may be calculated. The average unroofing rate is calculated to be 0.3 to 0.8 mm/year for the past 12 million years. This calculation agrees well with the estimated rate of 1 mm/year for the Coast Ranges, obtained using other data (Ring & Brandon 1994).

IV. Element Mobility During Metamorphism

1. Metamorphism at New Idria was accompanied by limited element mobility of Ti and other elements in metamorphic fluids. An element is considered mobile if measurable changes in its concentration relative to a specified reference frame occur during a particular process. The strongest case for significant Ti mobility is the appearance of Ti-bearing phases in a rock otherwise devoid of TiO_2, when these phases are limited to a boundary layer and where textural evidence shows advection across this boundary layer. The New Idria Serpentinite is an ideal place to look for such evidence because the country rock of depleted serpentinite has less than 1 ppm TiO_2, while Ti-enriched phases occur in the tectonic blocks.

2. M2 "cats eye" garnets in the lateral transition zone at the Melanite Mine show evidence for meter-scale Ti mobility. Cores of Ti-rich garnet overgrown by Ti-poor garnet are found only in the lateral transition zone. These are interpreted as the result of Ti-

bearing fluids moving out of the Ti-rich chlorite-diopside-garnet rock into Ti-free serpentinite rock.

3. Presence of M2 andradite garnets in the antigorite knockers at Santa Rita Peak and San Carlos Peak argue for Ca mobility in fluids. Interfingering of M2 diopside and serpentine at other localities also suggests local Ca mobility during in-situ recrystallization.

4. A blue sodic amphibole in an antigorite schist near the boundary fault between the serpentinite and Franciscan rocks suggests that Na was mobile in this environment. Local mobilty of Na, Ba, Ti, and other elements occurred in the mineralized zone at the Gem Mine, within Franciscan rocks.

5. Local mobility of Fe and Mg during M2 metamorphism is suggested by the large number of vein-filling ferromagnesian minerals. On the other hand, there is no solid evidence for mobility of Al at New Idria.

V. Progressive Serpentinization

1. Serpentine formed after dunite often has a knobby outcrop texture formed by intersecting serpentine/brucite veins which isolate rounded kernels of unserpentinized dunite. This texture is widespread at New Idria because of the abundance of dunite in the protolith.

2. Serpentine formed after harzburgite often has a slabby texture, and the serpentinized rock fractures leaving sharp edges, rather than the rounded kernels of serpentinized dunite. This texture is found locally at New Idria.

3. Models for serpentinization are frequently expressed in the MSH system. A more general model for serpentinization of fertile ultramafic rocks in the system CMASH and CFTMASH is proposed in this study. The resulting low-temperature CMASH phases all lie inside the brucite-talc-diopside-chlorite tetrahedron.

4. Ca is considered a mobile component during serpentinization; Al, Fe and Ti are generally conserved. Element behavior during serpentinization is as follows, to an excellent approximation: Mg partitions into serpentine; Al, Mg, and Fe into chlorite; Fe into magnetite and garnet; Ca into diopside and garnet; Si into all of these silicates. Mg and minor Fe form brucite. Coleman (1977) noted additionally that:

$$X_{Mg}^{Srp} > X_{Mg}^{Ol} > X_{Mg}^{Brc}$$

VI. Formation of Short Fiber Chrysotile Asbestos

1. New Idria is one of the largest deposits of chrysotile asbestos in the world and the site of the only operating asbestos mine in the United States at the present time. New Idria is unique in that the mineralogy of the serpentinite is dominated by chrysotile. Chrysotile asbestos from New Idria is also remarkable in that the fiber length is much shorter (5 μm typical) than other occurrences.

2. Most serpentinites are lizardite-dominated. Lizardite is much less abundant at New Idria than chrysotile, possibly due to the recrystallization of earlier lizardite under shearing stress. An alternative explanation for the abundance of chrysotile is the extensive growth of cataclastic fabric due to the predominance of dunite in the protolith.

Figure 7.1a - Kinematic model for development of chrysotile asbestos by block rotation of partially serpentinized dunite kernels under dextral shear. Note that sense of shear between kernels is everywhere sinistral; a particle between kernels will be repeatedly milled; irregular kernels will develop slickensided fabric. The process leads to effective destruction of the rock fabric.

Figure 7.1a - Kinematic Model for Dunite Kernel Rotation

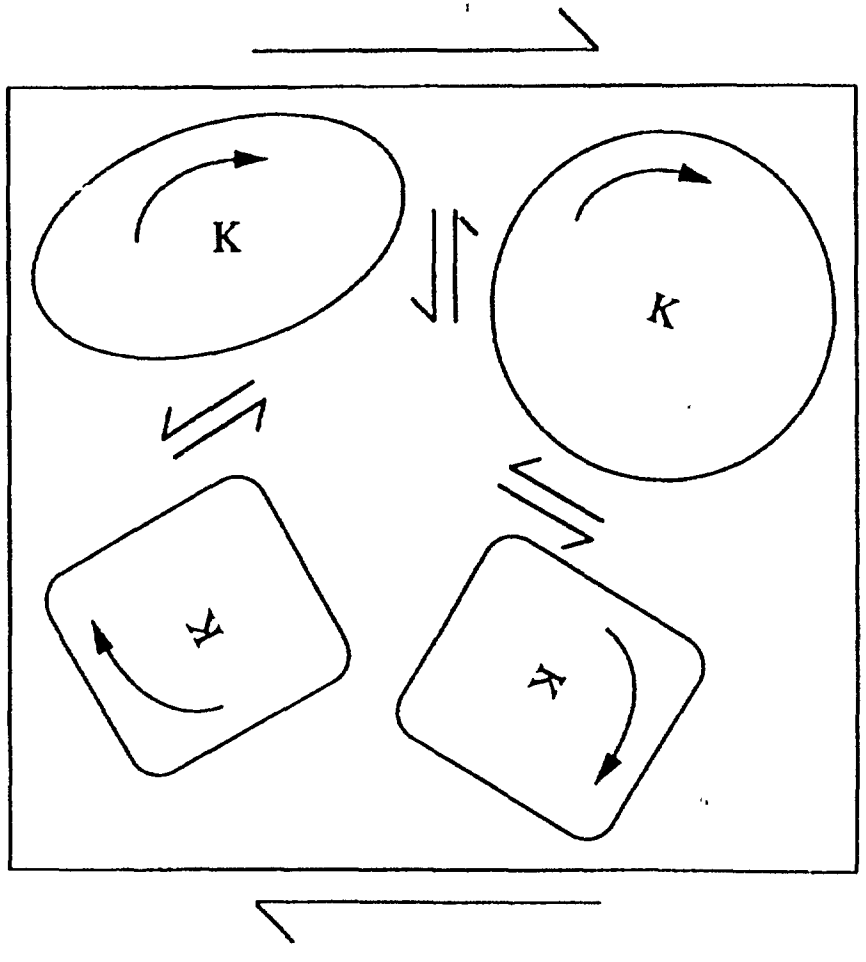

Figure 7.1b - Kinematic model for development of subparallel shear planes in slabby, partially serpentinized harzburgite lacking kernel pattern. Note sense of shear is everywhere dextral, repeated milling of particles reduced by comparison with Figure 7.1a. Mechanical integrity of rock is preserved for a relatively long time.

Figure 7.1b - Kinematic Model for Development of Shear Planes in Harzburgite

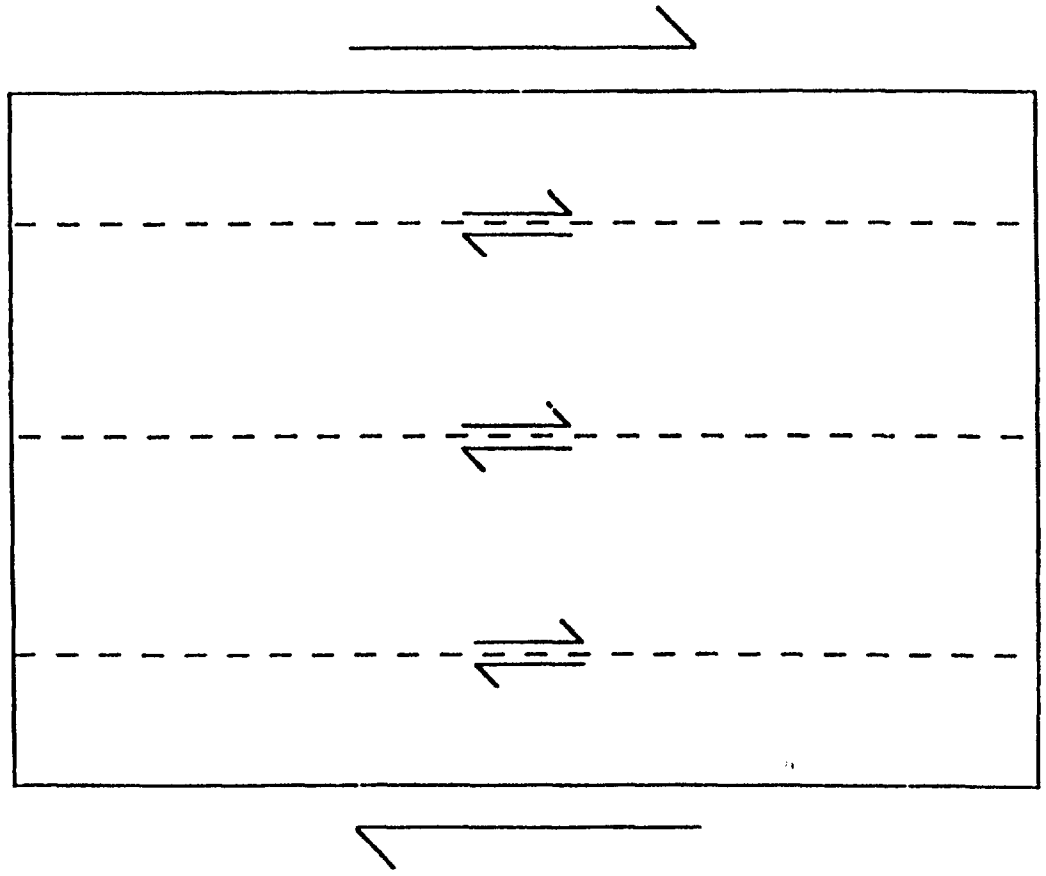

3. Chrysotile asbestos is the habit of serpentine that forms at low temperatures in rocks that are being deformed. The reason for the abundance of short fiber chrysotile asbestos at New Idria has been attributed to repeated recrystallization under shearing stress, leading to a continual size reduction (Mumpton & Thompson, 1975). However, evidence for repeated recrystallization is ambiguous.

4. An alternative model, suggested in the field to the author by David O'Hanley, has to do with the progressive serpentinization of dunite summarized in the previous section. Once serpentinization has proceeded far enough to mechanically isolate kernels of dunite, block rotation and shearing of isolated kernels under tectonic stress could produce the slickensided textures and repeated milling of fibers in the veins between kernels (**Figure 7.1a**). This process would mechanically destabilize the rock and permit introduction of more serpentinizing fluids; positive feedback between progressive serpentinization and the mechanical properties of the rock would lead to effective destruction of the rock fabric. New Idria may well approximate the end-state of these chemical and physical processes. Isolated dunite kernels from New Idria show development of slickensides in a variety of orientations relative to a single kernel, suggesting a chaotic process.

5. Progressive serpentinization of harzburgite would produce a more slablike texture, in which the mechanical integrity of the rock would be maintained for a relatively long time. Asbestos would form preferentially in the shear planes, leading to slip-fiber asbestos deposits typical of Vermont and the Eastern Townships of Quebec (**Figure 7.1b**).

VII. Regional Implications

A. Tectonic History

At this point it is necessary to summarize the tectonic environment in which the New Idria Serpentinite formed. While it is beyond the scope of this study to examine the full story of the tectonic history of California, certain ideas must be kept in mind as the following description unfolds. For a more complete discussion of California tectonics, the reader is referred to Ernst (1981) or Irwin (1990). Since the oldest rocks in the District are of Jurassic age, our discussion is confined to events since that time.

B. Jurassic Tectonics

During the Late Jurassic period the western margin of North America was geologically active. The Farallon Plate was being subducted under the North American Plate during this time. A forearc basin developed in front of the Sierra Nevada volcanic arc (Dickinson & Seely, 1979; Bartow, 1990). The forearc basin itself is now represented by the Great Valley of California. The Franciscan Formation, a tectonic melange of greywackes, metavolcanics and cherts was being deposited in the Jurassic as an accretionary prism near the trench. A flake of Farallon Plate oceanic crust or underlying mantle was obducted onto the North American continent in a structural position within the Franciscan accretionary prism. At roughly the same time, other ophiolitic flakes were obducted onto the continental margin; as a group these comprise the Coast Range Ophiolite (Ernst, 1981). Ages of these flakes, where established by crosscutting intrusives, range from 153-165 Ma, i.e. latest Jurassic. Blueschist metamorphism accompanied the subduction of the Farallon Plate.

C. Cretaceous and Neogene Tectonics

Sedimentation in the forearc basin was nearly continuous from the Cretaceous through the Pliocene; these sediments are now represented by the thick clastic rocks collectively named the Great Valley Sequence. As the Tertiary continued, the shallow forearc basin became isolated from the Pacific Ocean; the Great Valley Sequence includes both marine and nonmarine sediments. (Taliaferro, 1943). During this time, the flake of oceanic crust now exposed at New Idria was buried under these sediments, and was possibly undergoing serpentinization.

D. Miocene Plate Rearrangements in the Eastern Pacific

In the Oligocene/Miocene there was a fundamental reconfiguration of plate movements in the Eastern Pacific. At this time, the Farallon Plate began to break up into smaller pieces, and the dominant geometry became strike-slip rather than convergence (Atwater, 1986). A spreading center in the Gulf of California began to separate Baja California from the mainland (Stock & Hodges, 1989); the Juan de Fuca and Pacific Plates, separated by the Mendocino Fracture Zone, both lay in strike-slip contact with the North American plate, creating the San Andreas Fault. The triple junction at which the North American, Pacific, and Juan de Fuca plates all meet, named the Mendocino Triple Junction, began its northwest migration along the San Andreas Fault.

E. Miocene Events

By the late Miocene, the triple junction had reached a position directly under New Idria (Stock & Hodges, 1989) Triple junction passage occurred approximately 12 Ma ago (Figure 7.2). As noted in Chapter 1, the intrusion of the New Idria Syenite occurred at 12.4 ± 0.8 Ma. It is suggested here that the intrusion is related to passage of the

Mendocino Triple Junction, possibly due to the slab window mechanism described by Dickinson & Snyder (1979) and Hole et al., (1991). The locus of points that mark the trace of the Mendocino Triple Junction as it has progressed northward is also marked by volcanic and intrusive igneous activity (e.g. Glazner & Supplee, 1982; Johnson & O'Neill, 1984; Fox et al., 1985; Stanley, 1987; Liu & Furlong, 1992). As noted in Chapter 4, the age of mineralization at the Gem Mine is about 11.96 Ma (no error bar available). It is suggested that this marks the time of M2 metamorphism at New Idria in tectonic blocks of all types. Finally, as noted in Chapter 1, the late Miocene was a period of active tectonic uplift, during which the New Idria diapir breached the surface. This event is recorded by the sudden appearance of clastic serpentine in the sedimentary record of the Great Valley Sequence, in a unique boulder conglomerate mapped as the Big Blue member of the Tremblor formation (Anderson & Pack, 1915). The Miocene Big Blue member documents the uplift and emergence of the New Idria serpentinite; the large size of the clasts in this conglomerate (up to several meters) suggests that transport was only over a short distance.

F. Multiple Effects of Triple Junction Passage at New Idria

The following hypothesis is proposed: tectonic uplift, mineralization resulting from low-grade metamorphism (including mercury mineralization), and igneous intrusions all were effects of a single cause - passage of the Mendocino Triple Junction at about 12 Ma. The thermal energy required for uplift, development of tension cracks with a northeast orientation (Figure 4.1), M2 metamorphism, mercury mineralization along the New Idria Thrust Fault, and the intrusion of the New Idria Syenite came from upwelling asthenosphere caused by the slab window opened by the Mendocino Triple Junction (Dickinson & Snyder, 1979). The thermal coupling between the New Idria Syenite and M2 metamorphism was probably limited to contact aureoles such as the one described in Chapter 1. Hydrothermal fluids of rather ordinary composition, with moderate salinity,

Figure 7.2 - Plate configurations in late Miocene (Anomaly 5AA, 12.9.Ma), showing position of Mendocino Triple Junction, where North American, Pacific, and Juan de Fuca Plates meet near New Idria, which is attached to North American Plate. See Stock & Hodges (1989) for plate reconstruction details.

Figure 7.2 - Late Miocene Plate Configuration

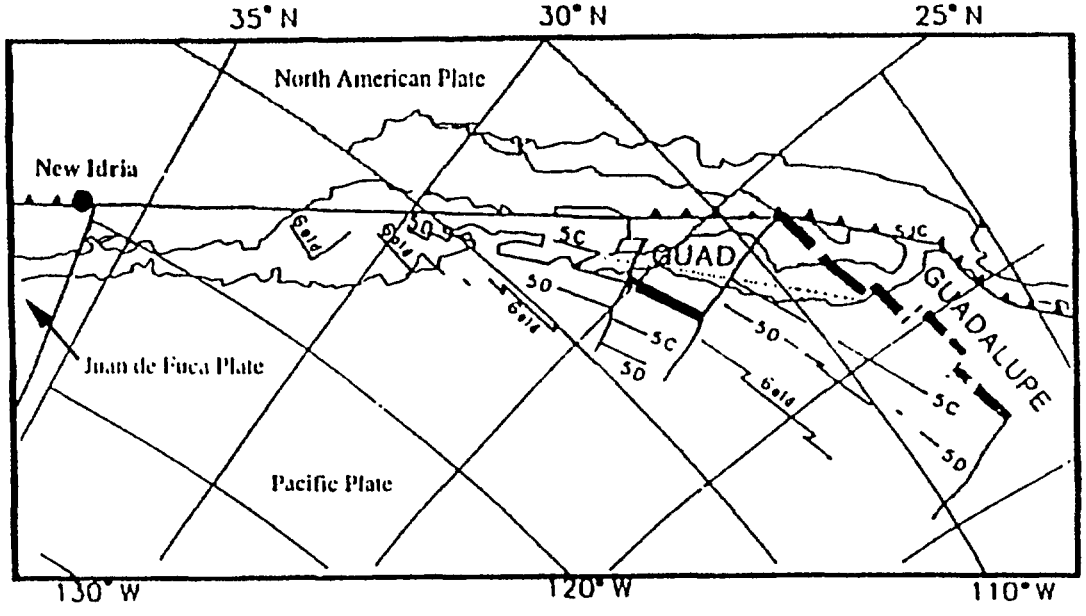

Anomaly 5AA 12.9 Ma

Figure 7.3 - Perspective drawing of tectonic windows in the Coast Ranges, after Irwin (1990), showing New Idria and other windows.

Figure 7.3 - Tectonic Windows in the Coast Ranges

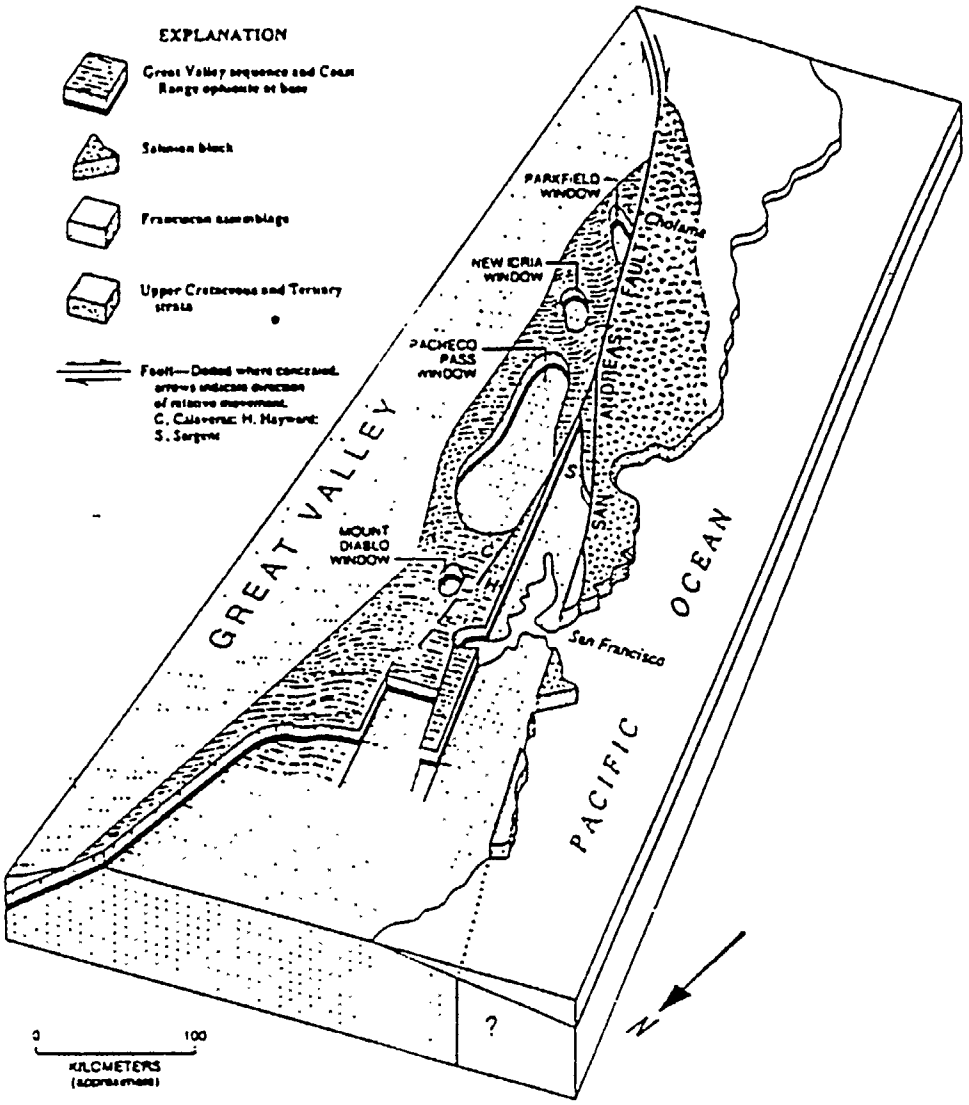

after Irwin, 1990

probably circulated only locally, and not on a widespread basis. Mobility of chemical components needed to form the vein-filling M2 minerals was apparently local as well.

VIII. New Idria and the San Andreas Fault Today

A. New Idria as a Tectonic Window

Today the New Idria Serpentinite is seen as a tectonic window into the Coast Range Ophiolite (Figure 7.3). The diapir protrudes through the surrounding clastic rocks on the steep western limb of the asymmetric Great Valley synclinorium. Compressional uplift of the Coast Ranges may be due to a small orthogonal component of the strike slip movement along the San Andreas Fault. This northeast directed compression is estimated to be as much as 10% of the strike slip movement, or 5 mm/yr (Montgomery, 1993).

B. Recent Seismicity

The region around and immediately to the south of the New Idria District is seismically active today, as shown in Figure 2.1. There are swarms of magnitude 1-3 earthquakes and an occasional larger event (e.g. the 1926 Idria, $M_W = 5.5$, 1982 M_W=5.4 New Idria, 1983 M_W=6.5 Coalinga, and 1985 M_W=6.1 Kettleman Hills events, ref. Stein & Ekström, (1992)). The 1983 earthquake of magnitude 6.5 effectively levelled the town of Coalinga, and stimulated research interest in this part of California (e.g. Rymer & Ellsworth, 1990). The 1983 event occurred near the crest of the Coalinga Anticline, a southerly continuation of the New Idria Thrust Fault. The predominant mode of recent seismicity has been reverse or thrust faulting, due to crustal shortening from compressional stress normal to the strike of the San Andreas fault, (e.g. Montgomery, 1993; Bartow, 1990; Wentworth &

Zoback, 1989). Another part of the seismic activity may be due to continued diapiric rise of the serpentinite massif, expressed as small ruptures of the boundary faults.

Closing Statement

A. Comparative Studies of Ophiolites

Ophiolites and the chemical and physical processes that accompany their evolution are as yet incompletely understood. Every serpentinite or other part of an ophiolite provides clues, but it is necessary to visit many such places in order to assemble a realistic and coherent picture. In this study I found visits to the Mont Albert Massif in Quebec, the Belvidere Mt. Complex in Vermont, and the Malenco Serpentinite in Italy to be crucial in the growth of my understanding. Much of what Alpine geologists have learned from study of Alpine ophiolites is directly applicable to the California Coast Ranges, which do not superficially resemble the Alps.

There is historical symmetry in this realization: in 1891, Gustav Steinmann, on field trip in the Coast Ranges with Andrew C. Lawson, recognized the common structural features between California and the Alps that led to development of his model of ophiolite structures known as the Steinemann Trinity. Comparative studies of the Alps and the California Coast Ranges were key to this development, according to Steinemann (1906).

B. Areas for Future Research

The three main areas most ripe for future research in the New Idria District are, in my opinion:

1. Subduction zone processes, including obduction of ophiolites and entrainment of tectonic blocks, and the role of fluids in metamorphism.

2. Structural processes, including modes of crustal shortening in strike slip environments such as the San Andreas Fault system. .

3. Public policy issues, related to the largely unfounded concerns about health hazards of chrysotile asbestos, have brought recent attention to New Idria. Fluvial transport of chrysotile asbestos from the New Idria District eastward via Los Gatos Creek and Cantua Creek into the San Joaquin Valley, as well as westward via the San Benito River, has been taking place for a great length of time, possibly for as much as 12 million years. Since the completion of the California Aqueduct, which interferes with normal drainage patterns, some of the chrysotile asbestos has gone into the canal, mainly under flood conditions. Therefore the downstream users of this water have found chrysotile asbestos fibers in the water. Concern about the possible health hazards of this condition has been greatly overstated; the hazard is negligible. It will be a matter for science and public policy together to find a safe and economical solution to this issue.

Fin

Table 7.1 - Correlation Chart for Mineral Generations

Age	Serpentinite	Syenite	Metapyroxenites	Mafic Schists	Antigorite Knockers
Recent ↑ ↓	hydromagnesite & artinite	calcite	hydromagnesite & calcite	aragonite & calcite	calcite?
Miocene ↑	serpentine 2: local atg + ol	prh & zo ab + amp	M2 minerals: chl + di + Ti-grt	M2 minerals: zeolites benitoite & neptunite	M2 minerals: andradite Cr-grt & Cr-chl
↓ Cretaceous ↑ ↓ Jurassic	*serpentine 1:* *ctl & liz* lherzolite veins dunite (ol ± opx ± cpx)		*M1 minerals:* *chl + di + Ti-grt* olivine websterite (ol + opx + cpx)	M1 blueschist minerals: crossite, jadeite Franciscan Fm: greywackes & volcanics	*serpentine 2: serpentine 1:* *antigorite antigorite* *serpentine 1:* *ctl & liz?* lherzolite or harzburgite (ol ± opx ± cpx)

Bibliography

Bibliography

Agapova, G.F., Modnikov, I.S. and Shmariovich, Ye.M., 1989, Experimental study of the behavior of titanium in hot sulfide-carbonate solutions. International Geology Review, 31, no. 4, pp. 424-430.

Agricola, Georgius (Bauer, Georg), 1546, De Natura Fossilium. Forben Press, Basel. English translation by Bandy, M.C. & Bandy, J.A., 1955, Geo. Soc. Am. Special Paper 63, 240 pp.

Akizuki, Mizuhiko, 1984, Origin of optical variations in grossular-andradite garnet. Am. Min. 68, pp. 328-338.

Anderson, R. & Pack, R.W., 1915, Geology and oil resources of the west border of the San Joaquin Valley north of Coalinga, California. USGS Bull. 603, 220 pp.

Arnold, R. & Anderson, R., 1908, Preliminary report on the Coalinga district, Fresno and Kings Counties, California. USGS Bull. 357, 142 pp.

Arnold, R. & Anderson, R., 1910, Geology and oil resources of the Coalinga district, California. USGS Bull. 398, 354 pp.

Atwater, T., 1986, Plate tectonic history of the Northeast Pacific and Western North America. *in* Winterer, E.L., Hussong, D.M., & Decker, R.W., The geology of North America, Vol. N: The Eastern Pacific Ocean and Hawaii. Geol. Soc. Am. DNAG Series., 563 pp.

Aubry, L.E., 1903, Quicksilver resources of California. Calif. State Mining Bur. Bull. 27, 273 pp.

Ayers, J.C. & Watson, E.B., 1991. Solubility of apatite, monazite, zircon, and rutile in supercritical aqueous fluids with implications for subduction zone geochemistry. Philos. Trans. R. Soc. London, A335, pp. 365-375.

Ayers, J.C. & Watson, E.B., 1993. Rutile solubility and mobility in supercritical aqueous fluids. Contrib. Mineral. Petrol., 114, pp. 321-330.

Babko, A.K., Gridchina, G.I. and Nabivanets, B.I., 1962. Study of titanium(IV) in hydrochloric acid by dialysis and ion-exchange chromatography. Russian Jour. Inorg. Chem. 7, pp. 66-70.

Baes, C.F. & Mesmer, R.E., 1986, The hydrolysis of cations. Robert. E. Krieger Pub. Co., Malabar, Florida, 489 pp.

Barnes, H.L., & O'Neil, J., 1969, The relationship between fluids in some fresh Alpine-type ultramafics and possible modern serpentinization, Western United States. Geo. Soc. Am. Bull., 80, pp. 1947-1960.

Barriga, F.J.A.S., Fyfe, W.S., Landefeld, L.A., Munha, J. & Ribeiro, A., 1992, Mantle eduction: tectonic fluidisation at depth. Earth Sci. Rev., 32, pp. 123-129.

Barsukova, M.L., Kuznetsov, V.A., Dorofeyeva, V.A. and Khodakovskiy, L.I., 1979. Measurement ot the solubility of rutile TiO_2 in fluoride solutions at elevated temperatures. Geochemistry International, 7, pp. 41-49.

Barth, T.F.W., 1952. Theoretical Petrology. John Wiley & Sons, New York, 416 pp.

Bartow, J.A., 1990, A summary of the Cenozoic stratigraphy and geologic history of the Coalinga region, central California. *in* Rymer, M.J. & Ellsworth, W.L., eds., The Coalinga, California earthquake of May 2, 1983. USGS Prof. Paper 1487., 417 pp.

Bebout, G.E. & Barton, M.D., 1989. Fluid flow and metasomatism in a subduction zone hydrothermal system: Catalina Schist terrane, California. Geology, 17, pp. 976-980.

Becker, G.F., 1888, Geology of the quicksilver deposits of the Pacific Slope. USGS Monograph 13, pp. 291-309.

Bell, J.M., Clarke, E. de C., & Marshall, P., 1911, The geology of the Dun Mountain Subdivision, Nelson Bull. N.Z. Geological Survey, 12 (new series), pp. 29-40.

Berman, R.G., 1988, Internally-consistent thermodynamic data for minerals in the system Na_2O-K_2O-CaO-MgO-FeO-Fe_2O_3-Al_2O_3-SiO_2-TiO_2-H_2O-CO_2. Jour. Pet., 29, pp. 445-522.

Berman, R.G., 1991, Thermobarometry using multiequilibrium calculations: a new technique with petrologic applications. Can. Min., 29, pp. 833-855.

Betechtin, A.G., 1961, Mikroskopische Untersuchungen an Platinerzen aus dem Ural. N. Jahrb. Min. Anh., 97, pp. 1-34.

Bolton, H.E., 1927, Fray Juan Crespi, missionary explorer of the Pacific Coast 1769-1774. Univ. Calif. Press, Berkeley, Calif., 402 pp.

Botto, R.I. & Morrison, G.H., 1976, Josephinite: a unique nickel-iron. Am. Jour. Sci., 276, pp. 241-274.

Bowen, N.L. & Schairer, F., 1935, The system MgO-FeO-SiO_2. Am. Jour. Sci., 29, pp. 150-217.

Bowen, N.L. & Tuttle, O.F., 1949, The system MgO-SiO_2-H_2O. Geo. Soc. Am. Bull., 80, pp. 1947-1960.

Boyd, F.R., 1973, A pyroxene geothermometer. Geochim. et Cosmochim. Acta., 37, pp. 2533-2546.

Bradley, W.M., 1909, On the analysis of the mineral neptunite from San Benito County, California. Am. Jour. Sci., 28, pp. 15-16.

Bradley, W.W., 1914, photograph of Dallas Gem Mine. *in* Sperisen, F.J., 1938, Gem minerals of California. Calif. Jour. Mines & Geol., 34, p. 70.

Bradley, W.W., 1918, Quicksilver resources of California. Calif. State Mining Bur. Bull. 78, p. 94.

Brewer, W.H., 1966, Up and Down California in 1860-1864, 3rd. edition. Farquhar, F.P., ed. Univ. Calif. Press, Berkeley, Calif. 583 pp.

Bright, E. & Readey, D.W., 1987. Dissolution kinetics of TiO_2 in HF-HCl solutions. Jour. Am. Ceramic Soc. 70, pp. 900-906.

Brown, G.E., Jr., Stebbins, J.F. & Parks, G.A., 1985, Field trip guide to mineral localities in the New Idria District, San Benito County, California. Stanford Univ Geology Dept., unpublished, 30 pp.

Bucher, K. & Frye, M., 1994, Petrogenesis of metamorphic rocks. Springer-Verlag, Berlin, 318 pp.

Byerly, P.E., 1954, Regional gravity in the central Coast Ranges and San Joaquin Valley, California. Harvard Univ. Ph.D. thesis, unpublished, 67 pp.

Carswell, D.A. & Gibb, F.G.F., 1987, Evaluation of mineral thermometers and barometers applicable to garnet lherzolite assemblages. Cont. Min. Pet., 92, pp. 448-511.

Cartledge, G.H., 1928. Studies on the periodic system. I. The ionic potential as a periodic function. Jour. Am. Chem. Soc. 50, pp. 2856-2872.

Caruso, L.J. & Chernosky, J.V., Jr., 1979, The stability of lizardite. Can. Min., 17, pp. 757-769.

Chernosky, J.V., Jr., 1975, Aggregate refractve indices and unit cell parameters of synthetic serpentine in the system MASH. Am. Min., 60, pp. 200-208.

Chidester, A.H., Albee, A.L. & Cady, W.M., 1978, Petrology, structure, and genesis of the asbestos-bearing ultramafic rocks of the Belvidere Mountain area in Vermont. USGS Prof. Paper 1016, 95 pp.

Cho, M. & Fawcett, J.J., 1986, A kinetic study of clinochlore and its high temperature equivalent forsterite-cordierite-spinel at 2 kbar water pressure. Am. Min., 71, pp. 68-77.

Coleman, R.G., 1957, Mineralogy and Petrology of the New Idria District, California. Stanford Univ. Ph.D. thesis, unpublished, 160 pp.

Coleman, R.G., 1961, Jadeite deposits of the Clear Creek area, New Idria District, San Benito County, California. Jour. Pet. 2, pp. 209-47.

Coleman, R.G., 1977, Ophiolites: ancient ocean lithospheres? Springer-Verlag, Berlin, 229 pp.

Coleman, R.G., 1980, Tectonic inclusions in serpentinites. Archives des Sciences (Genéve) 33, pp. 89-102.

Coleman, R.G., 1986, Field trip guide to New Idria area, California. 14th general meeting of the International Mineralogical Association, Stanford Univ., July 1986. 36 pp.

Compagnoni, R., Ferraris, G. & Mellini, M., 1985, Carlosturanite, a new asbestiform rock-forming silicate from Val Varaita, Italy. Am. Min., 70, pp. 767-772.

Conrad, M.E., 1990. The relation of propylitic alteration and ^{18}O depletion patterns to Ag/Au vein deoposits in the Tayoltita mining district of Durango, Mexico. Harvard University, Ph.D. thesis, unpublished, 370 pp.

Cross, W., Iddings, J.P., Pirsson, L.V. & Washington, J.S., 1902, A quantitative chemico-mineralogical classification and nomenclature of igneous rocks. Jour. Geol., 10, pp. 555-690.

Dann, K.T., 1988, Traces on the Appalachians. Rutgers Univ. Press, New Brunswick, N.J., 159 pp.

Dibblee, T.W., Jr., 1971, Geologic map of the New Idria quadrangle, California. USGS Open File map 71-87. Scale 1:62,500.

Dibblee, T.W., Jr . 1979, Geologic map of the central Diablo Range between Hollister and New Idria, San Benito, Merced and Fresno Counties, California. USGS Open File map 79-358. Scale 1:125,000.

Dickenson, W.R. & Seely, D.R., 1979, Structure and stratigraphy of forearc regions. Am. Assoc. Pet. Geol. Bull., 63, pp. 2-31.

Dickenson, W.R. & Snyder, W.S., 1979, Geometry of subducted slabs related to San Andreas transform. Jour. Geol., 87, pp. 609-627.

Dowty, E., 1969, Crystal chemistry of titanian garnet: site distribution and valence of cations. Stanford. Univ. Ph.D. thesis, unpublished,134 pp.

Duke, J.M. & Bonardi, M., 1982, Chromian andradite from Reaume Township, Ontario. Can. Min., 20, pp. 49-53.

Eckel, E.B. & Myers, W.B., 1946, Quicksilver deposits of the New Idria district, San Benito and Fresno Counties, California. Calif. Jour. Mines & Geol., 42, pp. 81-124.

Erickson, R.L., & Blade, L.V., 1963. Geochemistry and petrology of the alkalic igneous complex at Magnet Cove, Arkansas. USGS Prof. Paper 425, 95 pp.

Ernst, W.G., 1965, Mineral parageneses in Franciscan metamorphic rocks, Panoche Pass, California. Geo. Soc. Am. Bull. 76, pp. 879-913.

Ernst, W.G., 1981, Summary of the geotectonic development of California, *in* Ernst, W.G., ed., The geotectonic development of California; Rubey Volume 1, Prentice Hall, Englewood Cliffs, N.J., pp. 601-613.

Evans, B.W., 1977, Metamorphism of alpine peridotite and serpentinite. Ann. Rev. Earth Planet. Sci. 5, pp. 397-447.

Evans, B.W., Johannes, W., Oterdoom, H. & Trommsdorff, V., 1976, Stability of chrysotile and antigorite in the serpentinite multisystem. Schweiz. Min. Pet. Mitt., 56, pp. 79-93.

Evans, B.W. & Guggenheim, S., 1988, Talc, pyrophyllite, and related minerals. *in* Bailey, S.W., ed., Hydrous Phyllosilicates (exclusive of micas). Min. Soc. Am. Rev. in Min. V. 19, pp. 225-294.

Evans, B.W. & Trommsdorff, V., 1970, Regional metamorphism of ultramafic rocks in the Cantral Alps: parageneses in the system CaO-MgO-SiO_2-H_2O. Schweiz. Min. Pet. Mitt. 50, pp. 481-492.

Faust, G.T. & Fahey, J.J., 1962, The serpentine-group minerals. USGS Prof. Paper 384A, 88 pp.

Flohr, M.J.K. & Ross, M., 1989, Alkaline igneous rocks of Magnet Cove, Arkansas: metasomatized ijolite xenoliths from Diamond Jo quarry. Am. Min. 74, pp. 113-131.

Force, E.R., 1991. Geology of titanium-mineral deposits. Geo. Soc. Am. Special Paper 259, 112 pp.

Forstner, W., 1903, The quicksilver resources of California. Calif. State Mining Bur. Bull. 27, pp. 125-147.

Fowkes, E.J., 1982, An educational guidebook to the geologic resources of the Coalinga District, California. West Hills College, Coalinga, Calif. 260 pp.

Fox, K.F., Jr., Fleck, R.J., Curtis, G.H. & Meyer, C.E., 1985, Implications of the northwestwardly younger age of the volcanic rocks of west-central California. Geo. Soc. Am. Bull., 96, pp. 647-654.

Frye, M., de Capitani, C. & Liou, J.G., 1991, A new petrogenetic grid for low-grade metabasites. Jour. Met. Geol., 9, pp. 497-509.

Gale, H.S., 1912, Late developments of magnesite deposits in California and Nevada. *USGS Bull. 540*, pp. 503-509.

Gardner, L.R., 1990, Geochemical analysis of silicate rocks and soils by XRF using pressed powders and a two-stage calibration procedure. Chem. Geol. 88, pp. 169-182.

Gieré, R., 1990. Hydrothermal mobility of Ti, Zr, and REE: examples from the Bergell and Adamello contact aureoles (Italy). Terra Nova, 2, pp. 60-67.

Gieré, R., 1992. Formation of accessory REE-minerals in titanium-rich veins. V.M. Goldschmidt Conference, Program & Abstracts, May 8-10, 1992, Reston, VA. The Geochemical Society. p. A41.

Gilbert, C.A., 1984, Prospectors, capitalists and bandits: the history of the New Idria Quicksilver Mine, 1854-1972. San Jose St. Univ., M.S. thesis, unpublished.

Glazner, A.F. & Supplee, J.A., 1982, Migration of Tertiary volcanism in the southwestern United States and subduction of the Mendocino fracture zone. Earth. Plan. Sci. Lett., 60, pp. 429-439.

Goguel, R., 1988. Ultratrace metal analysis of New Zealand geothermal waters by ICP-MS. Proceedings of the 2nd Conf. of N.Z. Trace Element Group, Christchurch, N.Z., Nov-Dec 1988.

Goldschmidt, V.M., 1954. Geochemistry. Oxford University Press, New York. 730 pp.

Grant, J.A., 1986. The isocon diagram - a simple solution to Gresens' equation for metasomatic alteration. Econ. Geol., 81, pp. 1976-1982.

Green, D.H., & Ringwood, A.E., 1967, The stability fields of aluminous pyroxene peridotite and garnet peridotite and their relevance in the upper mantle structure. Earth Plan. Sci. Lett., 2, pp. 41-57.

Griffin, D., Phillips, W.R., & Hatch, D.M., 1990, Refinement of the crystal structure of a natural tetragonal garnet. Geo. Soc. Am. Abst. Prog., p. A215.

Guidotti, C.V. Cheney, J.T. and Guggenheim, S., 1977. Distribution of titanium between coexisting muscovite and biotite in pelitic schists from northwestern Maine. Am. Min., 62, pp. 438-448.

Guillemin-Tarayre, E., 1867, Carte géologique de la haute Californie et de la Nevada, *in* Guillemin-Tarayre, E., 1871, Description des anciennes possessions Mexicaines du nord: Mission scientifique au Mexique et dans l'Amérique Central, Géologic. Paris, 216 pp.

Guthrie, G.D. & Mossman, B.T., 1993, Health effects of mineral dusts. Min. Soc. Am. Rev. in Min. V.28, 584 pp.

Haggerty, S.E., 1987. Metasomatic mineral titanates in upper mantle xenoliths. *in* Nixon, P.H., ed., Mantle Xenoliths. John Wiley & Sons, New York. pp. 671-690.

Hall, A., 1987, Igneous Petrology. Longman Scientific & Technical, Essex, England. 573 pp.

Harris, N.B. & Einaudi, M.T., 1982, Skarn deposits in the Yerington District, Nevada: metasomatic skarn evolution near Ludwig. Econ. Geol., 77, pp. 877-898.

Harte, B., 1877, The story of a mine. Houghton Mifflin, Boston. 172 pp.

Hazen, R.M., 1976, Effects of temperature and pressure on the cell dimension and X-ray temperature factors of periclase. Am. Min., 61, pp. 266-271.

Helgeson, H.C., Delany, J.M., Nesbitt, H.W., & Bird, D.K., 1978, Summary and critique of the thermodynamic properties of rock-forming minerals. Am. Jour. Sci. 278-A, 229 pp.

Helgeson, H.C., Kirkham, D.H. and Flowers, G.C., 1981. Theoretical prediction of the thermodynamic behavior of aqueous electrolytes at high pressures and temperatures, IV. Calculation of activity coefficients and apparent molal standard and relative partial molal properties to 600°C and 5 kb. Am. Jour. Sci. 281, pp. 1249-1516.

Henderson, F.B., 1965, Deposition and oxidation of "serpentinite-type" mercury deposits. Harvard Univ. Ph.D. thesis, unpublished, 140 pp.

Hill, D.P., Eaton, J.P., Ellsworth, W.L., Cockerham, R.S., Lester, F.W., & Corbett, E.J., 1991, The seismotectonic fabric of central California. *in* Slemmons, D.B., Engdahl, E.R., Zoback, M.D. & Blackwell, D.D., eds., Neotectonics of North America. Boulder, CO, Geol. Soc. Am. Decade Map Volume I., pp. 107-132.

Hole, M.J., Rogers, G., Saunders, A.D. & Storey, M., Relation between alkalic volcanism and slab-window formation. Geology, 19, pp. 657-660.

Holland, H.D., 1967, Gangue minerals in hydrothermal deposits. *in* Barnes, H.L., ed., Geochemistry of Hydrothermal Ore Deposits. Holt, Rinehart & Winston, New York, 670 pp.

Holland, H.D., 1979, Solubility and occurrence of non-ore minerals. *in* Barnes, H.L., ed., Geochemistry of Hydrothermal Ore Deposits, 2nd ed. J. Wiley & Sons, New York, 798 pp.

Hoppe, H.J., 1941. Untersuchungen an Palagonittuffen und über ihre Bildungsbedingungen. Chemie der Erde, 13, pp. 484-514.

Hopson, C.A., Mattinson, J.M., & Pessagno, E.A., Jr., et al., 1981, The Coast Range Ophiolite. *in* Ernst, W.G., ed., The geotectonic development of California; Rubey Volume 1:, Prentice Hall, Englewood Cliffs, N.J., pp. 418-510.

Howie, R.A. & Wooley, A.R., 1968, The role of titanium and the effect of TiO_2 on the cell-size, refractive index, and specific gravity in the andradite-melanite-schorlomite series. Min. Mag., 36, pp. 775-790.

Huckenholz, H.G., 1969, Synthesis and stability of Ti-andradite. Am. Jour. Sci., 267-A, pp. 209-232.

Huckenholz, H., Hölzl, E., Huggins, F.E. & Virgo, D., 1976, A reconnaissance study of the Ti-garnet stability field at defined oxygen fugacities. Carnegie Inst. Wash. Yearbook 76, pp. 711-720.

Huggins, F.H., Virgo, D. & Huckenholz, H.G., 1977a, Titanium-containing silicate garnets. II. The distribution of Al, Fe^{3+}, and Ti^{4+} between octahedral and tetrahedral sites. Am. Min., 62, pp. 475-490.

Huggins, F.H., Virgo, D. & Huckenholz, H.G., 1977b, Titanium-containing silicate garnets. II. The crystal chemistry of melanites and schorlomites. Am. Min., 62, pp. 646-665.

Irvine, T.N., 1967, Chromian spinel as a petrogenetic indicator, part 2: petrologic applications. Can. Jour. Earth. Sci., 4, pp. 71-103.

Irwin, W.P., 1990, Geology and plate-tectonic development. *in* Wallace, R.E., ed., The San Andreas Fault System, California. USGS Prof. Paper 1515, pp. 61-82.

Isaacs, T., 1965, A study of uvarovite. Min. Mag., 35, pp. 38-45.

Isaacs, T., 1968, Titanium substitution in andradites. Chem. Geol., 3, pp. 219-222.

Ito, J. & Frondel, C., 1967, Synthetic zirconium and titanium garnets. Am. Min., 52, pp. 773-781.

IUGS, 1973, Classification and nomenclature of plutonic rocks - recommendations by the IUGS subcommission on the systematics of igneous rocks. Neues Jahrb. Min. Monat., 1973, pp. 149-164.

Jachens, R.C., 1991, New Idria isostatic map, 1:100,000. Unpublished.

Jan, M.Q., Windley, B.F. & Wilson, R.N., 1984, Chromian andradite and olivine-chromite relations in a chromitite layer from the Jijal complex, northwestern Pakistan. Can. Min., 22, pp. 341-345.

Jarosewich, E. & Boatner, L.A., 1991, Rare-earth element reference standards for electron microprobe analysis. Geostandards Newsletter, 15, pp. 397-399.

Jenkins, D.M. & Chernosky, J.V., Jr., 1986, Phase equilibria and crystallochemical properties of Mg-chlorite. Am. Min., 71, pp. 924-936.

Jennings, C.W. & Strand, R.G., 1958, Geologic Map of California, Olaf P. Jenkins edition, Santa Cruz Sheet (1:250,000). Calif. Div. Mines.

Johnson, C.M. & O'Neil, J.R., 1984, Triple junction magmatism: a geochemical study of Neogene volcanic rocks in western California. Earth Plan. Sci. Lett., 71, pp. 241-262.

Johnson, J.W., Oelkers, E.H. & Helgeson, H.C., 1991, SUPCRT92 computer code. Lawrence Livermore Laboratory.

Kalamarides, R.I. & Berg, J.H., 1988, Coexisting Cr-rich and Cr-poor garnet from a calc-silicate gneiss, Labrador. Can. Min., 26, pp. 335-342.

Kingma, K.J. & Downs, J.W., 1989, Crystal structure analysis of a birefringent andradite. Am. Min., 74, pp. 1307-1316.

Klein, C., 1993, Rocks, minerals, and a dusty world. *in* Guthrie, G.D. & Mossman, B.T., eds., Health effects of mineral dusts. Min. Soc. Am. Rev. in Min. V.28, pp. 7-60.

Kranov, S.R., 1973. Geokhimiya redkikh elementov v podzemnykh vodakh (v svyazi s geokhimicheskimi poiskami mestorozhdeniy [Geochemistry of rare elements in ground water and geochemical prospecting]. Nedra Press, Moscow. (in Russian)

Kretz, R., 1983, Symbols for rock-forming minerals. Am. Min. 68, pp. 277-279.

Kruckeberg, A.R., 1984, California serpentines: flora, vegetation, geology, soils, and management problems. Univ. Calif. Press., Berkeley, Calif. 180 pp.

Kühberger, A., Fehr, T., Huckenholz, H.G. and Amthauer, G., 1989, Crystal chemistry of a natural schorlomite and Ti-andradites synthesized at different oxygen fugacities. Phys. Chem. Min., 16, pp. 734-740.

Kunze, G., 1956, Die gewellte Struktur des Antigorits, I. Zeit. Krist., 108, pp. 82-107.

Kujawa, F.B., Dunning, C.A., & Eugster, H.P., 1965, The derivation of stable unary phase diagrams through the use of dual networks. Am. Jour. Sci., 263, pp. 429-444.

Labotka, T.C. & Albee, A.L., 1979, Serpentinization of the Belvidere Mountain ultramafic body, Vermont: mass balance and reaction at the metasomatic front. Can. Min. 17, pp. 831-845.

Lager, G.A., Armbruster, T., Rotella, F.J. & Rossman, G.R., 1989, OH substitution in garnets: X-ray and neutron diffraction, infrared, and geometric modeling studies. Am. Min. 74, pp. 840-851.

Laird, J., 1988, Chlorites: metamorphic petrology. *in* Bailey, S.W., ed., Hydrous phyllosilicates (exclusive of micas). Min. Soc. Am. Rev. in Min. V. 19, pp. 406-453.

Laird, J. & Albee, A.L., 1972, Chemical composition and physical, optical, and structural properties of benitoite, neptunite, and joaquinite. Am. Min., 57, pp. 85-102.

Laizure, C.M., 1922, San Benito County - Asbestos: 18th report of the State Mineralogist. Calif. State Mining Bur. Bull., p. 46.

Levine-Fricke Consultants, 1989, Offsite characterization/regional soil sampling and watershed modelling report, Volume 1. Prepared for the U.S. Environmental Protection Agency, Region 9, San Francisco. 141 pp.

Liberti, A., Chiantella, V. and Corigliano, F., 1963. Mononuclear Hydrolysis of Titanium (IV) from Partition Equilibria. Jour. Inorg. Nucl. Chem., 25, pp. 415-427.

Liu, M. & Furlong, K.P., 1992, Cenozoic volcanism in the California Coast Ranges: numerical solutions. Jour. Geophys. Res., 97, pp. 4941-4951.

Loney, R.A., Himmelberg, G.R. & Coleman, R.G., Structure and petrology of the Alpine-type peridotite at Burro Mountain, California, USA. Jour. Pet., 12, pp. 245-309.

Louderback, G.D., 1907, Benitoite, a new California gem mineral. Univ. Calif. Bull. Dept. Geol. Sci., v. 5, no. 9, pp. 149-153.

Louderback, G.D., 1909, Benitoite, its paragenesis and mode of occurrence. Univ. Calif. Bull. Dept. Geol. Sci., v. 5, no. 23, pp. 331-380.

MacGregor, I.D. & Basu, A.R., 1979, Petrogenesis of the Mount Albert ultramafic massif, Quebec. Geol. Soc. Am. Bull., part 2, 90, pp. 1529-1627.

Maruyama, S., Cho, M., & Liou, J.G., 1986, Experimental investigations of blueschist-greenschist transition equilibria: pressure dedendence of Al_2O_3 contents in sodic amphiboles - a new geobarometer. *in* Evans, B.W., & Brown, E.H., eds., Blueschists and eclogites. Geo. Soc. Am. Memoir 164, p. 13.

Mason, B. & Moore, C.B., 1982. Principles of Geochemistry, 4th ed. John Wiley & Sons, New York. 344 pp.

Matsyuk, S.S., Vishnevskii, A.A., Cherenkova, A.F., & Egorova, L.N., 1991, K-richterite-bearing ilmenite-clinohumite dunite: a new variety. Sov. Geol. Geophys., 32, pp. 64-70.

Matthews, R.A., 1961, Geology of the Butler Estate Chromite Mine. Calif. Div. Mines & Geol. Spec Rpt. 71, 20 pp.

Meagher, E.P., 1982, Silicate Garnets. in Ribbe,, P.H., ed., Orthosilicates. Min. Soc. Am. Rev. in Min., V. 5, pp. 25-66.

Mellini, M. & Zanazzi, P.F., 1987, Crystal structures of lizardite-1T and lizardite $2H_1$ from Coli, Italy. Am. Min., 72, pp. 943-948.

Mielenz, R.C., 1939, The geology of the southwest part of San Benito County, California. Univ. Calif., Berkeley Ph.D. thesis, unpublished, 295 pp.

Millage, A.H., 1981, Mineralogy of the Victor Claim, New Idria district, San Benito County, California. Stanford Univ. M.S. Thesis, unpublished, 172 pp.

Milnes, A.R. & Fitzpatrick, R.W., 1989. Titanium and zirconium minerals. *in* Dixon, J.B. & Weed, S.B., eds., Minerals in Soil Environments. Soil Science Society of America, Madison, Wisconsin, 1244 pp.

Montgomery, D.R., 1993, Compressional uplift in the central California Coast Ranges. Geology, 21, pp. 543-546.

Morison, S.E., 1974, The European discovery of America: the southern voyages. Oxford Univ. Press, New York, 758 pp.

Mueller, R.F., 1967. Mobility of the elements in metamorphism. Jour. Geology, 75, pp. 565-582.

Mumpton, F.A. , & Thompson, C.S., 1975, Mineralogy and origin of the Coalinga asbestos deposit. Clays & Clay Mins., 23, pp. 131-143.

Müntener, O. & Hermann, J., 1994, Titanian andradite in a metapyroxenite layer from the Malenco ultramafics (Italy): implications for Ti-mobility and low oxygen fugacity. Cont. Min. Pet., 116, pp. 156-168.

Murdoch, J. & Ingram, B.L., 1966, A cerian vesuvianite from California. Am. Min. 51, pp. 381-387.

Nabivanets, B.I. & Lukachina, V.V., 1964. Hydroxyl complexes of titanium (IV). Ukrain. khim. zhurn., 30, pp. 1123-1128. (in Russian)

Niggli, P., 1940. Mineralien der Schweizer-Alpen, Band I, II. B. Wepf, Basel, 300 pp.

O'Hanley, D.S., 1992, Solution to the volume problem in serpentinization. Geology, 20, pp. 705-708.

O'Hanley, D.S. & Dyar, M.D., 1993, The composition of lizardite 1T and the formation of magnetite in serpentinites. Am. Min. 78, pp. 391-404.

O'Hanley, D.S., Chernosky, J.V., Jr. & Wicks, F.J., 1989, The stability of lizardite and chrysotile. Can. Min., 27, pp. 483-493.

Ohashi, Y., Burnham, C.W., & Finger, L.W., 1975, The effect of Ca-Fe substitution in the clinopyroxene crystal structure. Am. Min., 60, pp. 423-434.

Onuki, H., Yoshida, T. & Nedachi, M., 1981, Electron probe study of Ti-rich hydroandradites in the Sangabawa metamorphic rocks. Jour. Japan Assoc. Min. Petr. Econ. Geol., 76, pp. 239-247.

Orians, K.J., Boyle, E.A. and Bruland, K.W., 1990. Dissolved titanium in the open ocean. Nature, 348, No. 6299, pp. 322-325.

Otten, M.T., 1993, High-resolution transmission electron microscopy of polysomatism and stacking defects in antigorite. Am. Min. 78, pp. 75-84.

Page, B.M., 1966, Geology of the Coast Ranges of California, *in* Bailey, E.H., ed., Geology of Northern California. Calif. Div. Mines & Geol. Bull. 190, pp. 255-276.

Patterson, S.H., 1971. Investigations of ferruginous bauxite and other mineral resources of Kauai and a reconnaissance of ferruginous bauxite deposits on Maui, Hawaii. USGS Prof. Paper 656, 74 pp.

Peabody, C. E. 1989, Association of petroleum and cinnabar in mercury deposits of the California Coast ranges, USA. Stanford Univ. Ph.D. thesis, unpublished, 256 pp.

Peabody, C.E. & Einaudi, M., 1992, Origin of petroleum and mercury in the Culver-Baer cinnabar deposit. Econ. Geol., 87, pp. 1078-1103.

Peacor, D.R., 1973, High-temperature, single crystal X-ray study of natrolite. Am. Min., 58, pp. 676-680.

Pearce, T.H., 1968. A contribution to the theory of variation diagrams. Contrib. Min. Pet., 19, pp. 142-157.

Perdikatsis, B. & Berzlaff, H., 1981, Strukturverfeinerung am Talk. Zeit. Krist., 156, pp. 1771-86.

Peretti, A.,1988, Occurrence and stabilities of opaque minerals in the Malenco serpentinite (Sondrio, Northern Italy). ETH Zürich Ph.D. thesis, unpublished.

Peretti, A, Dubessy, J., Mullis, J., Frost, B.R., and Trommsdorff, V., 1992, Highly reducing conditions during Alpine metamorphism of the Malenco peridotite (Sondrio,

Northern Italy) indicated by mineral paragenesis and H_2 in fluid inclusions. Cont. Min. Pet., 112, pp. 329-340.

Perfit, M.R., Gust, D.A., Bence, A.E., Arculus, R.J. and Taylor, S.R., 1980. Chemical characteristics of island-arc basalts: implications for mantle sources. Chem. Geol., 30, pp. 227-256.

Peters, T., 1968, Distribution of Mg, Fe, Al, Ca and Na in coexisting olivine, orthopyroxene and clinopyroxene in the Totalp Serpentinite (Davos, Switzerland) and in the alpine metamorphosed Malenco Serpentinite (N. Italy). Cont. Min. Pet., 18, pp. 65-75.

Philippot, P. & Selverstone, J., 1991. Trace-element-rich brines in eclogitic veins: implications for fluid composition and transport during subduction. Contrib. Min. Pet., 106, pp. 417-430.

Piners, M., 1894, Über Topazolith und Melanit. Zeit. Krist., 22, pp. 479-496.

Piotrowski, D.J., Long, D.J. and Vogel, D.T., 1989. A study of the first row transition elements as a group in black shales. Geol. Soc. Am. Abstr. Prog., A272.

Poty, B.P., Stalder, H.A. and Weisbrod, A.M., 1974. Fluid inclusion studies in quartz from fissures of Western and Central Alps. Schweiz. Min. Pet. Mitt., 54, pp. 717-752.

Prichard, H.M., 1979, A petrographic study of the process of serpentinization in ophiolites and the ocean crust. Cont. Min. Pet., 68, pp. 231-241.

Quick, J.E., 1981, Petrology and petrogenesis of the Trinity Peridotite, and upper mantle diapir in the Eastern Klamath Mountains, Northern California. Jour. Geophys. Res., 86, pp. 11,837-11,863.

Rahmdohr, P., 1967, A widespread mineral association connected with serpentinization. N. Jahrb. Min. Anh., 107, pp. 241-265.

Reagan, M.K. & Meijer, A., 1984. Geology and geochemistry of early arc-volcanic rocks from Guam. Geo. Soc. Am. Bull., 95, pp. 701-713.

Roberts, C.W., Jachens, R.C., & Oliver, H.W., 1990, Isostatic residual gravity map of California and offshore Southern California (1:750,000). Calif. Geologic Data Map Series no. 7. Calif. Div. Mines & Geol.

Roberts, W.L., Campbell, T.J. & Rapp, G.R., Jr., 1990, Encyclopedia of minerals. Van Nostrand Reinhold, New York. p. 81.

Robertson, M.S., 1940, Petrography of the soda-rich White Creek stock, Fresno County, California. Univ. Calif., Berkeley M.A. thesis, unpublished, 49 pp.

Robie, R.A., et al., 1978, Thermodynamic properties of minerals and related substances at 298.15 K and 1 bar (105 Pascals) pressure and at higher temperatures. USGS Bull. 1452, 456 pp.

Roedder, E., 1984, Fluid Inclusions. Min. Soc. Am. Rev. in Min. V.12, 646 pp.

Ronov, A.B., Bredanova, N.V. and Migdisov, A.A., 1992. General trends in the evolution of the chemical composition of sedimentary and magmatic rocks of the continental earth crust. Sov. Sci. Rev. G. Geology, 1, pp. 1-37.

Rost, von F., Fuchs, B. & Saddredini, H., 1979, Über Demantoid aus dem Ural und seine Farbe. Aufschluss, 30, pp. 51-56.

Rubin, J.N., Price, J.G., Henry, C.D., Pinkston, T.L., Tweedy, S.W., Koppenaal, D.W., Peterson, S.B., Harlan, H.M., Miller, W.T., Thompson, R.J., Grabowski, R.B., Laybourn, D.P., Schrock, G.E., Johnson, A., Staes, D.G., Gaines, R.V. and Miller, F.H., 1989. Mineralogy of beryilium deposits near Sierra Blanca, Texas. *in* Torma, A.E., and Gundiler, I.H., eds., Precious and rare metal technologies. Elsevier, Amsterdam, pp. 601-614.

Ryerson, F.J. & Watson, E.B., 1987. Rutile saturation in magmas: implications for Ti-Nb-Ta depletion in island-arc basalts. Earth Plan. Sci. Letters, 86, pp. 225-239.

Rymer, M.J. & Ellsworth, W.L., 1990, The Coalinga, California earthquake of May 2, 1983. USGS Prof. Paper 1487., 417 pp.

Rynearson, G.A., 1946, Chromite deposits of the North Elder Creek area, Tehama County, California. USGS Bull. 945-G, pp. 191-210.

Sack, R.O. & Ghiorso, M.S., 1991, Chromite as a petrogenetic indicator. *in* Lindsley, D.H., ed., Oxide minerals: petrologic and magnetic significance. Min. Soc. Am. Rev. in Min., V. 25, pp. 323-354.

Sanford, R.F., 1978, Regional metamorphism of ultramafic bodies and their contact zones, Western New England. Harvard Univ. Ph.D. thesis, unpublished. 376 pp.

Sanford, R.F., 1981, Mineralogical and chemical effects of hydration reactions and applications to serpentinization. Am. Min. 66, pp. 290-297.

Schmets, J., Van Muylder, J. and Pourbaix, M., 1966. Titanium. *in* Pourbaix, M., ed., Atlas of electrochemical equilibria in aqueous solutions. Pergamon Press, New York. pp. 213-222.

Schneider, M.E. & Eggler, D.H., 1987. Fluids in equilibrium with peridotite minerals: implications for mantle metasomatism. Geochim. et Cosmochim. Acta, 50, pp. 711-724.

Schuiling, R.D. & Vink, B.W., 1967. Stability relations of some titanium-minerals (sphene, perovskite, rutile, anatase). Geochim. et Cosmochim. Acta, 31, pp. 2399-2411.

Selverstone, J., Morteani, G. and Staude, J.-M., 1991. Fluid channeling during ductile shearing: transformation of granodiorite into aluminous schist in the Tauern Window, Eastern Alps. Jour. Met. Geology, 9, pp. 419-432.

Shervais, J.W. & Beaman, B.J., 1994, Major and trace element geochemistry of the Elder Creek Ophiolite, California Coast Ranges. Geol. Soc. Am. Abstr. Prog., V.26, no. 7, p. A38.

Shoji, T., 1974, $Ca_3Al_2(SiO_4)_3$ - $Ca_3Al_2(O_4H_4)_3$ series garnet: composition and stability. Jour. Min. Soc. Japan 11, pp. 359-372 (in Japanese).

Skrabal, S.A., Ullman, W.J. and Luther, G.W., 1992. Estuarine distributions of dissolved titanium. Marine Chemistry, 37, pp. 83-103.

Slansky, E. & Glen, R.A., 1982, Neptunite from the Woodsreef Serpentinite, New South Wales: a new occurrence. Tsch. Min. Petr. Mitt., 30, pp. 237-247.

Smyth, J.R. & Bish, D.L., 1988, Crystal structures and cation sites of the rock-forming minerals. Allen & Unwin, Boston, 332 pp.

Sorensen, S.S., 1986, Petrologic and geochemical comparison of the blueschist and greenschist units of the Catalina Schist terrane, southern California, *in* Evans, B.W. & Brown, E.H. eds., Blueschists and Eclogites. Geo. Soc. Am. Memoir 164, pp. 59-76.

Sorensen, S.S., 1988. Petrology of amphibolite-facies mafic and ultramafic rocks from the Catalina Schist, southern California: metasomatism and migmatization in a subduction zone metamorphic setting. Jour. Met. Geology, 6, pp. 405-435.

Sorensen, S.S. & Grossman, J.N., 1989, Enrichment of trace elements in garnet amphibolites from a paleo-subduction zone: Catalina Schist, southern California. Geochim. Cosmochim. Acta, 53, pp. 3155-3177.

Spinnler, G.E., 1985, HRTEM study of antigorite, pyroxene-serpentine reactions and chlorite. Arizona State Univ. Ph.D. thesis, unpublished.

Stanley, R.G., 1987, Implications of the northwestwardly younger age of the volcanic rocks of west-central California: alternative interpretation. Geo. Soc. Am. Bull., 98, pp. 612-614.

Staudigel, H. & Schreyer, W., 1977, The upper thermal stability of clinochlore at 10-35 kb P_{H_2O}, Cont. Min. Pet., 61, pp. 187-198.

Stebbins, J.F., Carmichael, I.S.E. and Moret, L.K., 1984. Heat capacities and entropies of silicate liquids and glasses. Cont. Min. Pet. 86, pp. 131-148.

Stein, R.S. & Ekström, G., 1992, Seismicity and geometry of a 110-km-long blind thrust fault: 2. Synthesis of the 1982-1985 California earthquake sequence. JGR, 97, B4, pp. 4865-4883.

Steinmann, G., 1906, Geologische Beobachtungen in den Alpen. Berichte der Naturforschenden Gesellschaft zu Freiburg I. Br., 16, pp. 18-66.

Stock, J.M. & Hodges, K.V., 1989, Pre-Pliocene extension around the Gulf of California and the transfer of Baja California to the Pacific Plate. Tectonics, 8, pp. 99-115.

Switzer, G., Melson, W.G. & Thompson, G., 1970, Garnet from the Mid-Atlantic Ridge near 43° N. latitude. Geo. Soc. Am. Bull., 81, pp. 895-898.

Taliaferro, N.L., 1943, Geologic history and structure of the central Coast Ranges of California. Calif. State Mining Bur. Bull. 118, pp. 119-163.

Taylor, B.E. & Liou, J.G., 1978, The low-temperature stability of andradite in C-O-H fluids. Am. Min. 63, pp. 378-393.

Thompson, J.B., Jr., 1959. Local equilibrium in metasomatic processes. *in* Abelson, P.H., ed., Researches in Geochemistry. J. Wiley & Sons, New York. pp. 427-457.

Thompson, J.B., Jr., 1978, Biopyriboles and polysomatic series. Am. Min., 63, pp. 239-249.

Thompson, J.B., Jr., 1981, An introduction to the mineralogy and petrology of the biopyriboles. *in* Veblen, D.R., ed., Amphiboles and other hydrous pyriboles - mineralogy. Min. Soc. Am. Rev. in Min. V. 9a, pp. 141-188.

Thompson, J.B., Jr., 1982, Reaction space: an algebraic and geometric approach. *in* Ferry, J.M., ed., Characterization of metamorphism through mineral equilibria, Min. Soc. Am. Rev. in Min. V. 10, pp. 33-52.

Thompson, J.B., Jr., 1991, Modal space: applications to ultramafic and mafic rocks. Can. Min., 29, pp. 615-632.

Trommsdorff, V. & Evans, B.W., 1974, Alpine metamorphism of peridotitic rocks. Schweiz. Min. Pet. Mitt., 54, pp. 333-354.

Tschermak, G., 1885, Lehrbuch der Mineralogie. Alfred Holder, Wjen, 597 pp.

Van Baalen, M.R., 1991. A fluid inclusion study of garnets from New Idria, California, USA: new evidence for titanium mobility in aqueous fluids. (abstract) for ECROFI XI. *in* Plinius, No. 5, April 1991, p. 235.

Van Baalen, M.R., 1993, Titanium mobility in metamorphic systems: a review. Chem. Geol. 110, pp. 233-249.

Van Baalen, M.R. & Zbinden, E.A., 1989. Garnets record compositional evolution of Ti-bearing fluids. (abstract) EOS, 70, pp. 1393-4.

Vasil'ev, V.P., Vorob'ev, P.N. and Khodakovskii, I.L., 1974. Standard formation potentials at constant pressure for the formation of hydroxyl complexes of titanium and the Ti^{4+} ion in aqueous solutions. Russian Jour. Inorg. Chem., 19, pp. 1481-1483.

Vaughan, F.E., 1943, Geophysical studies in California. Calif. Bur. Mines Bull. 118, pp. 67-70.

Virgo, D., Rosenhauer, M. & Huggins, F.E., 1976, Intrinsic oxygen fugacities of natural melanites and schorlomites and crystal-chemical implications. Carnegie Inst. Wash. Yearbook 75, pp. 720-729.

Waychunas, G.A., 1987, Synchrotron radiation XANES spectroscopy of Ti in minerals: effects of Ti bonding distances, Ti valence, and site geometry on absorbtion edge structure. Am. Min., 72, pp. 89-101.

Wells, P.R.A., 1977, Pyroxene thermometry in simple and complex systems. Cont. Min. Pet., 62, pp. 129-139.

Wenner, D.B. & Taylor, H.P., Jr., 1971, Temperatures of serpentinization of ultramafic rocks based on $^{18}O/^{16}O$ fractionation between coexisting serpentine and magnetite. Cont. Min. Pet., 32, pp. 165-185.

Wentworth, C.M. & Zoback, M.D., 1989, The style of late Cenozoic deformation at the eastern front of the California Coast Ranges. Tectonics, 8, pp. 237-246.

White, D.E., Hem, J.D. and Waring, G.A., 1963. Data of geochemistry: chemical composition of subsurface waters. *USGS Prof.* Paper 440-F, pp. 47-8.

Whitney, J.D., 1865, Geological Survey of California: Report of progress and synopsis of the field-work, from 1860-1864. Volume 1, Geology. Geol. Survey Calif., Philadelphia, pp. 52-60.

Whittaker, E.J.W. & Middleton, A.P., 1979, The intergrowth of fibrous brucite and fibrous magnesite with chrysotile. Can. Min., 17, pp. 699-702.

Wicks, F.J. & O'Hanley, D.S., 1988, Serpentine minerals: structures and petrology. *in* Bailey, S.W., ed., Hydrous phyllosilicates (exclusive of micas). Min. Soc. Am. Rev. in Min. V. 19, pp. 91-168.

Wicks, F.J. & Plant, A.G., 1979, Electron microprobe and X-ray microbeam studies of serpentine textures. Can. Min., 17, pp. 785-830.

Wicks, F.J., & Whittaker, E.J.W., 1977, Serpentine textures and serpentinization. Can. Min., 15, pp. 459-488.

Williams, J.F., 1891. Geol. Survey Annual Report from Arkansas for 1890, v.2, pp. 1-432, paraphrased by C.S. Ross, 1941, USGS Prof. Paper 198, p.26.

Willis, M.A., Pasteris, J.D. and Shock, E.L., 1990. Hydrothermal transport of titanium as exemplified by quartz-titanium dioxide veins near Magnet Cove, Arkansas. Geo. Soc. Am. Abstr. Prog., A363.

Willis, M.A., Pasteris, J.D. and Shock, E.L., 1991. Microanalytical investigation of the titanium mineralization at Magnet Cove, Arkansas, and possible mechanisms for titanium transport. Geo. Soc. Am. Abstr. Prog., A291.

Wise, W.S. & Gill, R.H., 1977, Minerals of the Benitoite Gem Mine. Mineralogical Record, Nov.-Dec. 1977, 8, pp. 442-452.

Wise, W.S., Pabst, A. & Hinthorne, J.R., Jonesite, a new mineral form the Benitoite Gem mine, San Benito County, California. Mineralogical Record, Nov.-Dec. 1977, 8, pp. 453-456.

Wood, B.J. & Banno, S., 1973, Garnet-orthopyroxene and orthopyroxene-clinopyroxene relationships in simple and complex systems. Cont. Min. Pet., 42, pp. 109-124.

Woodward-Clyde Consultants, 1990, Characterization of disturbances related to mining and exploration in the New Idria/Coalinga/Table Mountain study region. Prepared for the U.S. Environmental Protection Agency, Region 9, San Francisco. 73 pp.

Yada, K., 1967, Study of chrysotile asbestos by a high resolution microscope. Acta Cryst. 23, pp. 704-710.

Zigan, F. & Rothbauer, R., 1967, Neutronenbeugungsmessungen am Brucit. Neues Jahrb. Min. Monat., pp. 137-143.

Zigler, J.L., Wentworth, C.M. and Bartow, J.A., 1986, Structure contour map of the tops of the Kreyenhagen Formation and Cretaceous strata in the Coalinga area, Fresno and Kings Counties, California. Reston, Va: U.S. Geological Survey map MF-1843.

Note to the cataloger: this thesis contains 482 pages and one folded map.

UNITED STATES
DEPARTMENT OF THE INTERIOR
GEOLOGICAL SURVEY

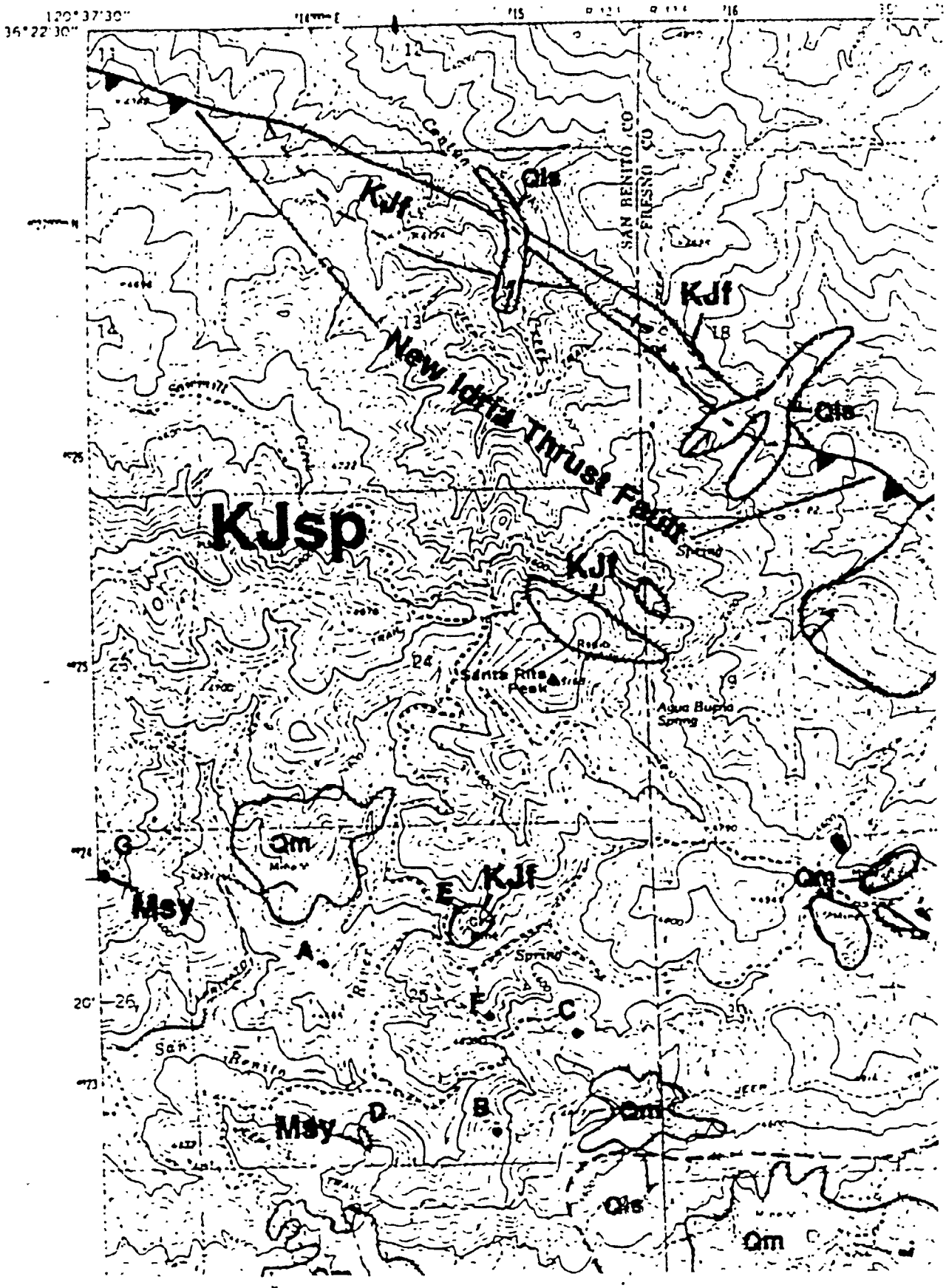

PLA

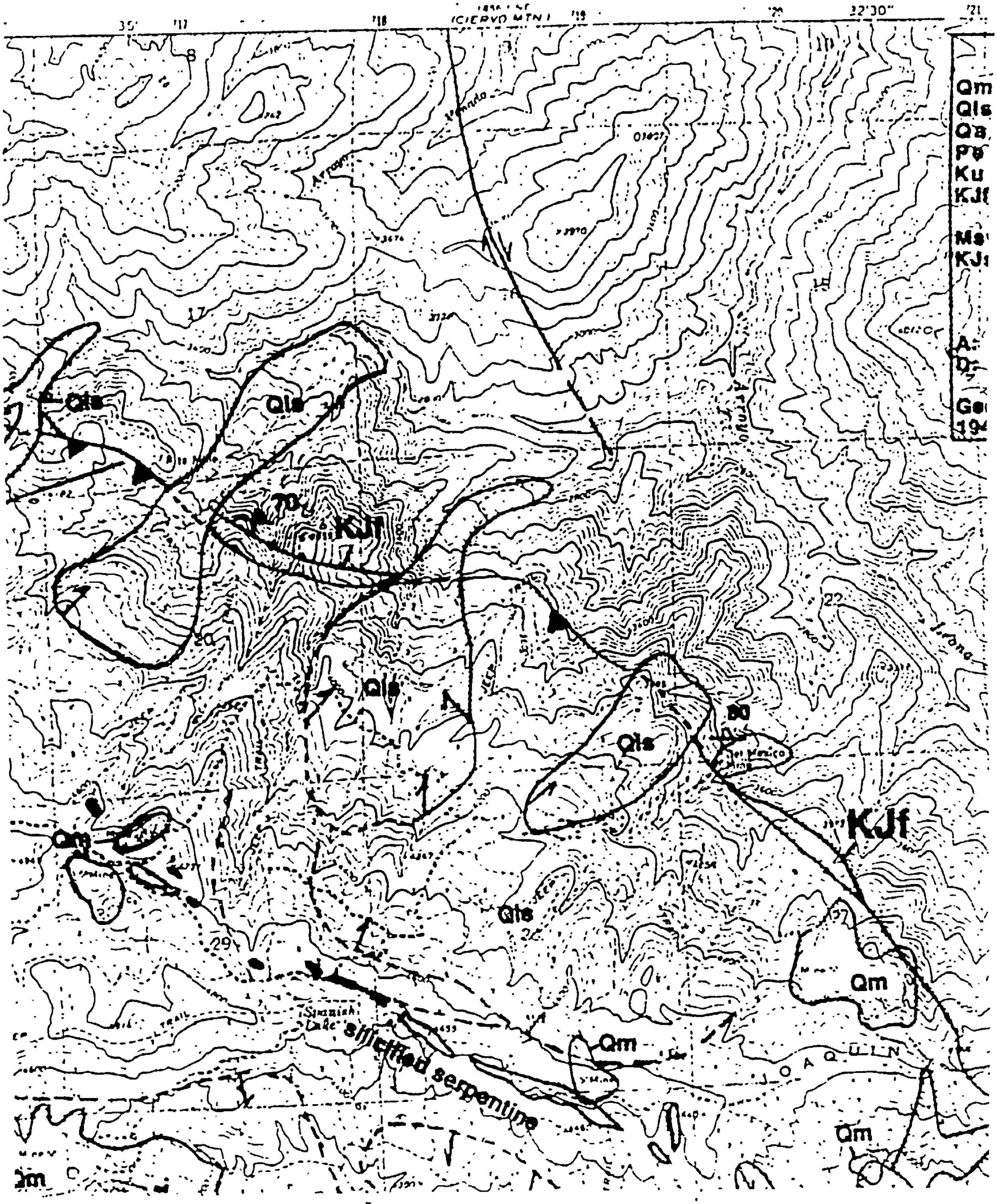

35'
(CIERVO MTN)
32'30"
Qm
Qls
KJf
Qls
Qls
KJf
Qls
Qls
Qls
80
70
KJf
Qm
Qm
Qm
Qm
Spanish Lake
silicified serpentine
JOAQUIN

PLATE 1.1

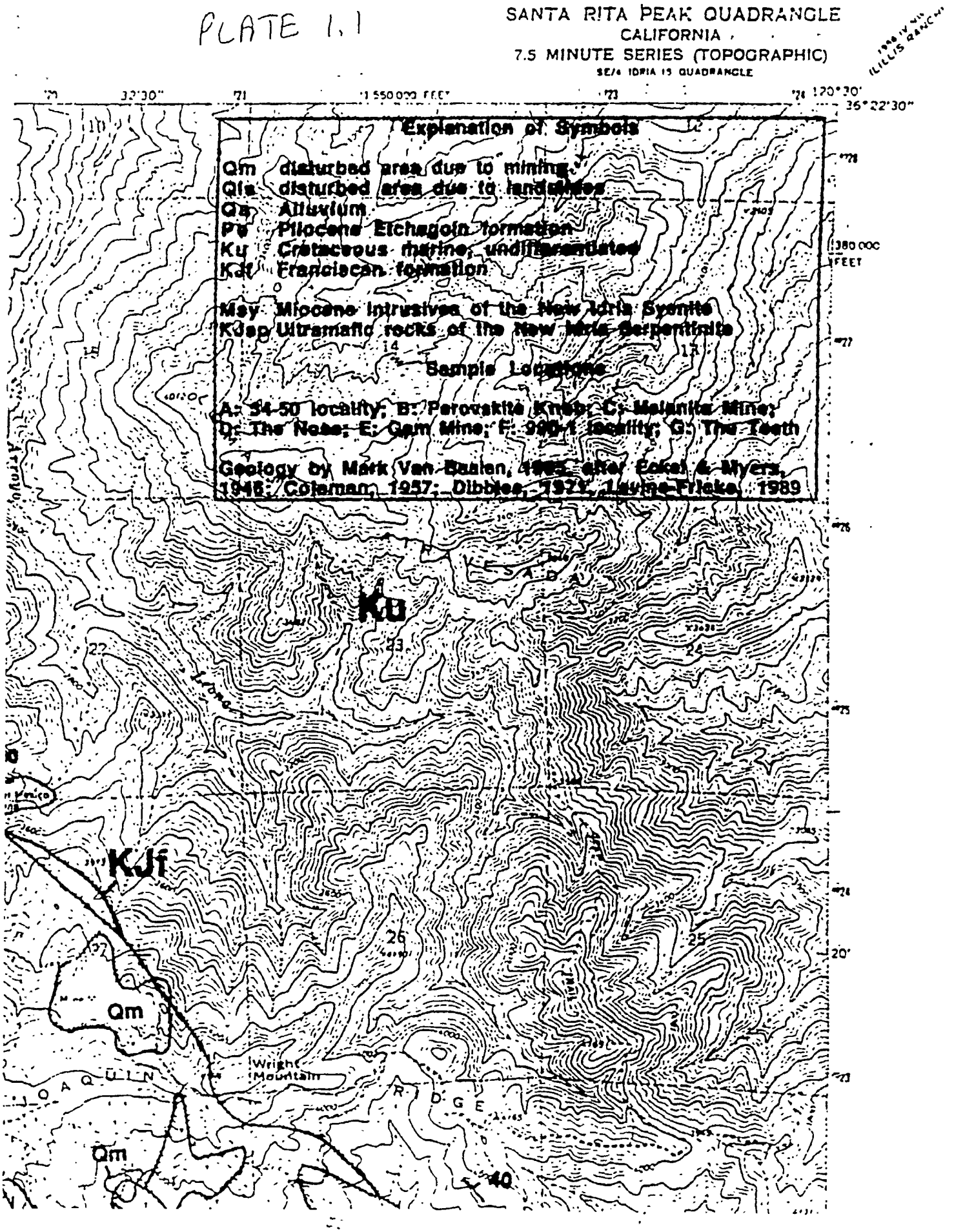
SANTA RITA PEAK QUADRANGLE
CALIFORNIA
7.5 MINUTE SERIES (TOPOGRAPHIC)
SE/4 IDRIA 15 QUADRANGLE
1958 IV NW
(LILLIS RANCH)
32°30"
71
1 550 000 FEET
73
120°30'
36°22'30"
Explanation of Symbols
Qm disturbed area due to mining
Qls disturbed area due to landslides
Qa Alluvium
Pe Pliocene Etchegoin formation
Ku Cretaceous marine, undifferentiated
Kjf Franciscan formation
Msy Miocene intrusives of the New Idria Syenite
Kusp Ultramafic rocks of the New Idria Serpentinite
Sample Localities
A: 84-50 locality; B: Perovskite Knob; C: Melanite Mine;
D: The Nose; E: Gem Mine; F: 990-1 locality; G: The Tooth
Geology by Mark Van Baalen, 1985, after Eckel & Myers, 1946; Coleman, 1957; Dibblee, 1973; Layne-Frieke, 1989
Ku
Kjf
Qm
Qm
Wright Mountain
RIDGE
380 000 FEET
22
23
24
25
26
27
40

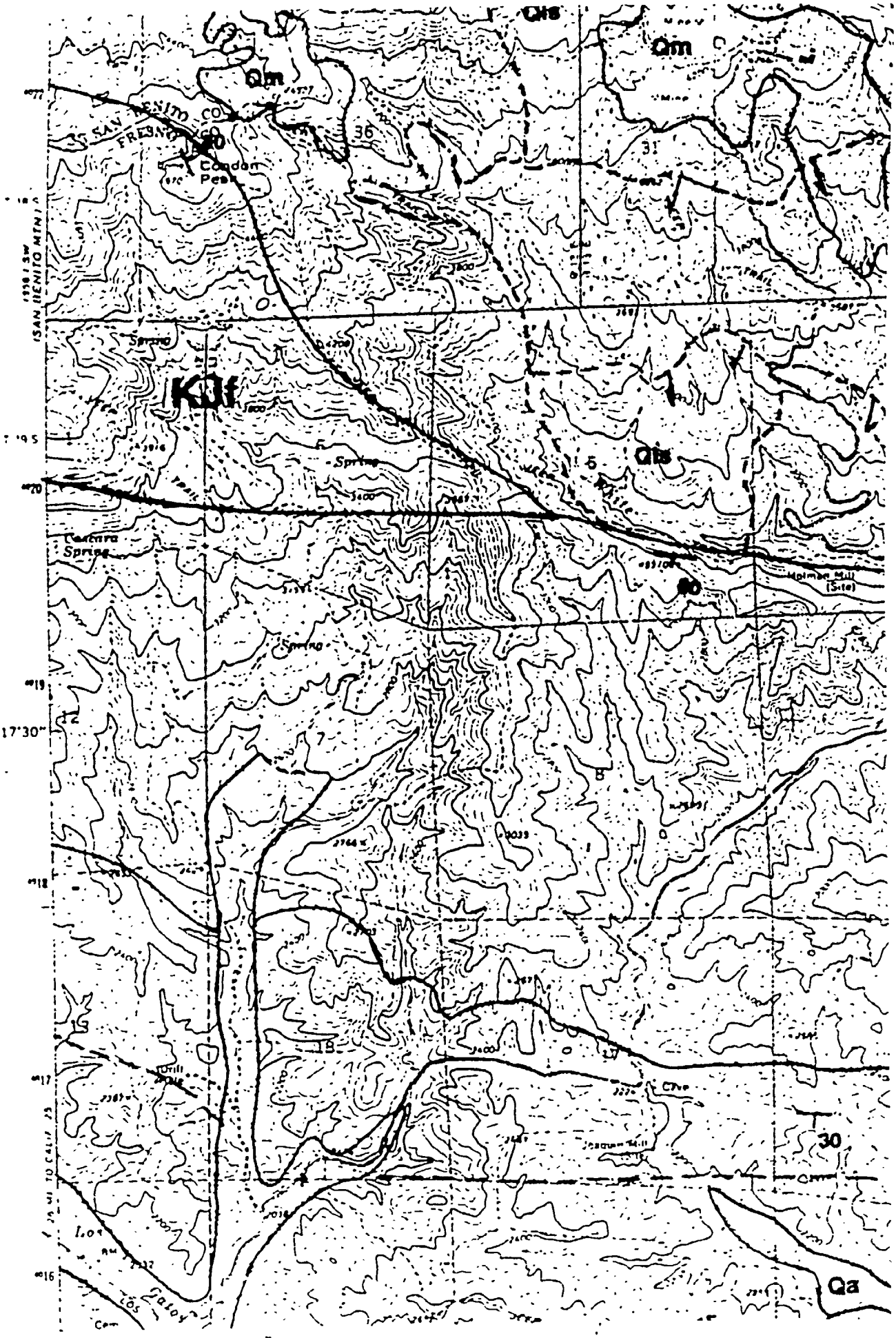
Qm
Qm
Qm
SAN BENITO CO.
FRESNO CO.
Condon Pea
36
31
Spring
KJf
Spring
Qls
5
Cuyama Spring
Holman Mill (Site)
80
Spring
17'30"
7
8
18
Drill Hole
Cmv
30
Qa
Los Gatos

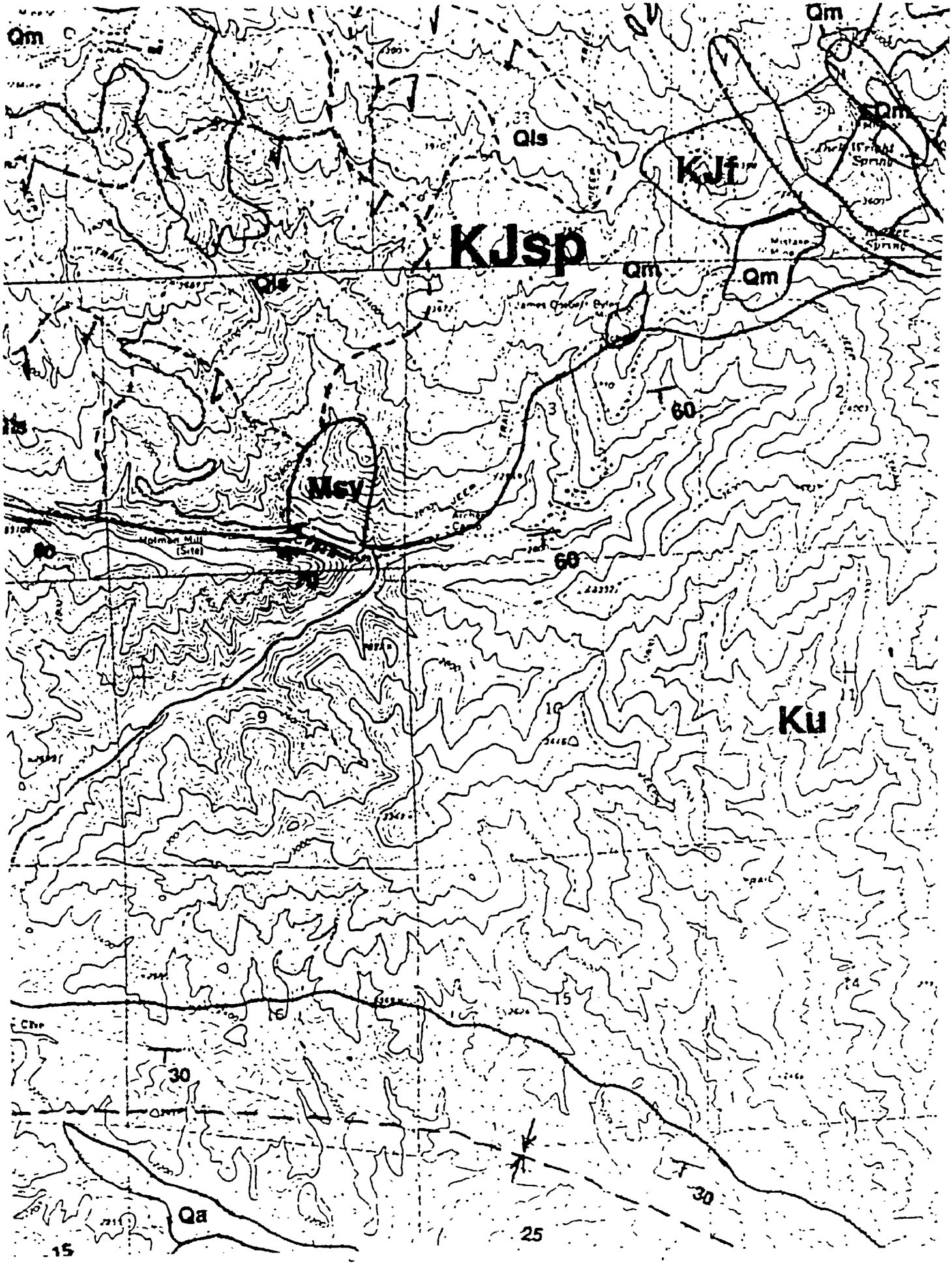
Qm
Qm
Qm
Qls
KJf
KJsp
Qm
Qm
Qls
Mcy
Holman Mill (Site)
Ku
Qa
60
60
30
30
25
15

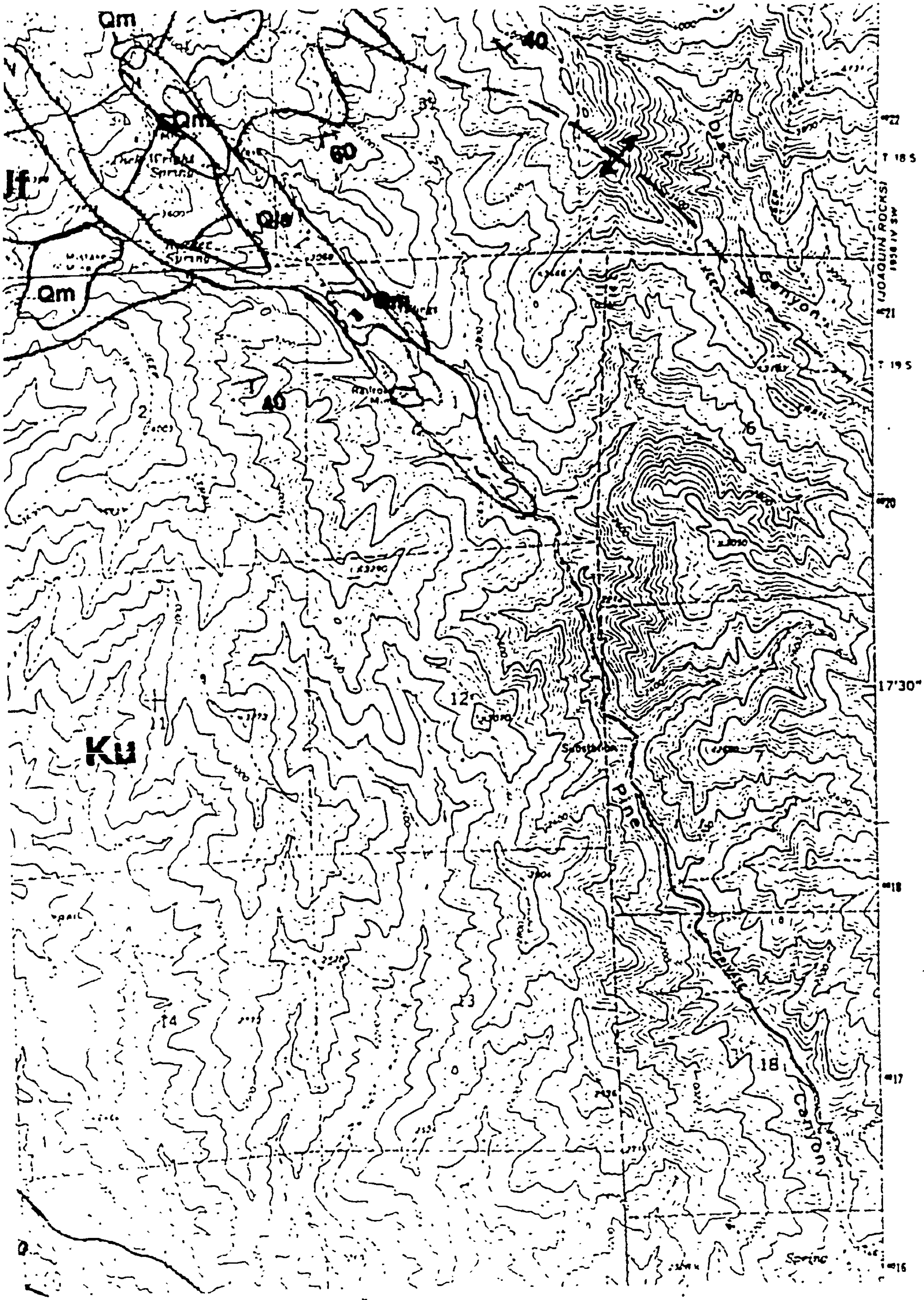

Qm
Jf
Qm
Qls
Qm
40
60
40
Ku
Pine
Canyon
Canyon
Spring
Substation
Railroad
17'30"
T 18 S
T 19 S
(JOAQUIN ROCKS)

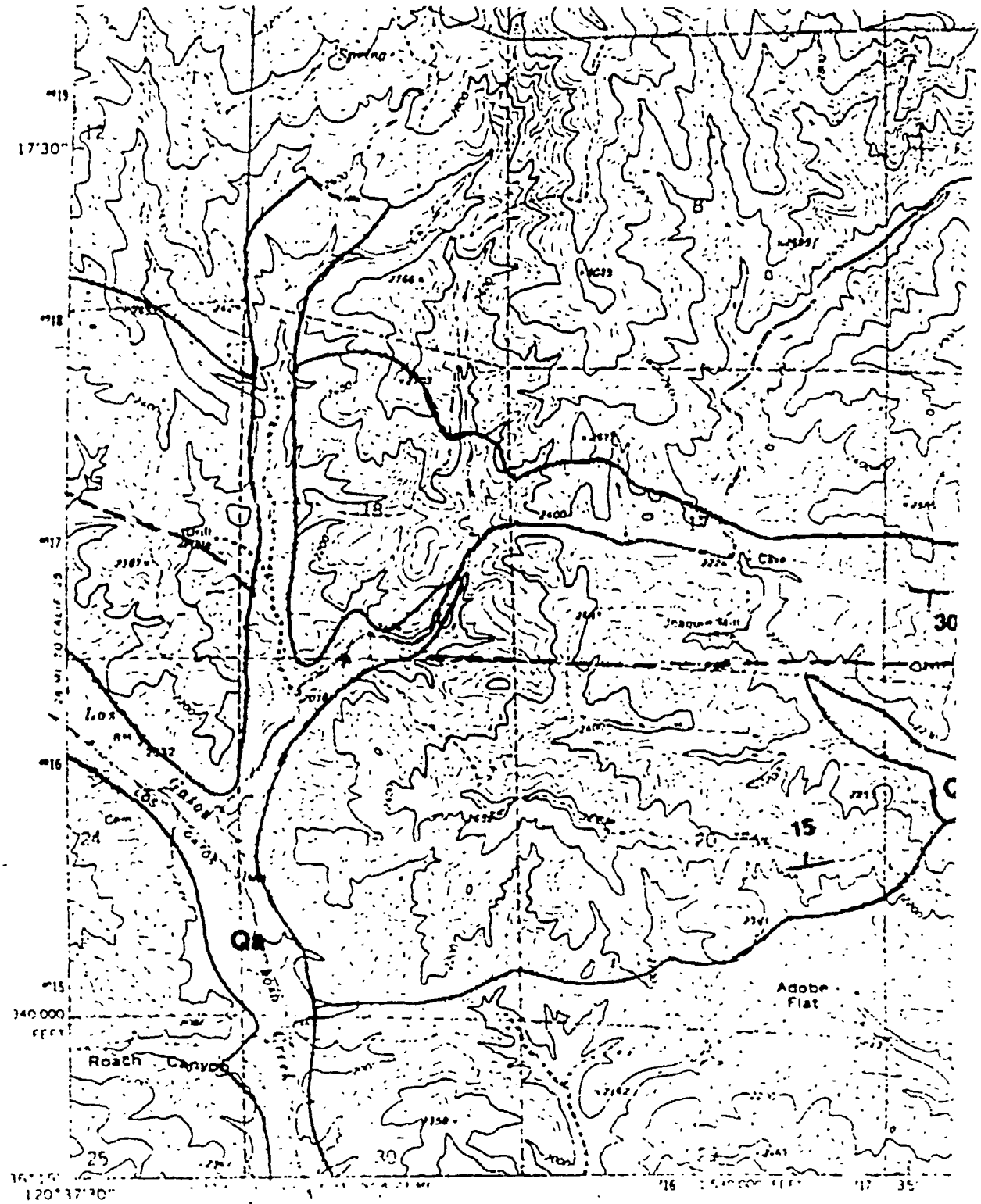

Mapped, edited, and published by the Geological Survey

Control by USGS and USC&GS

Topography by photogrammetric methods from aerial photographs taken 1957. Field checked 1969

Polyconic projection. 1927 North American datum
10 000-foot grid based on California coordinate system, zone 4
1000-meter Universal Transverse Mercator grid ticks,
zone 10, shown in blue

To place on the predicted North American Datum 1983, move the projection lines 8 meters north and

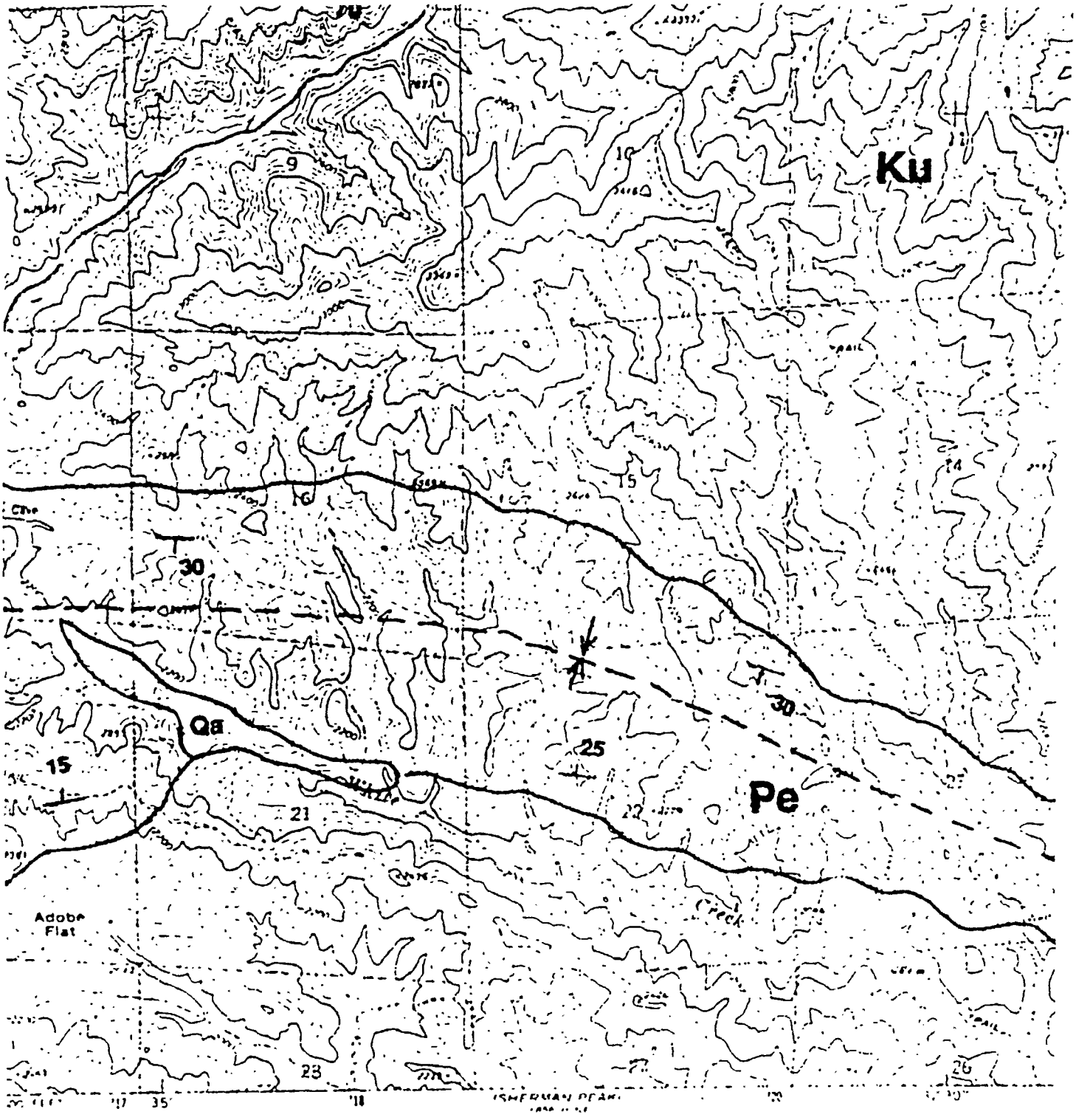
Ku
Qa
Pe
Adobe Flat
Creek
9
10
15
16
21
22
23
25
26
30
30
15

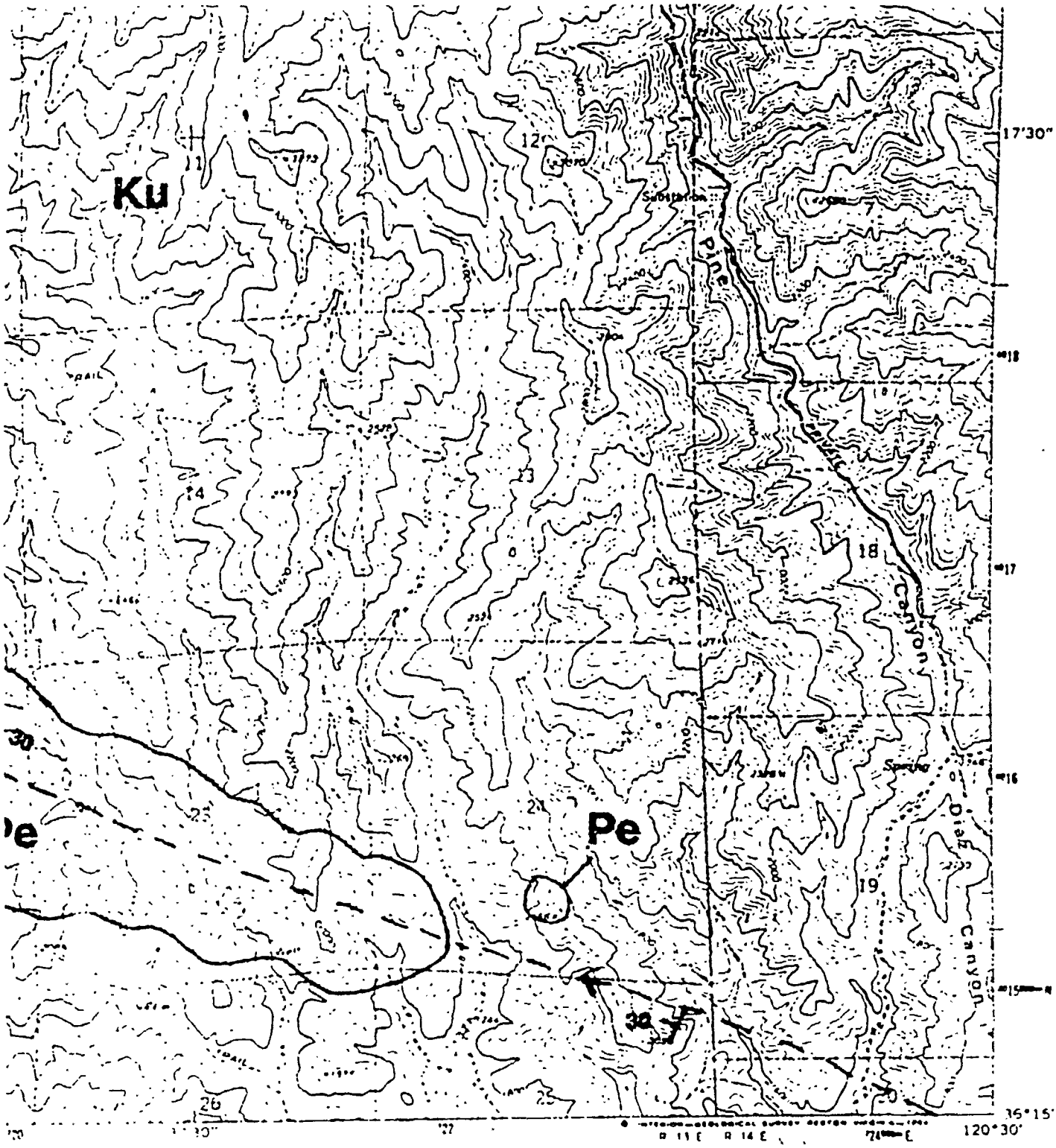

ROAD CLASSIFICATION

Primary highway, hard surface

Secondary highway, hard surface

Light duty road, hard or improved surface

Unimproved road

Interstate Route U S Route State Route

SANTA RITA PEAK, CALIF.

SE/4 IDRIA 15 QUADRANGLE

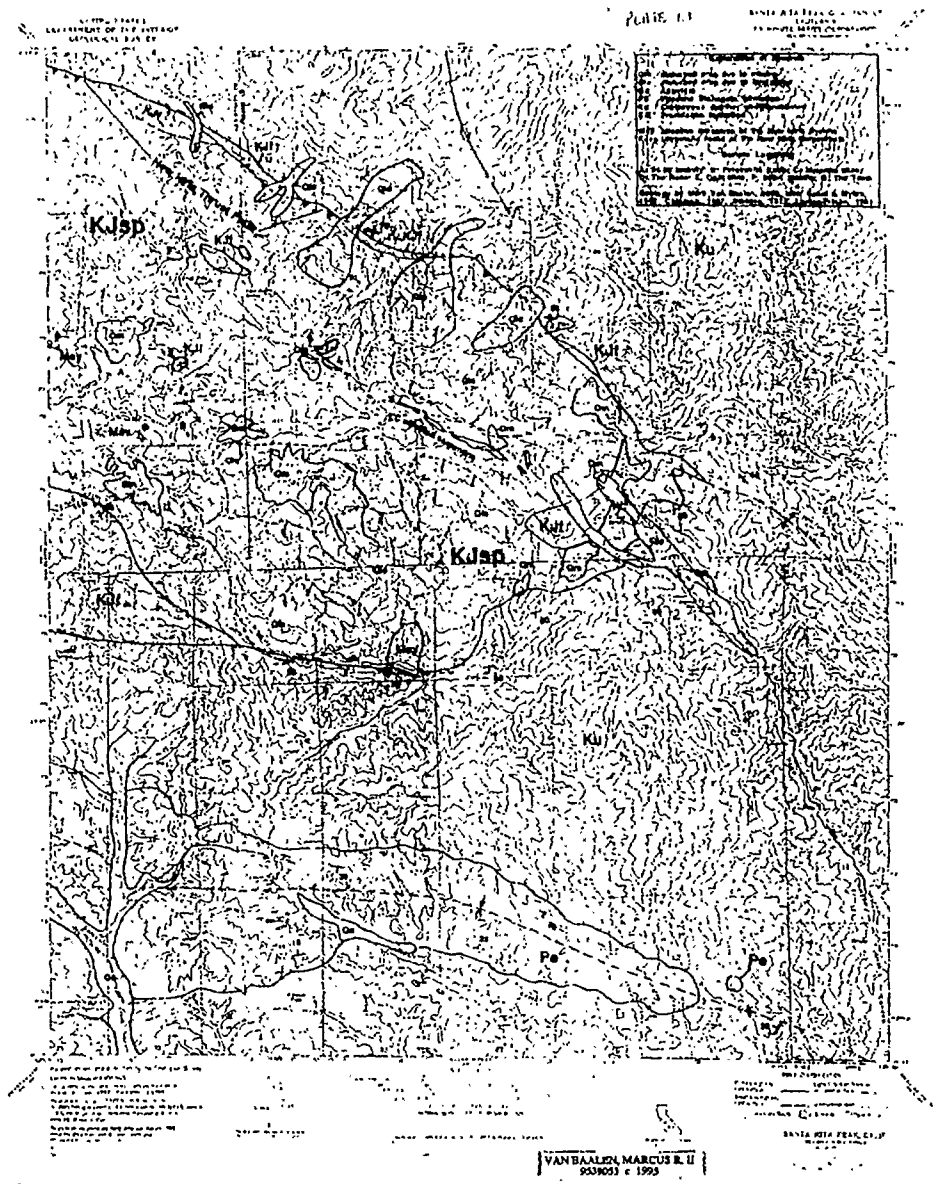
KJsp
Ku
Kuf
KJsp
Kuf
Ku
Pe
VAN BAALEN, MARCUS R. II